UNIVERSITÀ
DEGLI STUDI
DI TRIESTE

UNIVERSITÀ DEGLI STUDI DI TRIESTE

XXXIV CICLO DEL DOTTORATO DI RICERCA IN NANOTECNOLOGIE

Borsa MIUR/Ateneo cofinanziata dal Dipartimento di Fisica su fondi CNR-IOM

Terahertz Sensing with Golay cells microarray device

Settore scientifico-disciplinare: FIS/03

DOTTORANDO / A

ERIK BETZ-GÜTTNER

COORDINATORE

ALBERTO MORGANTE

SUPERVISORE DI TESI

MARCO LAZZARINO

TUTOR

SIMONE DAL ZILIO

ANNO ACCADEMICO 2020/2021

Acknowledgments

First and foremost I am extremely grateful to my supervisor, Marco Lazzarino, and my tutor Simone Dal Zilio for their continuous support and guidance, and their neverending patience during my Ph.D. study. Their immense knowledge and plentiful experience have taught me everything that I’ve learned during these 3 years.

My gratitude extends also to the Nano-Region project, which provided financial support for this project and allowed me to work and study in an environment full of ideas and innovation.

I would like to thank Elena Magnano and Silvia Nappini, for their treasured expertise and the help they lent me for XPS analysis. Another thank goes to Andrea Perucchi and Johannes Schmidt for their invaluable help and experience in the THz radiation, to Davide Truccolo, Laura Andolfi, and Alessia Matruglio for their technical support that was fundamental in my study, and to Alessandro Pitanti and the CNR-NANO group, for their support and advice in the THz detection. I would also like to thank all the members of the 3M laboratory and CNR-IOM that helped me during the Ph.D., and especially my colleagues Martina Conti, Michele Zanetti, and Pietro Capaldo. It is their kind help and support that has made my study and stay at the CNR-IOM laboratories a wonderful time. Finally, I would like to express my gratitude to my family, my friends, and especially my loved one, Arianna. Without her continuous encouragement and support, it would have been impossible for me to reach where I am now.

Contents

Abstract

The THz radiation is a part of the electromagnetic spectrum between microwaves and infrared. When described as made of photons, their quantum of energy is lower than k_BT at room temperature, and the strategies used in photon detection cannot be applied. When described in terms of high-frequency EM waves, the associated electron velocity in a material is faster than any known material. So the strategies used to generate or detect the radiofrequency cannot be applied. Hence, the use of the term THz gap to denote the lack of resources in a field that has otherwise many potential applications. Among the incoherent detectors commercially available in the market, the Golay cell is one of the most sensitive thermal detectors, however, its design remained practically unchanged since its invention in 1947. The advent of new technologies and materials like graphene could allow the breakthrough needed to innovate this detector and partially close the gap. Unfortunately, many practical limitations hindered its development towards application on the microscale. Here, I developed a fabrication method for the efficient sealing and enclosure of an array of micrometer-scale cells with an ultrathin membrane. The membrane is composed of CVD single-layer graphene and a reinforcing nm-thin titanium layer. A back-side sealing was provided by a silicone rubber cork: the two-side sealing allows the transfer of mm-sized membranes avoiding the problems arising during the membrane transfer from solution. These water- and gas-tight cells could be used for all those applications that require the efficient sealing of a wide variety of liquids and gases, such as the Golay cells. Throughout this thesis, I also explored different modifications of the membrane to improve its applicability into other fields, in particular improving its transparency to the photoelectron emitted in XPS analysis and proving its potential application in ultrahigh vacuum applications. Finally, I demonstrated the potential of the sealed arrays as Golay cells detecting the THz radiation emitted by a Globar source.

Introduction

Chapter 1

THz radiation

THz radiation is a part of the electromagnetic spectrum which falls between the microwaves and the infrared and like them it is non-ionizing. Historically, it was considered as a portion of the adjacent spectral regions, and named *submillimetre radiation* (as its wavelengths range from 1 mm to 10 µm [1]), if considered part of the microwaves, or *far-infrared*, if considered part of infrared radiation. Recently, many studies highlighted its hidden potential and over the years many names were used to describe the frequencies ranging from 0.3 to 10 THz, like T-rays, T-waves, terahertz light, T-light, T-lux, and so on[2].

THz radiation can pass through many non-conducting materials like fabrics, ceramics, cardboard, plastics, etc. however, it is limited in its penetration in metals, as they reflect most of the incident radiation, and water-filled materials like wet wood and hydrogels, as water is a strong absorber[3]. The water absorption bands also limit the use of THz waves on the ground, as the earth's atmosphere itself it's a strong absorber, affecting its use over distances more than a few tens of meters. Nevertheless, it can find many applications in the field of imaging and high bandwidth wireless networking, especially in indoor systems[4]. The main limiting factor towards achieving superior performances in these fields lies, however, in the difficulties in producing and detecting this radiation. The difficulty is particularly relevant due to its nature bridging between the radio frequencies (which are measured mainly by their frequency) and the optical band (which are generally measured considering the wavelength and its photon energy) of the electromagnetic spectrum. Unfortunately, its frequency is too high to be measured directly through electronic devices like antennae, as their commercial limits lie in the GHz frequencies. At the same time, its photon energy is also too low to be measured through semiconductor devices like in the optical part of the electromagnetic spectrum[2]. For the same reason, it’s also difficult to produce radiation employing the conventional electronic devices used for radio and microwaves generation or semiconductor devices such as laser, used for shorter wavelengths. Owing to these limitations, this part of the electromagnetic spectrum is still underdeveloped in comparison to the higher or lower frequencies, hence the name “THz gap”[1]. In Figure 1 is illustrated in particular the “gap” of the THz sources: electronics-based sources, such as **IMP**act ionization **A**valanche **T**ransit-**T**ime diode (IMPATT) or **M**onolithic **M**icrowave **I**ntegrated **C**ircuit (MMIC), becomes inefficient in the generation of high-frequency radiation, while semiconductor lasers suffer from the same problem at lower photon energy. In the middle of the “gap” have recently emerged new technology such as **Q**uantum **C**ascade THz **L**asers (THz-QCL) that shows promising results in the hope of closing the “gap”[5].

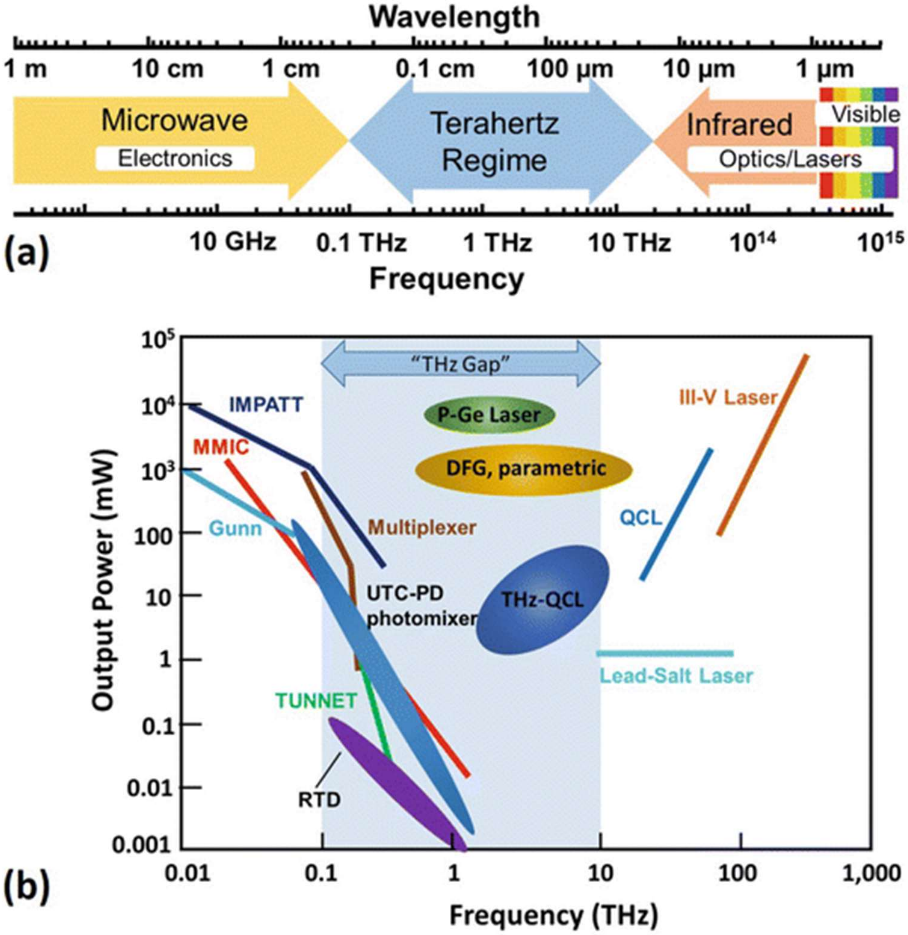

Figure 1 Illustration of the “terahertz gap” related to the lack of efficient sources (and detectors). Electronic devices like Resonant-tunneling-diode (RTD), the uni-traveling-carrier photodiode (UTC-PD) photomixer, or the tunnel injection transit time negative resistance diode (TUNNET) cannot generate an high power output in the higher frequency THz region, while semiconductor based devices are limited by the band gap at lower energies. [5]

Nonetheless, its remarkable properties, like the long penetration into many materials, the "terahertz fingerprints" that are unique to each material and allow for precise qualitative characterization, or its non-ionizing nature, which is a requirement to be deemed as safe to use in biomedical applications, made the terahertz into a promising candidate for many different applications in a large variety of fields[6].

THz Applications

The applications of the THz radiation are mainly based on two types of setup for its generation and detection: pulsed systems, and Continuous Wave (CW) systems. In the pulsed systems, the evolution over time of the THz electric field of a single pulse is analyzed. Through the Fourier analysis of the measured pulse, a high amount of information can be retrieved about the media in which the radiation has passed through thanks to the unique frequency and phase response of each material[7]. The main disadvantage of this technique is related to the high acquisition time required for each sample analysis[8]. Nevertheless, the recent introduction of new sampling and analysis algorithms such as asynchronous optical sampling (ASOPS) allowed for reasonable analysis time without information loss, widening the field of application for this technique[9]. The continuous wave (CW) approach, instead, provides information on the average intensity of the electromagnetic field using relatively simple and cost-effective setups [10], [11]. These systems use the attenuation of the THz wave passing through a medium. Phase information can be acquired as in the previous case, however, it is more time-consuming and complex[12]. The time required for each analysis is generally shorter than with TDS, which makes it a better candidate for higher production rate lines in the industry.

THz imaging applications, based on both pulsed and CW systems, are a major topic for its relevance as one of the most important practical applications of THz. The ability to image complex systems to identify possible defects and damages in 2D as well as in 3D has long been studied, and its currently applied for instance in the maintenance of large cement-based infrastructure. Due to the complexity of THz systems, usually, the 2D images are taken with raster scanning techniques[13], but recently alternative ways such as impulse scanning[14] or electro-optical conversion in which part of the femtosecond laser probe is used for detection while part of the beam is used for generation in pulsed setup [15]. The main techniques for 3D images instead are computer-based[16] and diffraction tomography[17], which uses the terahertz to create 2D "slices" on different planes of the sample that are reconstructed through automated systems. THz spectroscopy instead is based on the changes of both phase and amplitude of the THz field passing through a medium and are directly correlated to the absorption coefficient and refractive index of said material[18]. Furthermore, thanks to a complex material identification algorithm based on pattern recognition and the aid of high-performance computing, this technique can be applied as either single-point measurements as well as 2D images or 3D reconstructions[19]–[22].

Biomedical and clinical

THz radiation presents both advantages and disadvantages when applied to the biomedical field. The low energy of THz photons (1-12 meV) does not directly damage cells and tissues and it is limited to the heating of the irradiated tissue. The photon energies in the order of $\sim 10^{-21}$ J are also extremely promising for vibrational spectroscopies as they are of the same order of magnitude of molecular vibrational, torsional, and librational modes in liquids and solids[23]. However, the same sensitivity to molecular modes is also the cause for the broad absorptive loss of THz energy in water as shown in Figure 2, which leads to the high absorption of the human body, (which is composed of ~70% of water)[26].

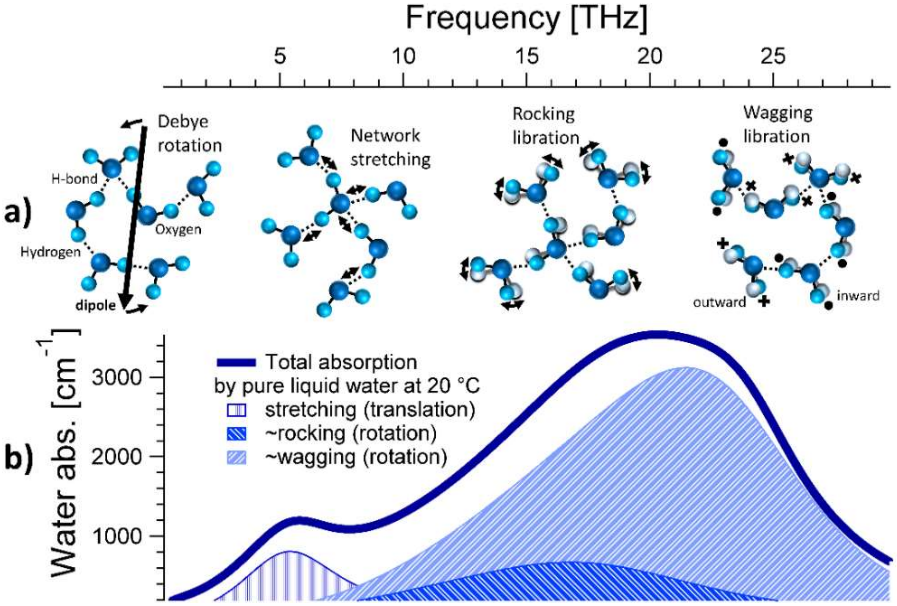

Figure 2 Molecular rotation libration and stretching modes of water are the cause for its high absorption of radiation in the THz regime. [23]

Nevertheless, the same large absorption of THz by the human body that limits the penetration of the radiation also promotes the high contrast between substances with different degrees of water saturation. Thanks to this property, THz has been used for the identification and imaging of tissues both in-vivo and ex-vivo through the detection of changes in refractive index, or absorption on the surface, or near-surface of skin lesions, or in wax mounted samples[24]. Assessing burn damage[26], skin hydration[27] and tumor infiltration[13], [28] are also studies directly interested by the possibilities offered by this technology. The imaging is especially promising towards the identification of tissues with different water content as in Figure 3. The contrast in the THz image of Figure 3c and g for instance highlights the difference between a tissue with low water content (like adipose tissue) and cancerous tissue with high water content. The THz also offers the possibility of tomographic imaging, capturing 3D images of the tissue of interest (like teeth[29] bone, or fat[30]) while highlighting the presence of different chemical or structural compositions, with or without the use of contrast agents. The difficulty in the use of this technique lies in the generally low contrast between the affected and healthy tissue (which does not always present a large difference in the water content) and many studies are currently focused on the implementation of systems or methodologies to overcome this problem, such as acquiring large dataset to confront with the help of the machine learning or the use of contrast agents that binds to the tissue of interest[31]–[34].

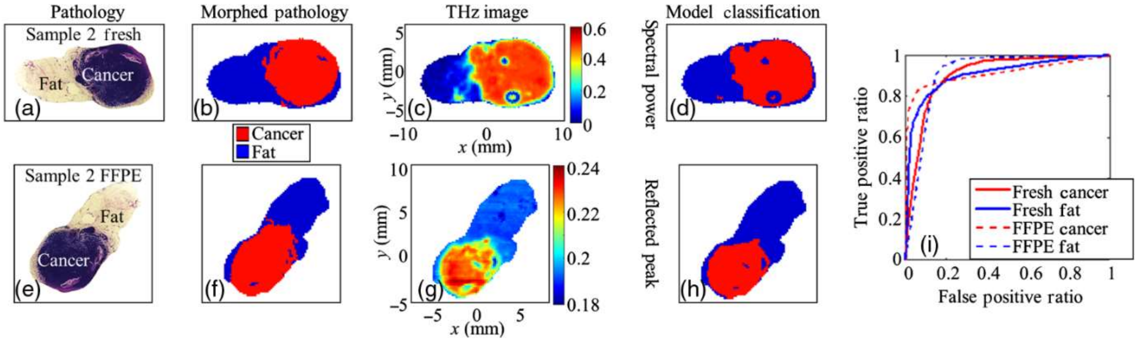

Figure 3 Tumor identification and imaging. The tumorous mass is clearly differentiated from the adjacent adipose tissue even in the absence of contrast agent but only based on the different absorption due to the water content of the tissue. [30]

Non-Destructive Testing

Almost all engineering and structural materials are particularly vulnerable to the presence of defects, voids, delaminations, cracks, inclusions, etc. The presence of these vulnerabilities in the final materials may be due to a variety of causes and can be introduced in every part of the production and lifetime of any material. For this reason, extensive work has been implemented to avoid them, optimizing processes and selecting the best starting material. Nevertheless, their presence cannot be completely prevented, and often the only solution consists of careful testing and continuous analysis over the entire lifetime of the manufactured item[35]. Among the non-destructive testing (NDT) techniques commercially available, the THz has attracted particular interest, especially in the last two decades thanks to the drastic improvement in the field of detectors and THz sources. The main reasons for this interest are the penetration and imaging capabilities of THz radiation. The former is due to the high transparency that many engineering materials, like wood, ceramics, and polymers, present towards this part of the electromagnetic spectrum[36]. The imaging instead, even if limited by the diffraction limit of its relatively large wavelength, it's still widely better than other material inspection techniques, i.e., ultrasonics, thermography[37]–[39]. Another important aspect is the possibility of integration in highly automated processes which is a fundamental requirement for the current industrial era.

Direct applications of THz-based techniques to NDT can be found in composite materials production and quality controls, searching for the presence of voids and defects, thanks to the sensibility of THz imaging systems to the orientation of the fibers, inclusions, and delamination[40]–[42]. In this particular field, THz imaging provides better information and contrast for the recognition of defects compared to other NDT approaches like ultrasound imaging[43]. Other applications in this field include the analysis of pharmaceutical coatings for modified-release dosage, car and marine protection and anti-fouling paints, thermal barrier coating for high-temperature application, and wood and cement constructions quality assessment. In pharmaceutical drugs production, the tablets containing the active ingredients are required to present uniform thickness and material distribution, which may otherwise affect the sustained release of the therapeutic drug. THz has been used especially for the thickness characterization and distribution in multilayered films coating as well as the recognition of hidden defects and inclusions inside the tablets[44]–[46]. Car and marine paints have both aesthetic and

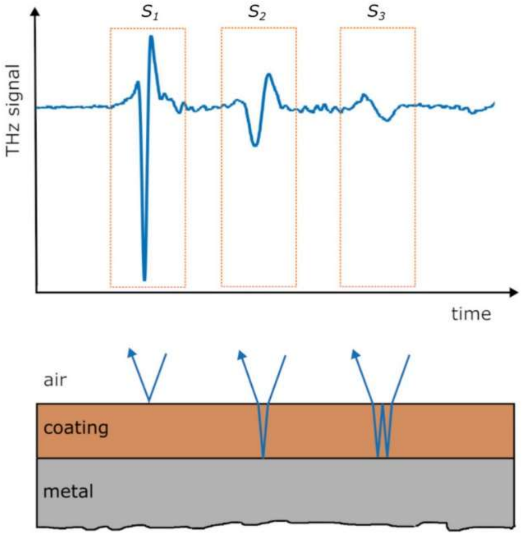

Figure 4 Determining the thickness of thermal barrier coating through THz-TDS Reflection measurements [53]

functional purposes, such as protection from UV, corrosion, and scratches and for this reason, the uniformity and absence of hidden defects are mandatory requirements for the creation of high-quality coatings. THz in this field has been used in particular for thickness characterization with similar results to X-ray and ultrasound testing, but with non-contact and safety advantages[47]–[49]. Thermal barrier coatings (TBC) are advanced systems applied to gas turbines and aero-engines to protect them from the extreme conditions required for their functioning. The submillimeter radiation is used for the thickness assessment of coatings thicker than 10 μm as shown in Figure 4 and becomes very interesting in the monitoring of the lifetime of thermally grown oxides which increase in thickness over working hours[50]–[52]. For large structures of either wood or cement, during the construction and lifetime of the manufact, defects and organic or chemical damage usually arise, reducing the safety and usability of that particular structure. In an effort to constantly monitor these manufacts conditions, THz radiation offers interesting opportunities for the detection of water intrusion, cracks, and voids during both the life of the product and its construction [53]–[56].

Security

As plastic explosives, fertilizer-based bombs (like ammonium-nitrate explosives, also called ANFO), and chemical and biological agents propagate as weapons for terrorism and illegal drug trafficking, new, fast and reliable technologies for security emerge against them[57]. In this field, THz radiation has come to light for its promising applications, such as revealing and qualitatively analyzing substances even through layers of clothing. Compared to other technologies like millimeter-wave imaging (MMW) already used in security applications[58], [59], the THz indeed offers a higher spatial resolution coupled with the

Figure 5 Imaging results of a real-life THz application for the detection of body-borne concealed threats, a belt with explosives and a gun [63]**.**

spectroscopic signatures of many dangerous materials such as explosives like C-4, HMX, RDX, and TNT, and drugs like methamphetamine, where each of them presents its unique spectrum[60]–[62]. The high reflectance of metals also demonstrated high contrast in the imaging of concealed weapons like knives and guns as shown in Figure 5 [63].

The dominant feature for the former application is derived from the sharp absorption peaks caused by phonon modes directly related to the crystalline structure[64]. This results from the vibrational modes and intramolecular vibrations that characterize crystalline explosives and drugs. Unfortunately, the same advantage becomes a disadvantage towards amorphous solids like ammonium nitrate (AN) which is one of the most common “dirty” explosives used in improvised explosive devices (IED)[65]. Solutions for this problem are still under discussion but include the confrontation of different spectral absorption on different THz frequencies as a standard, instead of using the recognizable spectrum over a broad emission, or the search for other more crystalline secondary components in the explosives. The drugs detection suffers from the same problem but remains promising for its ability to efficiently detect MDMA, methamphetamine, and Naproxen sodium, through the complex packaging used to hide them to border controls[66].

Food and Agriculture

The rising food quality standards necessitate fast measuring methods for the objective characterization of the products as they move from producer to consumer. While mid-infrared and near-infrared provide intramolecular information, such as characteristics bonds that indicate the presence of determined molecules, the THz can be used to obtain intermolecular information like alignment, the presence of hydrogen bonds, or the presence of crystalline or amorphous structure[67]. The use of THz spectroscopy has become especially relevant in the latest years due to the increase in the use of pesticides, hormones, and chemicals which raises concerns for public health. The fast, cost-effective, and non-destructive THz analysis has shown promising results by demonstrating the distinct spectral signatures of many chemicals like pesticide residues that were detected in tomatoes, cabbages, spinach, and strawberry. These chemicals showed distinct lines in the spectrum between 20 to 400 cm^{-1} compared to the untreated control[68]. Many other pesticides spectra were defined and may be used to detect residues in rice and potato-based products[69]. TDS was also used for the identification of melamine residues in milk powder, which is a fundamental safety issue in child care[70]. Another field concerned with the identification of contaminants is livestock production, as the systematic use of veterinary drugs is a challenge for consumer health and environmental contamination. For these reasons, monitoring plans are being implemented and the THz demonstrated its feasibility for the identification of antibiotics (such as Sulfapyridine) in pure feed, milk, and egg powder samples as reported in Figure 6 [71].

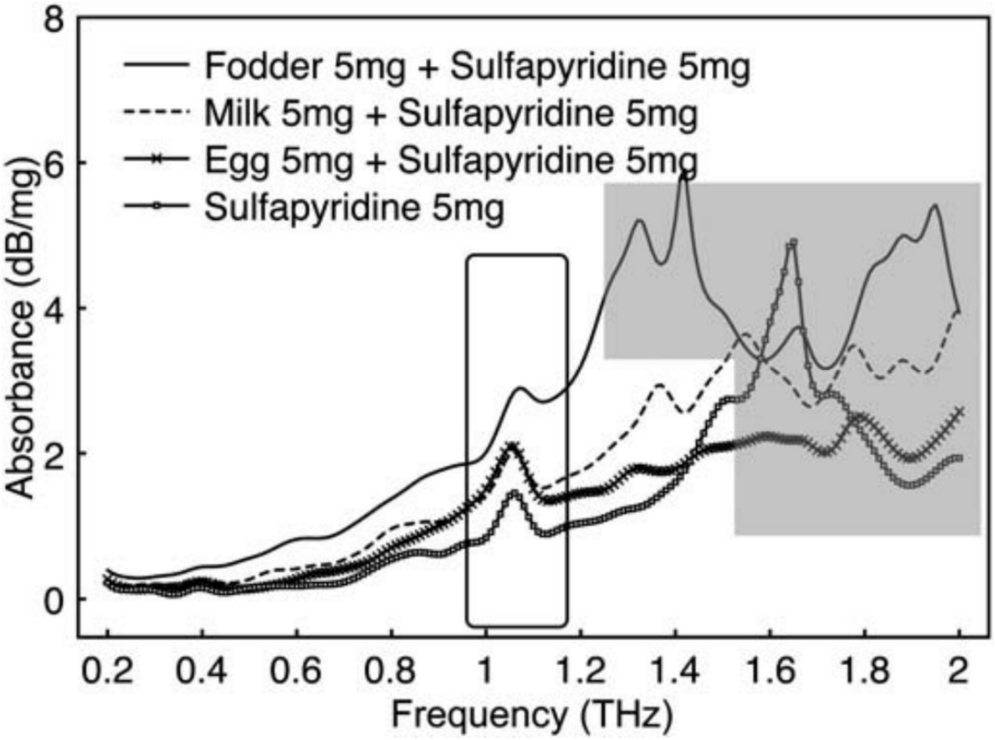

Figure 6 Sulfapyridine mixed with the three food matrices at 50% ratio. The peak at 1.05 THz identified in the three matrices, is unique to the antibiotic. The grey area indicates the region of peaks representative for each food matrices. [71]

On the same line of research, the THz was used to monitor the presence of food additives like saccharin in soft drinks thiabendazole,o-phenylphenol in grapes, bananas, and lemons, and ethylenediaminetetraacetic acid disodium salt dehydrate in mayonnaise and canned food[72]. The high absorption of THz by the water content is another important aspect of this application, as TDS was applied in the determination of the water content in butter, the dielectric properties of vegetable oils and lard, and the moisture content in intact food samples[73]–[76]. Its applications extend also to the aqueous solution, for the quantitative determination of alcohol and sugar contents in alcoholic beverages[73]. THz imaging has also been applied in the food industry, thanks to its penetration through common food packaging which allows non-destructive and safe testing compared to X-ray and other techniques[77]. For instance, THz imaging has been proven useful in the determination of foreign bodies in chocolate tablets, demonstrating the ability to differentiate between hazelnuts and other particles (such as plastic, glass, or stones used for testing) through phase imaging[78]. Another example of application is the imaging of ripe grapes, differentiating them from stems and leaves and demonstrating the possibility to predict the yield of certain high water-content crops[79].

Sources and Detectors

Natural and artificial sources

In nature, THz is emitted by all objects in the universe, albeit this emission is very weak. Its spectrum is described as blackbody radiation and it becomes relevant for cold objects, like dust or gas clouds in galaxies with temperatures between 3 K to 100 K and whose emission peak is in the THz band as shown in Figure 7 [80]. For this reason, natural sources have been widely studied in astronomy[6].

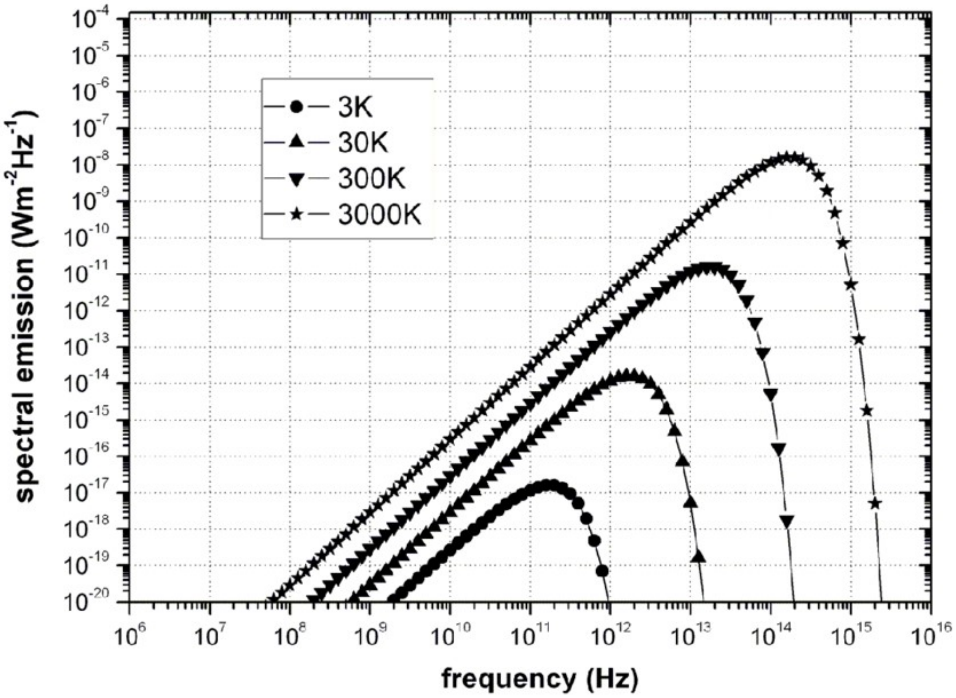

Figure 7 Black body emission as described by Planck's equation for various temperature. At low temperature the blackbody radiation is peaked in the THz, for this reason this band is interesting for the analysis of cold bodies and dust in astronomy[80]**.**

Artificial sources, instead, can offer many more possibilities to the THz field of applications. Indeed, as the THz radiation is heavily absorbed by the water present in the atmosphere, thus the sources of radiation need to be close to the detector (usually a few meters). Due to this requirement, the recent research focused on relatively portable and efficient sources [81] like solid-state devices and lasers. Other sources mainly used for research instead of direct application, focus on high brilliance radiation and are based on complex structures like synchrotron and free-electrons lasers. Solid-state devices (like Gunn, IMPATT, or TUNNET diodes) are commonly used to generate GHz at THz frequencies[82], even while being affected by noise due to avalanche processes or thermal instability, thanks to their relatively low cost and fast pulses. Lasers instead use the stimulated emission between two energy states in a gain medium to produce THz radiation. These states can be molecular rotational levels (used in Far-Infrared gas lasers), Landau levels (used in p-type Germanium lasers), or intraband transitions within a semiconductor conduction band (as in quantum cascade lasers)[83]. Finally, electron accelerators generate electromagnetic radiation by accelerating and bending electrical charges. Since the acceleration depends on the charge-to-mass ratio of particles, THz generation is based on electrons as charged particles[84]. These electrons can be free-electrons in vacuum (as in the case of synchrotrons, gyrotrons, free-electron lasers), or free charge carriers as for photoconductors (like photoconductive antennas or photo mixers) [85]–[87].

Gunn Diode

This solid-state source is based on a two-terminal negative differential resistance (NDR) device, that in conjunction with a tuned alternated current resonator, is capable of generating radio frequencies. It is typically composed of a uniformly doped n-type semiconductor formed by elements III-IV (like GaAs, or InP) placed between heavily doped regions at each terminal. In the semiconductor, the valence and conduction band present valleys that create a varying energy gap (ΔW) along the semiconductor crystal orientation (k) as shown in Figure 8 The electronic structure of the semiconductor in the GUNN diode is characterized by different valleys in which the electrons present different effective mass and mobility. Bottom, increasing the voltage applied on the diode induce part of the carriers to change valley, resulting in a different mobility and thus presenting a negative resistance region.. The electron that resides in each valley presents different effective mass (m) and mobility (μ)[88]. When a bias is applied across the Gunn diode, the electron achieves enough energy to transfer to a valley that presents higher effective mass and lower mobility (for this process the Gunn diode is also known as transferred-electron device). Increasing the voltage in this diode causes a proportional decrease in the current passing through the device due to the drift velocity of the electron being reduced by their increasing effective mass when some of them pass to the higher energy valley. This phenomenon exhibited by the Gunn diode in the NDR region gives rise to AC oscillations at the contacts when the diode is biased due to the local perturbations in the net charge. Finally, the Gunn diode is placed in a cavity or resonant circuit in such a way that its negative resistance cancels out the resistance of the resonator, causing an oscillation of the circuit and the generation of electromagnetic radiation up to the THz region. The Gunn diode has a low fabrication cost coupled with good reliability and bandwidth and low noise compared to avalanche devices, however, it is limited by the sensitivity of the emission frequency to the change in temperature and bias, which originates from the instability of the NDR region.

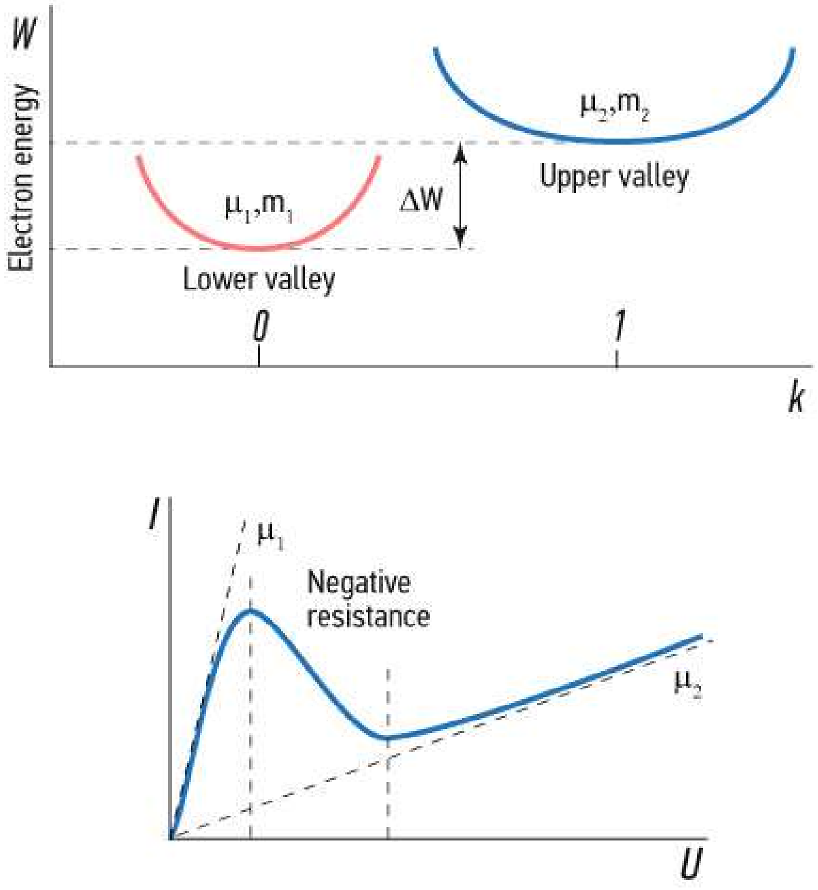

Figure 8 The electronic structure of the semiconductor in the GUNN diode is characterized by different valleys in which the electrons present different effective mass and mobility. Bottom, increasing the voltage applied on the diode induce part of the carriers to change valley, resulting in a different mobility and thus presenting a negative resistance region. [88]

IMPATT diode

The IMPATT (or impact ionization avalanche transit time) diodes are NDR devices like the Gunn diodes. Their basic structure is represented in Figure 9 The basic structure of the IMPATT diode is composed by an avalanche and a drift region between a p-n junction. In the avalanche region an impact ionization occurs when bias is applied to the diode. By tuning the length of the drif region it possible to induce a NDR zone in the diode, that could work for the THz detection when coupled with a resonant .external circuitis composed of a p-n junction and a high resistivity layer on which is applied a reverse bias[89]. When the bias applied exceeds a specific threshold. An avalanche breakdown due to the impact ionization occurs. This results in a large number of carriers in the avalanche region that is formed by the p-n junction. The electrons then move in the high resistivity layer towards the other electrode in a time known as the "*transit time delay*". By increasing the voltage over the threshold while applying an AC signal, the carriers are generated with a rate dependent on the electric field as well as the number of carriers already present. For this reason, the current continues to rise even as the AC voltage decreases with a delay of 90° with respect to the voltage. By tuning the length of the diode it is possible to generate a further delay of 90° resulting in a negative differential resistance[89]. By coupling this device with an external resonant circuit as for the Gunn diode its possible to generate electromagnetic radiation. The main disadvantage of this device is the phase noise generated by the random avalanche process.

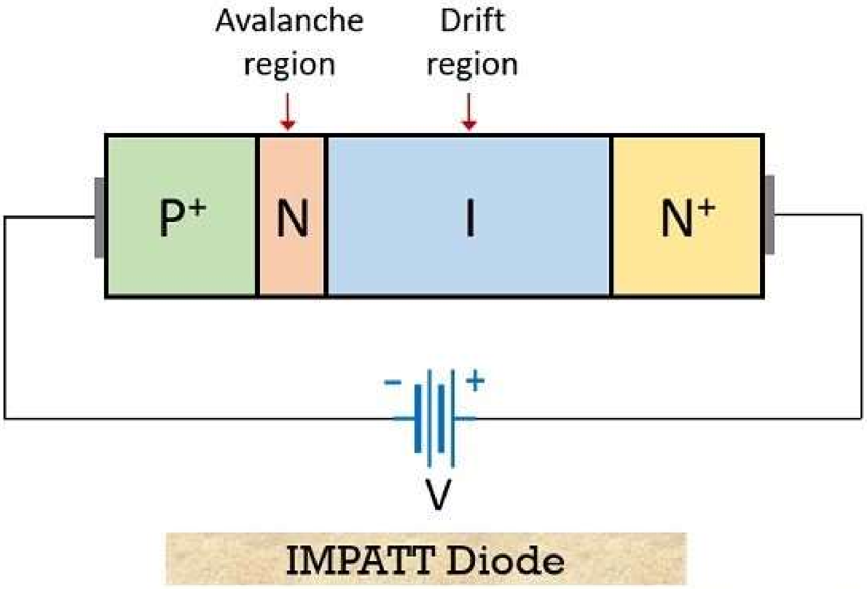

Figure 9 The basic structure of the IMPATT diode is composed by an avalanche and a drift region between a p-n junction. In the avalanche region an impact ionization occurs when bias is applied to the diode. By tuning the length of the drif region it possible to induce a NDR zone in the diode, that could work for the THz detection when coupled with a resonant .external circuit. [89]

TUNNETT diode

The “TUNNEl injection Transit Time diodes” are based on a highly doped and narrow junction based on a p^{++} n^{+} nn^{+} structure. This peculiar structure changes the carrier generation mode when the frequency applied is increased over a certain threshold. Indeed, the dominant carrier injection mechanics changes from avalanche to mixed tunnel-avalanche mechanism[90]. In the previously described IMPATT diode the avalanche carrier generation was proportional to the increase in the current applied to the device, in the TUNNET diode instead, the tunneling mechanism does not depend on the current density. Due to this reason, there is no injection delay, and the negative differential resistance (NDR) region is reached by the transit time of the carriers through a drift region with a lower electric field than the IMPATT diodes. Like the other NDR devices described previously, the TUNNET diode needs to be coupled with an external resonant circuit to generate electromagnetic radiation up to the THz region. Thanks to the tunneling process, this diode is faster and presents less noise than the impact-ionization-based diode, providing a medium power at high frequencies[90].

Far-IR Gas Laser

Also called optically pumped THz lasers (OPTLs), they emit THz radiation using the transitions between rotational states of gas molecules that present a permanent electric dipole moment, like CH_3, CH_2F_2, or CH_3OH[91]. Optical pumping is a process that uses a light source (typically a CO_2 laser) to excite (or pump) electrons from a lower energy level to a higher one as shown in Figure 10 [92]. Exciting electrons to higher vibrational level results in a state in which more of the electrons exist in the excited state than in the lower. This state called “population inversion” between the rotational states, give rise to THz radiation with transitions depending on the type of gas molecule in use. Due to the large energy gap between the rotational and vibrational state, the overall process is inefficient, resulting in most of the radiation from the pump source being converted to heat. Another limitation lies in the untunable nature of these lasers, as their emission is a property of the gas used cannot be tuned to higher or lower frequencies. Still, these lasers can produce up to 100 mW to frequencies up to 8 THz in the parallel or orthogonal direction to the pump radiation, and are for these reasons are widely used in the research field [91].

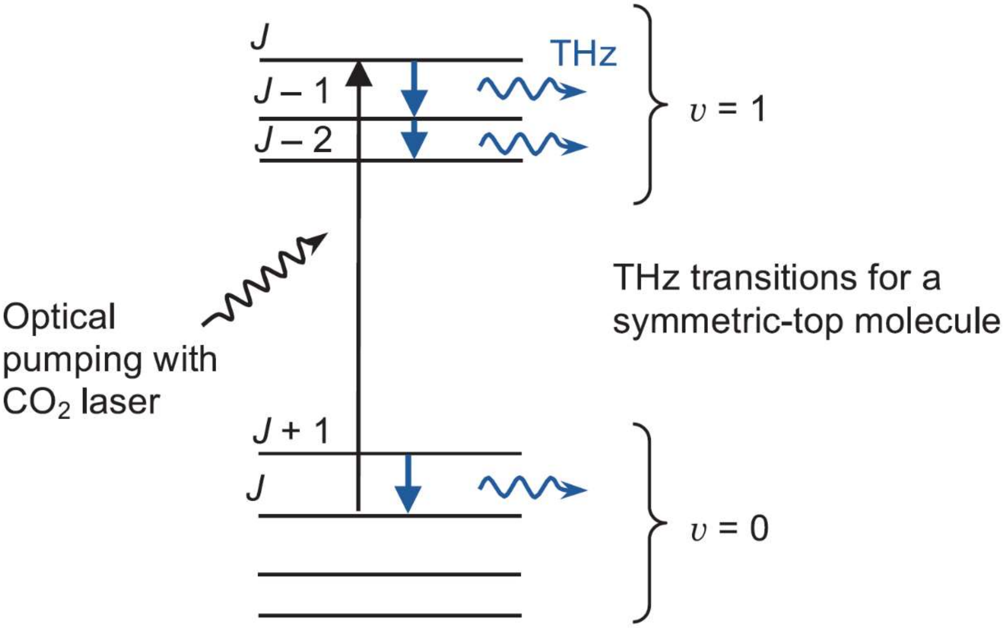

Figure 10 The emission of a Far-IR laser is based on the transitions between vibrational states of simple molecules. To excite electrons to an higher level, an optical pump (generally based on a CO_2 laser) is used. [92]

p-Type Germanium Laser

The p-Ge lasers are tunable, solid-state lasers based on the population inversion between valence subbands in a crossed electric and magnetic field. The top of the valence band of germanium consists of degenerate bands in the p-doped semiconductor where the holes have different masses, namely light- and heavy-hole bands. In the presence of a magnetic field, these bands show a quantization of their energies into discrete levels known as Landau levels [92]. When an electric field is applied perpendicular to the magnetic field, the heavy and light holes can be accelerated to different energies. By regulating the ratio between the magnetic and electric fields, it is possible to adjust the energy of the light holes to be lower than that of the heavy holes. If this condition is achieved, the heavy holes can spontaneously emit phonons and scatter to the light-hole band, while the light holes are not able to emit phonons. This induces a *population inversion*, as most of the holes present in the semiconductor under the crossed electric and magnetic field are composed of the light-hole Landau levels. The emission of the laser is generated by the direct optical transition between the light and heavy-hole subband which occurs over a wide frequency range [93]. Thanks to these transitions, the p-Ge lasers are tunable on frequencies ranging from 1 to 4 THz, but require constant cooling to liquid He temperatures to avoid optical and acoustic lattice scattering phenomena. Additionally, due to the high heat generated at each impulse, these lasers are limited to short pulses and slow repetition rates.

Quantum Cascade Laser

QCLs are based on heterostructures of semiconductors that work as unipolar devices exploiting the two phenomena of quantum mechanics: quantum confinement and tunneling. In these devices, only the electrons are exploited for their transitions (unipolar) between conduction band states (intersubband transitions) as opposed to conventional interband lasers that use the recombination of electron-hole pairs. The semiconductor is deposited in alternating layers of a few nanometers of different materials (such as GaAs/AlGaAs) with different conduction bands offsets that create a series of quantum wells and barriers. Due to the thickness of the layers having a size comparable to the electron's De Broglie wavelength, the conductions band energy levels are quantized and split into subbands that represent the allowed electron states in the well as shown in Figure 11 [94]–[96].

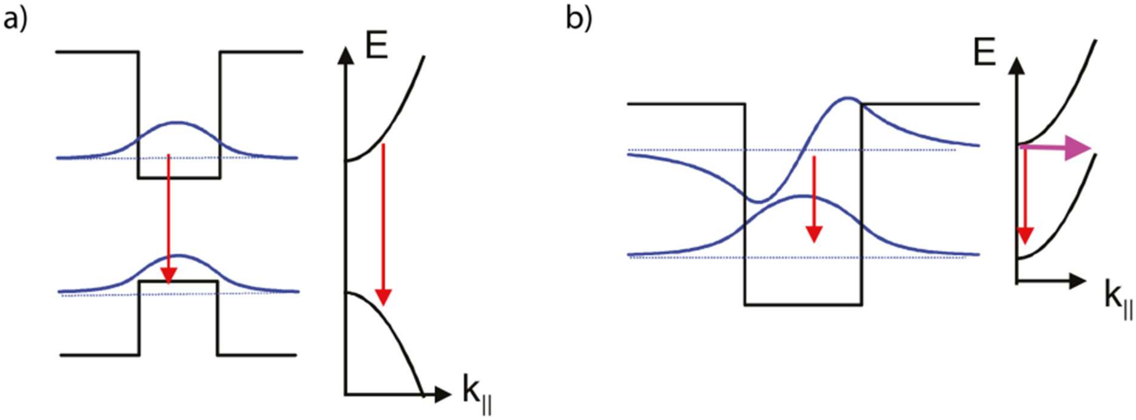

Figure 11 a) The band gap of conventional lasers based on electron-hole recombination and b) subband transition used in quantum cascade lasers. The splitted conduction band states originate from the dimension of the quantum wells being close to the electron De Broglie wavelength. [95]

Based on the thickness of a stack of individual layers it can form either an active region or an injection region. Under the right bias, the electrons are injected via resonant tunneling from the injection to the active region in its highest energy level (3) as illustrated in Figure 12. The laser emission is then generated by their transition to the lower level 2, after which the electron quickly relaxes to the lower level 1. The fast transition to the lowest level is ensured by tuning the thickness of the semiconductor layer, generating a population inversion as most of the electrons are present in the lower level 1. From this point, the electrons are transferred through the relaxation region and injected in the following period where the process is repeated.

Moreover, if the population inversion condition between level 2 and 3 is maintained, the emitted power depends linearly on the injected current. In this process, each electron can emit at most a photon for each period when cascading across the device.

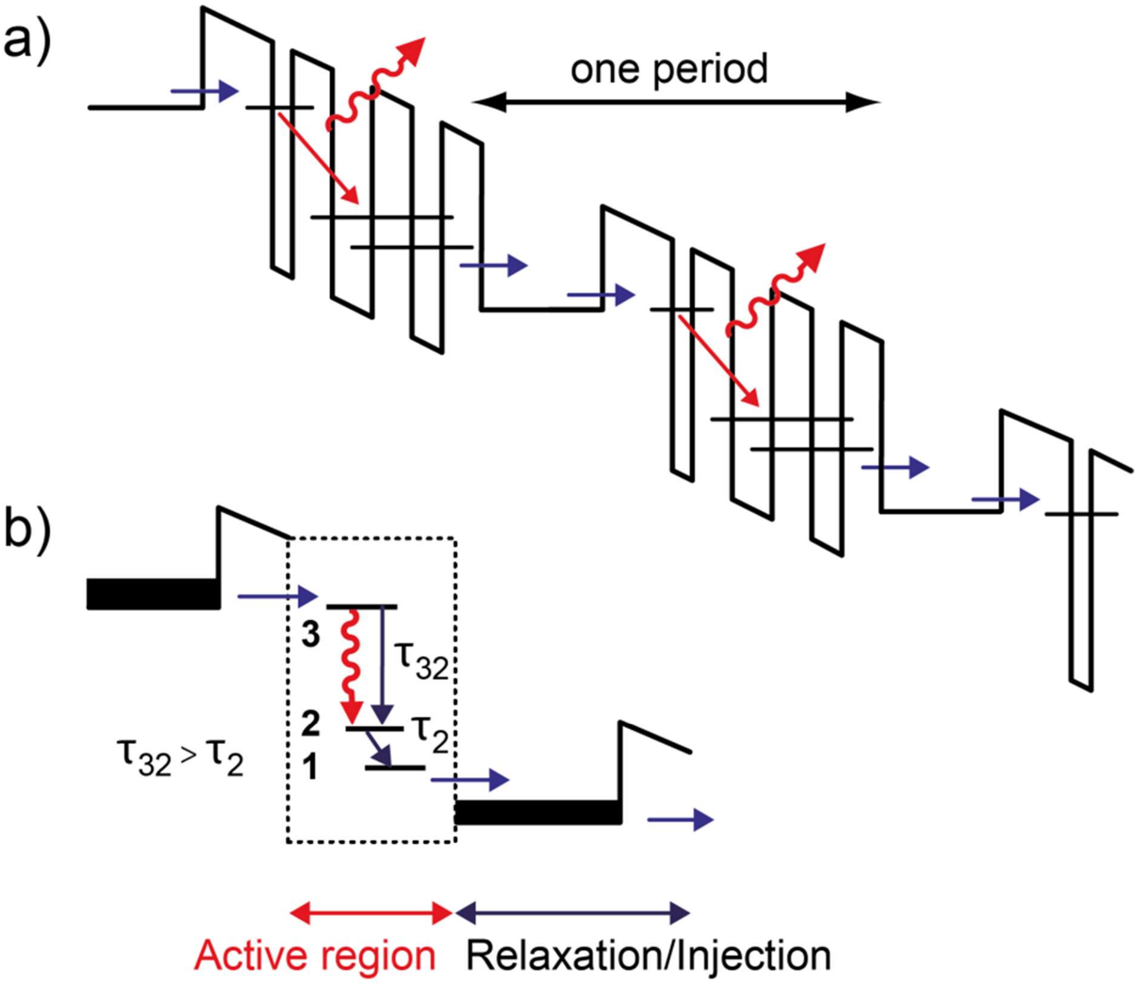

Figure 12 Illustration representing a) the basic electronic structure of a multiperiod QCL b) the operation of a single period: an electron from the injection region cascade in the active region emitting a THz photon from the electron energy level 3 to the level 2. This electron then relaxes quickly to the level 1 with a time-constant smaller than the transition 2-3. This faster transition ensures the population inversion which allow the efficient emission of THz radiation. The electron finally is transferred to the next period where the process repeats with the emission of another photon. [97]

Thanks to its unipolar nature and ultrafast electron transition, this device does not suffer from surface recombination and can reach higher working frequencies than other THz lasers. For QCLs working in the THz regime, cryogenic temperatures are still required due to their sensitivity to the phonon population inside the system that hinders the radiative emission. Nonetheless, the tunability of the emission frequency over a wide range in the THz region, through the control of the thickness of the layer, and its especially high power, makes this device one of the most promising THz sources for both industrial and research purposes [4].

Synchrotrons

A charged particle under acceleration emits broadband electromagnetic radiation. If the particle is a relativistic electron undergoing a circular motion in a magnetic field, this radiation is called synchrotron radiation and it is emitted in a narrow cone tangentially to the curvature of the electron beam. Usually, to generate coherent radiation, “bunches” of electrons (around 10^{12} electrons for each group of electrons) with dimensions comparable to the radiation wavelength are used. The most common synchrotron radiation sources are the storage rings with over 50 facilities worldwide [97]. In these systems the electrons are kept in a circular path by bending magnets at predetermined positions, producing radiation each time the bunches are transversely accelerated by “wigglers” and “undulators” [98]. Both of these devices consist of a series of bending magnets placed in series in short sections of the ring. At each magnet, the electrons emit synchrotron radiation in the direction of that specific section and the radiation overlap increases in intensity. Like for the bending magnets, broadband radiation is emitted during the process, however, the experiments based on the synchrotron radiation generally use a specific and narrowband leading to a large part of the radiation not being used. To overcome this problem, modern synchrotrons use an improved layout called undulator. This type of device is based on a wiggler uniquely designed for specific electron beam energies, that uses interference instead of the overlapping of the synchrotron radiation. The final result is coherent radiation peaked at the frequency of interest (and its harmonics) with a higher brilliance compared to wigglers and bending magnets as shown in Figure 13. As both wigglers and undulators are based on a series of magnets, the same system can be used as either of the two by modifying the magnetic field and the magnet's position with respect to the electron beam in the storage ring[98]. The advantage of the THz emitted through synchrotron sources is given by the tunability, coherence, polarization, and very high brilliance of the radiation. However, the high cost for the construction, use, and maintenance of these structures limit their usability to research purposes.

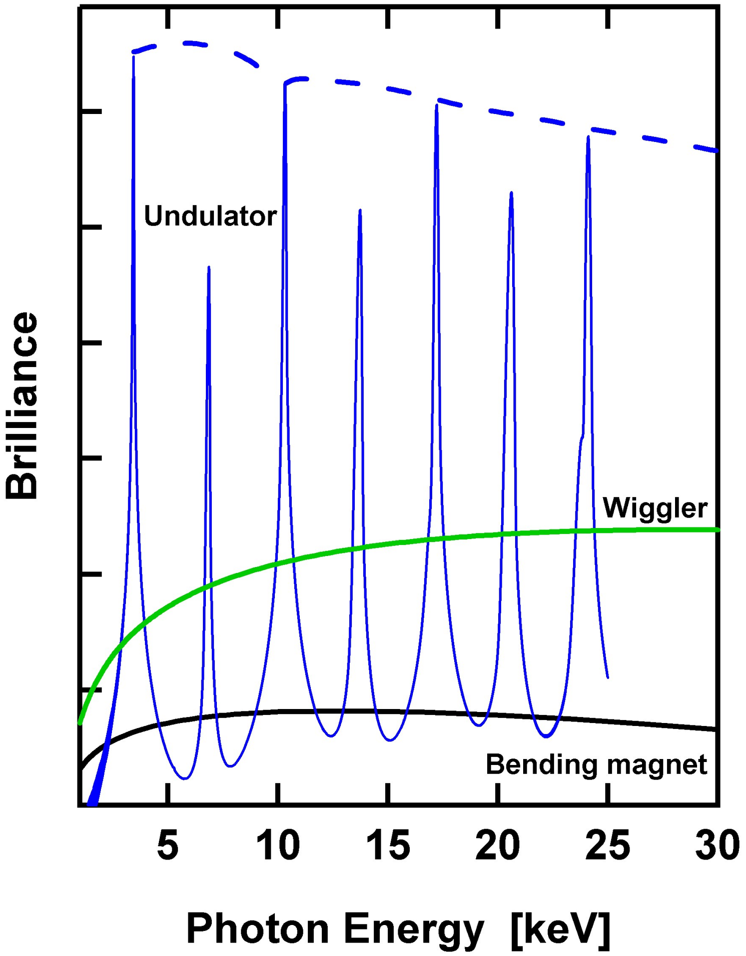

Figure 13 The emissions of the synchrotron radiation from bending magnets, wigglers (series of opposed polarity bending magnets) and undulators, which are similar to wigglers as linear series of bending magnets, but are specifically designed to work at determined electron energies, concentrating the radiation emitted to specific frequencies and their harmonics. [98]

Detectors

Detectors for THz radiation can be classified as either coherent or incoherent depending on whether they can measure both the amplitude and phase of the THz field or only its intensity respectively. Incoherent detectors (also called "direct") are generally broadband as they detect the THz radiation in its entirety. Among the direct detectors, the most used are thermal-based detectors. These devices are based on exploiting temperature-dependent properties, like electrical resistivity (used by bolometers), electrical polarization (employed in pyroelectric detectors), and gas pressure (exploited in Golay cells), that change due to the increase in temperature of the sensing element (absorber) [99]–[101]. Dependent on the absorption spectra of the absorber, these detectors are generally broadband and slow as the sensing element must reach thermal equilibrium before taking the measurements. The fastest thermal bolometer at liquid He temperatures reach 0.1 ms of time constant while for pyroelectric and Golay cells detectors this constant is usually around one second. Rectification techniques, originally designed for microwaves detection, have also been applied to higher frequencies up to the THz band. Rectifiers, such as Schottky diodes, use a non-linear current-voltage interaction to produce an output voltage, which is proportional to the amplitude squared of an input current induced at the THz radiation frequency[102]. In the case of photodetectors, individual photons interact with electrons in the detectors, exciting them from donor states or into acceptor states and the change in the number of free carriers is measurable through the device resistance[87]. In the THz band, the energy is low and therefore the energy gap involved are those between shallow impurity states and the conduction or valence band in extrinsic semiconductors. On the contrary, intrinsic photo-excitation of free carriers in semiconductor materials usually require higher energy photon compared to THz[103]. However, photoconductive antennas (PCA) can be used also as a detector by allowing the incident radiation to induce a current through the photoconductive gap once the carriers have been generated by a probe pulse.

Bolometer

Bolometers are incoherent thermal detectors that use a material whose electrical resistance is correlated to the temperature change. The material can be a metal, a superconductor, or a semiconductor like ion-implanted silicon or neutron-trasmutation-doped (NTD) germanium. In order to reach a high sensitivity, this device is operated in cryogenic conditions, generally using liquid helium as a coolant. While their structure allows for the detection of radiation over an extremely wide band (from THz to X-rays) they were developed and are mainly used for the THz and infrared wavelengths due to higher sensitivity in this spectral range [104], [105]. The bolometer designs can be composed of single or separate elements for radiation absorption and temperature sensing; in the latter case, they are called composite bolometers. The incoming radiation increases the temperature of the adsorber which is thermally connected to the thermometers resistor. A heat sink is generally used to dissipate the excess heat after detection, thus reducing the response time of the detector. At cryogenic temperature the semiconductor doping ensures the electron hopping between the donors as a conduction mechanism, consequently maintaining the free carriers coupled to the lattice. Thanks to this mechanism the temperature of the device rises as a whole, and it is not limited only to the free carriers. The sensitivity of this device can be increased using an absorber with low heat capacity and good absorptivity over a wide range, such as graphene[106]. When a superconductor is used as a resistor the bolometer is also called Transition-Edge Sensor or TES and the detection is operated in a narrow temperature range close to the transition between the normal and the superconducting state. The sharp phase transition from the normal to the zero electrical resistance state that makes them extremely sensitive, however, requires a complex cooling system to maintain the temperature close to the transition temperature[107]. Another type of bolometers are the Hot-Electron Bolometers (HEBs) which are based on the use of non-equilibrium electrons (namely *hot electrons*). In normal bolometers the crystal lattice absorb and transfer the energy through phonons (collisions) to the electrons, in the HEB illustrated in Figure 14 instead, the electrons are only weakly bonded to the lattice, and the radiation is directly absorbed by them, reducing the response time of the device[108], [109].

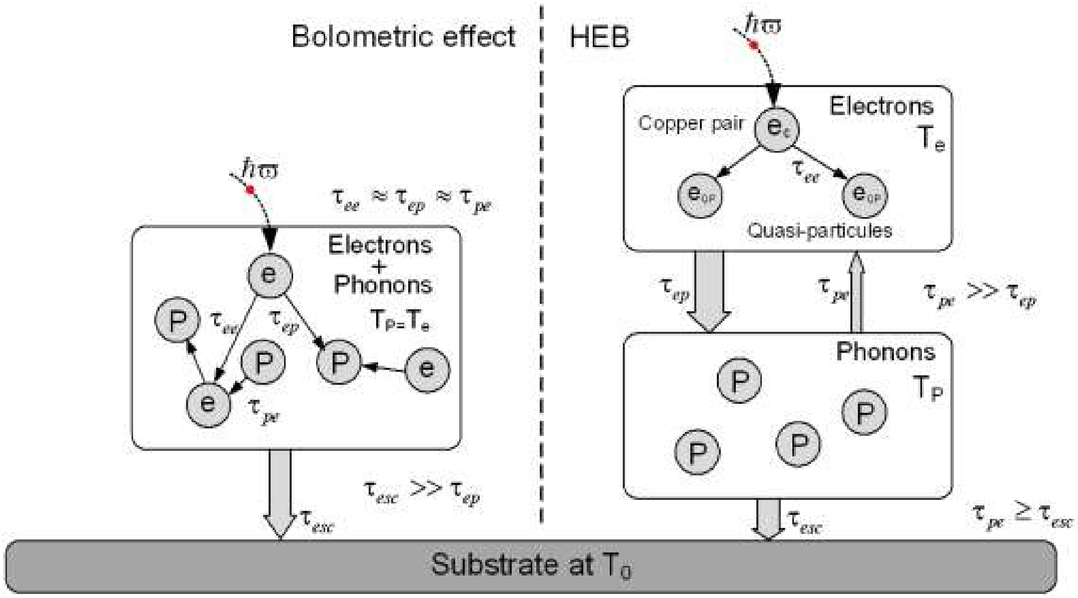

Figure 14 The difference between a conventional bolometer, in which electrons and photons present the same temperature due to inelastic interactions between them, and a hot-electron bolometer (HEB) which uses hot-electrons not coupled to the phonons in the material, resulting in a faster and more sensitive response [110].

One of the most promising applications for this device is the creation of microbolometer arrays allowing both high yields and moderate costs. These systems were originally implemented micromachining Si wafers with lithographic techniques and using ion implantation for the creation of the resistors The disadvantage of this type of detector lies in the difficulties related to the cryogenics temperature needed for their efficient use and application.

Pyroelectric detector

This detector is an uncooled thermal detector that uses spontaneous electric polarization in a pyroelectric crystal. Pyroelectricity is the property possessed by those crystals that present a permanent electric dipole moment along one axis. In a steady state, the charge that can be expected on a surface perpendicular to this axis is generally neutralized by free carriers and thus not observable. However, when the temperature change, the lattice spacing, and by consequence the spontaneous polarization and surface charge, also change. The typical design for this device is composed of two electrodes positioned on the opposite faces of the crystal to form a capacitor[110]. The current flowing in the circuit compensates for the change in the charge and therefore pyroelectric detectors must be used in AC mode, modulating the incident radiation. The most used pyroelectric crystals for THz detection comprise triglycine sulfate (TGS) and its deuterated form (DTGS), lithium tantalite ($LiTaO_3$), and barium titanate ($BaTiO_3$)[92]. Thanks to operating at ambient temperature and at low currents, this detector does not require high usage cost when compared to the bolometers. However, due to its uncooled nature, it is also affected by ambient thermal noise which limits its sensitivity in standard conditions, and it is relatively slow in response time, presenting time constant in the order of the seconds.

Golay Cell

The Golay cell is one of the first incoherent detectors that have been developed for the detection of infrared and terahertz radiation through a thermal process. As shown in Figure 15 is composed of a semi-transparent absorbing film placed inside a pneumatic chamber. The incident THz radiation is absorbed increasing the temperature of the sealed gas and therefore intensifying the pressure which is applied to a flexible mirror on the opposite side to the incident radiation[111]–[113]. The deflection of the mirror is then measured through the optical reflectivity of the mirror. Overall, in this technique, the THz incident radiation is converted into an optical signal.

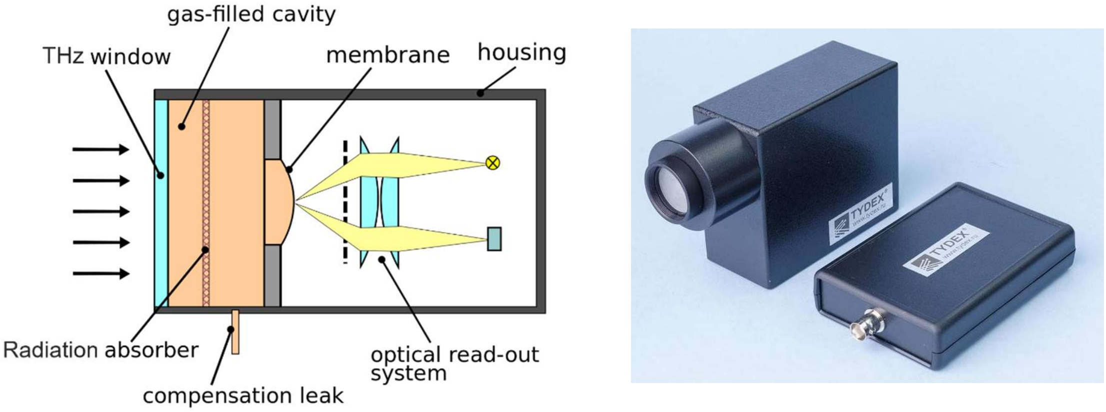

Figure 15 Left, schematic representation of a Golay cell and its components and (right) a commercial device [99] [100]. When the radiation hit the absorber, the gas sealed in the chamber is heated and expands corrispondingly. The expansion of the elastic membrane is then measured through an optical system

The gas generally used in this kind of detector is Xenon for its low thermal conductivity, but air and nitrogen have also been tested [114]. The window and the walls separating the sealed chamber from the outside are also made of good heat insulators and the spectrum absorbed by the device is dependent on the material used for the window (usually amorphous polymeric materials, transparent to the THz wavelengths ranging from 20 to 1000 μm). The absorber is composed of a blackened metal thin film with carbon black or aluminum black, which increases the light absorption in the THz region[111]. This device is a sensitive, room-temperature detector but its limited in the response time due to the thermal inertia of the gas and mechanical properties of the deflecting membrane[115].

Schottky Diode

Rectifying diodes present a nonlinear response to an electric field and, limitedly to small signals, produce an output proportional to the square of the input voltage. The Schottky diodes in particular are based on the Schottky barrier present on the interface of a metal-semiconductor junction in conventional p-n diodes. In n-type semiconductors, the two Fermi levels are equalized by the flow of electrons from the semiconductor to the metal. This flow creates a depleted region in the semiconductor due to the ionized donor locations left behind, generating an electric field that eventually inhibits the electron flow to the metal. In the case of a positive bias applied to the metal, its Fermi level is lowered in relation to the semiconductor, and a Schottky barrier Φ_B as represented in Figure 16 impedes the passage of electrons[116], [117].

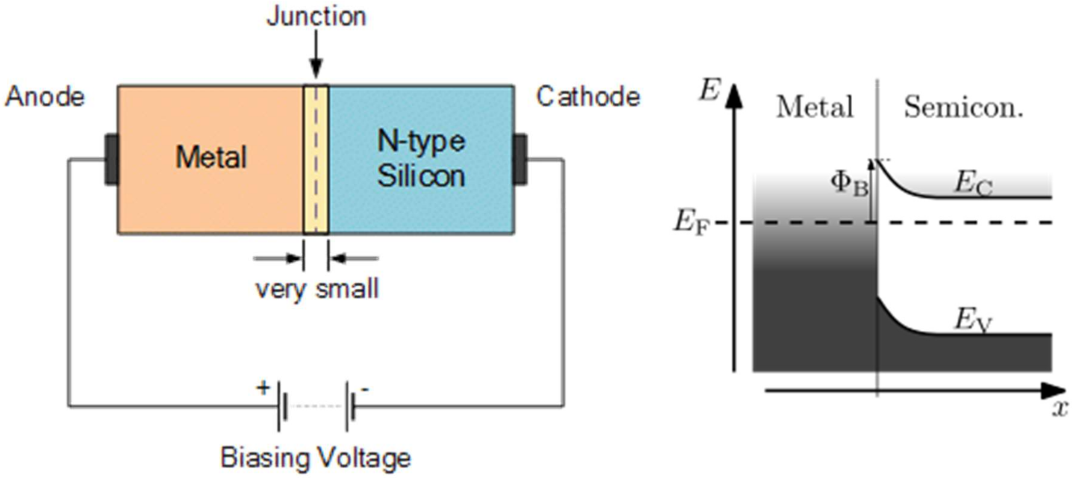

Figure 16 Basic structure of a Schottky diode (left) and its electronic structure under bias (right). The Schottky barrier present at the interface between the semiconductor and the metal impedes the passages of electrons rectifying an AC current [116], [117].

The electron energy is thus increased relatively to the barrier height, allowing the flow of electrons in the junction towards the metal. The current derived by this flow then presents a voltage comparable to that of the bias applied as in a conventional forward semiconductor diode. If, on the contrary, a negative bias is used, almost no current flow, resulting in a marked rectifying behavior. The nonlinear current-voltage response of this diode is also the reason for its use as the mixing element in a heterodyne receiver[118]. In this type of receiver, the incoming radiation signal is combined with a local oscillator signal, creating an output that contains components that are easier to filter and amplify compared to the original signal. The Schottky diode becomes especially interesting in this receiver when the frequencies involved are high (up to 1 THz) thanks to the fast transition between the conducting and the nonconducting states when compared to other p-n rectifiers. These detectors are fast and efficient, however, at frequencies higher than 1 THz its efficiency drops, while on practical use they tend to heat up quickly, requiring a cooling system even for working at ambient temperature. Its cost is also high, which limits its application towards the research.

Extrinsic Semiconductor detector

The semiconductors present an energy gap between the conduction and the valency band which is often used to detect photons with enough energy to excite an electron from the conduction to the valence band. This phenomenon is referred to as intrinsic excitation and generates the formation of electron-hole pairs that cause a measurable variation of the conductivity of the material. Unfortunately, THz photons do not have enough energy to overcome the gap in conventional semiconductors, hence impurities are added to create donor and acceptor states close to the band edges. The low-energy THz photons are then capable of exciting electrons from the valence band to the acceptor states from the donor states in the conduction band. This process called extrinsic excitation requires a temperature lower than 4 K and low impurity concentrations to avoid thermal excitation and noise[92]. The semiconductor most used for the THz detection is the mechanically stressed gallium-doped germanium (Ge:Ga). This type of detector is fast and sensitive but its high cost for both production and use (due to the liquid He cooling) limits its practical application.

Photoconductive Antennas (PCAs)

This device can be used for both the generation of broadband THz radiation as well as its detection as illustrated in Figure 17 [119]. As a photoconductive detector, the THz pulses are directed to an unbiased PCA, producing a bias across the antenna electrodes varying over time. Through an incident femtosecond laser pulse (called "probe" and generally produced by a Ti:sapphire laser) onto the gap between the electrodes, the free carriers are excited in the semiconductor[120]. Under the excitation of the electric field of the THz pulses, the excited electrons are accelerated generating a photocurrent that can be then amplified and measured externally. For this device, the most used semiconductor is low-temperature grown gallium arsenide (LT-GaAs) thanks to its short carrier lifetime and large resistivity. Indeed, the duration of the photocurrent is dependent on the carrier lifetime, which is in the order of picosecond, and a fast response thus allows for time-resolved waveform measurements as it is usually shorter than the THz pulses [121]. This device, when coupled with a photomixer and two laser sources can also be used as a coherent detector. In this case, while the THz field generates a time-dependent voltage across the electrodes of the PCA, the conductivity of the semiconductor is modulated by the difference (or beat frequency) of the two lasers. For this to happen, the energy of the photons needs to be greater than the bandgap, thus generating free carriers. The resulting photocurrent induced by the THz radiation and modulated by the difference in frequency of the two lasers, present an amplitude proportional to the THz incident radiation, and the relative phase between the laser beats and the radiation is often optimized to maximize this DC element[122]. While PCA presents a good sensitivity with fast response time and the possibility to be used as coherent detectors, their drawback is characterized by their low detection current and relatively high cost when compared to other THz detectors.

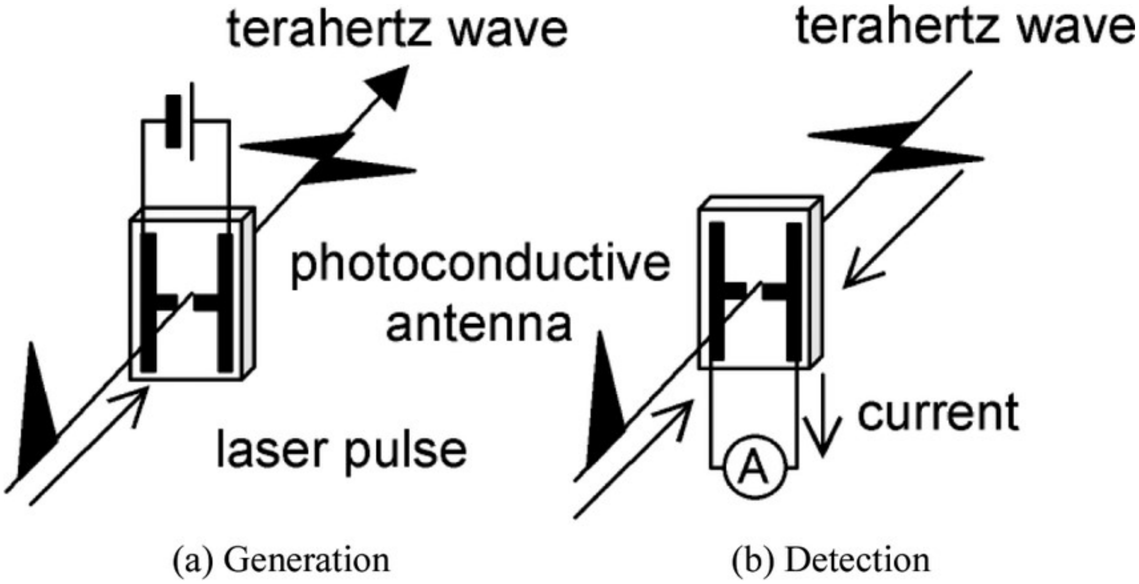

Figure 17 Schematic illustration of a PCA working for both the generation and the detection of THz radiation. a) under the irradiation of the PCA with a femtosecond laser, the antenna generates a broadband THz radiation. If on the contrary the THz is incident to the antenna working as a detector b), using the femtosecond laser as a probe, the current is measured revealing information on the intensity of the THz wave[119]**.**

Chapter 2

Graphene

In nature, the prevalent physical forms of pure solid carbon are diamond and graphite. In these forms, their atoms are arranged in covalently bonded networks, and up to the mid- 1980s, they were thought to be the only possible forms entropically allowed. Graphite, the most abundant one, is used commonly as the main ingredient of lead pencils, battery electrodes, industrial-grade lubricants, etc, and differs from diamond by the diverse structure and bonding between the carbon atoms. In the diamond, the atoms are closely packed together in a 3D rigid structure that limits the presence of interstitial impurities and exhibits a high optical dispersion and transparency. On the contrary, the graphite shows a layered structure in which each layer is connected to the other thanks to Van der Waals interactions. This soft structure is what allows the pencil to write on paper: thanks to the attrition between the two materials, the graphite is subjected to mechanical exfoliation leaving on the paper hundreds of layers or even just a monolayer of carbon sheet. In the latter, the 2D carbon structure takes the name of *Graphene*. This name, proposed in 1986[123], is composed of the suffix "-ene" used in organic chemistry for polycyclic aromatic hydrocarbons such as naphthalene and anthracene and the prefix "graph-" from graphite. It was later recommended by the International Union of Pure and Applied Chemistry [124] as the name for a single two-dimensional layer of carbon atoms bonded with sp^2 hybrid orbitals, which occurs in graphite intercalation compounds. Since then only a few papers reported on this allotrope of carbon, up to its practical discovery and characterization in 2004 by Andre Geim and Konstantin Novoselov[125] peeling off the graphite sheet from the highly oriented pyrolytic graphite. Then, they stuck both sides of the sheet to a special type of tape. The graphite sheet can be divided into two by tearing the tape and the resulting sheets become much thinner with the repeated operations. Finally, they achieved a film made of only one layer of carbon atoms: again graphene. Most physicists believed that thermodynamic fluctuations would not allow any real two-dimensional crystals to exist at a finite temperature before the discovery of graphene. Although both theoretical and experimental communities believed that a perfect two-dimensional structure could only be stable at absolute zero degrees, monolayer graphene demonstrated the effectiveness of the unique potentiality of two dimensions materials even at room temperature [126]–[128]. Therefore, the discovery of graphene immediately shocked the academic community. This research incredibly soon, in 2010, received the Nobel prize for physics opening the road for a flood-like number of publications in this field up to the first very large scale industrial application of graphene in China in 2018, with the opening of a fully automated mass production graphene for organic solar optoelectronic device production launched in Heze, Shandong[129].

Carbon Nanomaterials

Together with diamond, graphite, and graphene, there are many more different physical forms of carbon. Each of them possesses specific forms, like the tubular shape of carbon nanotubes, the spherical shapes of fullerenes (whose full name is Buckminsterfullerene from Buckminster Fuller, famous architect and creator of geodesic domes of similar structure) and they found a wide field of application and research such as electronics, optics, optoelectronics, biomedical engineering, tissue engineering, medical implants, medical devices, and sensors [130]. Carbon materials were proposed to be classified based on the type of covalent bonds of their constituent carbon atoms using sp^3, $sp^{2,}$ and sp hybrid orbitals (Figure 1). The sp^3 orbitals compose diamonds, while sp orbitals are the constituents of an elusive linear (wire-like) form of carbon allotropes given the name of *Carbyne*[131]. The sp^2 hybrid orbitals can be also further divided into flat forms, like graphene, or curved forms like fullerenes. Layers composed of these orbitals are intrinsically anisotropic with π-electron clouds on both sides, from which originates the ample range of structures and properties of these materials. Carbon nanotubes can be considered as a combination of both a fullerenes structure and graphene structure, as the tip of the tubes presents the characteristic five-membered rings (fullerene-like) and the wall, although rolled, has the six-membered rings (graphene-like). Most of the carbon materials derived from the flat sp^2 hybrid orbitals also produce strongly different properties in the presence of layered structures because of their anisotropic nature and the existence of π-electron clouds. Large numbers of layers stacked with regularity have been called graphite, and various graphite-related materials have been produced and used as important industrial materials. However, the order of stacking as well as the final structure brings a wide variety of different mechanical and thermal properties, ranging from a fully amorphous structure to a strongly anisotropic one[132].

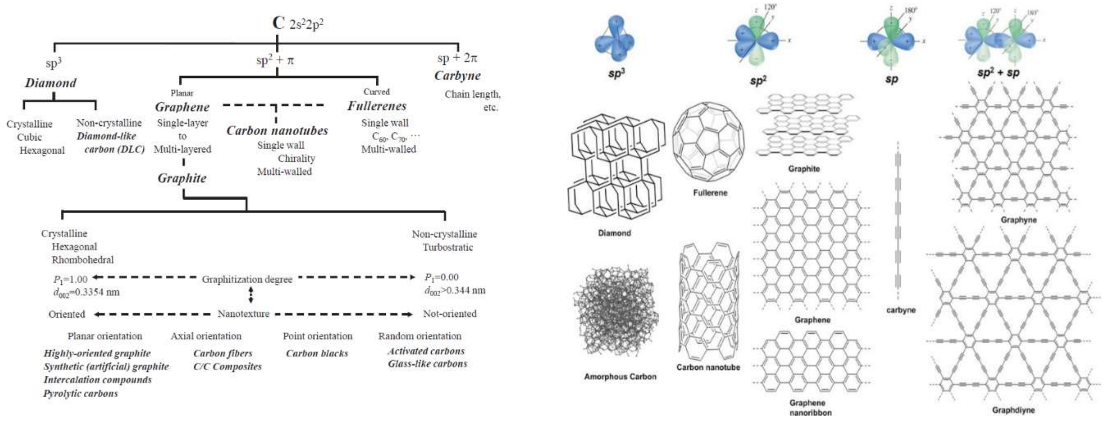

Figure 1 Schematic representation of the wide family of carbon and its allotropes. [132][133]

Graphene

Graphene is one of the most known allotropes of carbon [125], and since its discovery has seen an explosive increase in the number of papers, articles, and reviews describing and implementing its unique optical, mechanical, electrochemical, and electrical properties. The name "*graphenes*" is also used to indicate a family of graphene-like materials shown in Figure 2, including mono-, bi-, and multi-layer graphene (which differ by the number of stacked layers of graphene), graphene oxide, and reduced graphene oxide (which differ by surface chemistry and defect density and composition)[134]. Among all of these variations, the only true graphene remains the single-layer pristine graphene, which is comprised of an ideally planar, 2D honeycomb-like structure of carbon atoms sp^2 bonded via hybridization of s, p_x, and p_y atomic orbitals, forming strong σ bonds with each adjacent atom. The remaining p_z orbital on each carbon overlaps with those from neighboring atoms, establishing a filled band of π orbitals (valence band) and an empty band of π* orbitals (conduction band). The formers are also the main cause for graphene hydrophobicity and its π-π interaction with respect to the basal plane. The highly oxidized form of graphene is graphene oxide (GO) in which the carbon sheet is partially occupied by the presence of carboxylic acid, epoxide, and hydroxyl groups. The carboxylate group provides colloidal stability and pH-dependent negative surface charge. The epoxide and hydroxyl groups instead are uncharged but polar, allowing for hydrogen bonding and other surface reactions[135], [136]. Finally, by chemically reducing the surface of GO, it is possible to obtain a highly defective version of graphene, the reduced graphene oxide (rGO)[137]. In this material the lateral groups are erased, leaving vacancies and defects in the final structure.

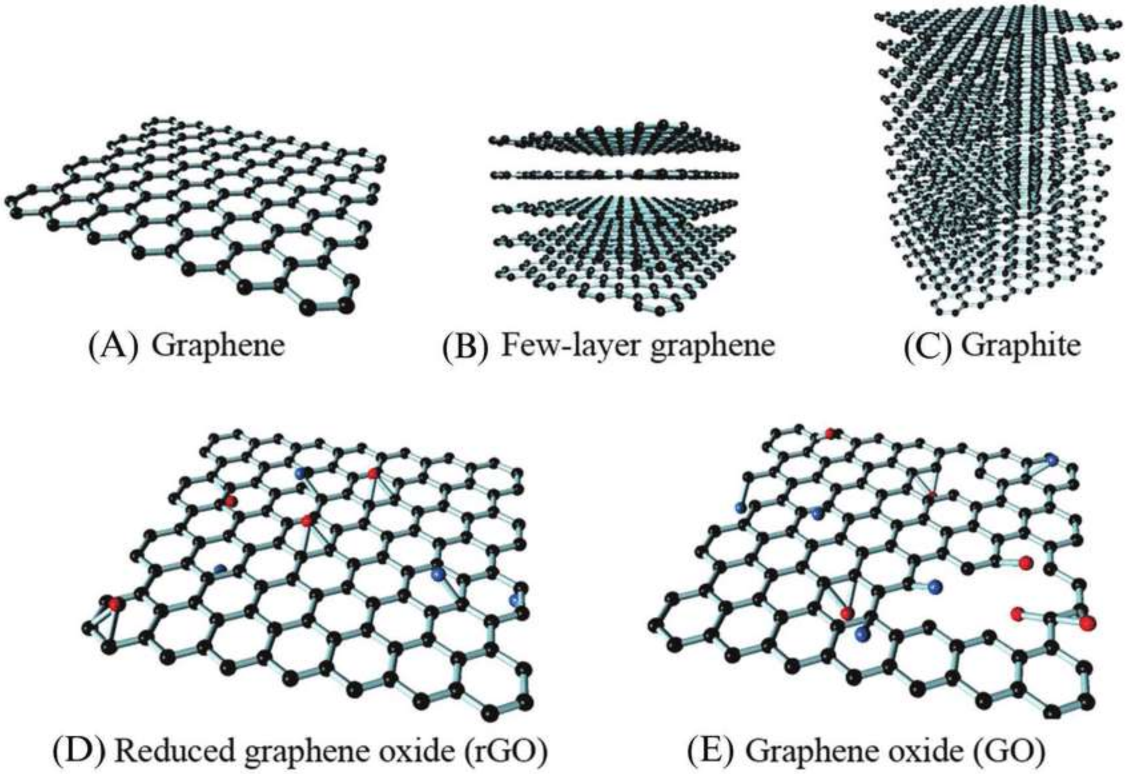

Figure 2 Structure of the most common forms of graphene-like materials. [134]

Graphene synthesis

Thanks to its peculiar properties and wide field of application, graphene has been in the research spotlight for the last decade and the interest in this 2D material promoted the swift development of technology aimed at its synthesis. The production of graphene can be divided into two main categories: top-down and bottom-up approaches. The top-down starts from bulk graphite to mechanically or chemically isolate single atomic layers of graphene. The bottom-up approach, on the contrary, uses carbon atoms from various sources as building blocks, directing the synthesis of the characteristic honeycomb lattice[138]. The top-down approaches include mechanical and electrochemical exfoliation[139], [140], ball milling[141], and sonication[142], etc., for the separation of the stacked graphene layers. The bottom-up approach instead applies process like chemical vapor deposition[143], epitaxial growth on silicon carbide[144], growth from metal-carbon melts[145], electrostatic deposition[146] etc (Figure 3). All of these techniques present advantages and disadvantages and the choice usually depends on the final application for which the graphene is used.

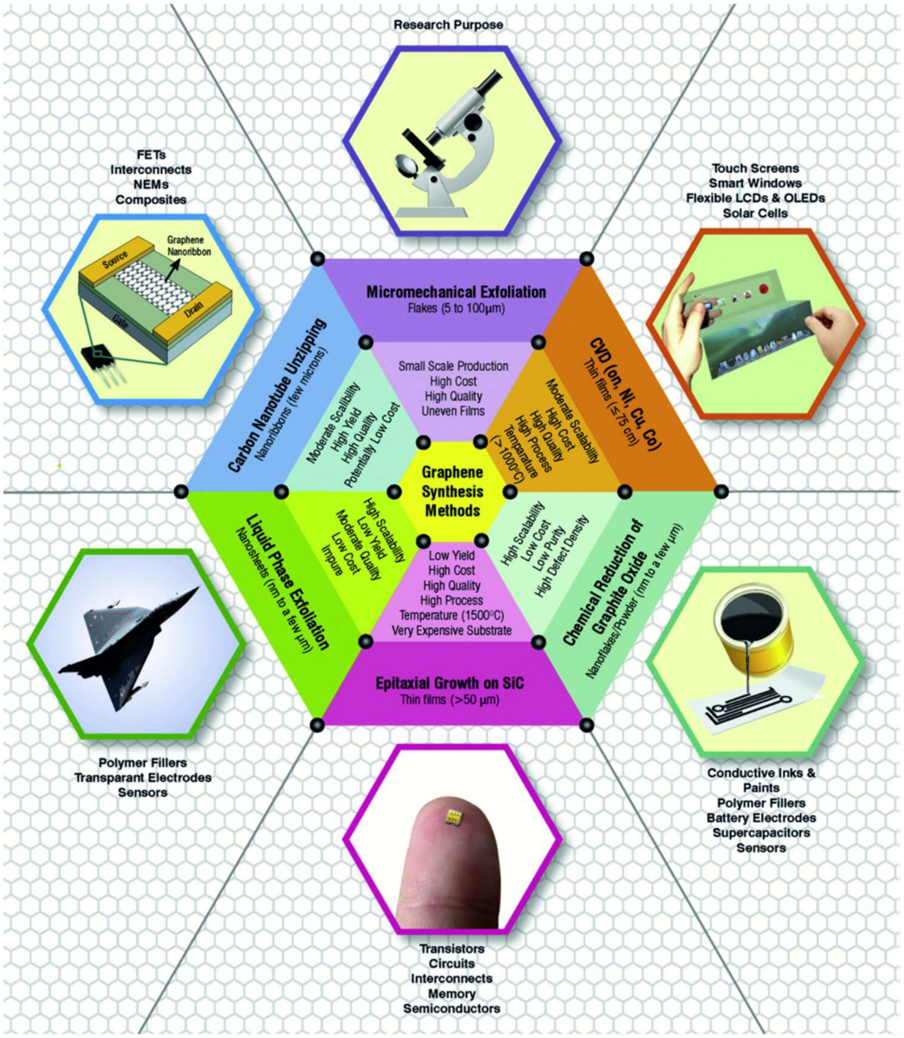

Figure 3 Illustration of the most used graphene synthesis methods and their applications. [138]

Top-Down Approach

Mechanical Exfoliation


Figure 4 Display of the graphite, Scotch tape, and graphene transistor donated by the physicists to the Nobel Museum in Stockholm. [147]

The most known method for the production of graphene is mechanical exfoliation, which is also considered the starting line for research in this field. The mechanical stripping method is based on the repeated peel of the surface of highly oriented pyrolytic graphite (HOPG) using adhesive tape until a single layer or few layers of graphene are obtained. These graphene layers were then separated from the tape using acetone to dissolve the substrate, leaving them to sediment on a substrate like a silicon wafer. This method was the one applied in 2004 to obtain the first practical monolayer graphene[125][147] and resulted in the Nobel prize in 2010 (Figure 4). The “scotch tape method” (also known as the fancier “micro-mechanical exfoliation method”) repeatedly split graphite crystals into increasingly thinner layers, demonstrating that 2D dimensional crystals can exist at room temperature[125], [148], [149]. By further improving the technique graphene flakes up to 1 mm visible to the naked eye were isolated[150]. This mechanical or micromechanical method is still used as a means to produce high-quality single-layer graphene for research purposes, however, its low efficiency, controllability, high cost, and the small sizes of the sample produced, limit its use to small scale research applications. Other mechanical methods for the production of graphene are for example shear exfoliation in stabilizing liquids, which give results similar to those obtained with sonication, or the use of a diamond wedge to scrape the surface of HOPG, aided by ultrasonic oscillations[151] however the small size of the sample, as well as the damage induced during the process, lead to worse results compared to those obtained with the scotch tape method.

Graphite Intercalation

Graphene can also be synthesized by intercalating graphite, which means including via covalent or non-covalent bonding, small molecules (the intercalate) between the graphene sheets stacked in the graphite crystal. The result of this process is the formation of graphite intercalation compounds (GICs) which can be divided mainly into two groups based on the type of interaction between the carbon and the intercalate. The first group is defined by covalent bonding (or homopolar) and includes graphite oxide, carbon monofluoride, and tetracarbon monofluoride. This type of bonding is supported by the conjugated double bonds within the carbon planes. The layer planes assume a wavy form due to the variation of the carbon bonding from the trigonal (sp2) form to the tetrahedral (sp3) form. These compounds are non-conducting and lack the semi-metallic properties of graphite. The second group, in which the bonding is partially ionic (or polar), includes graphite salts (e.g., graphite nitrate, graphite bisulfate), graphite-alkali metal compounds, graphite-halogen compounds, graphite-metal chloride compounds, etc. The ionic species are used to interfere with the interaction of the layers, gradually separating them as shown in Figure 5 [152]. Due to the semi-metallic nature of pure graphite, by ionically bonding with the intercalate, the graphite π-bonds can gain electrons from or lose electrons to the intercalate, thus shifting the position of the Fermi energy, with the intercalate atoms acting as donors or acceptors to dope the graphite. The GICs' properties are greatly dependent on the intercalant chosen, as their presence increases the distance between graphite layers affecting the interlayer electronic coupling and modifying the electronic cloud of graphene[152]. Based on the final applications, the properties can be tuned and modified, increasing the electrical[153], [154], thermal[155], magnetic[154], chemical[156], [157], and catalytical[158] performance of the final graphene-based material.

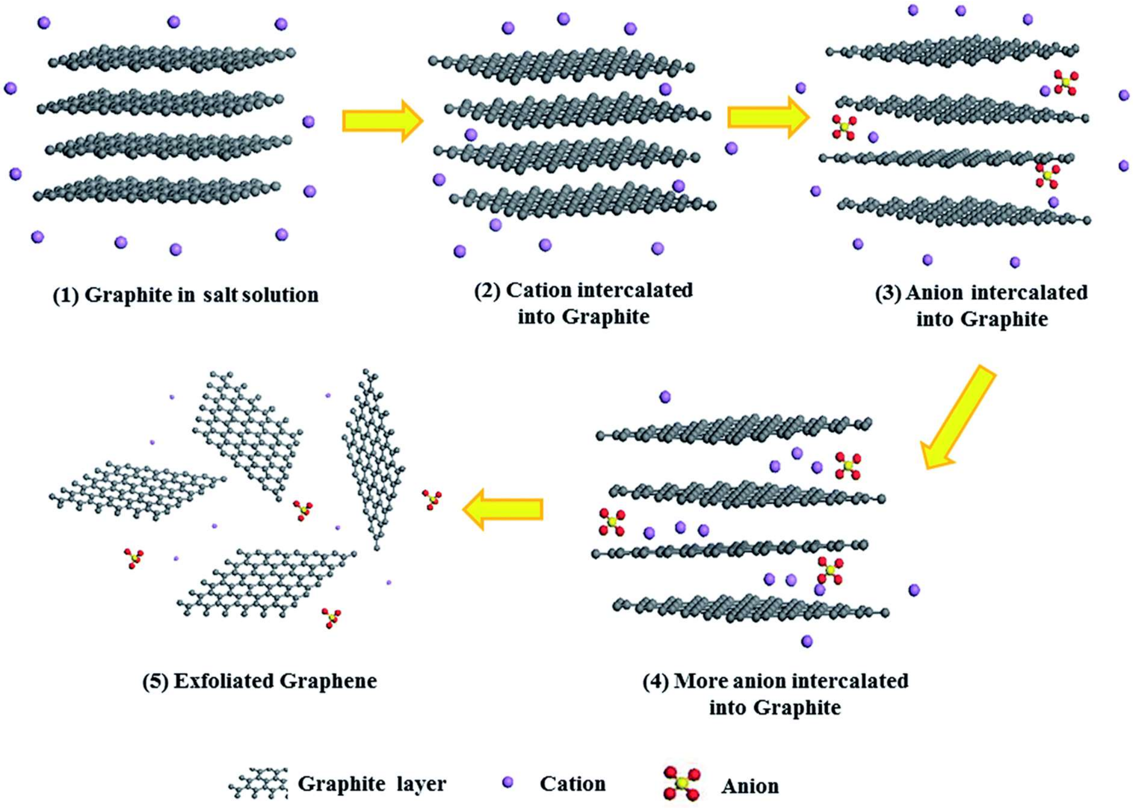

Figure 5 Intercalation of graphite with ionic species to exfoliate graphene. [152]

Nanotube Unzipping

Carbon nanotubes (CNT) can also be used for the production of graphene nanoribbons up to a few microns in size[159] and, theoretically, graphene sheets[160]. To slice open the CNTs several methods have been studied, like plasma etching of nanotubes partly embedded in an organic film[161], or placing them in a solution of sulfuric acid and potassium permanganate[162]. Both methods allowed to obtain high-quality graphene sheets for research purposes. Instead, For a production focused on industrial application, the carbon nanotubes were abraded on a glass substrate with constant pressure, using friction to forcefully unzip the CNTs[163]. The limit of these techniques lies in the high production cost required for the precursor (CNT) fabrication compared to other carbon precursors, like graphite or high carbon-content gases that are used in the other fabrication processes.

Reduction Of Graphene Oxide

To produce large quantities of graphene-based sheets with lateral dimensions ranging from a few nm to a few microns, the chemical reduction of graphene oxide (GO) has demonstrated remarkable efficiency. The graphene obtained in this process is suitable for many uses like conductive inks, polymer fillers, battery electrodes, supercapacitors, sensors, etc[164]. The precursor material (GO) is usually produced through Hummer's methods, which consists in stirring in an ice bath a solution of graphite flakes, sodium nitrate, sulfuric acid, permanganate, and deionized water[165]. After centrifugation and filtration, the powder obtained is mainly composed of multilayered GO which can be exfoliated by sonication in water and reduced through thermal, UV, or chemical treatment under reducing conditions with hydrazine or other reducing agents[166]–[168] (Figure 6). The thermal treatment is based on rapid heating of the GO resulting in a dispersed carbon powder with few percent of carbon flakes[169], while the chemical reduction uses acids like HCl to eliminate the oxidized groups and thus reduce the GO[170]. The reduction process was even demonstrated with the help of bacteria reducing the GO dispersed in their culture[166]. While this chemical reduction method can rely on its low cost and lower process temperature, the graphene obtained presents a high density of surface defects and low purity, drastically reducing its properties when compared to mechanically exfoliated or CVD graphene.

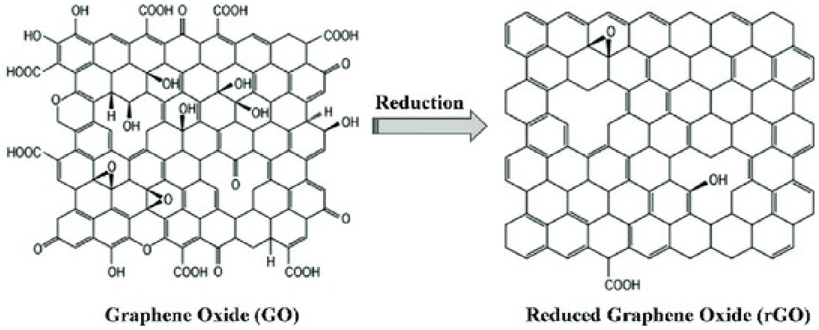

Figure 6 Structure change between GO and rGO after the reduction process. [169]

Electrochemical Exfoliation

Starting with the graphite as a precursor, this method uses a solution of sulfuric acid (which serves as the electrolyte) in which is immersed an anode of graphite flakes and a platinum cathode. By applying a positive bias of 10V the graphite flakes begin to dissolve in the solution and are later collected through vacuum filtration[171]. Other electrolytes and potentials were also studied for the production of different carbon nanomaterials[172]. This method, however, is difficult to control and requires high-cost carbon electrodes while the resulting graphene produced is usually contaminated by the electrolytes.

Sonication

It is one of the most used approaches for the fabrication of high-quality un-oxidized graphite and graphene flakes. This top-down method uses ultrasonic energy to separate the graphene layers stacked together in the precursor[173]. The graphene produced with this method is usually dispersed in organic solvents like N-methyl-pyrrolidone at concentrations of up to 0.001 mg/mL[174] and incorporated in composites or polymers through spray coating, vacuum filtration, solvent casting, or drop casting[173]. The solvent aid in the sonication process, reducing the total amount of energy required and simplifying the separation from the residual precursor[175]. Unfortunately, its use also induces the re-stacking of the graphene layers caused by the presence of Van der Waals interactions. To avoid this disadvantage dispersing agents and surfactants, like non-ionic surfactants, are added to both sides of graphene through hydrophobic interaction, to produce steric repulsion and separate the graphene sheets as in Figure 7 [176]. This addition however also increases the concentration of contaminants on the graphene[177], [178]. Other solutions include the use of aromatic-ring organic molecules or immiscible liquids like heptane and water[179]–[181]. The former takes advantage of π-π interactions to prevent the graphene re-staking while the latter uses the high surface energy between the two liquids to hold the graphene sheets after sonication. The large quantity of energy, most of which is dispersed in the liquid medium, can be a concern for the scaling up of this method[151] as well as the removal of impurities introduced during the exfoliation which drastically reduce the electrical and electrochemical properties[138].

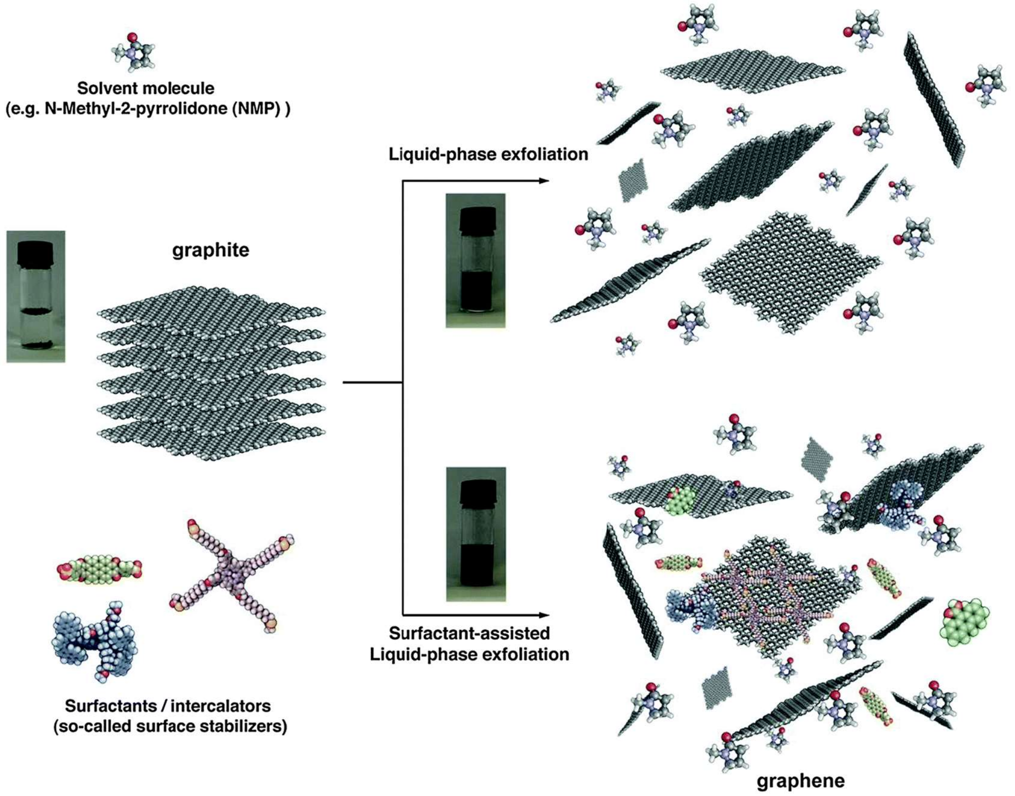

Figure 7 Liquid-phase exfoliation of graphene with and without the assistance of surfactants. [176]

Ball milling

This process has been since long used for mixing and particle size reduction both in the industry as well as in research. It consists of a rotating metallic cylinder along the horizontal axis with a precursor material and steel or ceramic balls. After reaching the top of the cylinder due to the rotation the spheres fall toward the bottom, hitting the precursor material and applying high normal and shear stresses. For the production of graphene, the precursor is graphite and the process is usually aided by magnetic fields[138], chemicals[182], or solvents[183]. The magnetic field is used to filter metallic residues in the precursors, while the chemical aid is mainly focused on avoiding the restacking and agglomeration of graphene sheets. The graphene produced through this technique is mainly FLG (few layers graphene) with a high production yield but the small size and low controllability of the final product quality, which limits its application in the research field.

Radiation-based methods

The radiation-based methods have been proved as a viable alternative for the production of graphene for the reduction of GO sheets. Different methods are applied based on the type of radiation used for the reduction. It was reported that aqueous dispersion of GO in isopropyl alcohol exposed to electron beam irradiation (140 kGy doses) and separated by centrifugation, were reduced to rGO[184]. Another radiation-based method is laser scribing, akin to a pyrolysis in which a laser acts as the energy source. Examples of these applications used the laser of a DVD drive[185], UV and Xenon sources[186], [187], femtosecond, and pulsed laser[188]–[190] to produce the same phenomena of GO reduction. The yield of these processes is low and difficult to scale but is still used in research for the relatively short time required for graphene production.

Bottom-up approach

Growth from metal-carbon melts

This method uses the decrease in the solubility of carbon in a molten transition metal that occurs when the temperature is lowered. In this process, the precursor is graphite powder which is placed on top of the transition metal before its melting. During the phase change of the metal, the carbon diffuses in the liquid metal up to the solubility limit. When the temperature is lowered, the carbon is segregated to the surface due to the solubility change and precipitates as different carbon forms like graphite, and few-layers or single-layer graphene. The main metal used in this process is nickel due to its favorable lattice properties[145]. Ruthenium and iridium are also valid alternatives, but their higher cost and the lower quality of the graphene film reduce their use[191], [192]. For the production of large areas of graphene with high quality, nickel foils are inserted in the reaction chamber and exposed to a constant pressure of methane gas at 900-1000°C. The carbon from the gas precursor dissolves in the metal lattice and resurfaces when the methane flux is stopped, forming polycrystalline graphene films[193]. The use of different precursor gases, such as ethane and propane tend to produce bilayer and other structures due to the higher carbon concentration[194]. The films produced through this method present a very high purity and high control over the film thickness over large areas and is currently one of the most used techniques for the production of monolayer graphene for the research field.

Epitaxial growth on silicon carbide

By heat-treating silicon carbide (SiC) wafers at 1100°C, the silicon thermally separates from the carbon leaving a layer of carbon atoms in a process called graphitization (Figure 8). After this process, the carbon can epitaxially reorganize and grow as graphene films with dimensions limited by the size of the wafer itself[195], [196]. The surface of the SiC can influence the properties of the resulting graphene and in particular thickness, carrier mobility, and density[197]. The peculiar properties of the graphene as-grown on the wafer surface are especially useful in the production of transistors and circuits thanks to the very high carrier mobility as well as the reduced influence of multi-layered formation on the electronic properties compared to other graphene-like materials (e.g. FLG)[198], [199]. Other notable properties demonstrated by graphene grown on SiC are the weak anti-localization and the presence of massless Dirac fermion even prior to the transfer of the carbon sheet[200], [201]. The high quality of this graphene comes with the disadvantage of high production costs due to the precursor, the SiC wafers. Also, the crystalline domains formed through this process are usually small (30-200 nm) and due to the absence of limits over the growth of carbon layers, often different regions with various thicknesses coexist on the same sample[202]. Overall, the process offers peculiar graphene properties, but the disadvantages involved in its production limits this process to research purposes.

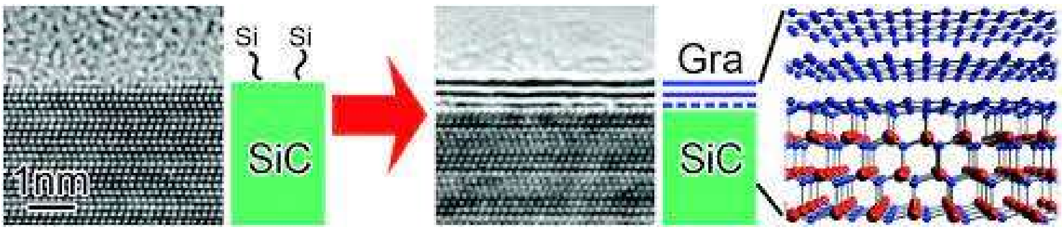

Figure 8 Graphitization and growth of graphene layers of a SiC wafer. [197]

Chemical Vapor Deposition

The large field of deposition techniques for the synthesis of graphene has been in the spotlight for many years due to the ease of fabrication of large areas of graphene with great scalability. The main deposition process for high quality single and few-layer graphene remains the chemical vapor deposition (CVD) that alone is comprehensive of over 20 variants of the process differentiated by various parameters such as temperature, pressure, gas flow, deposition time as well as substrate material or radiation used to aid the process[203]. This process was also used for the first reported synthesis of graphene[204]. The CVD process involves a substrate material (a transition metal or alloy) that is placed in a heated chamber under the constant pressure of a gaseous precursor (methane and other high carbon-content gases). Various substrates produce different surface reactions based on the solubility of carbon species in the metal. In the case of high solubility, like for nickel substrates, the carbon precursor is adsorbed and decomposed on the surface, the carbon atoms then diffuse and dissolve in the metal and when the gas flux is stopped, the carbon is segregated to the surface where nucleates and grow forming graphene layers[205], [206] (Figure 9a). In the case of copper substrates, where carbon has lower solubility, the carbon atoms are not allowed to diffuse in the metal and begin the nucleation and growth without the segregation as in Figure 9b. This process continues until a layer of graphene cover the surface of the metal, thus reducing the active surface and stopping the process, and for this reason, this second reaction is called “self-limiting”[205]. Apart from nickel and copper, other materials have also been used such as transition metals (Fe, Ru, Co, Rh, Ir, Pd, Pt, Au) and alloys (Co–Ni, Au–Ni, and Ni-Mo)[207]. By modifying the CVD parameters and composition of catalysts and precursors, is also possible to control the graphene layer number, grain size, bandgap, and doping[208]–[211]. The downside is represented by the financial investment needed for starting and maintaining the production as well as the need to etch the substrate material producing toxic waste and increasing the cost[212]. Nevertheless, the large area, high-quality graphene produced through this scalable technique is often referred to as the gold standard in pristine graphene studies.

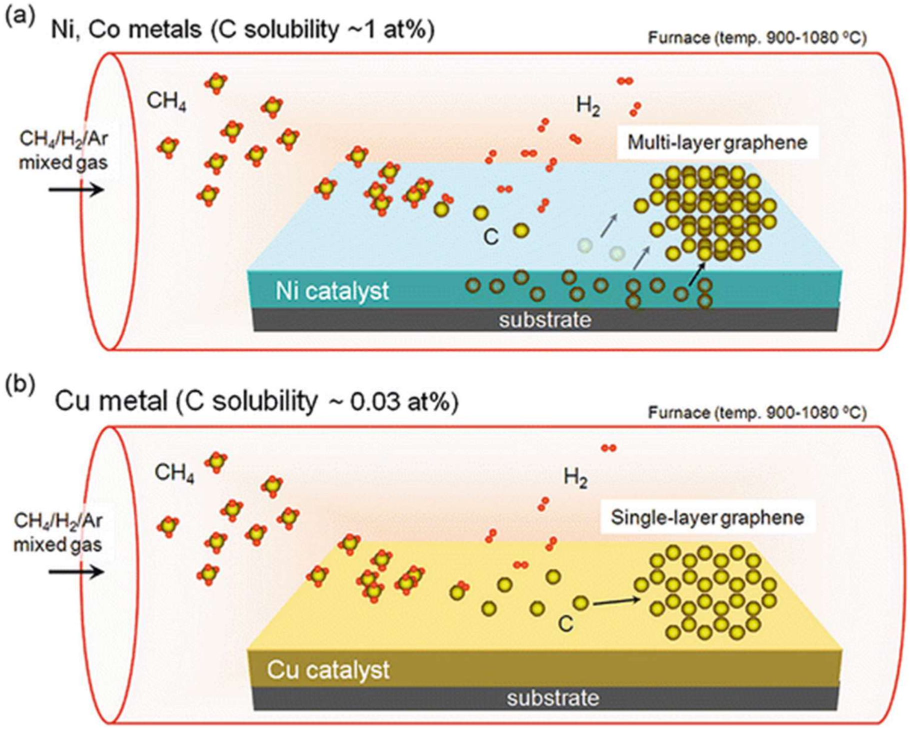

Figure 9 CVD synthesis with different substrate solubility.[212]

Properties

Electrical Properties

The π electron cloud of the graphene is the reason for its excellent electrical conductivity in-plane. When electrons are transported in the 2D material, they present "giant" intrinsic carrier mobility because extrinsic factors like phonon scattering are removed, even beyond 200 000 cm^2/V s, approximately 140 times that of electrons in silicon[213]. This record-high electrical transport stimulated the research towards improving and broadening the applications of graphene as a way to enhance the properties of new materials. Pristine graphene's electrical conductivity is also high (10^4 S/m) thanks to the electron moving in orbit without scattering due to lattice defects or the presence of foreign atoms[214]. The graphene oxide and reduced graphene instead present vastly lower electrical properties (10^{-1} S/m) due to the larger presence of defects and different functional groups which modify and impede the electron transport in the material[215]. The electron mobility of suspended graphene is also greatly affected by the presence of impurities on the graphene surface and by those trapped between the substrate and graphene itself [216]

Mechanical properties

Given the 2D structure of graphene, its mechanical properties are generally separated between in-plane and out-of-plane properties. The formers are concerned with deformation or loading in the basal plane, while the latter with deformation out of the basal plane. The main mechanical characteristics explored in previous studies are Young modulus[217]–[219], Poisson's ratio[220], [221], fracture toughness[222], [223], and friction coefficient under in-plane loading[224]–[226]. Due to the monoatomic thickness of the material the in-plane mechanical properties direct characterization is extremely challenging[227], and the simplest way is an indirect characterization of the membrane through out-of-plane nanoindentation of a suspended membrane[228]. By measuring the relationship between the displacement of the indenter and the force, it's possible to calculate the ultimate tensile strength and to fit the results using the thin shell model for continuous material, deriving pretension and Young modulus of the graphene[217].

$$F = T(\pi a)\left(\frac{\delta}{a}\right) + E^{2D}(q^3 a)\left(\frac{\delta}{a}\right)^3$$

where F is applied force, δ is the deflection at the center point, T is the pretension in the film, E^{2D} is the planar Young modulus, a is the radius of the freestanding area of the membrane, v is Poisson's ratio (which was usually taken as 0.165, as the Poisson's ratio for graphite in the basal plane[229]), and $q = \frac{1}{1.05 - 0.15v - 0.16v^2} = 1.02$ is a dimensionless constant.

While considering the thickness as uniform and fixed at ~0.34 nm, with freestanding pristine CVD graphene the Young modulus was found to be as high as 1.0 ± 0.1 TPa and its strength 130 ± 10 GPa[217]. Always using the nanoindentation method with an Atomic Force Microscope (AFM), the spring constant of graphene was found to be in the range of 1 to 5 N/m[230]. These fitting, however, are limited by the approximations of the continuous models that create problems when the thickness becomes monoatomic as in the case of graphene. With this aim, new research is also published to find improved and comprehensive models for graphene[231]–[233]. Working in parallel to the practical experiment, a wide range of properties were studied through theoretical modeling and numerical simulations (such as first-principles calculation like local density approximation (LDA) and generalized gradient approximation (GGA), and molecular dynamics (MD)) such as the Young Modulus, the phonon dynamics, the Poisson ratio, and other chirality dependent properties.

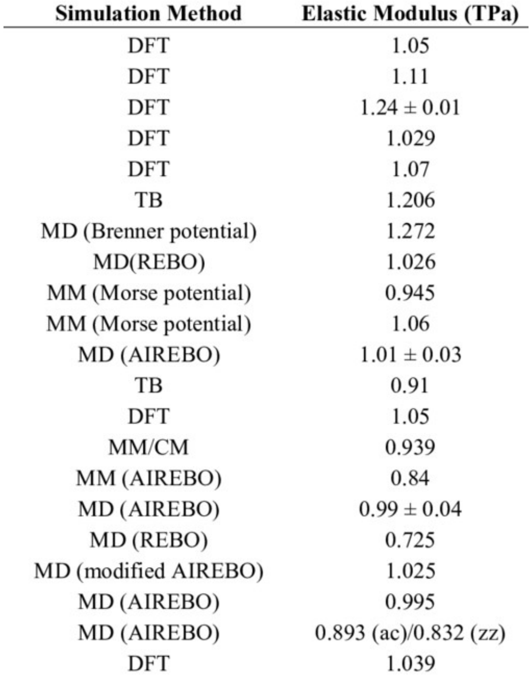

Simulation Method	Elastic Modulus (TPa)
DFT	1.05
DFT	1.11
DFT	1.24 ± 0.01
DFT	1.029
DFT	1.07
TB	1.206
MD (Brenner potential)	1.272
MD(REBO)	1.026
MM (Morse potential)	0.945
MM (Morse potential)	1.06
MD (AIREBO)	1.01 ± 0.03
TB	0.91
DFT	1.05
MM/CM	0.939
MM (AIREBO)	0.84
MD (AIREBO)	0.99 ± 0.04
MD (REBO)	0.725
MD (modified AIREBO)	1.025
MD (AIREBO)	0.995
MD (AIREBO)	0.893 (ac)/0.832 (zz)
DFT	1.039

Figure 10 Different Young modulus obtained with diverse application of computer-simulations and modelling. [236]

This resulted in many different results reported for properties like the Young modulus which showed values ranging from 0.725 TPa[234] up to 1.25 - 1.23 TPa[235] as shown in Figure 10 [236].

The gap between theoretical studies and experimental ones was especially emphasized in 2014 when it was demonstrated that, despite previous studies showing single-layer graphene as strong and tough, it was actually a brittle material with low strength and toughness: the fracture toughness of graphene is only 4.0 ± 0.6 MPa $m^{1/2}$, and the equivalent critical strain energy release rate is only 15.9 J m^{-2} [222]. At the same time, it was also found that, although the fracture strength of graphene is not as high as predicted, the energy delocalization effect due to the high speed of phonon, leads to specific penetration energy for multilayer graphene 10 times higher than steel[237].

Physicochemical Properties

Pristine graphene is hydrophobic by nature, with a water contact angle in the range of 95-100° thanks to its low surface energy[238], [239]. This property poses severe limitations when stable water solutions are needed, as the adding of a surfactant or another stabilizing agent is required to prevent agglomeration and precipitation. The oxidized form of graphene instead presents a much lower water contact angle (30.7°) because of its ability to form hydrogen bonds and metal-ion complexes thanks to the polar basal plane and negative charges originating from the carboxylate groups on the edge sites[238]. The reduced form instead, has the vacancy defects formed during the deoxygenation, which results in properties between the pristine and oxidized form, being less hydrophobic than graphene and exhibiting less reactivity than graphene oxide[240], [241]. Another important aspect of graphene is its tribological properties, as it was shown that multilayer graphene exhibits super lubricity[242], [243] up to the micrometer scale under non-vacuum conditions[244]–[247]. This property is linked to the peculiar electronic structure of the cloud of electrons of the graphene and becomes especially evident in the case of few-layers graphene and multilayer graphene, in which the various layers are relatively free to slip from each other.

Thermal Properties

The thermal properties of graphene are mainly caused by lattice vibrations since its electronic-based thermal conductivity represents less than 1% of the total thermal conductivity at room temperature[248], [249]. The thermal conductivity resulting from the interactions of phonons in the graphene is extremely high and was demonstrated to reach up to 5000 W/mK for pristine graphene. This property was demonstrated to be even higher than other carbon nanomaterials such as single- and multi-walled carbon nanotubes (~3500 W/mK and ~3000 W/mK respectively) or graphene oxide (~2000 W/mK) and far higher than other thermally conductive materials such as aluminum and copper (160 W/mK and 380 W/mK respectively)[250], [251]. However, the thermal properties of graphene are shown to be strongly dependent on its interaction with the substrate and the presence of defects that interfere with the phonon's distribution and movement in the material. For instance, the thermal conductivity of graphene supported by silicon carbide substrate is significantly lower (~600 W/mK) than unsupported pristine graphene[252]–[254]. Nevertheless, its thermal properties, find many applications as additive materials for graphene-based composite with high thermal conductivity.

Optical Properties

Graphene presents an unexpectedly high opacity on a broad range of frequencies, ranging from visible to the terahertz, from which derives the characteristic black color of graphite. The absorbance of a single layer of graphene was demonstrated to be 2.3% (for reference, the same thickness of Silicon atoms would absorb less than 0.05%) and linearly scalable for multilayer graphene as shown in Figure 11 for up to 4 layers [255], [256]. At the same time, its monoatomic thickness counterbalances its high absorbance so that the monolayer graphene allows the passage of over 97% of the light. Thanks to its transparency, thickness, low permeability, and mechanical properties, is also used as transparent windows for liquid analysis, such as in Transmission Electron Microscopies (TEM) [257]–[259] and X-ray Photoelectron Spectroscopies (XPS) [260]–[262], both of which require extreme thinness to avoid interactions with low kinetic energy electrons. This high absorbance is shared among the whole family of carbon-based materials, as shown for example in the case "smoke black" an amorphous carbon form derived from the incomplete combustion of organic materials, or carbon nanotubes, which showed the record absorbance of 99.995% of the incident light when hierarchically distributed on metal surfaces [263]

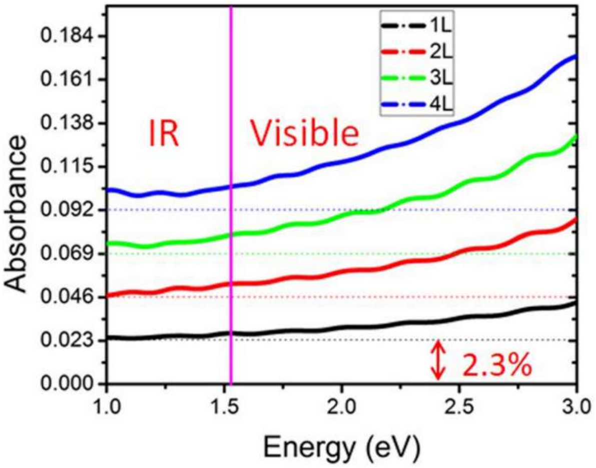

Figure 11 Graph representing the absorption of visible light by an increasing number of stacked graphene layers. [257]

Thanks to the linear dispersion of the Dirac electrons, which enables ultrawideband tunability of graphene-based devices, the optical and electronical properties of graphene have become especially attractive for applications in the fields of optoelectronics, plasmonics, and photonics [264]–[269]. Another interesting optical property is the ability of graphene to become luminescent when cut or converted to nanoribbons and quantum dots, thus introducing a suitable bandgap [268], [270]. These properties together with high charge mobility, light transmittance, and photoluminescence, make graphene also a promising material in magnetic resonance imaging and biomedical imaging [271]–[273]

Biological properties

Graphene and other carbon-based materials' interaction with tissues, cells, and biomolecules is based on the number of layers, dimensions, surface functionalization, hydrophilicity, etc. Thanks to the wide tunability of these properties, graphene has been demonstrated as a promising material for the development of specific applications in the biological and biomedical fields [274], [275]. Graphene-based materials have shown, for instance, unique interactions with nucleic acids, making them attractive for the sensing and delivery of DNA and RNA. The oxide form of graphene (GO) shows preferential adsorption of single-stranded DNA compared to double-strand DNA while protecting the adsorbed nucleotides from the activity of nuclease enzymes [276]–[278]. Thanks to the interaction between the negative charges on DNA and graphene, the adsorption of small oligomers was heightened in high ionic strength solutions at low pH. As opposed to the interactions with DNA and RNA, graphene is less likely to interact with proteins and lipids. Nevertheless, it was shown to form stable and functional hybrid structures with lipids[279]. Unfortunately, because of its non-biodegradable nature, the use of pristine graphene is limited in in-vivo applications, and its interactions with the cellular membranes were studied only recently. The intake mechanism is of particular interest for ex-vivo and in-vitro applications, and the complete process is still subject of debate as recent studies showed differences based on the type of cells involved as well as the shape, dimension, and functionalization of the graphene or carbon nanomaterial involved[280], [281]. Graphene sheets of 10micron of thickness were shown to enter the cell edge- or corner-first and are completely engulfed in the case of lung epithelial cells, plate-like graphene micro sheets instead physically disrupted the cell cytoskeleton. Few-layer reduced graphene showed an enhanced attachment induced by increased extracellular matrix production while highly reduced did not support the cell adhesion. Graphene membranes have also been used as a substrate for neuronal cell culture demonstrating peculiar interactions as semipermeable and conductive membranes and stimulating the neuronal firing[282]. Thanks to its conductive properties, regenerative medicine applications have been studied to implement novel 2D and 3D scaffolds to enhance the regeneration of neuronal tissue. These applications showed promising results in particular demonstrating the proliferation of neuronal cells ex-vivo onto graphene substrates[283] (Figure 12).

Graphene is also studied for its antimicrobial activity as many studies report antibacterial activity of graphene, graphene oxide, and reduced graphene oxide against E. coli and S. aureus, with rGO demonstrating their effectiveness[284], [285]. However, other families of bacteria with metal-reducing capabilities like Shewanella showed no inhibition of bacterial growth[286]. The antibacterial activity of graphene-based materials can be exploited by modifying the shape, size, and chemistry of the 2D material for specific wound healing applications as well as infections prevention[287].

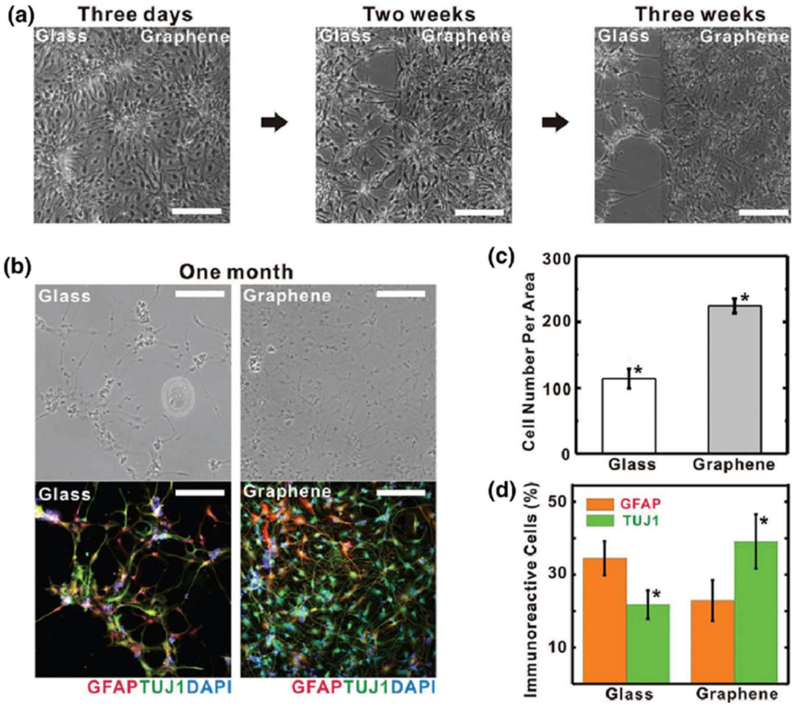

Figure 12 a) micrograph of the boundary between graphene and the glass substrate in neuronal cell colture. b) Fluorescence image of neuronal cells on glass and graphene substrates. c) and d) count and immunoreactive essay of the cells grown for one month on the different substrates. [283]

Applications

Energy storage

The constant worldwide increase of electricity-based devices, and especially the automotive industry has encouraged the creation of new compact and portable energy storage devices. These devices can be mainly divided into two types: batteries and capacitors. The batteries store the electrical energy in chemical reactions, while the capacitors store electrostatic energy in an electric field[288]. The application of graphene in these devices allowed for example the creation of longer-lasting and lighter energy storage devices, which is of high interest in the automotive industrial sector[289]. In the case of batteries, graphene has been proposed to substitute the graphitic carbon anode and as cathodes material in Li-Ion batteries, due to its superior electrical conductivity, high surface area, and chemical tolerance[290]. Thanks to these properties novel Li-based batteries with ultrafast charging and discharging have been investigated[291], presenting the graphene in both the anode and cathode as shown in Figure 13.

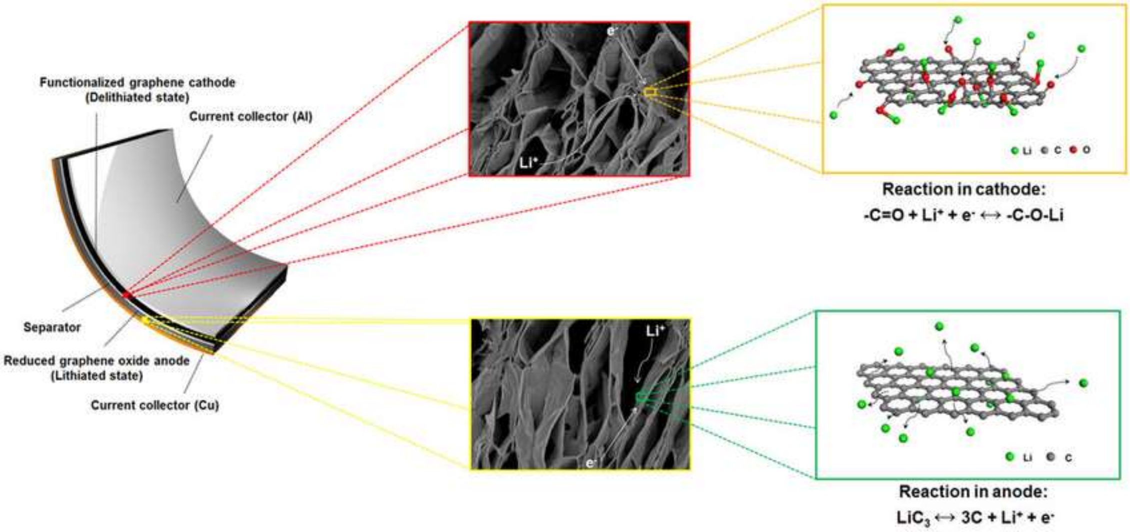

Figure 13 Example of an all-graphene battery, that uses the 2D material for both anode and cathode. [290]

Another advantage of the 2D structure of graphene is the possibility to create stretchable devices able to withstand large deformation preserving their functionalities[292]. These properties opened the door to wearable electronic devices capable of monitoring body functions, integrating the batteries directly in contact with the skin or woven in the fabric of the clothes[293]. For the development of capacitors, graphene has been used to substitute the activated carbon electrodes resulting in supercapacitors with ultrahigh energy densities, over ten times higher than commercial capacitors[294]. In this field, graphene is also a promising candidate for the fabrication of transparent electrodes. Generally, the energy storage devices are composed of two electrodes, a separator, and an electrolyte. Unfortunately only the electrolyte is usually transparent and the only solution to reach transparent devices is to make them extremely thin or micropatterned[295], [296]. In both of these solutions, single-layer graphene is interesting thanks to its high optical transparency.

Gas and Biosensors

One of the most promising applications of graphene is in the production of sensors. The main effect on which these sensors are based is the change in the electrical conductivity of the graphene when molecules are adsorbed on its surface. This derives from the modification of the carrier concentration due to the adsorbed molecules acting as donors and acceptors. Furthermore, the high surface area of graphene, the high quality of the crystal lattice in pristine graphene, and its low electronic noise by thermal agitation are all properties that made it one of the most promising candidates for the fabrication of novel sensors[297]. Graphene-based sensors were demonstrated to be able to detect NO_2, NH_3, H_2O, and CO with fully recoverable properties are vacuum annealing or UV illumination[298]. To increase the sensitivity towards specific gases, the graphene was also functionalized with the electrodeposition of Pd nanoparticles and the resulting sensor showed enhanced properties for H_2 sensing[299]. In addition to gas sensing the properties of graphene have been utilized also in biosensing. For instance, graphene was used in combination with polyvinylpyrrolidone for the fabrication of an electrochemical sensor, which presented a linear response up to concentration 14 mM of glucose[300]. In this field, graphene has also demonstrated superior properties for the biosensing performance than carbon nanotubes devices in the detection of neurotransmitters such as dopamine and serotonine[301]. The main limitation in these applications however resides in the fabrication of the graphene layer without the presence of contaminants. Indeed the residual layer or carbon contaminants left by the transfer, impede the properties of the graphene as a sensing device, and extensive work is directed towards the fabrication of contaminants-free pristine graphene layers[302], [303].

Membranes

The membranes are elements that separate two different environments while still partially allowing the passage of information or specific material between them. They are used in various fields ranging from physics to biology, from chemistry to engineering. Among them, graphene is considered the definitive membrane as it is composed of a single layer of carbon atoms but is impermeable to ions and molecules, and is stronger than any metal, but also electrically conductive. Its surface can demonstrate even more interesting and catalytically active roles in its oxidized forms, and when reduced back to rGO the pores and defects can be tuned to allow the passage of specific molecules[304]. Another way to create nanoporous graphene is through the use of electron/ion bombardment which allows for the fabrication of specific patterns on the membrane[305]. Due to these properties, it has been applied in filtration application for both liquids and gases where the tunability of its design allow for the selection of species down to the passage of single molecules of helium[306]. The pristine graphene instead, thanks to its low permeability, is used in applications where the two environments need to avoid the exchange of mass. For this purpose, graphene has been used as a mechanical pressure sensor or X-ray- or electron-transparent membrane in ultra-high vacuum electron spectroscopies and microscopies[307], [308]. Indeed, since the early days of electron microscopies, using high pressure inside the analysis chamber was critical to analyze and observe samples that would have otherwise been destroyed by the pressure difference[309]. The first thin membranes developed for this use were aluminum [309] and amorphous carbon[310], later followed by SiO_2, Si_3N_4, and polymer membranes which presented good mechanical and optical properties and widened the applicable field of electron microscopies

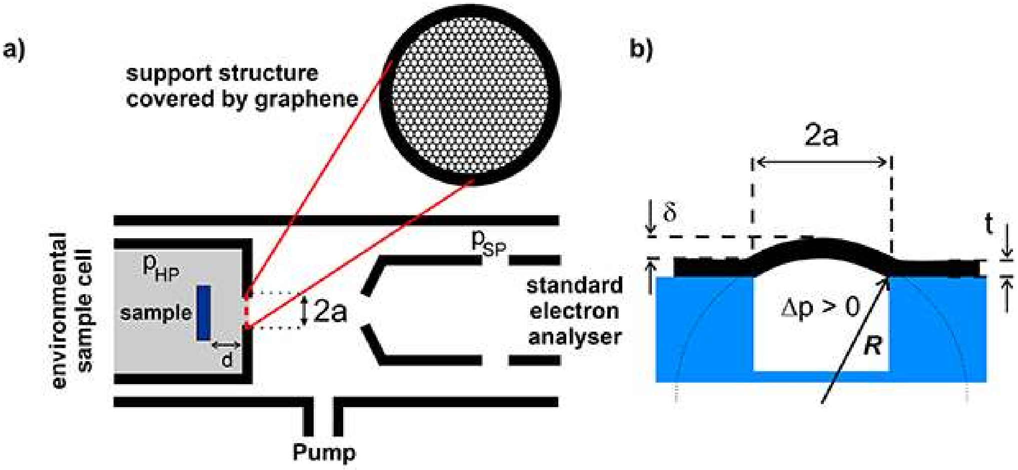

Figure 14 a) single-layer graphene membrane used for the separation of the enviroment of the sample and the vacuum of the analysis chamber in electron spectroscopies, b) deformation of the membrane under the pressure difference. [317]

through the first commercial solutions[311]–[316]. These membranes boosted high transparency to the 10–300 keV electrons and 10^3 to 10^4 eV X-rays but are too opaque towards the relatively low kinetic energy electrons emitted in surface electron spectroscopies.. This opacity is mainly due to the short electron inelastic mean free path (IMFP) λ_{IMFP} which is in the order of a few nanometers in solid materials. Finally, graphene and other 2D materials have been recently used to create even thinner membranes allowing increased sensibility for lower-energy electron microscopies and spectroscopies like X-ray Photoelectron Spectroscopy (XPS) [260], [317]–[319], electron energy loss spectroscopy (EELS)[320] and Auger Electron Spectroscopy (AES)[318], [321] High-Resolution Transmission Electron Microscopy (HRTEM) and Scanning Electron Microscopy (SEM)[322], [323]. Graphene also carries others advantages, as its electrical conductivity aid to avoid charging during X-ray irradiation and can be used to measure electrochemical phenomena at the interfaces[308]. Pristine graphene is also relatively chemically inert which helps in avoiding unwanted interactions with the sample or even protecting a metal surface from oxidation during the handling of the sample[324]. However, there are also disadvantages in its use as a ultrathin membrane, as the the presence of unavoidable grain boundaries and lattice defects greatly reduces both the mechanical properties and the impermeability, thus limiting its effective area of application to nanometer scale surfaces.

Golay Cells

As described in the previous chapter, the Golay cell is a thermal incoherent detector invented in 1947 by Marcel Golay[111]. Its original structure consisted of a cavity of 1.5 millimeters in diameter covered with a collodion (nitrocellulose) membrane with an evaporated metal such as antimony or aluminum[111]. It was first invented to be used for the detection of infrared radiation in astronomy applications. Later, it was also applied to detect the longer wavelengths of the THz radiation proving to be an efficient and moderately sensitive broadband detector. Over the years its design remained practically unchanged but the advancement of micromachining technology and the advent of graphene introduced new possibilities for its improvement. The main aim of the studies that approached the Golay cell is generally related to the miniaturization of this device. The problem with the miniaturization comes from the need to proportionally reduce the thickness of the membrane to keep constant the sensitivity. Indeed, in the presence of a smaller diameter of the suspended membrane, its stiffness becomes increasingly more important when considering its final deflection under pressure[325]. Only the discovery of graphene and its production on large areas with high quality allowed us to consider again the miniaturization and improvement of the Golay cell. Its extremely low bending rigidity in particular was the property missing from the materials available 15 years ago. Thanks to this innovation, new studies were published that simulated the improvement of this uncooled detector over a relatively broad range of frequencies (from 0.5 to 4 THz)[100]. Later, more practical studies applied directly the graphene over micromachined wells and tested their response under heating through interferometry and atomic force microscopy[115], [326]. These experiments, however, used cavities of a maximum of 20 μm of diameter, as shown in Figure 15, due to the presence of grain boundaries and defects of the graphene that limited their application over large, suspended areas. However, considering that the wavelengths of the THz radiation are ranging from 1 mm to 10 μm, the efficiency of such small detectors is severely limited by the relatively small size imposed by pristine graphene membranes.

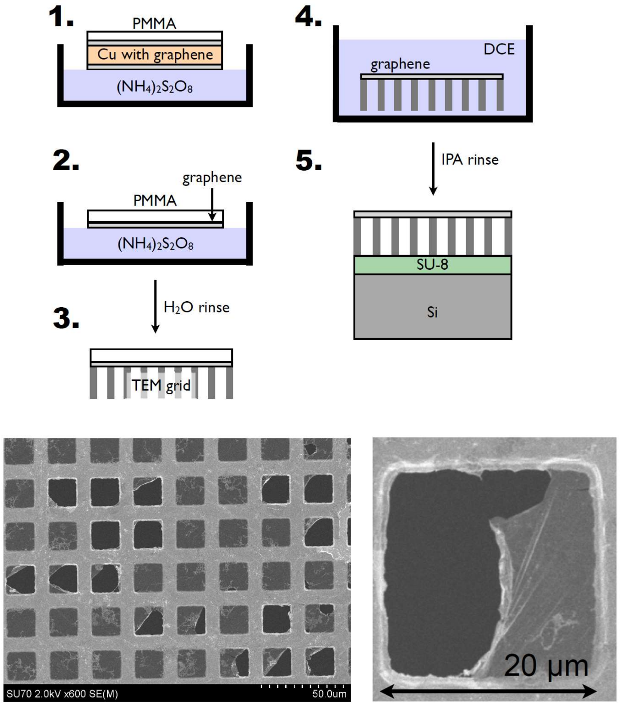

Figure 15 Fabrication process and Golay cell fabricated onto a TEM grid. The final yield of the transfer is relatively low due to the suspended surface being close to the grain size of the graphene layer. [313]

In order to overcome the size limitations and disadvantages of the pure single-layer graphene, in the following chapters, I investigated an nm-thin composite titanium/graphene as an alternative membrane for efficient Golay cells and XPS windows over large suspended areas. For the XPS application, the membranes were lithographically patterned, demonstrating interesting mechanical properties as well as the electron transparency required in the electron spectroscopies. For the THz detection instead, mm^2-sized arrays of Golay cells with lateral sizes up to 50 μm were efficiently fabricated and used for the detection of the THz emission of a Globar source. These applications demonstrated the potential of these membranes reaching beyond the limits of the single-layer graphene over larger suspended areas, while preserving the advantages of its low bending rigidity, high transparency, low permeability, and high mechanical strength.

Aim of the thesis

In recent years, the advent of graphene and other 2D materials stimulated the design and, seldom, the realization of new and improved devices that make full use of the peculiar properties of these bidimensional materials. Graphene unique properties like high thermal and electrical in-plane conductivity[214], [327], high tensile strength and Young modulus, ideal optical absorbance[255], a gapless electronic band structure[328], and its negligible permeability to gases[329], in particular, have led to consider graphene as a promising candidate for the creation of a new generation of devices based on suspended membranes, which find applications in many different fields, such sensors, membranes and energy storage as described in the previous chapter. When trying to exploit the particular properties of the novel ultrathin materials in actual applications, however, several severe limitations emerge: ideal electronic properties are degraded by the presence of atomic impurities[330], reactivity and in particular, oxidation, benefits from unsaturated bonds[331], gas and liquid impermeability is hindered by cracks and defects[332], and mechanical stability is jeopardized by the presence of grain boundaries in films larger than few microns[333]. Indeed, especially for large chemical vapor deposition (CVD) graphene films, since the growth proceeds through multiple seeding, the films are polycrystalline, and thus very brittle [222], which in turn limits its application on large freestanding areas. The brittleness becomes particularly relevant during the transfer of the graphene membrane, as most of the stress is induced on the membrane during this phase of the fabrication [334]. These stresses are mostly induced by two key elements of the transfer protocol: the first is the intrinsic stress of the sacrificial layer used during the wet-transfer method and the lack of uniform adhesion of the graphene to the substrate before the sacrificial layer removal[335]; the second is correlated with the liquid phase introduced in most of the transfer protocols and involves the surface tension of the solvent used for the removal of the sacrificial layer and the negative pressure difference that is formed between the inside and the outside (when the membrane is used to seal a closed volume) during the solvent evaporation. To overcome these stresses to the membrane, either dry transfer is applied, that, however, brings generally worse results compared to wet transfer methods [336], or the sealing of the cells is completed in the second step, which, however, introduce a complex alignment and handling, which are fundamentals when taking into considerations large array of cells. Another way to increase the efficiency of the transfer of the nanomembrane is to directly increase and modify the properties of the membranes themselves. To exploit the peculiar properties of graphene over large areas, while avoiding the disadvantages of brittleness that arises on surfaces higher than grain size, the formation of composite materials is considered as one of the most promising engineering applications[228], [337]–[339]. Graphene composites are materials in which graphene is used as an additive or as a matrix to improve the physical properties of the system. Among these graphene-based composites, the most interesting one for the creation of high strength nano-membranes is the fabrication of metal-graphene nanolayers composite (MGNC), which improve the mechanical, thermal, and electrical properties of the final system[340], [341], like the Poisson ratio (even to negative values)[342], the fatigue resistance [343], the bending rigidity [344] or its tensile [345] and failure strength [340]. These membranes, however, are usually in the order of tens or hundreds of nanometers and most of the mechanical properties out-of-plane are limited, like the bending rigidity which is very low for graphene but becomes increasingly higher with the thickness of the membrane. Another problem with the excessive thickness of MGNC is the loss of transparency to electrons as their transmission or escape path is limited to a few nanometers in solid materials such as the metals used in the composite layers.

As the purpose of this thesis, I aimed at overcoming the limitations imposed on these novel materials through the creation of ultrathin composites, combining them with the microfabrication techniques required for the creation of a new generation of Golay cell for the THz detection. To create membranes with enhanced mechanical properties and suspended over large areas without losing their peculiar properties, I developed a fabrication method for the creation and transfer of ultrathin membranes on an array of micrometer-scale holes. The membrane was composed of CVD single-layer graphene and a nm-thin titanium layer and reached a transfer yield larger than 95%. The arrays were composed of thousands of cells distributed over an area of more than 16 mm^2, with a total freestanding area of up to 2500 μm^2 for each cell. The membranes designed were also modified through the patterning of the metal layer for improved electron transparency, widening their field of application to electron spectroscopy and microscopies.

Chapter 3

Ultrathin suspended membranes

To challenge the microscale limitations of freestanding graphene, in this chapter I investigate the fabrication and characterization of composite membranes composed of monolayer graphene and evaporated titanium. The titanium serves as a reinforcing layer for the membrane, allowing the efficient transfer of these ultrathin membranes over large areas. The membrane was also characterized with the use of X-ray photoelectron spectroscopy to investigate the oxidation state and elemental composition of the membrane. To suspend these membranes, large arrays of square holes were fabricated on silicon wafers by UV lithography and micromachining techniques, resulting in silicon grids with both open and closed wells. Finally, the mechanical properties of the suspended membrane were characterized with atomic force microscopy (AFM), revealing the correlation between the mechanical response and the thickness of the membrane.

Fabrication and transfer of the ultrathin membranes

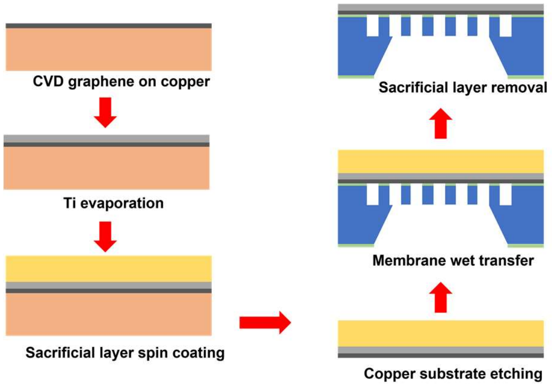

Figure 1 Schematic illustration of the process used for the production and transfer of the composite membrane to the silicon substrate.

To produce the ultrathin membrane, commercial CVD graphene from GRAPHENEA® was used as a substrate for the deposition by e-gun evaporation of titanium layers of thicknesses 2.5 nm, 5 nm, 7.5 nm, and 10 nm. The electron gun was ramped up to 30 mA to deposit titanium with a rate of 0.4 Å/s. The thickness, as well as the rate of deposition of the metal layer, was controlled using a quartz crystal microbalance. As shown in Figure 1, after the titanium evaporation, the sample was spin-coated with mr-I 7020R photoresist (MICRORESIST). $FeCl_3$

30% copper etchant solution (SIGMA ALDRICH) was used to dissolve the copper substrate, leaving the Gr/Ti/photoresist film floating on the solution surface at room temperature as shown in Figure 2a. Finally, the film was rinsed 3 times in clean DI water as in Figure 2b to remove FeCl$_3$ residues, and manually fished out from the aqueous solution with a silicon substrate as demonstrated in Figure 2c. The substrate with the membrane was annealed for 5 min at 140° to increase the adhesion to the substrate and relax internal stresses in the sacrificial layer[335] and then dipped in acetone and isopropanol for 30 seconds each to remove the resist layer, leaving only the ultrathin membrane of graphene-titanium on top of the grid. For the final removal of the solvent, to minimize surface tension stress generated during evaporation, the samples were left 24 hours under a petri dish on cleanroom paper to slow down the evaporation process. The same wet-transfer process was used to transfer single-layer graphene without titanium.

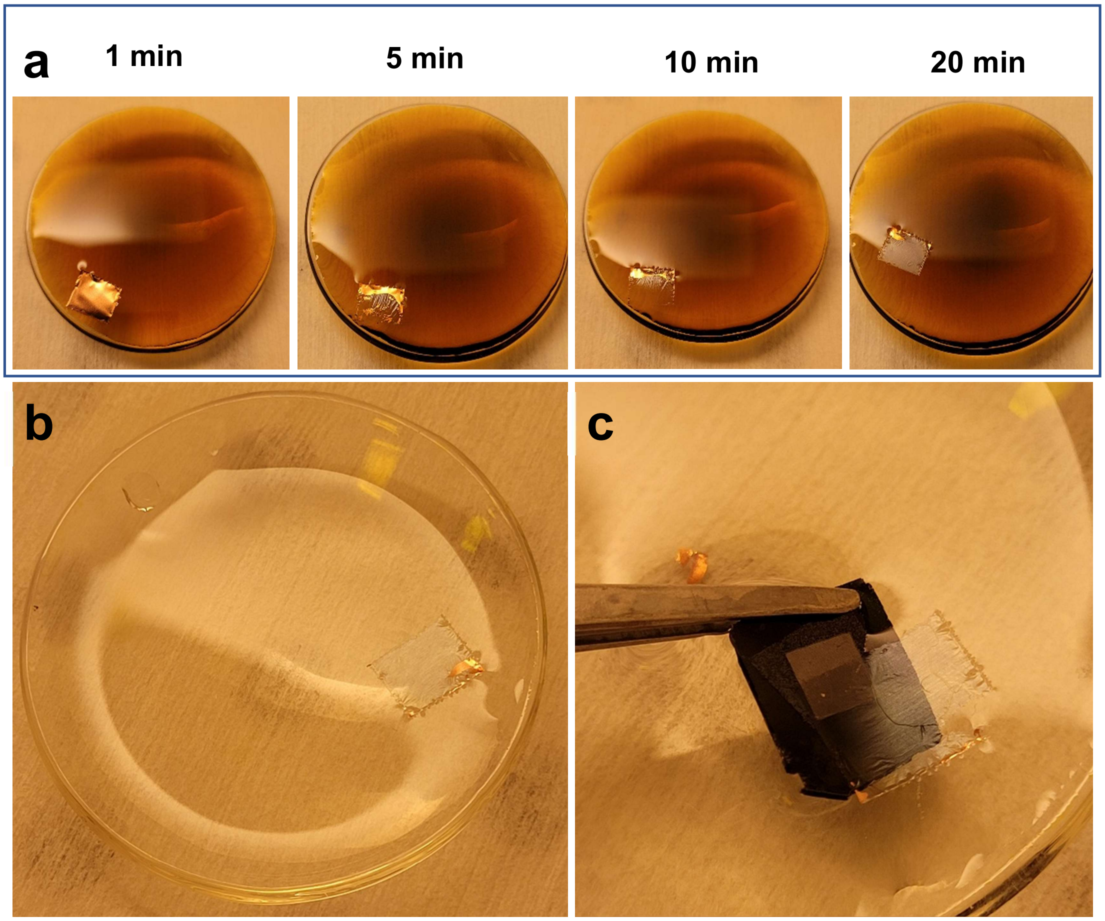

Figure 2 Wet-Transfer of graphene/titanium membrane. a) Copper substrate etching, the residual unetched copper in the corner of the sample is covered by the sacrificial resist that during the spin coating was absorbed on the backside of the copper foil due to surface tension. b) The membrane with the sacrificial layer is left floating on DI water to remove any impurities of the etching solution. c) Pulling up the membrane floating on the surface with a micromachined Silicon wafer chip. The substrate is semitransparent due to the holes micromachined through the silicon. The yellow color of the images is caused by the filtered illumination of the cleanroom environment.

X-Ray Photoelectron Spectroscopy

A thin layer of Titanium rapidly oxidized when exposed to the atmosphere, thus modifying its chemical and mechanical properties. For this reason, to evaluate the chemical status of the Ti/Gr membrane, an XPS characterization was carried out at Elettra Synchrotron BACH Beamline. This allowed us to define the elemental components of the membranes. This technique uses monochromatic X-Ray to excite core level and valence band electrons that are emitted in a vacuum with a kinetic energy characteristic of a given element and its chemical environment. Due to the very short path electrons can travel inside a material without experiencing any interaction, this technique can provide information only on a very shallow portion of the sample, up to a few nanometers of depth. The first experiment took into consideration two different thicknesses of the titanium, 2.5 nm, and 5 nm. These Gr/Ti membranes were deposited on silicon wafer substrates evaporated with an adhesion layer of 10 nm of titanium and 30 nm of gold. To characterize the elemental composition of the membrane a survey was performed with different photon energy, 649 eV, 1200 eV, and 1596 eV. To detect the emitted photoelectron a VG-Scienta R3000 hemispherical analyzer was used for the measurements. This first surface analysis, reported in Figure 3, allowed for the identification of the 2p, 3p, and 3s core levels peaks of titanium on a 2.5 nm membrane, however, at 649 eV, the photon couldn't stimulate the emission from the deepest core level of the titanium, the 2s. Other notable elements on the surface were carbon and oxygen, mostly derived from organic contaminants resulting from the polymer sacrificial layer used in the wet transfer method. No peaks related to the etchant ($FeCl_3$) or the copper foil were found, indicating the complete removal of the wet etchant.

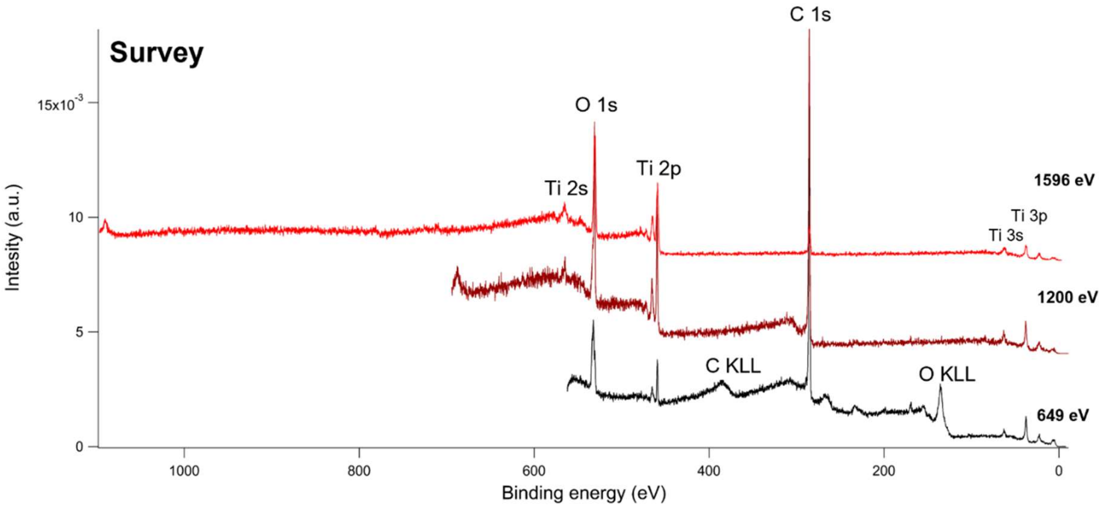

Figure 3 Survey of the surface at different photon energies of a 2.5 nm Ti membrane. These survey were used to identify the elements present on the surface of the membrane, namely carbon, oxigen and titanium.

The 2p peaks of titanium were monitored for the qualitative analysis of the metal layer as they presented the highest photoemission intensity. A Shirley background was subtracted to the spectrum to separate the elastic from the inelastic photoelectron signal and then a Voigt function was used for the peak fitting. By deconvoluting the curve, the peaks illustrated in Figure 4 were confronted with the literature to identify the metallic titanium and its oxidized forms (Ti^0, Ti^{2+}, Ti^{3+}, and Ti^{4+})[346]–[348]. The predominant oxidation state was Ti^{4+} (TiO_2) which presented two peaks at 459 eV and 464.5 eV, followed by Ti^{3+} (Ti_2O_3) which presented peaks at 457.5 eV and 463.5 eV. The absence of the Ti^0 indicated the complete oxidation of the titanium at room temperature and an atmospheric pressure of oxygen.

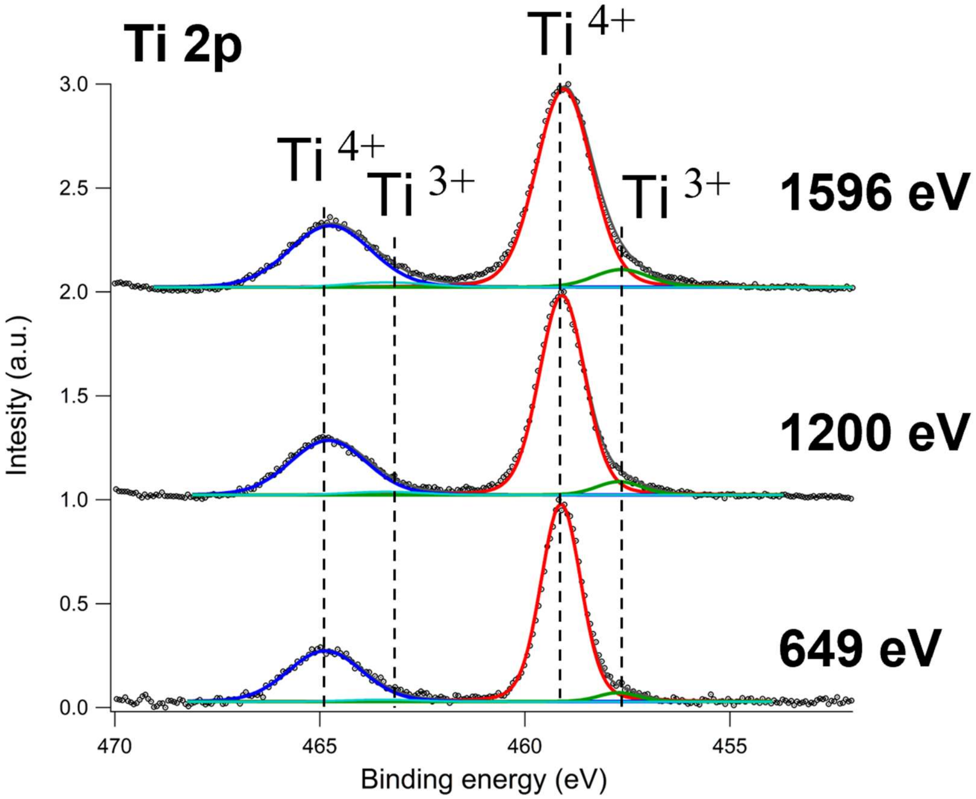

Figure 4 Peaks of the Ti 2p core level. The only oxidation states found were Ti^{4+} and Ti^{3+} indicating the full oxidation of the titanium on the 2.5 nm membrane.

The different photon energies allowed to characterize the membrane at different depths. Indeed, by increasing the photon energy, the emitted photoelectron proportionally increases its kinetic energy. In Figure 5 is illustrated the relation between this kinetic energy and the mean free path λ of the photoelectron in the material [349]. Increasing the kinetic energy of the photoelectron increases its path in the material, thus it is possible to detect the elements deeper in the material. With the highest photon energy (1596 eV) the mean free path of the electrons was calculated to be higher than the thickness of the membrane (~3 nm). No notable difference was observed in Figure 4 between the different photon energies which can be explained by a uniform oxidation of the titanium membrane.

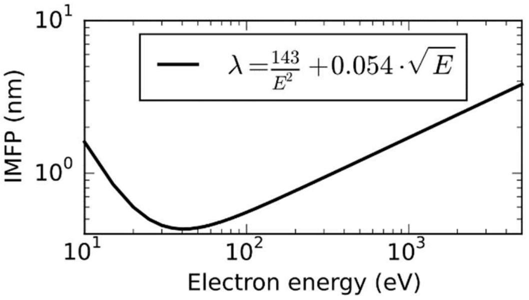

Figure 5 The graph illustrate the relationship between the mean free path of a photoelectron in a solid medium and its kinetic energy. [349]

The next peak of interest was the O 1s core level, which originates from both contaminants on the surface and titanium oxide. The peaks, reported in Figure 6, presented a marked variation at different photon energies. After applying the same fitting described for the titanium, the peaks were deconvoluted and it was possible to differentiate between the oxygen derived from the organic contaminants and the oxygen bonded to the titanium. The former is limited to the outermost surface and is highlighted with the lowest photon energy (649 eV). Its peaks are those relative to O=C and H-O-C at 532 eV and 533 eV respectively. The oxygen covalently bonded to the titanium, instead, peaked at 530.5 eV and it is present both on the surface and in the first nanometers of the membrane as shown at the highest photon energy of Figure 6.

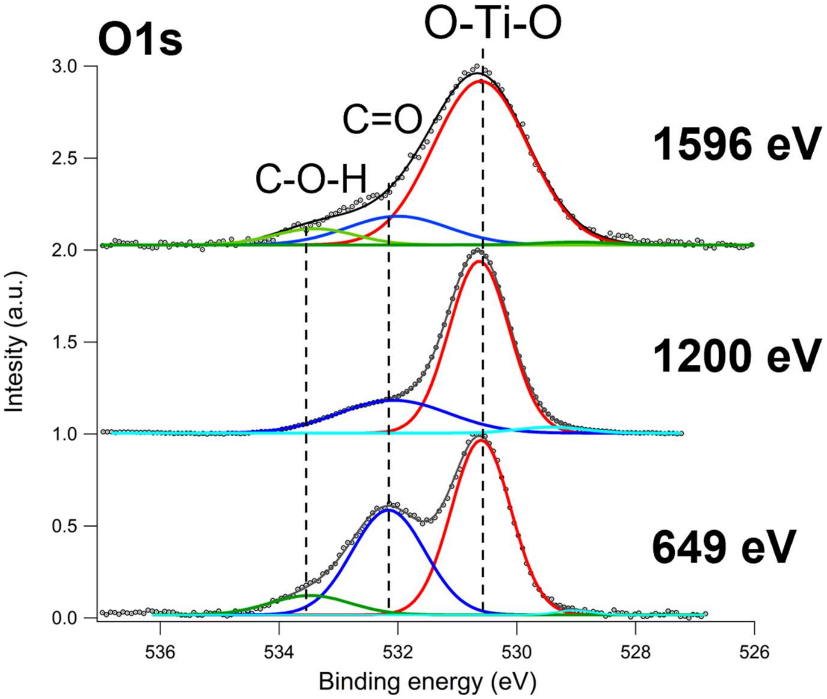

Figure 6 O 1s peaks with different photon energies. The peak change denotes the different signal coming from the contaminants on the surface, that are more relevant in the lower energy photon, and the oxygen bonded to the titanium, which is dominant at the higher photon energy.

Because the mean free path of the photoelectrons with the highest energy photon (1596 eV), was similar to the thickness of the membrane, the sample was also investigated for the presence of the photoelectrons coming from the gold substrate. As shown in Figure 7 two peaks were identified. They correspond to the peak $4f_{5/2}$ with a binding energy of 88 eV and the peak $4f_{7/2}$ at 84 eV. The photoelectrons emitted by the gold confirmed that the membrane was fully characterized, and thus proving the complete oxidation of the 2.5 nm Ti membrane.

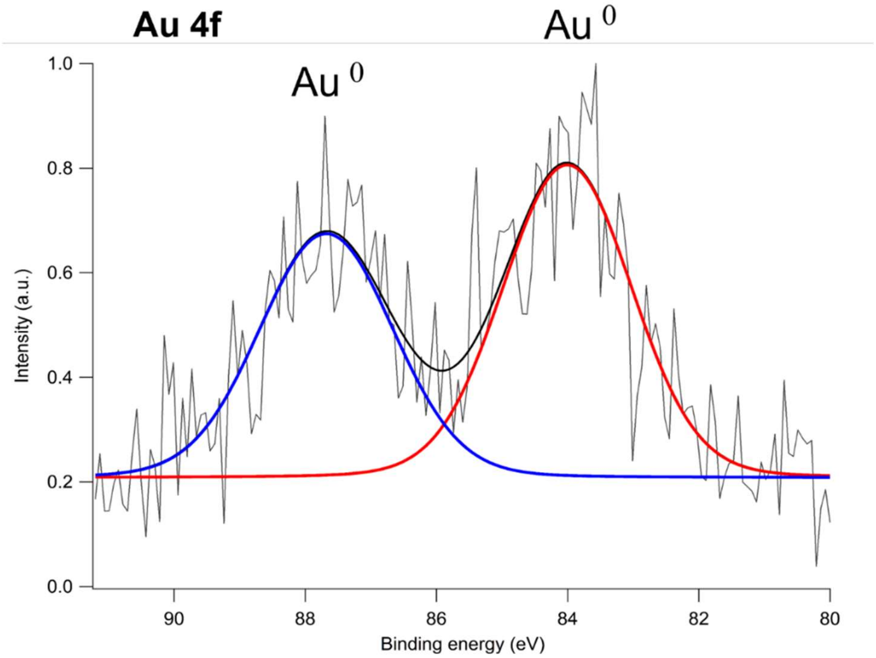

Figure 7 Peaks representing the photoelectrons emitted by the 4f gold core level with the highest photon energy used, 1596 eV on the 2.5 nm membrane. The presence of these peaks indicates the full penetration of the 2.5 nm membrane.

After characterizing the oxidation state of the 2.5 nm Ti membrane, another experiment was conducted on a 5 nm Ti membrane on the same substrate. This membrane revealed analogous results to the previous membrane. The 1s core level of the oxygen once again showed carbon contaminants on the surface, and the signal coming from the oxygen bonded to the titanium was dominant at the higher photon energies. The 2p peaks of the titanium shown in Figure 8 demonstrated the complete oxidation up to the middle of the membrane. While the graphene on the backside of the membrane may offer some protection against titanium oxidation, it is

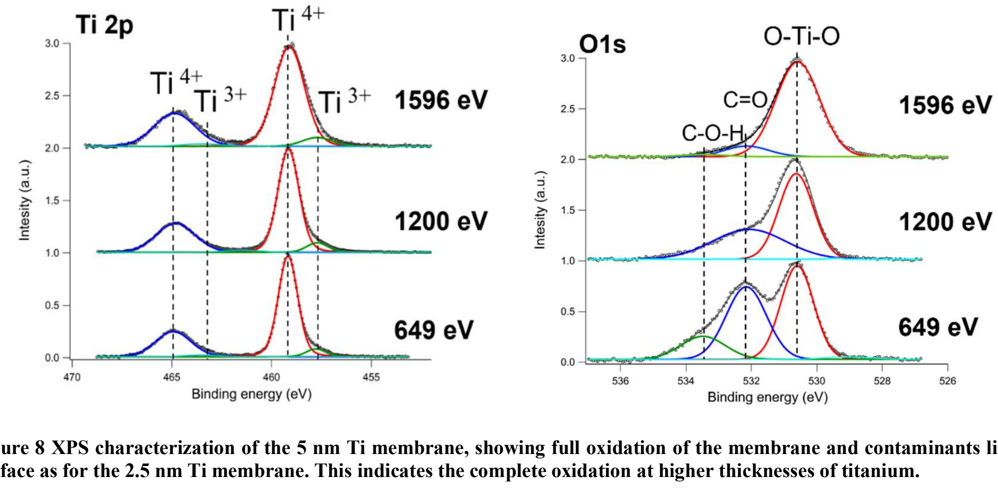

Figure 8 XPS characterization of the 5 nm Ti membrane, showing full oxidation of the membrane and contaminants limited to the surface as for the 2.5 nm Ti membrane. This indicates the complete oxidation at higher thicknesses of titanium.

still reasonable to assume that the membrane may be fully oxidized when exposed to the atmosphere at room temperature.

Grid substrate fabrication

The grid substrates were fabricated through standard micromachining techniques on a silicon wafer with a 2 µm-thick layer of low-stress CVD silicon nitride (Si_3N_4) on both sides. As illustrated in Figure 10a the wafer was coated on both sides with a 150 nm thick layer of chromium by magnetron sputtering, intended as a hard mask for the subsequent dry etching. The patterning was transferred by optical lithography using MEGAPOSIT® SPR 220 1.2 positive resist (SHIPLEY). The pattern on the wafer backside consisted of a square window of 4.5 mm x 4.5 mm at the center of each 10x10 mm single-chip sample. On the wafer front side instead, was lithographed the pattern shown in Figure 9 that was composed of a grid of square holes of two different sizes as reported in Table 1, 25x25 µm and 50x50 µm with a density of the two grid of 810 holes/mm^2 and 230 holes/mm^2 respectively.

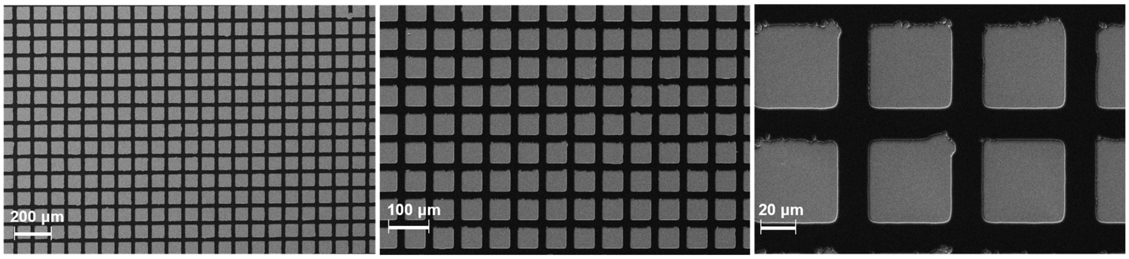

Figure 9 Pattern of grid with 50 µm squares on the front side surface of the silicon prior the chromium mask etching.

Grid Size	50x50µm	25x25µm
Period	65µm	35µm
Array Density	230 holes/mm^2	810 holes/mm^2

Table 1 Basic characteristics of the grid structure lithographed on the silicon windows

After the pattern transfer on the chromium layer by wet-etching, the silicon nitride layer was dry-etched only on the backside for 1 hour with reactive ion etching (CF_4 and O_2). The silicon wafer was then wet etched in KOH solution 30%wt for 6 hours at 70°C: the etching was stopped before reaching the Si_3N_4 on the opposite side, leaving a 30 µm thick silicon layer as shown in Figure 10a. The silicon thickness left was required to avoid excessive brittleness of the grid. Indeed, if the silicon was etched until reaching the silicon nitride, the final substrate would be too thin and brittle to handle the stress induced during the wet transfer of the membrane. Even the presence of the water tension could produce stresses strong enough to damage such a large area array of cells. To maximize the uniformity of the final etched surface on the bottom of the silicon window during the whole etching process, the solution temperature and concentration were kept constant, and isopropyl alcohol was added as modulating agent [37, 38]. The etching rate was controlled every 30 minutes taking the sample out of the basic solution, rinsing in DI water at 70°C, drying with clean nitrogen, and measuring the etching depth with an optical

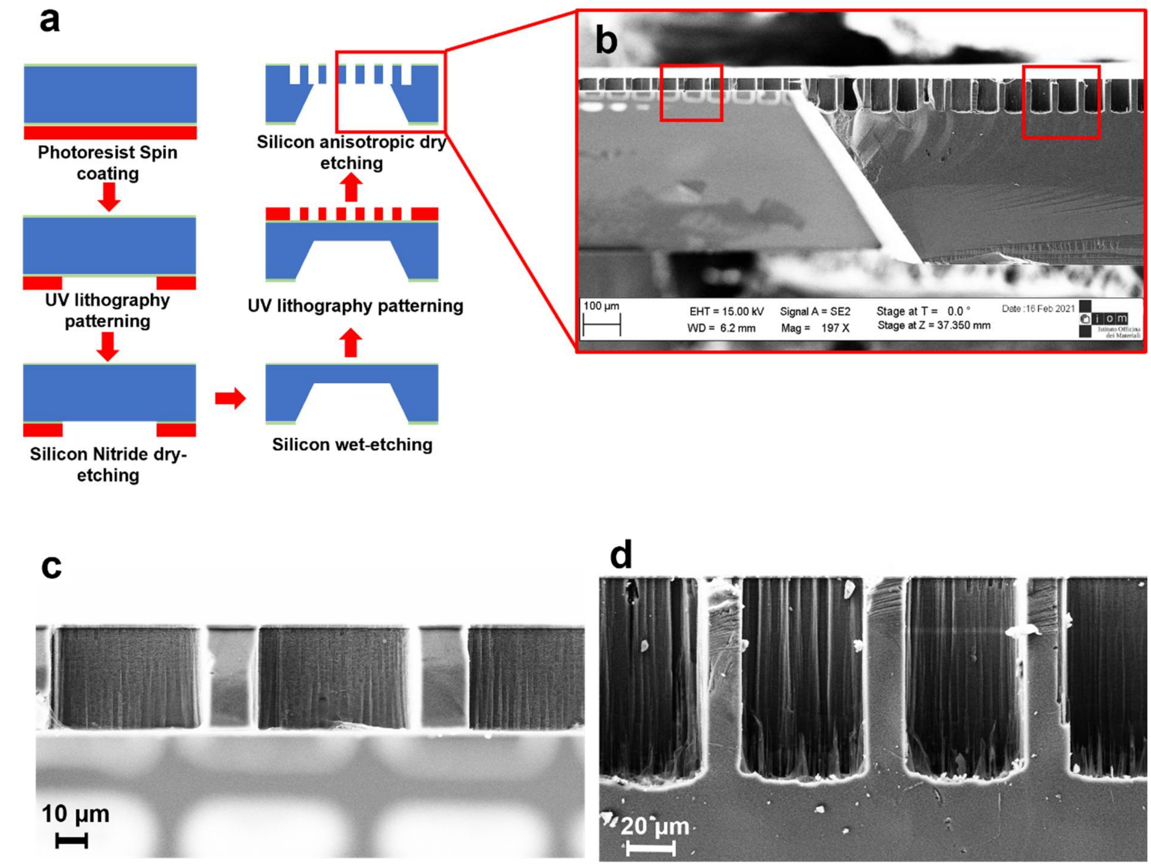

Figure 10 a) schematic summary of the microfabrication protocols for the grid b) Section view of the grid microfabricated through the silicon wafer. c) particular of open (passing through) and d) closed cells respectively. The closed-cell part of the sample was created when the dry-etching Bosch-like process micromachined the pattern outside of the silicon wet-etched window.

profilometer (FILMETRICS Profilm 3D®). Finally, after transferring the pattern on the front SiN layers as shown in Figure 10a, a second dry-etching with a Deep Reactive Ion Etching (DRIE) process, based on SF_6, C_4H_8, and Ar, was used to vertically etch the patterned grid on the front side through the silicon window and create the wells shown in Figure 10 [351]. To avoid the complex alignment between the pattern on the frontside and backside, the pattern micromachined in the silicon also extended outside the silicon window, resulting in both open and closed cells shown in Figure 10b and highlighted in Figure 10c and d, on the same wafer chip.

Transfer yield and morphology of the membranes

After the transfer, the samples were examined with an optical microscope to assess the efficiency of the transfer and count the number of surviving membranes per substrate. In particular the collapsed membranes were counted with respect to the number of wells visible in the field of view of the optical microscope (~121 cells for the 50 µm wells) for each array. This efficiency was determined by the percentage of membranes still suspended and not presenting any visible damage or defects after the transfer, thus was defined as the yield of the transfer. The membranes studied in this chapter differed by material and thicknesses which are also summarized in Table 2, and were transferred on both the grid sizes fabricated previously.

Thickness	2.5 - 5 - 7.5 - 10 nm	2.5 - 5 - 7.5 - 10 nm	monolayer
Material	Titanium/ Graphene	Titanium	Graphene

Table 2 Membranes transferred and studied on both sizes of the microfabricated grid (25 and 50 microns square holes)

The yield varied greatly with the thickness of the titanium and its effect are illustrated in Figure 11 where are reported the yield obtained after at least 10 transfers for each sample: membranes with 10 nm and 7.5 nm of titanium, demonstrated a yield of 99±1% for both the 50x50 µm and 25x25 µm holes; for the membranes with thinner Ti layers the yield depends on the size of the holes. 5 nm Ti membranes reached ~95±2% of coverage on 25x25 µm cells and 90±2% on 50x50 µm cells. 2.5 nm Ti membranes reached 70±2% of coverage on 25x25 µm and 40-50±10% on 50x50 µm cells. The pure single-layer graphene membrane instead demonstrated a yield of less than 1% over 25x25 µm and no cell membranes were successfully covered over 50x50 µm. In the case of only titanium, the 10 and 7.5 nm did not show any difference compared to the titanium/graphene bilayer, however, for 5 nm the yield was slightly lower as it was ~90% and ~85%. Finally, the 2.5 nm membrane of pure titanium demonstrated less than 1% of yield for the transfer on both 25x25 and 50x50 µm holes showing an increasing mechanical contribution of the graphene with a reduction of the metal layer.

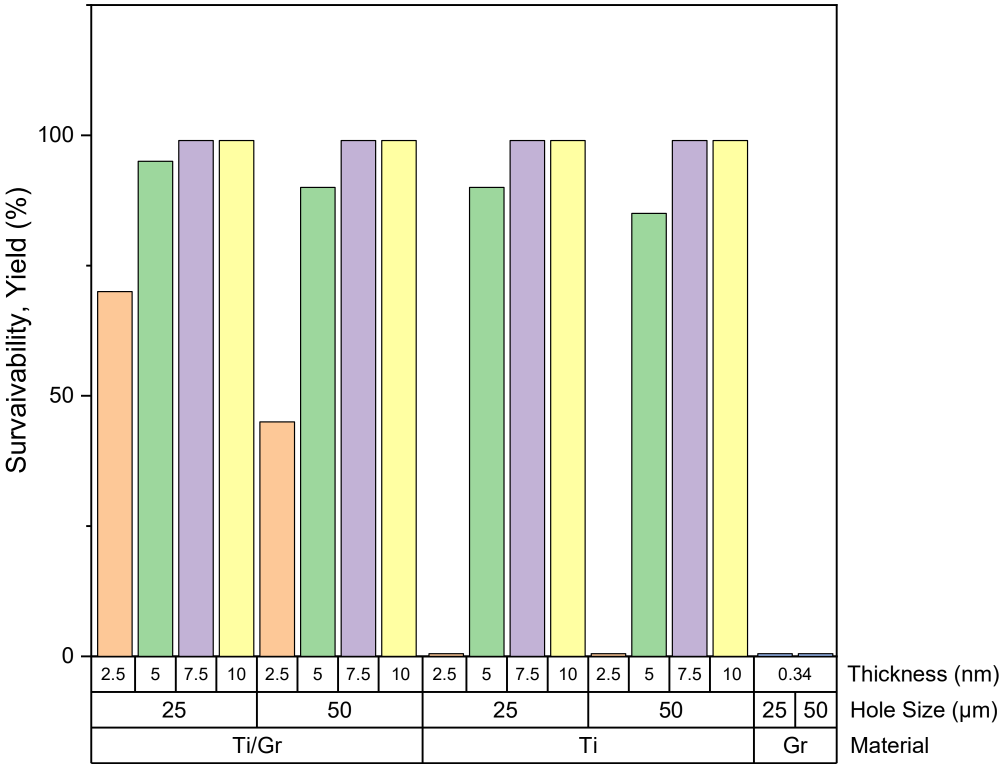

Figure 11 Graph representing the yield distribution of the membranes transferred over both the 25x25 and 50x50 µm holes with different thickness of titanium.

To characterize the morphology of the samples, electron microscopy was employed. The SEM micrographs shown in Figure 12 demonstrated an increasingly corrugated surface proportional to the increase of the thickness of the metal layer. The roughness of the 10 nm Ti membrane reduced the interaction between the membrane and the substrate, decreasing the overall adhesion to the grid. With 5 nm of titanium, the membrane presented less surface corrugation and a better adhesion is visible between the grid and the membrane. In the case of 2.5 nm of Ti, the resulting membrane was flat, with no observable corrugation. The presence of these corrugations on the membranes and their correlation with the thickness of the titanium may be explained by the thermal stress introduced during the titanium evaporation. The temperature required by this process reaches values above 1200°C and the different coefficient of expansion between the titanium and the substrate (the copper foil with the graphene) caused the formation of residual stresses in the membrane when it was cooled down to room temperature. When the copper substrate is etched during the transfer, the strained membrane deforms under the residual stress while floating on the etchant solution. After the removal of the sacrificial layer, the membrane finally relaxes, generating the corrugations of the surface.

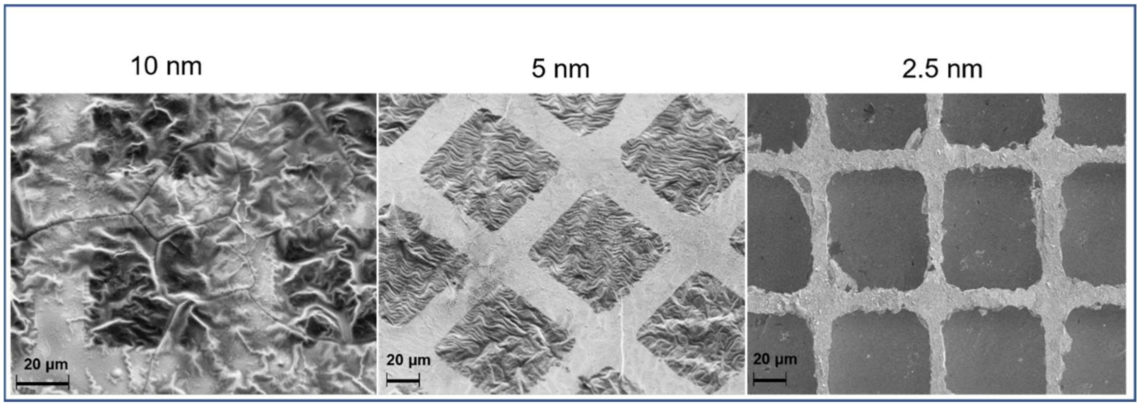

Figure 12 Morphology of the membranes with different thicknesses of titanium. Increasing the deposited titanium proportionally increase the corrugation of the membrane due to the thermal stresses induced during the evaporation of the metal.

Mechanical Properties

To investigate the mechanical properties of the suspended membranes described above, we performed a series of indentation measurements using an atomic force microscope (AFM). Shortly, the AFM is an instrument that measures the deflection of a cantilever of known mechanical properties (in particular elastic constant and resonant frequency), to determine the surface morphology or the mechanical characteristics of the substrate. In our experiment, the cantilever was pressed on the membranes at a constant speed with a piezoelectric element. By measuring the deflection of the cantilever during the membrane indentation, it was possible to derive the mechanical properties and response of the membrane. After approaching the membrane with a low setpoint (2 nN), it was repeatedly indented at a constant speed of 4 μm/s with a force increasing by 50 nN after each cycle, up to the rupture of the freestanding film. The mechanical response of membranes with different thicknesses is illustrated in Figure 13a: the 2.5 nm of Ti showed a non-linear response with a smooth indentation curve, on the contrary for 7.5 nm and 5 nm of Ti the indentation presented steps due to the unfolding of the corrugation during the indentation. Indeed, when the pressure was applied with the cantilever, the membrane responded with sudden changes in its morphology, as reported by the sequence shown in Figure 13c. The corrugations, in spite of their randomness, are reversible: Figure 13b shows repeated indentation on a single membrane. During the experiment, the steps occur in the very same position and with the same height which indicated that after each indentation, when the cantilever was retracted, the membrane elastically returned to the original conformation state. This highlights the reversibility of the unfolding process of the corrugations and the elastic mechanical response of the membrane.

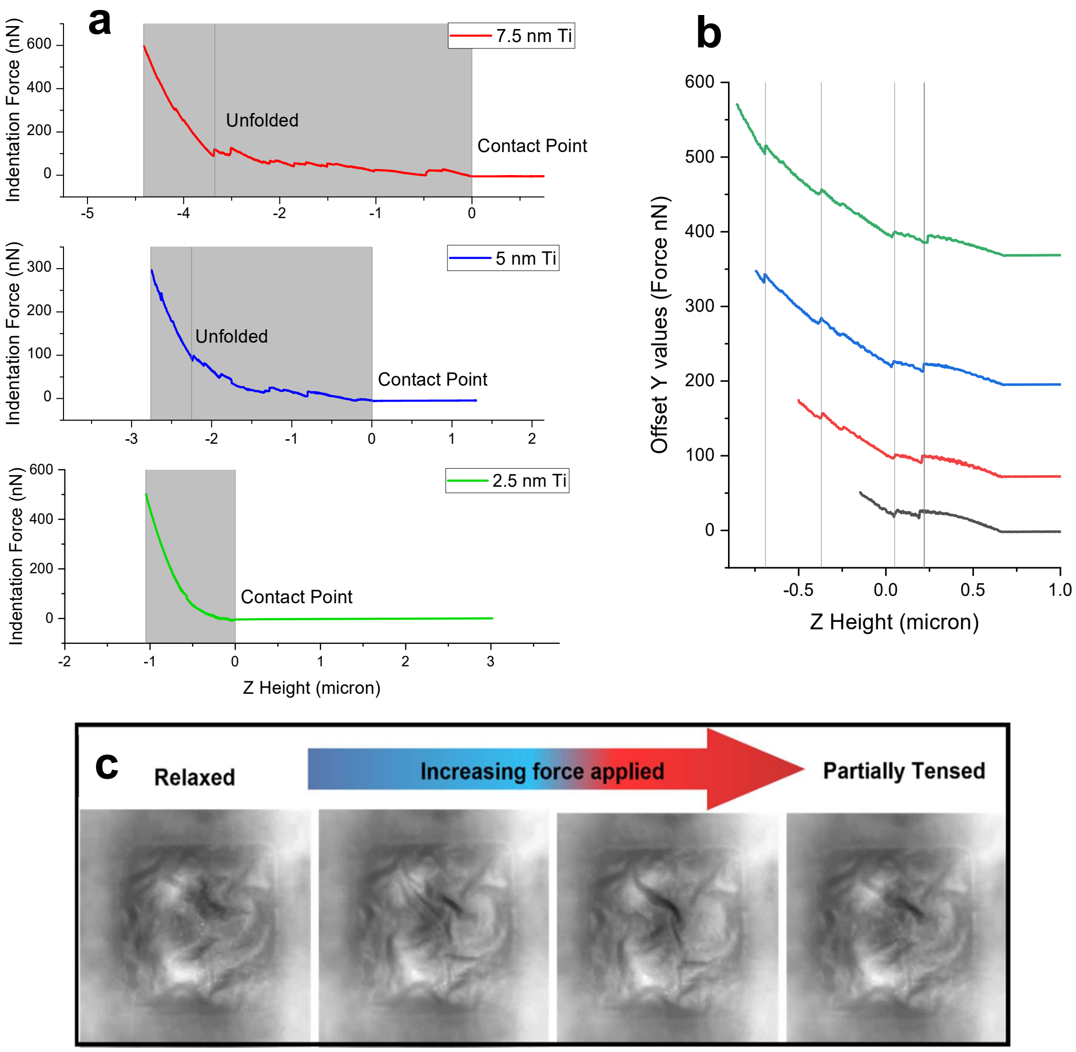

Figure 13 a) Different mechanical response for different titanium thickness. 7.5 and 5 nm of titanium showed a stepped mechanical response, while the flat 2.5 nm membrane presented a smooth stress-strain curve. b), the same 5 nm membrane subjected to repeated indentation with increasing force. The steps were constant in their position and the unfolding of the membrane was confirmed to be a reversible process. c) sequence of images of a 7.5 nm Ti membrane unfolding during the indentation.

The increase of the maximum deflection observed in Figure 13a can be explained by the gap between the surface of the stretched membrane (the real surface illustrated in Figure 14a) and the projected surface (which is the area of the patterned grid). The more corrugated the membrane, the larger is the real surface. The final cantilever extension required to completely unfold the membrane and start to exert tensile stress on it, is consequently greater as shown in Figure 14b.

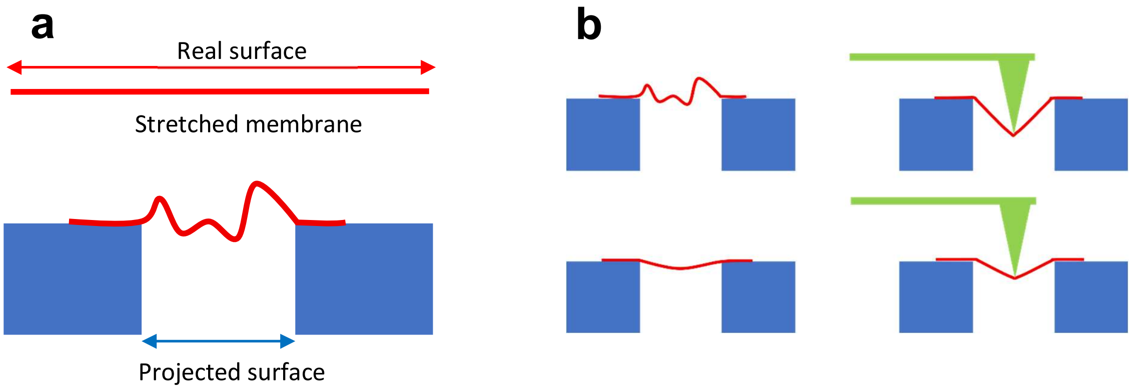

Figure 14 a), Illustration representing the gap of the real surface of the membrane compared to the projected surface. b), the corrugated membrane showed an increased deflection of the membrane during indentation due to the higher real surface.

To further confirm these findings, a statistical analysis was carried out on over 30 different membranes for the four used thicknesses. Each membrane was repeatedly indented with a force increasing in steps of 100 nN, until one of these conditions were reached: a) the load at which the membrane is pierced by the AFM tip was reached (as shown in Figure 15) b) the applied forces were outside of the AFM range.

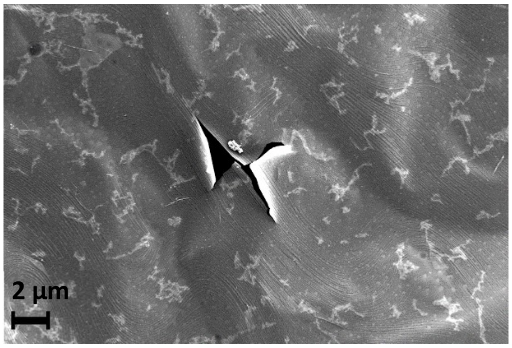

Figure 15 Membrane with 7.5 nm of Ti pierced by the cantilever tip during the indentation.

To derive the Young modulus and pretension data from the indentation curves while considering the different performance of the membranes, both the stretching contribution (which dominates in the case of 2.5 Ti) and the bending contribution (which dominates in the case of 10 Ti) were considered. The following mathematical models take into account both stretching and bending [352]–[354]:

$$F = \frac{4\pi E t^3 \delta}{3(1-v^2)a^2} + \frac{q^3 E t \delta^3}{a^2} + \pi T \delta$$

Where t is the thickness of the membrane, v is the Poisson's ratio, E is the effective Young modulus of the film, a is the radius of the freestanding area of the membrane, δ is the deflection at the center point, T is the pretension intrinsic to the membrane and q is a dimensionless parameter equal to:

$$\frac{1}{1.05 - 0.15\nu - 0.16\nu^2}$$

This fit function was then applied to each indentation curve under the assumptions that the membranes are isotropic and elastic as the ratio between the thickness and the film radius was less than 0.001. Only fit results with $R \geq 0.998$ have been considered. The results for the membrane pretension and Young modulus are reported in Figure 16 and Figure 17 respectively. Each dot represents the results of an indentation curve. The distribution is remarkably wide for both the pretension and the Young modulus, and that can be ascribed to the random generation of the surface corrugation, which increases with the Ti thickness.

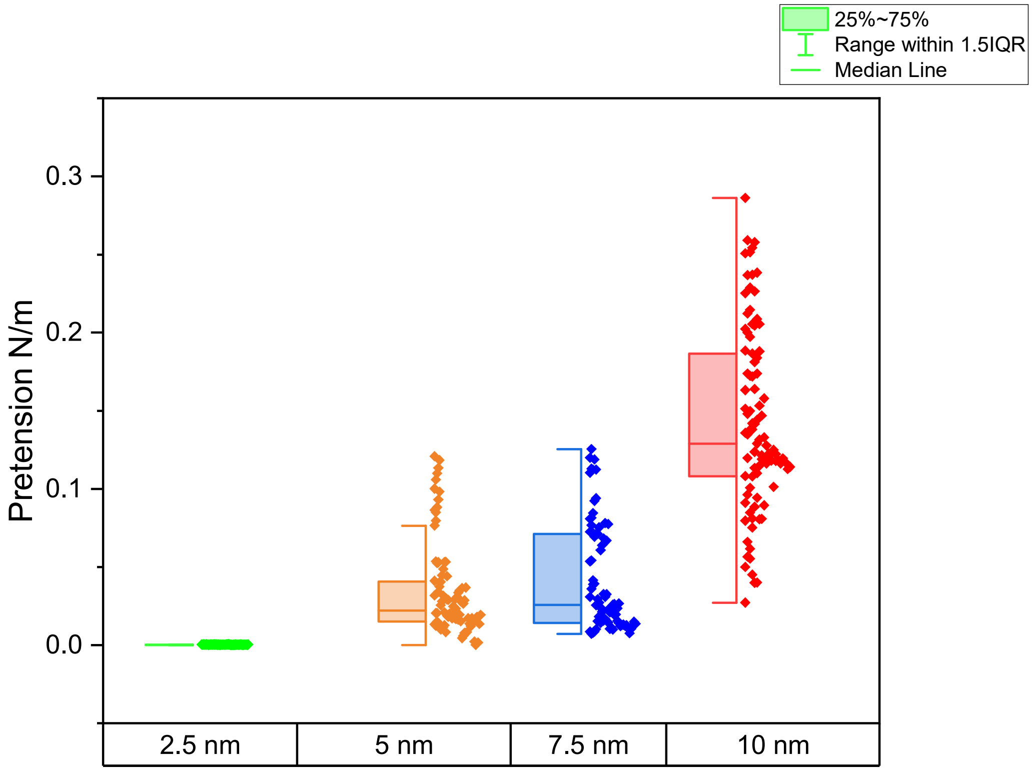

Figure 16 Statistical analysis of the fitted pretension. A trend is visible as the increase of the thickness is correlated to an increase in the pretension of the membrane.

The pretension is composed of the stress state of the membrane before the indentation, thus the increase in the titanium thickness proportionally intensifies the stress state of the membrane, as it accumulates the thermal stress induced in the titanium evaporation [355]. As demonstrated in Figure 16, the values of the pretension decrease with the reduction of the Ti on the membrane. The median values for the 10 nm were 0.13 N/m while for 7.5 nm and 5 nm were

0.021 N/m and 0.018 N/m respectively. The 2.5 nm membrane presented a pretension of 0.00037, however, it could not be directly compared to the other thicknesses due to the lower freestanding area over which the membrane tested were transferred. Indeed, due to its lower yield compared to the other thicknesses, only membranes transferred over 25 microns holes were tested, and the fitting parameters were accordingly modified.

The Young modulus values shown in Figure 17 were widely distributed, ranging from 10 to 800 Gpa with median values of 55 GPa, 44 GPa, and 43 GPa for the 5, 7.5, and 10 nm respectively. The median value for the 2.5 nm membranes, instead, was almost 4 times that of the other membranes, reaching 160 GPa,

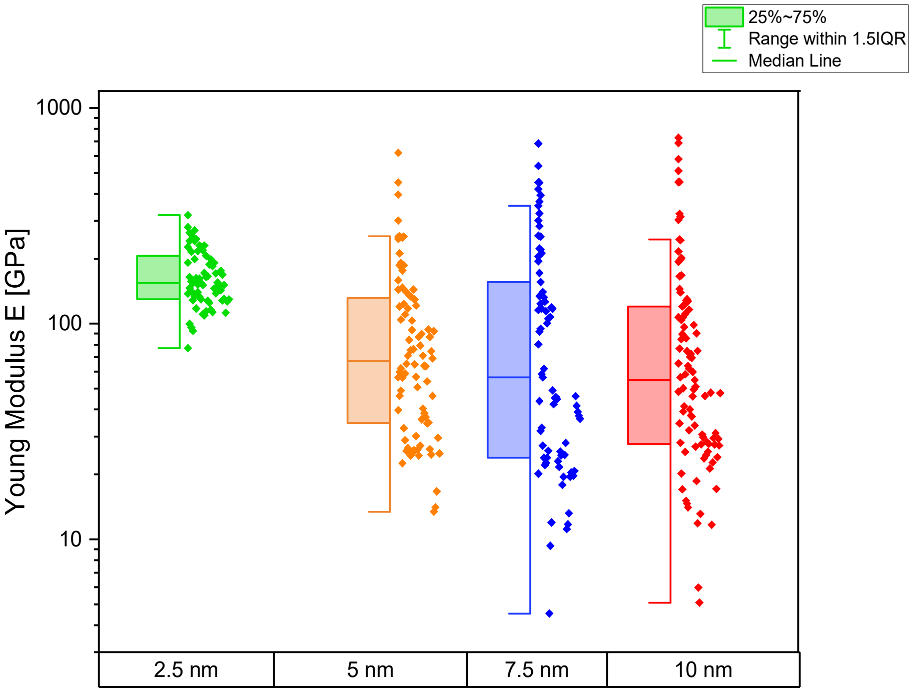

Figure 17 Young modulus distribution of the membranes with various thickness. The increase in thickness brought only a slight decrease in the Young modulus of the membrane.

In this chapter, membranes with different thicknesses of evaporated titanium were fabricated and their elemental composition and mechanical properties were characterized. The titanium layer resulted completely oxidized in the membrane with 2.5 nm and 5 nm of Ti while the surface presented residues and contaminants due to the sacrificial layer of the wet transfer. The membranes were then transferred over micromachined silicon grids demonstrating a yield for the transfer depending on the membrane thickness. The presence of higher thicknesses indeed showed higher yield, while the membranes composed of 2.5 nm of Ti or the pure single-layer graphene collapsed on most of the wells. Finally, the mechanical properties of the membranes were investigated, resulting in indentation curves with a strong correlation to the thickness of Ti. The membranes showed sudden changes in the morphology under stress due to the unfolding of the corrugation of the membranes induced by the thermal stress, that accumulated in the membrane during the evaporation of the titanium. These changes, however, were elastic and reversible, as the steps in the indentation curves maintained the same position and height during repeated indentation. To avoid or reduce the random effect of the accumulated stresses on the membrane different deposition techniques of the reinforcing layer could be applied. Among them, the most precise in terms of thickness of the layer would be Atomic Layer Deposition (ALD), a technique capable of creating a single atomic layer on the surface of the membrane with negligible residual stresses at each step of the process. While creating an almost stress-free layer could be an interesting solution to the stress-induced corrugations, the implementation of this technique could increase the complexity of the fabrication. Hence, instead of adding complex techniques and eliminating the stresses, solutions that reduce the stress (such as thermal treatments) or control its directionality (such as the patterning of the layer) could be much more promising for future applications. The Young modulus and pretension of the membranes were also investigated showing that higher thickness of Ti increased the pretension of the membrane due to the accumulated thermal stresses, Instead, for the Young modulus, the distribution was wider and was presenting similar median values for the higher thicknesses investigated.

Chapter 4

Patterned graphene/titanium membrane for XPS applications

The membranes described in the previous section demonstrated to be suitable for the transfer over large, suspended areas with an important success rate, however, the presence of the metal layer with a few nanometres of thickness reduces, if not completely cancel, one of the important properties of the graphene: its high transparency to electrons. Thanks to this property electrons can pass through a single or double layer of graphene with unperturbed kinetic energy, thus allowing the use of graphene membranes in electron spectroscopy. For this reason, I designed a new structure that reduces the coverage of titanium and exposes some parts of the single-layer graphene. In this combination, the graphene should maintain the strength obtained with the addition of the Ti layer, and emphasize the transparency required in electron spectroscopies. In this chapter, I will describe the membrane design, their fabrication, and their mechanical characterization, and finally, demonstrate that they satisfy the transparency requirements for XPS applications.

Fabrication of the patterned membranes

For the fabrication of the patterned membranes, an additional lithographic process was introduced before the titanium evaporation. The added lithography used the same process described in chapter 3 for the patterning of the grid, except for an added layer of lift-off resist LOR 3B (MICROCHEM ®). The lift-off resist was used to aid in the separation of the evaporated titanium by creating an undercut under the photoresist layer as shown in Figure 1. The metal evaporated could otherwise form bridges between the top and the bottom of the pattern, hindering the lift-off procedure. During the lift-off phase, the LOR layer is finally removed together with the excess titanium, leaving the patterned titanium on the graphene.

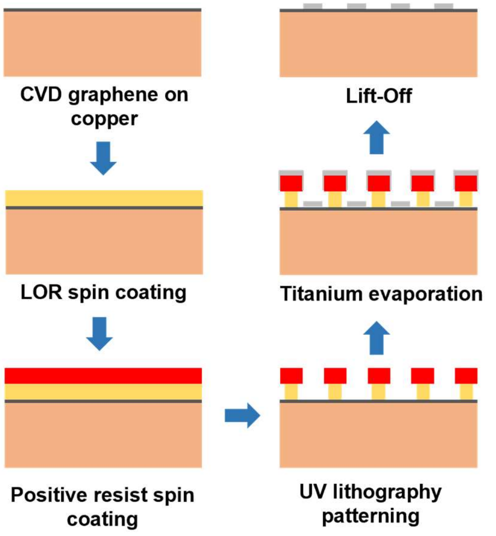

Figure 1 Schematic illustration for the fabrication of the patterned membranes with a lift-off process.

Two different patterns were tested, dots, which resulted in a titanium squared grid, and lines, which resulted in a titanium linear grid. As shown in Table 1 the width and the period of the squared dots and the lines were the same, however, they differed in the area of the free graphene i.e. not covered by the titanium layer.

Pattern	Width/Period (μm)	Exposed Gr/Ti ratio (%)
Dots	3/6	25
Lines	3/6	50

Table 1 Summary of the characteristics of the pattern used. The main difference was the exposed area of graphene.

The linear grid illustrated in Figure 2, resulted fragile in the direction parallel to the lines where only graphene was suspended, and during the transfer, the membrane ripped along the freestanding lines as in Figure 2b, probably also as a consequence of the stress generated during the high-temperature titanium deposition. On other occasions, the titanium lines adhesion was poor and they detached from the graphene, causing ulterior defects in the final membrane as in Figure 2c.

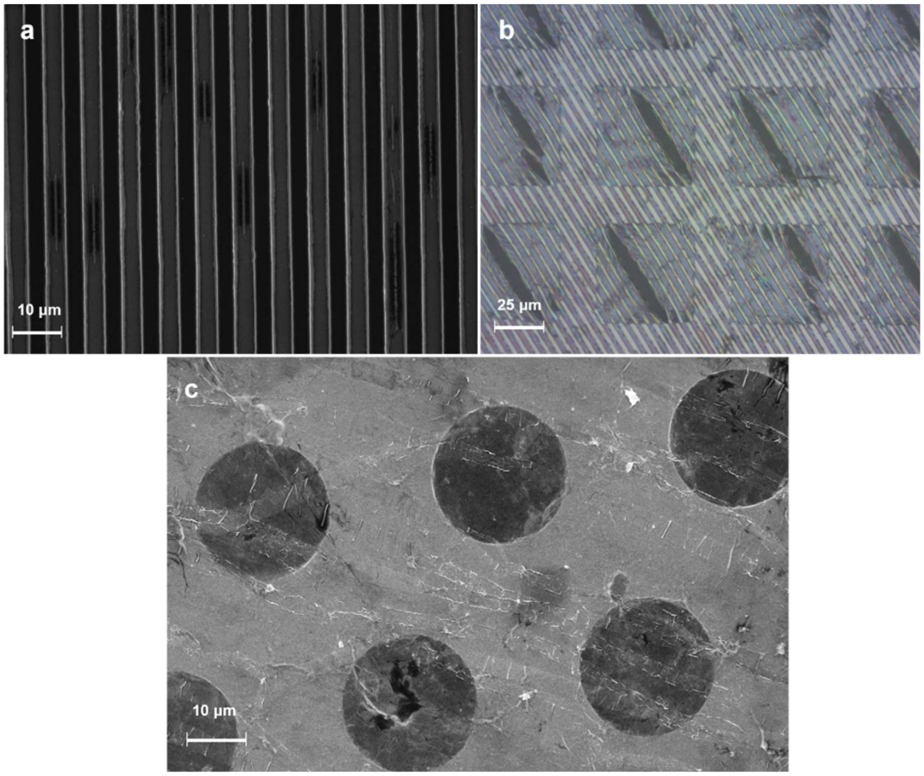

Figure 2 Patterned lines. a) lines lithography before lift-off. b) optical microscope image of the damage on the freestanding part of the membrane during the transfer. c) SEM images of the titanium lines occasionally detaching from the graphene.

The squared grid pattern on the contrary did not present detachment from the graphene and the membrane was transferred on the silicon substrate following the same procedure as described in chapter 3. The yield for the transfer was comparable to that of the full membranes described previously. The wide field SEM images in Figure 3 showed up to ~90% of the grid holes that were covered for thicknesses of 5 nm of Ti.

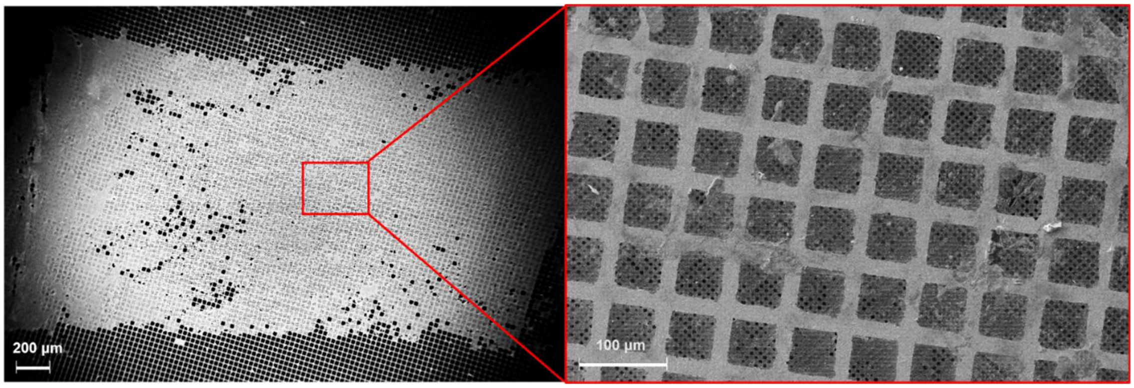

Figure 3 Left, Coverage of the array of holes with patterned membranes of 5 nm of Ti. Right, magnification of the same grid.

A high magnification inspection reported in Figure 4, however, revealed that in the regions where graphene was not covered by the Ti film, the graphene itself was not continuous, and was often completely missing. This problem may be caused by local defects or grain boundaries of the graphene exposed. On the other hand, as expected, the portion covered by the titanium film was not damaged.

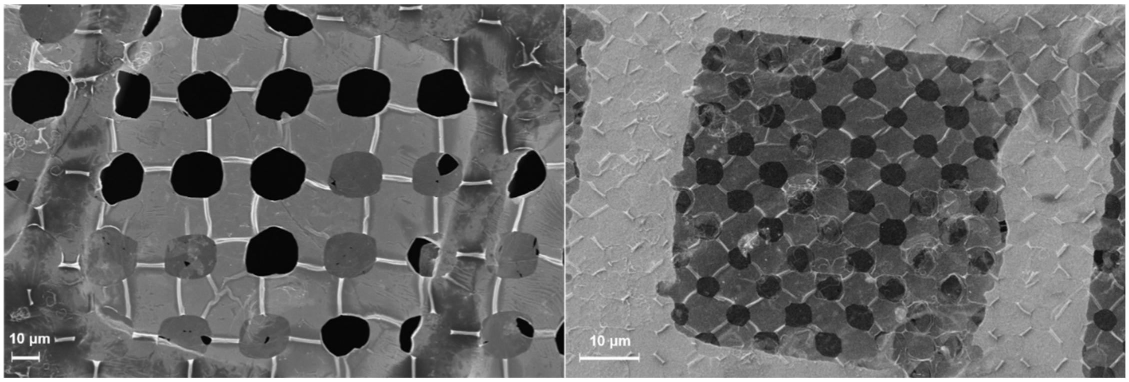

Figure 4 SEM images of the patterned grid with a membrane with most of the graphene windows damaged or collapsed (left) and a membrane with the graphene windows intacts.

This effect denoted how the titanium grid is essential for the mechanical robustness of the membrane, confining the damage on the patterned membrane to the single graphene windows. The yield of the graphene windows varied significantly from sample to sample and within the same membrane, with some samples consisting of hundreds of cells with almost complete coverages (>95%) and others with as low as 5% of the cells intact.

Interestingly, the morphology of the suspended patterned membranes was characterized by the presence of regular corrugations. Opposite to the previous random release of the thermal stress, which was traduced in a corrugated membrane, the stress release in the patterned membranes was concentrated in the areas where the distance between two only-graphene regions was minimal. Additionally, the size and the degree of order of these corrugations varied between different titanium thicknesses. In Figure 5 are shown membranes of 10 nm and 5 nm of Ti. The magnification on the graphene windows showed how the higher titanium thickness resulted in thicker and more regular corrugations. On the 10 nm Ti membrane the corrugations were organized in a quasi-squared lattice, while in the 5nm Ti the corrugations were more disordered, smaller, thinner, and rarely arranged in single lines between two graphene windows.

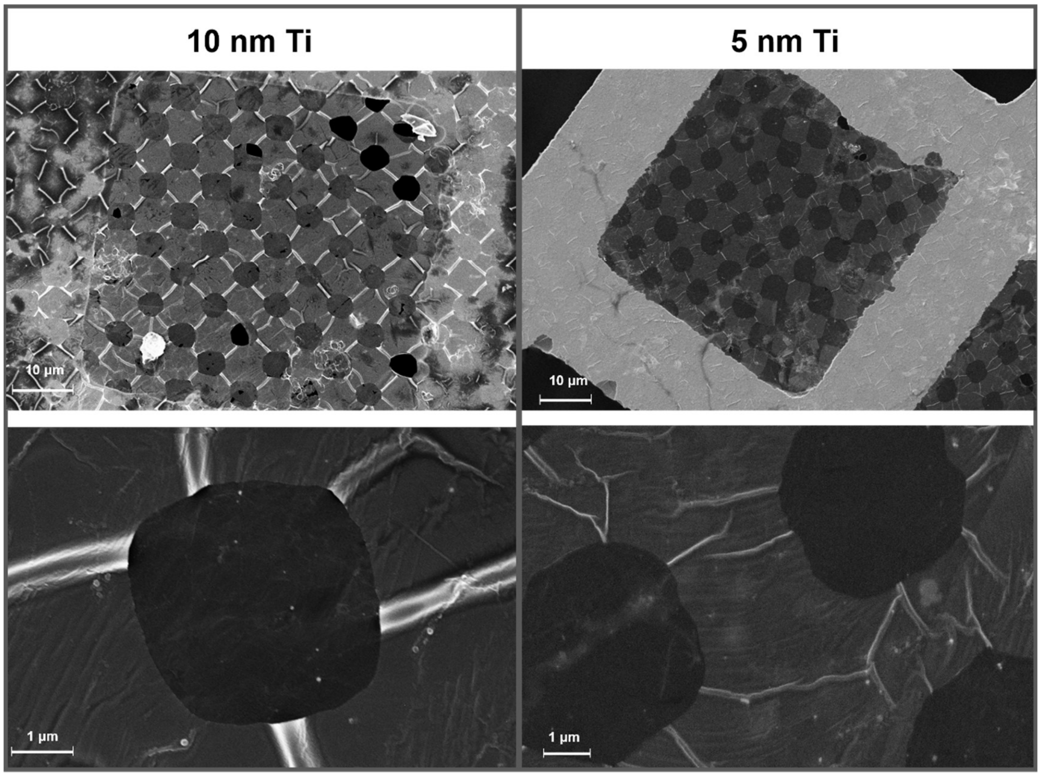

Figure 5 SEM images of the ordered corrugation induced by patterning the titanium layer on a 10 nm (a) and 5 nm (b) membrane.

Effects of patterning on the mechanical response

The mechanical properties of the patterned titanium/graphene bilayers showed significant differences compared to continuous ones. From the values of the mechanical properties obtained through the indentation force-maps reported in Figure 6, it was possible to distinguish the membrane regions according to their structure: graphene and titanium or bare graphene. The elastic constant was obtained for each point by fitting the slope of the extension portion of the indentation curves in the force maps. The value of the bare graphene was between 0.25-0.2 N/m while graphene-titanium showed a value as high as 0.37 N/m.

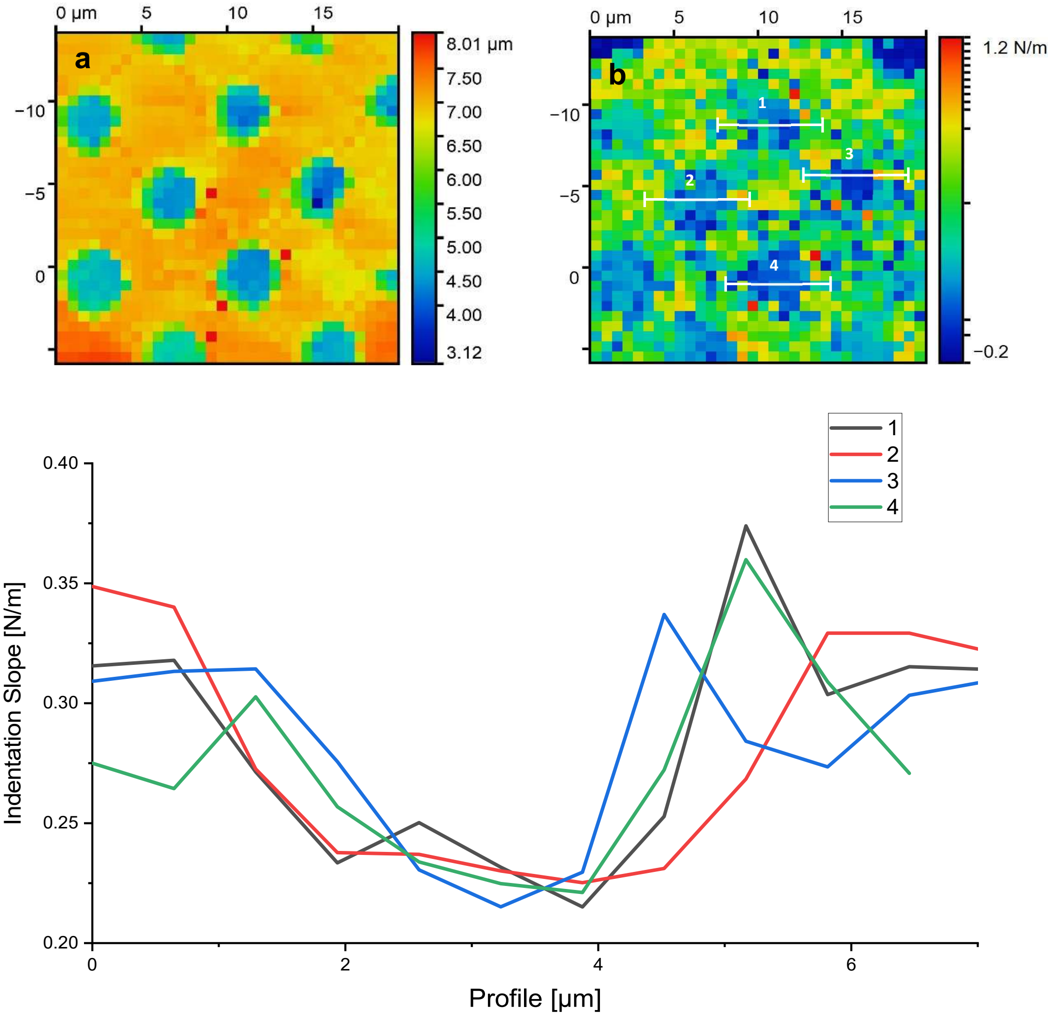

Figure 6 Force map of the patterned membrane. a) height and b) fitted slope channels of the force maps data of a 10 nm Ti membrane. In the graph below are represented the sections of the graphene windows slope signal, showing the different mechanical between the titanium and the graphene.

Another mechanical difference is the reduction of the number of steps observed in the force-distance curves that we attributed to a sudden unfolding of the membrane wrinkles. The patterned membrane presented as an example in Figure 7 no step were present in the indentation curve, while the full membrane presented up to 8 visible steps. This can be explained by the ordered corrugations, which provide higher resistance to the structure and prevent the step-unfolding mechanism observed for the full membranes in the previous chapter. The ordered corrugations distributed the stress applied more equally on the membrane compared to the random response of the corrugations on the full membrane, resulting in fewer steps in the indentation curve. The slope of the last part of the indentation curve was 0.46±0.25 N/m and 0.48±0.10 N/m for the full and patterned membrane respectively, demonstrating that the membranes presented a similar stiffness after their unfolding.

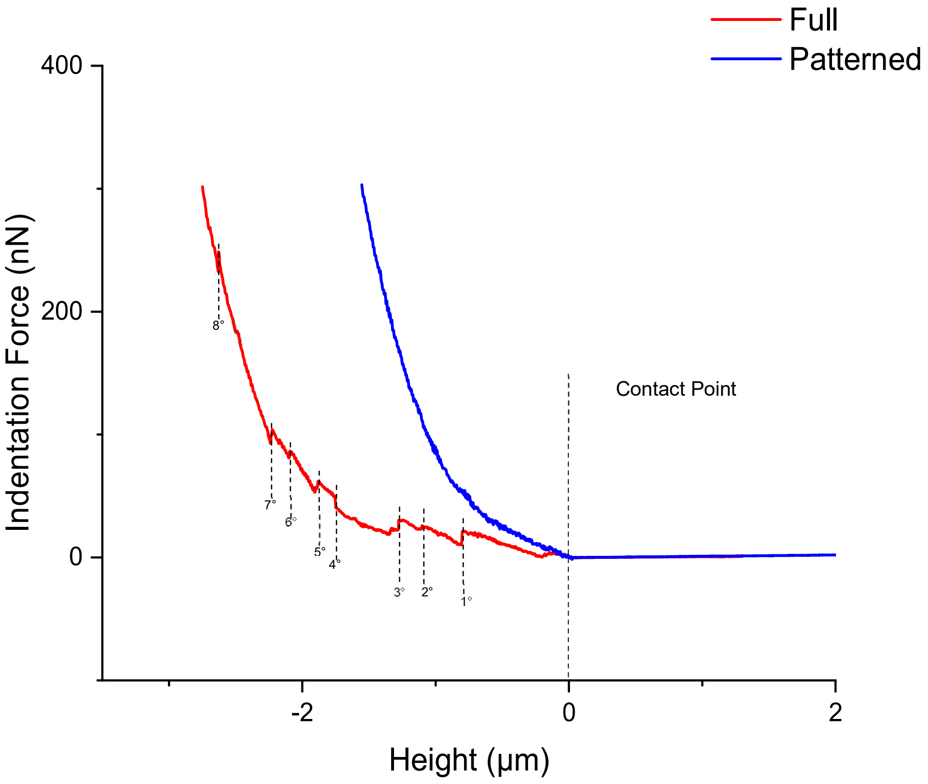

Figure 7 Comparison between indentation curves of patterned and full membranes with 5 nm of Ti evaporated. The patterning produced membranes with different mechanical properties which presented less steps than the full membrane.

The 10 nm of Ti full membrane presented a mechanical response far different from the membrane characterized in chapter 3 as shown in the example of Figure 8. Indeed, the previous statistical analysis of the different thicknesses showed a proportional increase of the pretension with the increase of the titanium layer up to 10 nm and an increase of the total deflection up to 7.5 nm. The 10 nm Ti full membrane, however, appears quite unlike what was demonstrated in chapter 3, with a stiff and linear response since the contact point with a slope of the indentation curve reaching 0.95±0.05 N/m at the end of the curve. The patterned membrane instead, steadily increased the slope, reaching 0.79±0.05 N/m at the end of the curve. However, even after reaching the maximum indentation force allowed by the AFM (~1.0 µN with a cantilever elastic constant of 4 N/m), the membranes did not break, and the membrane was yet to be unfolded, which may explain the lower total deflection compared to the patterned membrane as only a part of the indentation curve was measurable.

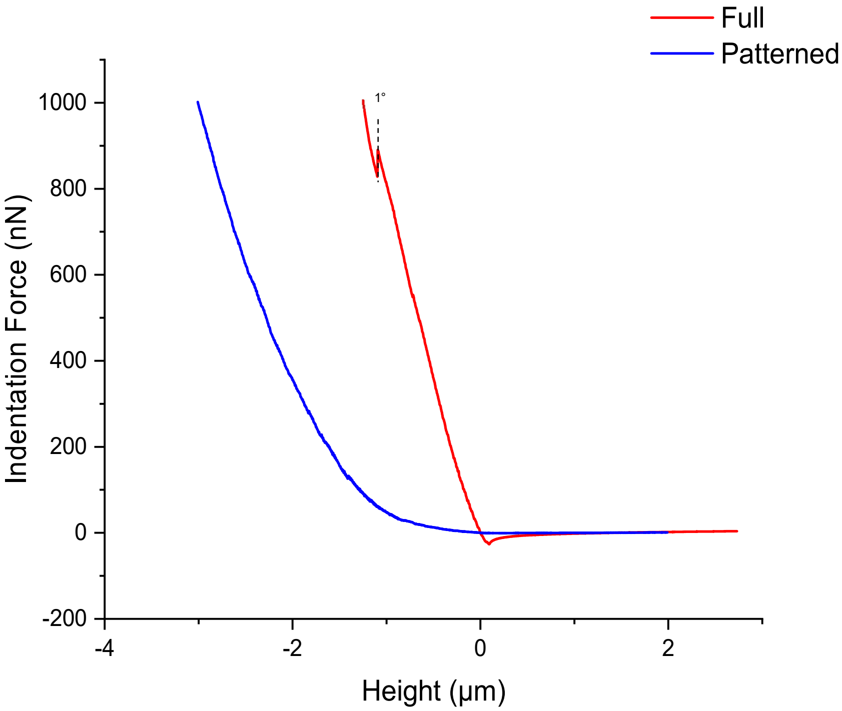

Figure 8 Comparison between the indentation curves of patterned and full membranes with 10 nm of Ti evaporated. The stepped behaviour is still present, but due to the high stiffness of the metal layer, the membrane was not completely unfolded.

Figure 9 shows the data distribution of the patterned membranes after the fitting described in chapter 3. The median values for the Young modulus were reduced to a third of those of the full membrane, with 15 GPa and 17 GPa for the 5 nm Ti and 10 nm Ti patterned membranes. The median values of the pretension also presented lower values as they were 0.011 N/m and 0.016 for 5 nm and 10 nm of Ti.

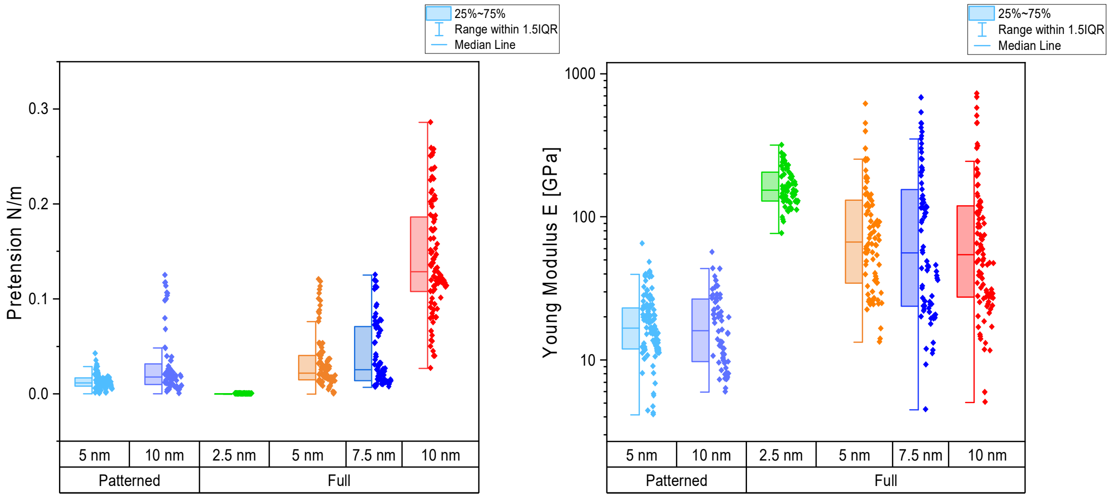

Figure 9 Comparison of the fitted Young modulus and pretension of the patterned and full membranes.

The fitting proved to be simpler compared to the full membranes, thanks to the more "ideal" indentation curve that was closer to the model as seen in Figure 10. Thanks to the advantage of having fewer steps in the indentation curve, the patterned membrane presented better fitting with an R-value usually higher than 0.998.

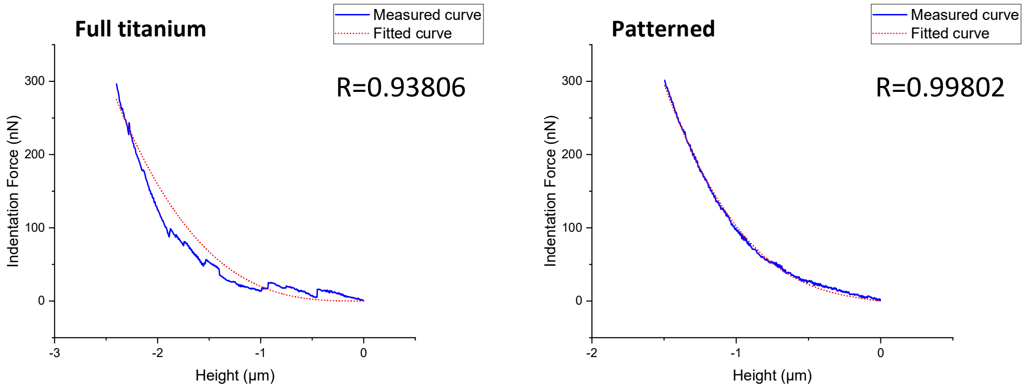

Figure 10 An example of "good" and "bad" fitting on 5 nm Ti patterned and full membranes. The bad fitting arises due to the presence of the steps in the indentation curve.

However, it’s difficult to directly compare the patterned and full membranes, as the patterned ones escaped the boundaries of the model applied, which required a homogenous film to be applied. Indeed, the titanium present on the membrane was reduced by the patterning by a third compared to the full membrane, while in the model the thickness of the titanium grid was used as a parameter. Apart from the direct application of the fitting model, the measurements may have also been affected by the cantilever tip position. Indeed, the alignment between the cantilever and the center of the membrane was operated manually, and could not always ensure the proper alignment with the membrane. If, for instance, the tip was positioned close to the border between the titanium and the graphene window, the tip may slide on the membrane during the measurement. This could result in sudden changes in the stiffness and the height of the indentation curve, due to the differences between the titanium grid and the graphene windows shown in Figure 6. Another variable was the orientation of the titanium grid with respect to the substrate as it may have affected the position of the patterned membrane over the silicon substrate, resulting in a different mechanical response. This effect, however, was difficult to control as the alignment of the membrane was handled manually during the transfer, and the grid could not be easily observed with the optical microscope during the indentations.

The patterned membrane as a semi-transparent window for XPS

To demonstrate the effectiveness of the membranes as XPS windows, a reference material was required to demonstrate the passage of its emitted photoelectrons through the graphene. We used a thin layer of gold as a known source of photoelectrons, with a well-defined signal which does not overlap with those emitted by the other elements present in the samples. This gold layer was deposited on the bottom of the substrate to measure only the signal coming through the suspended membrane. Unfortunately, to deposit the gold below the patterned membrane, the grid substrate used so far was not suitable. Indeed, the 30 µm of silicon would have scattered most of the photoelectrons inside the squared silicon wells before arriving at the detector, which was positioned at an angle of 60° with respect to the synchrotron beam as in Figure 11. For this reason, a shallower design was proposed, based on trenches with a width of 10 µm and a period of 20 µm, and a depth of 3.5 µm. These trenches were placed in the analysis chamber parallel to the direction of the detector to maximize the signal to the detector as in Figure 11. To fabricate these trenches the same micromachining process described in the previous chapter was used, with the addition of the gold deposition and lift-off. Figure 12 illustrates the process used, starting from the spin coating of the lift-off and positive resist layers on a silicon wafer. The resist was

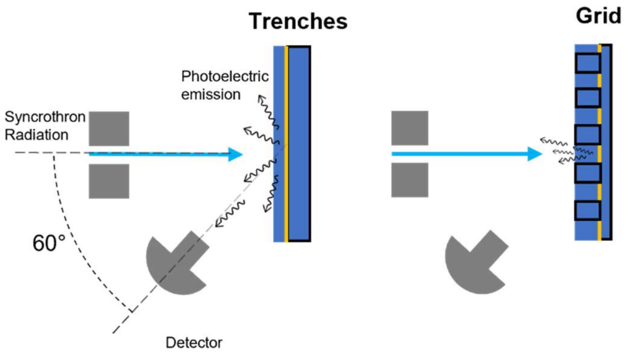

Figure 11 Section view of the samples on the detector plane and their position with respect to the incident beam. The trenches allowed for higher photoemission arriving to the detector thanks to their shallower design and the parallel orientation on the plane of the detector.

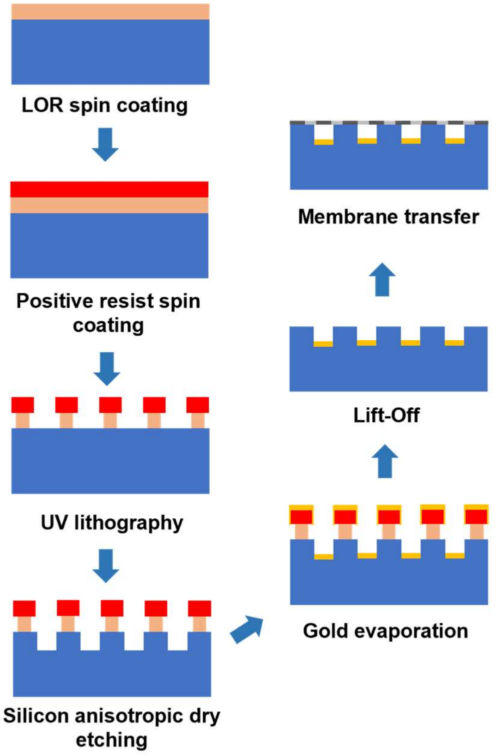

Figure 12 Illustration summarizing the micromachining process used to create the trenched substrate for the XPS analysis with the gold on the bottom.

then patterned through UV lithography and the silicon was anisotropically dry-etched to a depth of 3.5 µm. The sample was then evaporated with 10 nm of titanium (as an adhesion layer) and 30 nm of gold and with a lift-off the excess metal was removed. The membranes were then transferred with the wet-transfer process described in chapter 3 and characterized with SEM microscopy reported in Figure 13. The patterned membrane of the Figure 13a and b showed the titanium grid with the corrugation ordered in the quasi-squared lattice as described previously and presented over 95% of the graphene windows intact after transfer.

Together with the patterned membranes, also membranes with a continuous Ti film were transferred, as shown in Figure 13c and d. The full titanium/graphene membrane was transferred without the use of a sacrificial layer, as the stiffness of the 10 nm of titanium was enough to avoid the crumbling of the membrane when floating on the copper etchant during the transfer phase. The membrane presented random corrugations but was completely covering the graphene and the trenches. This sample was used to check that the Au XPS signal originated only from the deposited layer, and thanks to the well-known electron opacity of 10nm-thick titanium film we expect to observe zero signal. Another control sample shown in Figure 13e and f, was the patterned membrane exposed to an oxygen plasma process to remove the graphene, leaving a suspended titanium grid. This third membrane served as the control to estimate the graphene attenuation of the XPS signal.

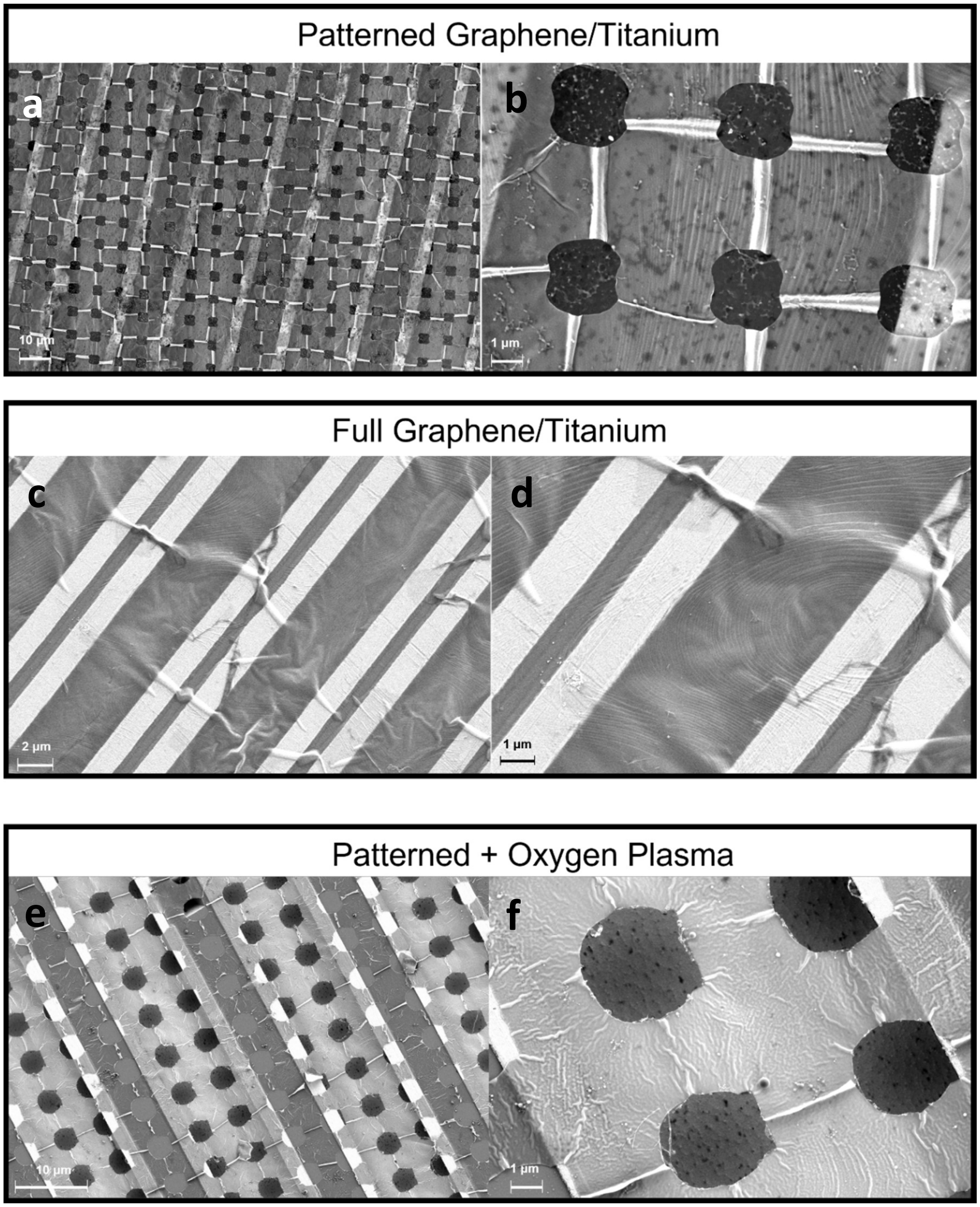

Figure 13 SEM characterization of the samples. The patterned membranes showed a high yield for the transfer and over 95% of the graphene windows were intact. The full graphene/titanium membrane shows a random corrugation. On the plasma treated sample, the gold on the bottom can be seen through the opened graphene windows.

Figure 14a shows a section view of the trenches with the full membrane covering them. Although the surface was corrugated, the full coverage was ensured by the 10 nm of titanium. In Figure 14b a plasma-treated membrane showed the graphene completely removed with only the residual layer under the titanium and indicated in the high magnification SEM image. In the image, it is also possible to observe the surface at bottom of the trenches, which is out-of-focus, since it lays 3.5 μm deeper than the focal plane.

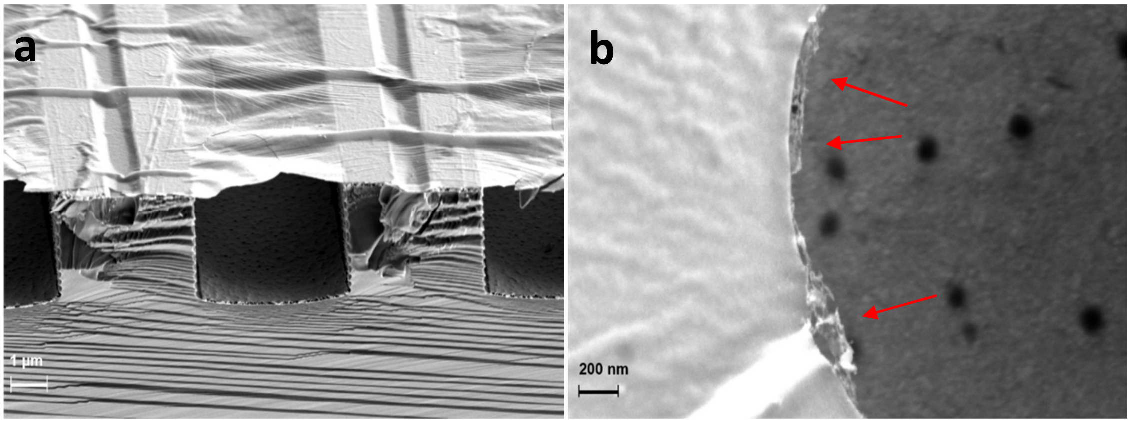

Figure 14 Full titanium membrane in section view and b) patterned membrane after oxygen plasma, the red arrows indicates the residues of graphene visible in proximity of the patterened titanium grid.

Only samples with a covered area larger than 300 μm x 300 μm with the transferred membrane and over 95% of yield were selected for the experiments. This threshold was defined taking into account the area of focus for the synchrotron radiation photon beam used for the photoemission measurements. To select the samples, low magnification SEM images were used to characterize the membranes as shown in Figure 15, demonstrating mm^2 areas of the trenched substrate completely covered. The SEM image also highlighted the presence of organic contaminants (introduced in the wet-transfer process) due to their low electrical conductivity, which results in the darker parts in Figure 15a. These darker spots are instead absent in Figure 15b and Figure 15c as the plasma treatment removed the carbon contaminants and on the full membrane the sacrificial layer was not used during the transfer.

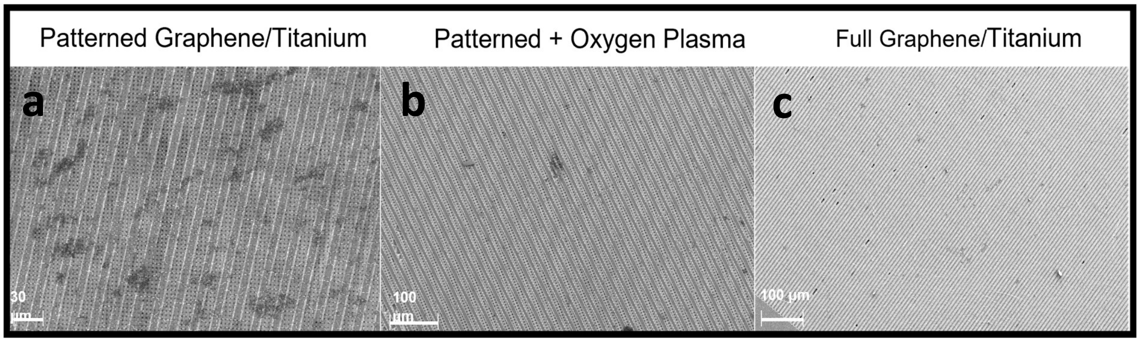

Figure 15 Low magnification images of the area of interest which was used for the XPS spectroscopy. The slightly darker areas on the patterned graphene/titanium sample are due to the presence of residues after the membrane transfer.

At higher magnifications, it was possible to evaluate the presence and the continuity of the single-layer of graphene. In Figure 16 are magnified the graphene windows. The transparency of graphene to electrons is evident in Figure 16a as its possible to recognize the blurred features of the golden layer across the membrane. In this case, the surface contaminants as indicated in Figure 16b, helped in recognizing the presence or the collapse of the graphene windows as they appear floating on the membrane focal plane, indicating the presence of a transparent supporting layer.

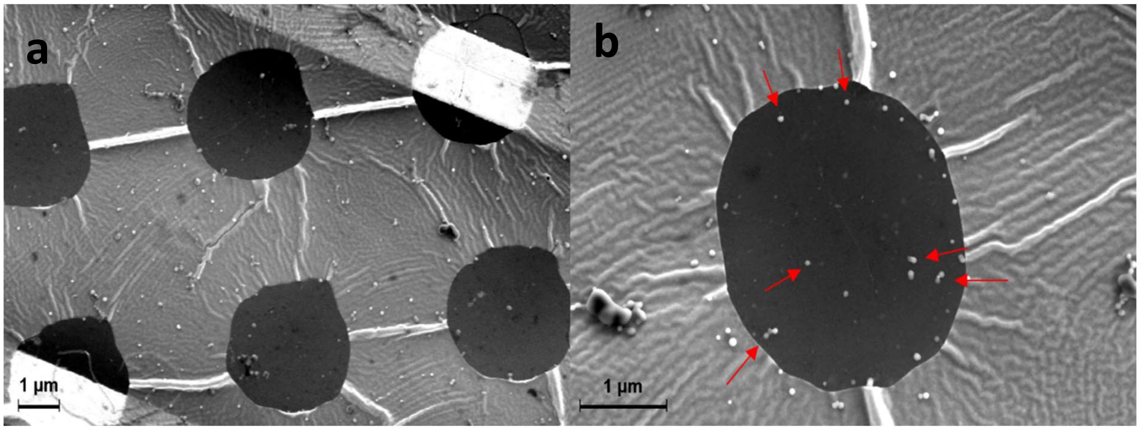

Figure 16 a) the transparency of the graphene to the electrons allows to see the out-of-focus bottom of the trenches. b) in the high magnification of the membrane are pointed out the small white dots formed by carbon contaminants suspended on the surface of the membrane.

The transparency demonstrated to the SEM electrons, however, does not directly prove that electrons can pass through the membrane without experiencing any kind of energy loss, and thus that can be used in XPS spectroscopy. Indeed, in the SEM, for the image formation, the energy of these slow electrons is not measured, thus the loss of energy due to inelastic scattering is not considered. The X-ray photoemission spectroscopy, instead, is based on the measure of the energy of the photoemitted electrons, and thus the measurement of their kinetic energy is the only way to assess the energetic transparency of the graphene layer.

XPS spectra of the patterned membrane

To characterize the attenuation of the photoelectrons due to the presence of graphene, an XPS analysis was carried out on the three samples. The photon energy used for this experiment, 548eV, was chosen as a trade-off between high flux, good energy resolution, high enough energy to excite the electron emission from the 2p core level of titanium, optimized with respect to the cross-section of the Au 4f core-level photoemission.

A first survey of the surface of the membranes allowed to identify the main peaks of interest and is reported in Figure 17. The full titanium membrane showed clear Ti 2p, 3s, and 3p peaks and carbon C1s. The spectra are normalized to the higher intensity, i.e. the C1s photoemitted electrons. The plasma-treated membrane showed analogous peaks with the added signal of the 4f core level of the gold. Finally, the patterned membrane with the graphene windows did not present clear 4f peaks of the gold, however, the signal from the titanium peaks was also much lower, which may indicate the presence of surface contamination reducing the photoelectrons emitted. Indeed, in contrast to the patterned membrane, the full Ti and plasma-treated membrane both showed a relatively high intensity of the titanium peaks. This can be explained by the absence of the sacrificial layer for the full titanium membrane and by the plasma treatment of the other control membrane, which reduced the presence of carbon contaminants from the surface.

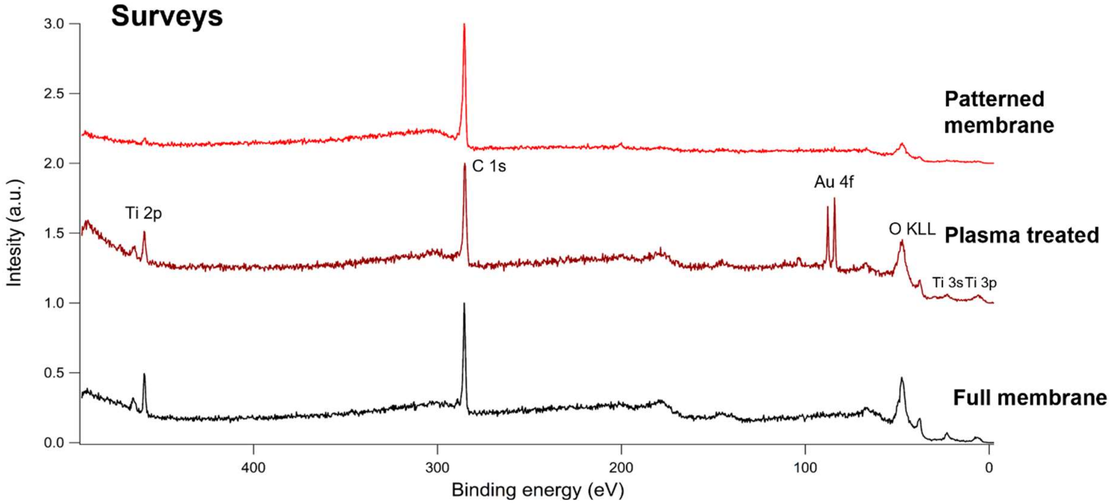

Figure 17 Surveys of the membranes to obtain the elemental composition of the membrane. The main peaks identified were the titanium 2p, 3s and 3p, the 4f of the gold and the carbon C 1s.

To confirm the signal attenuation due to contaminants, the Ti 2p peaks at 459.5 eV and 465 eV binding energy were used to characterize the titanium layer as shown in Figure 18. The peaks were fitted with a Voigt function after subtracting the Shirley background as in chapter 3. The areas were normalized to the largest signal which was the one coming from the full titanium control membrane, due to the absence of the PMMA sacrificial layer during its transfer. The plasma-treated membrane showed a signal that was 67% of the full titanium, while the patterned membrane with graphene showed 16% of the signal from the control. The signal attenuation due to the contaminants resulted in the reduction of the titanium signal to almost a tenth of the full titanium control as reported by the graph in Figure 18. The Ti 2p peak was dominated by the Ti^{4+} component at 459.5 eV of binding energy, indicating full oxidation of the titanium layer.

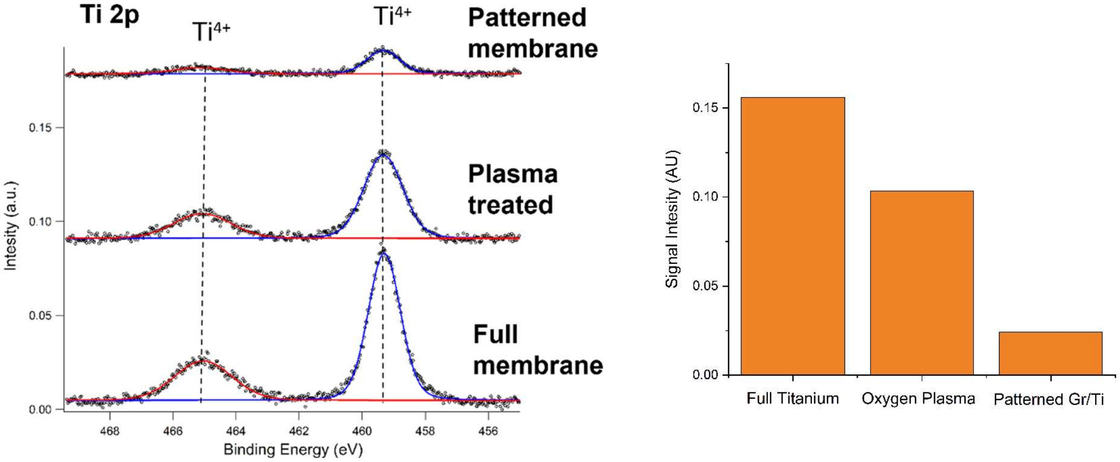

Figure 18 XPS spectrum of the Ti 2p peaks of the titanium. The intensity of the signal was reduced by almost an order of magnitude by the presence of contaminants on the surface.

To understand how the patterned membranes interfered with the electrons emitted by the gold present at the bottom of the trenches, the peaks 4f $_{7/2}$ and $_{5/2}$ of gold were chosen as the probe. Before measuring the signal passing through the membrane, a control was acquired on the trenches outside of the membrane-covered area and is shown in Figure 19. This measure, however, revealed an important difference among the samples. While the full titanium and patterned graphene/titanium samples presented the same photoemission spectra, with two single peaks relative to unoxidized Au 4f core level emission, the sample exposed to plasma treatment presented two more components relative to the oxidized forms Au^{3+} and Au^{1+} [356].

The presence of these peaks indicates the partial oxidation of the gold surface due to the plasma treatment.

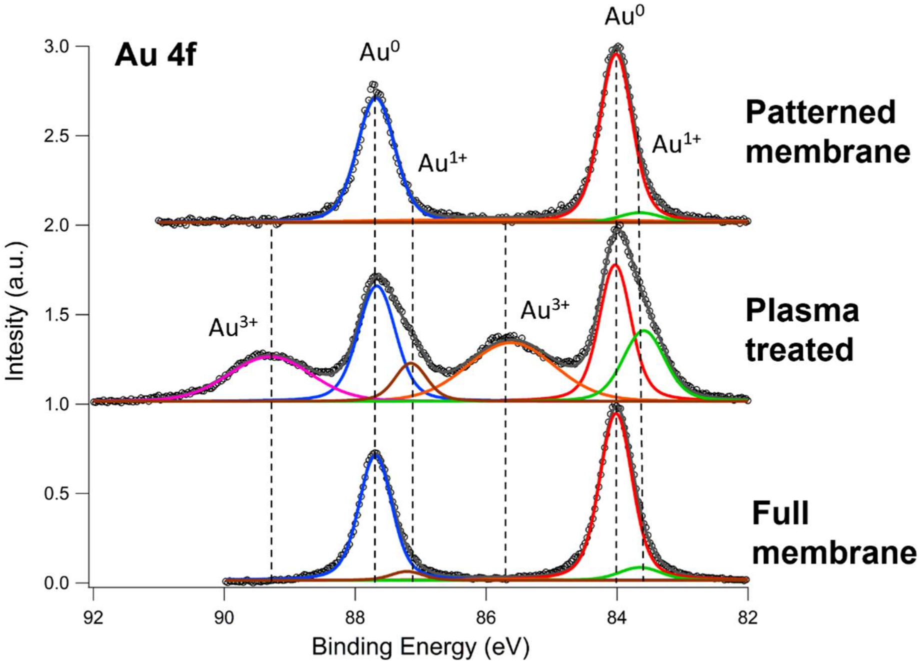

Figure 19 Gold 4f XPS spectra taken outside the area covered by the membrane which were used as a standard for the measure on the membranes. In the plasma treated sample Au^{3+} appeared as the gold surface was oxidized by the plasma treatment.

The XPS analysis of the gold covered by the membranes reported in Figure 21, showed that the 10 nm of titanium is electron-opaque, as expected: negligible Au 4f signal was measured and the few electrons recorded could be attributed to tiny holes in the membrane which exposed the underneath area, that affected anyway less than the 1% of the membrane (Figure 20).

In both the patterned membrane with and without graphene, the 4f peaks were visible, with lower intensity in the former one. In the plasma-treated sample, we observed again the Au^{3+} and Au^{1+} contribution as already discussed for the reference sample (Figure 19). The Au 4f signal measured on the patterned graphene/titanium membrane is attenuated by a factor of 10 compared to the signal measured on the plasma-treated membrane, indicating a 90%

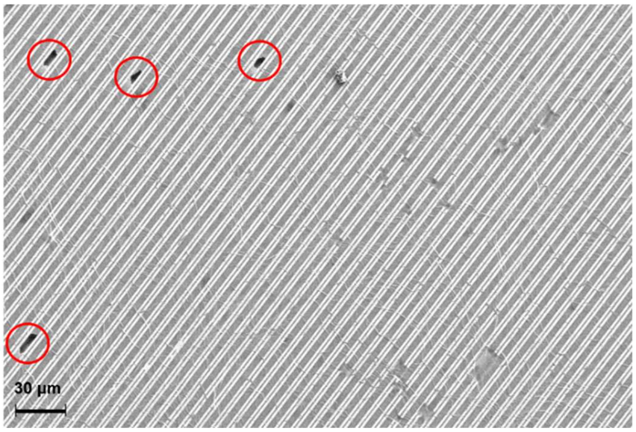

Figure 20 Localized damage on the full membrane can describe the weak Au 4f signal presented by this control sample.

attenuation due to the single-layer graphene. However, as already shown by the comparison of the Ti 2p peaks of the same membranes, a large part of this attenuation may be due to the presence of surface contaminants originated by the PMMA later used during the transfer process.

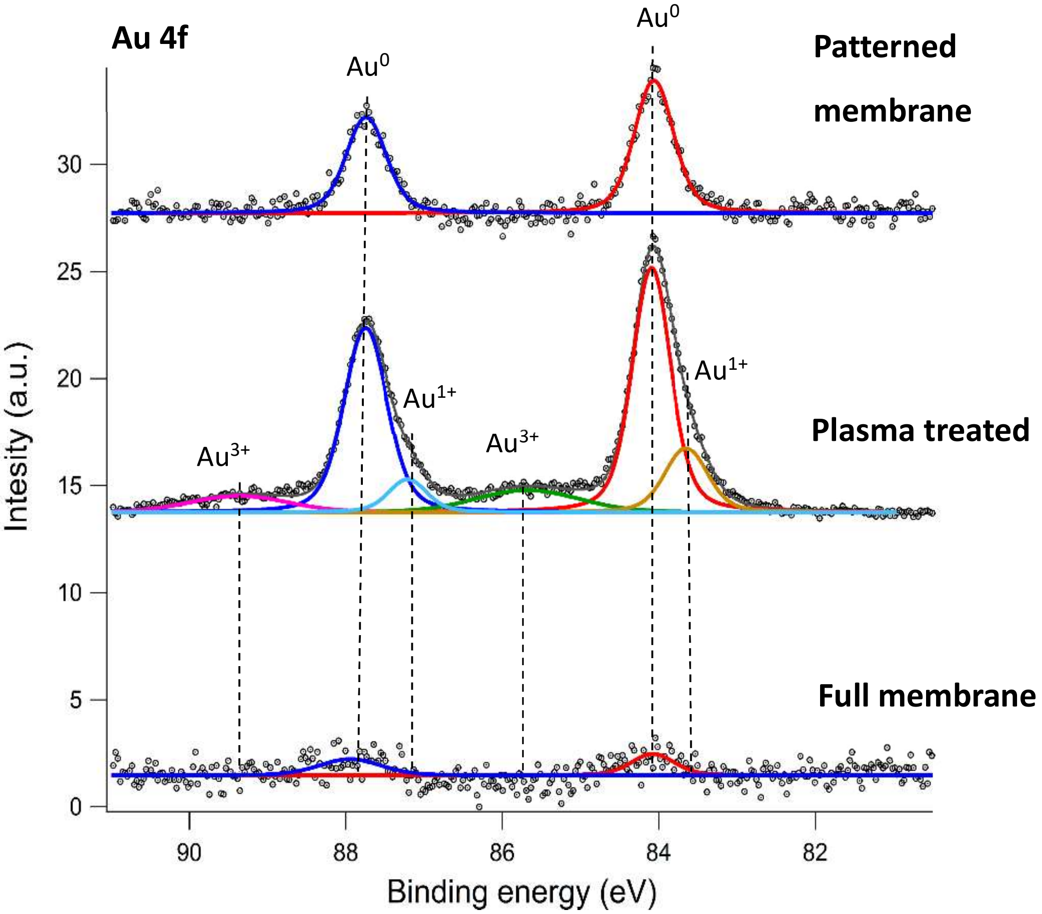

Figure 21 Gold spectra taken after 5 days of vacuum curing showing how the signal passing through the graphene was comparable to the signal passing through the plasma treated membrane, thus demonstrating the electron-transparency achieved by the patterned membrane. In order to demonstrate the (weak) gold photoemission in the full membrane, the signal was amplified by 3 times, while the signal of the patterned membrane (barely visible in Figure 17 due to the normalization to the C1s peak) was amplified by 1.5 times.

On every surface exposed to the atmosphere, there is the natural contamination of the organic compounds from the atmosphere and other gasses adsorbed on the surface. This was shown also in Figure 17 when the survey of the full titanium membrane revealed the C 1s peak even in the absence of direct contact of the membrane with any solid form of organic contaminants (as no PMMA was used, and the graphene was on the other side of the electron-opaque titanium). Due to the contamination nature of being volatile as it is derived from the atmosphere, it can be reduced with exposure to UHV conditions.

For this reason, the characterization was repeated after five days with the sample remaining under vacuum at a pressure lower than 10^{-8} bar. This allowed to analyze the degassing of the surface from organic contaminants and adsorbed gas on the surface. The samples degassed in UHV showed marked differences compared to the initial analysis, as the intensity of all the membrane-covered samples signal showed a significant increase as represented in Figure 22. In particular, for the full titanium membrane, the gold-emitted signal was increased by 128%, for the patterned membrane by 142%, and the plasma-treated membrane by 603%. The reference signal, taken outside the area covered by the membrane, instead, showed negligible change increasing by 3% and -2% for the plasma-treated sample and the patterned one respectively.

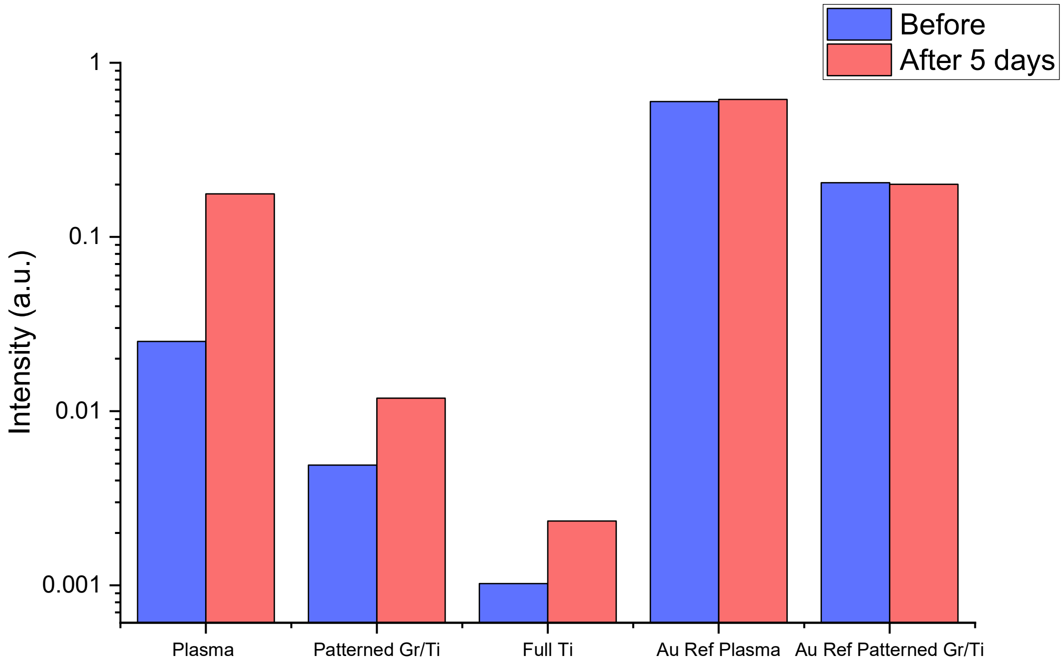

Figure 22 After 5 days in UHV conditions, the sample demonstrated a more intense signal. This slow degassing of the surface contaminants may have been induced by the low permeability of the membrane as shown in the comparison to the peaks referenced outside the covered area.

The increase may be explained by the degassing of the surface of the samples from the volatile contaminants and adsorbed gasses. These elements were previously interfering with the photoelectrons, hence their reduction consequently increased the XPS signal. The fact that the increase was limited to the membrane-covered part cannot be completely ascribed to the organic residues as even the full titanium membrane (for which no sacrificial layer was used) demonstrated an increased signal. For these reasons, the cause of the difference between the covered and non-covered parts can be explained by the low permeability of the membrane. Indeed the membrane limited the diffusion of the contaminants which impeded the emitted electrons, masking the gold XPS signal. This result especially highlights the low permeability of the membrane to separate the sample from the UHV even on open trenches as the sides of the membrane were not sealed. The higher increase in the signal for the plasma-treated membrane (6 times compared to 1.3 and 1.4 times) can instead be explained by the high quantity of oxygen adsorbed during the plasma process. During the vacuum treatment the oxygen easily diffused from the surface non-covered by the membrane to the vacuum chamber, resulting in a negligible change in the signal intensity. The covered part instead, presented limited diffusion of the adsorbed oxygen, leading to a major increase in the signal after the 5 days of treatment as it was allowed to diffuse to the chamber. In Figure 23, are reported the reference spectra of gold before and after the 5 days in UHV, revealing the increase in the intensity of the unoxidized gold compared to the oxidized peaks.

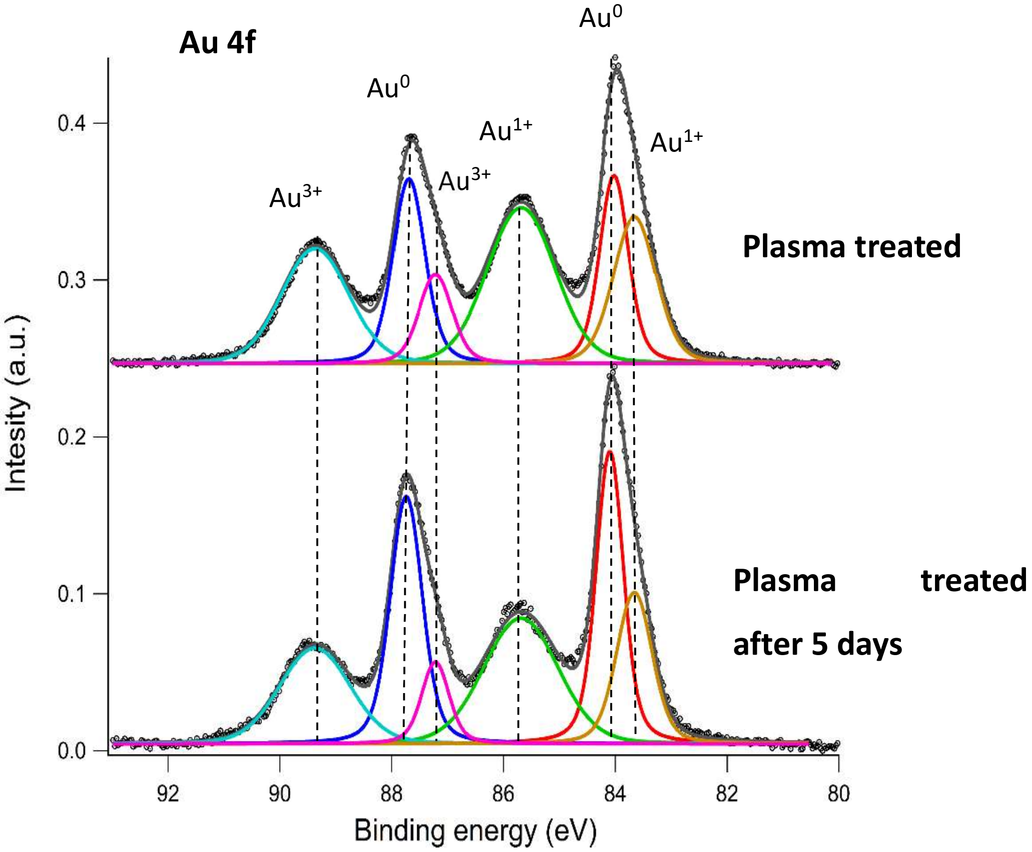

Figure 23 Reference of the gold on the plasma-treated sample before and after 5 days in UHV. The oxidized peaks were reduced in intensity compared to the unoxidized peak.

The patterned nanomembranes have shown promising results for their mechanical properties and the ability to effectively combine the characteristics of the evaporated titanium and CVD graphene over large areas. The worth of patterned membranes resides in the graphene's true freestanding surface that is reduced to the gap in the Ti patterned grid, overcoming the previous limitations of the mean grain size of the CVD graphene, and thus greatly reducing the probability to encounter a defect. The inhomogeneity of the full titanium membrane, which previously presented “stepped” and different behavior between each membrane, was not found in the patterned membrane. On the opposite, the patterning reduced the random nature of the stress-induced surface corrugation, smoothening the step-like mechanical response and obtaining arrays of membranes with uniform mechanical characteristics. With the XPS characterization, the membranes demonstrated both low permeability, as the signal intensity increased with the low diffusion in UHV of the gas entrapped in the trenches, and high electron transparency over large areas, as photo emitted electrons passed through the graphene windows without significant energy losses. Unfortunately, the carbon contaminants introduced during the sample fabrication, already reduced the signal intensity by almost an order of magnitude, both in the titanium and in the gold spectra, and further work will be required to ensure the cleanest graphene surface after transfer.

Chapter 5

Sealable microcells array

The membranes fabricated up to this point presented promising mechanical properties, an high yield of transfer, and even the transparency required for electron spectroscopies. However, for the applications described previously (electron spectroscopies and THz thermal detectors), there is also another requirement: the sealing of small volumes. The use of graphene as a membrane for sealing was already described in chapter 2, but the areas involved here go far beyond the mean grain size of the CVD monolayer. In this work, the titanium/graphene membranes demonstrated promising properties required for the sealing as shown in Figure 1. The sealed cell in the SEM images was covered with a 10 nm Ti membrane and when the sample was placed in the vacuum chamber of a SEM microscope a pressure difference of ~1 bar was applied across the membrane. The membrane demonstrated a large deflection while withstanding the pressure. However, such closed cells were rarely produced due to the main limitation in the membrane fabrication, which was related to the very low yield of the transfer on closed silicon wells (~1%). On the contrary, the open wells of the grid showed a high transfer efficiency, but they needed a secondary sealing step to close the open bottom of the cells. This secondary sealing also had to operate on each cell independently and not operate on them as a whole, thus leaving them interconnected. Indeed, if the array of cells is sealed as a whole, the presence of the few defected or collapsed membranes on an individual cell (inevitably introduced during the transfer as the yield never reached 100%) could result in the failure of the whole array. This is

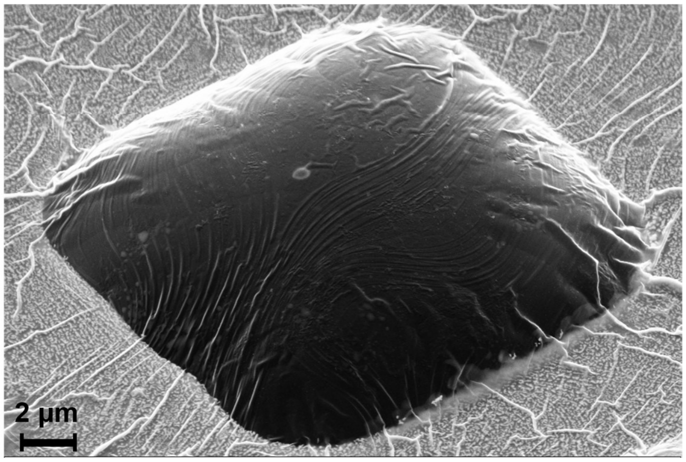

Figure 1 Example of a continuous, fully sealed Ti/Gr membrane with 10 nm of Ti forming a closed cell. The membrane is able to withstand the pressure difference in the SEM (1 bar) proving its potential as sealing membrane over large area.

not only limited to the defects introduced in the transfer phase, as a membrane can be damaged also during the subsequent handling and use; therefore, the independent sealing of all the cells is a mandatory requirement for the membrane practical applications. To efficiently and independently seal the membranes over a large area with a yield exceeding 90% of covered cells, I designed and demonstrated a secondary sealing based on the use of a silicone rubber "cork". Silicone rubber, based on polymeric organosilicon compounds whose most common example is polydimethylsiloxane (PDMS), is largely available for industrial sealing and thanks to its chemical structure (long chains of alternating silicon and oxygen atoms) is especially used where high resistance towards chemical, UV, and heat damage is mandatory. Silicone rubber mechanical properties can also be tuned over a wide range of mechanical properties, ranging from the viscosity of bubble gum to the strength of the heel of a shoe. For the silicone cork, I used a soft silicone rubber with stiffness comparable to the human skin, which resulted in a pliable cork, capable of adapting to the irregular bottom surface of the grids.

Fabrication of the sealed microcells

The grid and membrane fabrication as well as the membrane transfer were analogous to the ones previously described. For the fabrication of the silicone rubber cork, the polyaddition silicone rubber POOLKEMIE® Silimold ADT-08 was chosen for its low linear shrinkage (<0.05%) and low Young modulus (0.4 MPa). As mold for the silicone rubber, a Si wafer with a silicon nitride layer on both sides was patterned and wet-etched as in chapter 3, however, in this case, the Si was not patterned and dry etched on the frontside and instead was fully wet-etched on the backside up to the Si_3N_4 membrane. The resulting silicone cork shown in Figure 2b was a truncated rectangular pyramid of 4.5 mm of base and slightly higher than the cavity below the grid substrate (~30 µm higher as the silicon window was removed by the etching). As illustrated in Figure 2a the height excess was needed to ensure that the contact between the bottom of the silicon grid and silicone cork happened before the adhesion to the outer surface (not wet-etched) of the sample. Otherwise, in the case of slight variations of the thickness of the wet-etched grid (a process relatively difficult to control in its etch rate), the silicon may have not adhered resulting in an imperfect sealing of the bottom of the cells.

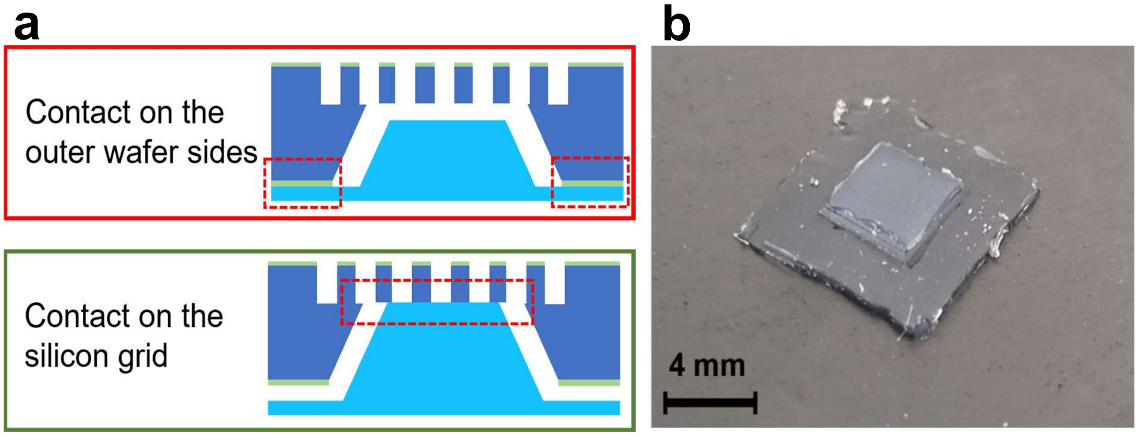

Figure 2 a) Illustration representing "good" and "bad" contact between the silicone cork and the sample. Only in the case of direct contact with the grid the sealing was assured. b) silicon rubber cork used for the sealing of the arrays.

The roughness of both the silicone and the grid bottom becomes relevant when the contact between the silicone rubber and the silicon needs to be air-tight. The presence of excessive roughness, or defects and particles left on the bottom of the etched silicon may hinder the contact between the two materials. For this reason, the wet-etching rate of silicon was checked with the optical profilometer, and the samples which presented excessive defects or roughness as shown in Figure 3 were discarded.

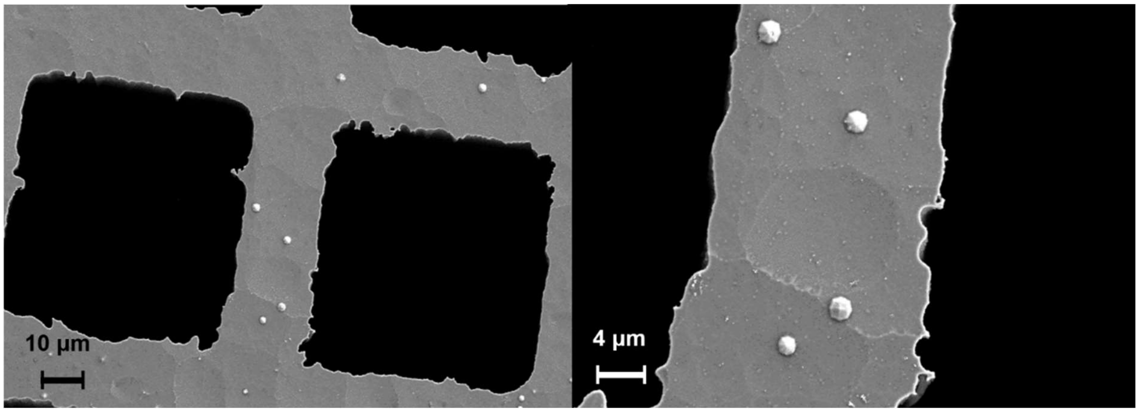

Figure 3 Roughness and defects on the bottom of a wet-etched silicon grid. The small octahedral silicon crystal introduced by the non-uniform etching process were limiting the full adhesion of the silicone rubber, hence in the presence of these defects, the sample was discarded.

The top surface of the silicone rubber presented an average surface roughness Ra ~25-40 nm as shown in Figure 4a, thanks to the complete wet etching of the silicon up to the Si_3N_4/Si interface, which presented a surface smoother than the surface obtained stopping the etching earlier, still within the silicon bulk (average surface roughness Ra ~60-80 nm)(Figure 4b). This denoted how the limiting factor for a good sealing was the roughness on the silicon window and not the silicone rubber.

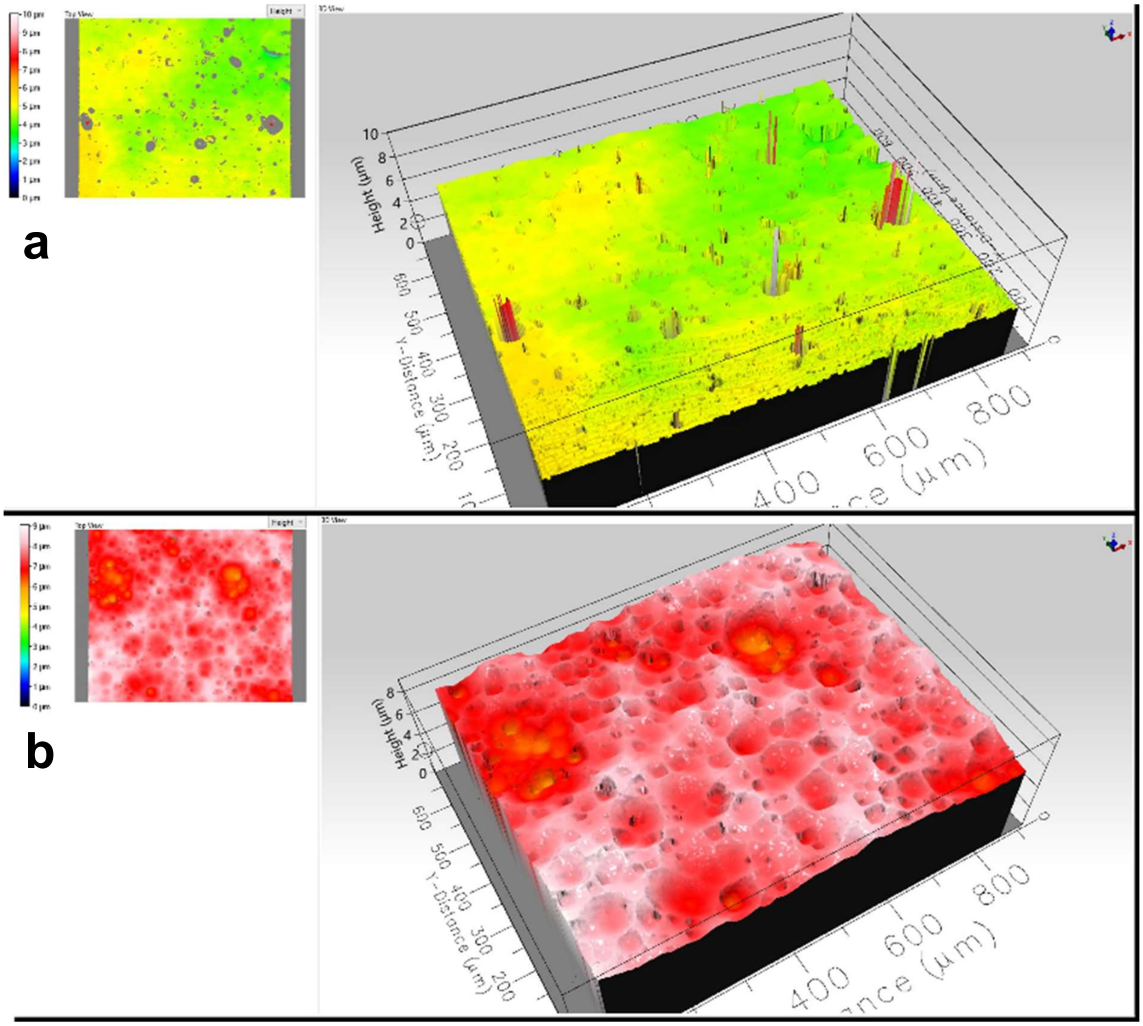

Figure 4 Comparison of the surface profile of the silicone cork (a) and the bottom of the wet etched silicon window (b).

The adhesion and sealing of the grid through the silicone rubber was achieved by using oxygen plasma treatment, to activate the surface of the silicone for increased interaction with the bottom of the silicon grid[357]. Afterward, the sample with the transferred membrane was placed on top of the silicone rubber and slightly rotated until it slid in position, self-aligning to the cork.

Sample holder design, fabrication, and pressure testing

The sealing of the membrane has been tested using a dedicated sample holder that was designed to mechanically clamp and apply pressure to the silicone on the bottom of the sample with the array of cells sealed by the membrane on top. The holder represented in Figure 5 was based on support 20x20x8 mm obtained from a PMMA sheet by laser cutting, with a cavity of 8 mm of diameter and 4 mm of depth in the middle, which was connected with a 1.2 mm (inner diameter) Teflon tube to a syringe. The flat silicone membrane was deposited over the cavity, and the sample was secured on top of it with 4 screws and a Delrin plate with a 5 mm hole in the center.

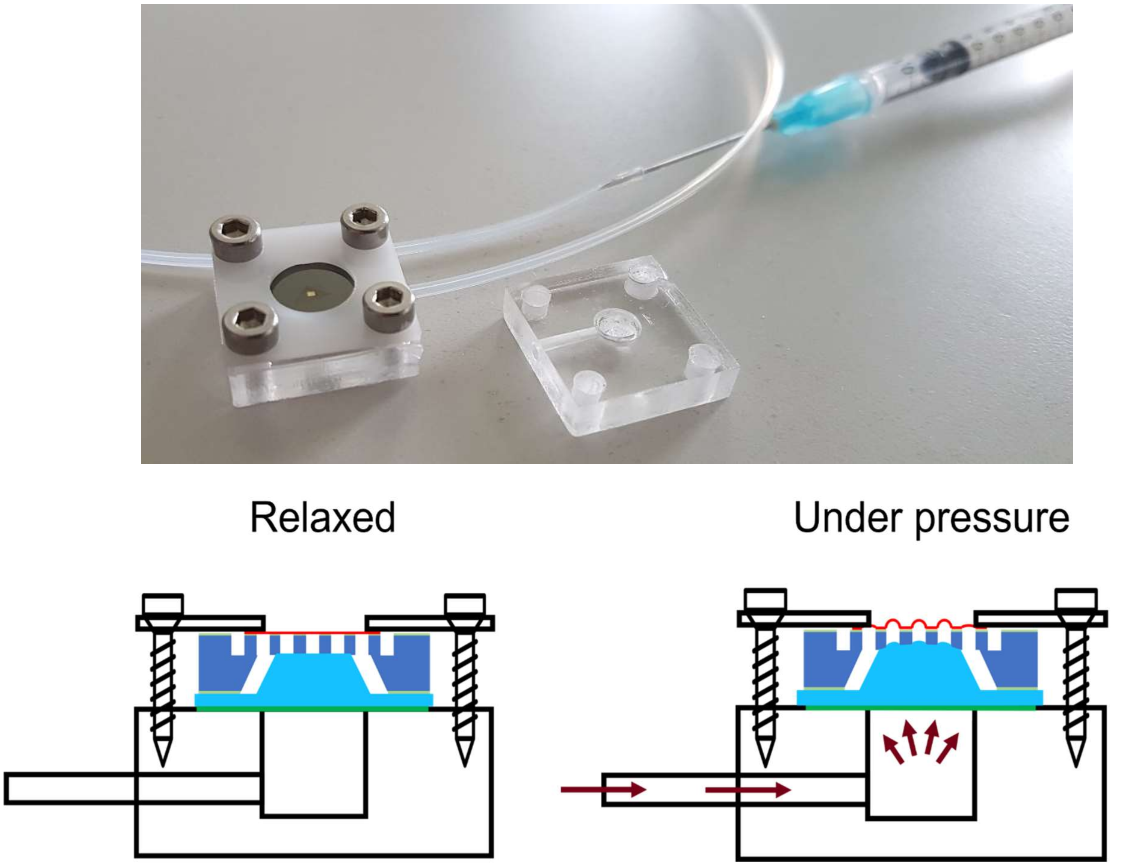

Figure 5 Top, the sample holder used for the pressure testing of the membranes. Bottom, schematic representation of the functioning holder. The pressure induced with the syringe was transmitted to the silicone cork and subsequently to the sample.

The pressure is first applied to a flat silicone membrane of thickness 250 microns (WACKER CHEMIE ELASTOSIL® Film 2030) which deforms under pressure, pushing the silicone cork up in contact to the bottom of the grid (Figure 5). The syringe was controlled during the experiment with a Syringe Pump NE-1000 and the pressure applied to the system was derived from the total volume change when the syringe was compressed using the ideal gas law:

$$P_i V_i \approx P_f V_f$$

As there was no exchange of mass and variation of temperature in the sealed holder the product of the initial pressure and volume must be equal to the final ones. The initial pressure was equal to the atmospheric pressure $P_i \approx 101\ kPa$ and the total volume of the system was the sum of the volumes of the tube, of the cavity in the PMMA and the syringe ($V_i = V_t + V_c + V_s \approx 0.34 + 0.31 + 0.5 \approx 1.15$ mL. The final volume was calculated in the same way, considering the volume variation of the syringe. The silicone rubber was considered as an ideally elastic material under the relatively low stresses applied, and the pressure was regarded as entirely transferred to the sealed cells.

Using the sample holder and the syringe, a uniform pressure of ~10 kPa (0.1 bar) was generated on the chamber underneath the silicone rubber, pushing the cork up and transmitting the pressure to the graphene sealed cells above. Indeed, the cork elastically deforms, partially filling the cell volume, and increasing the internal pressure of each cell. Continuous, defect-free, and leak-free membranes swell upwards. On the contrary, if defects or leaks are present, the internal pressure does not change, and the membrane remains still. The clamped system was observed under an optical microscope and afterward, the same experiment was repeated and measured with an optical profilometer. The pressure during the experiment was repeatedly increased to 10 kPa and brought back to atmospheric pressure. The membranes were also tested under constant pressure for up to 10 minutes without showing signs of relaxation confirming the absence of a leak. The difference in thickness, and the resulting variation of the corrugation, was also demonstrated to affect the adhesion to the substrate. For 10 nm and 7.5 nm of thickness, the membrane showed a detachment from the substrate as shown in Figure 6, affecting 30±5% and 10±5% of the cells respectively when the internal pressure was raised.

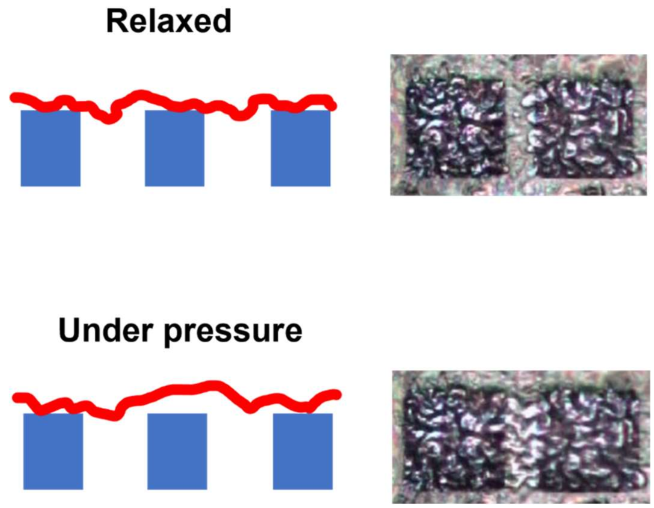

Figure 6 Detachment of a 10 nm membrane for the surface when the 10 kPa pressure difference was applied.

The detachment was due to the reduced area of the membrane in contact with the silicon frame, caused by the high membrane corrugation. As previously observed during the indentation measurements, the wrinkle geometry is reversible: upon membrane inflation, the membrane is stretched and the corrugation is reduced, however, when the system is returned to the initial pressure, the corrugation reverts to the initial configuration, re-establishing the contact with the silicon frame. When the Ti thickness is lower, 5 nm and 2.5 nm of Ti, and consequently the corrugation is minimized and the area of contact larger, no pressure-induced detachments membrane were observed. Figure 7 reported an array of cells responding to the pressure difference by swelling up to a vertical deflection of 3.5 µm over holes of 50x50 µm. Interestingly, when a broken cell

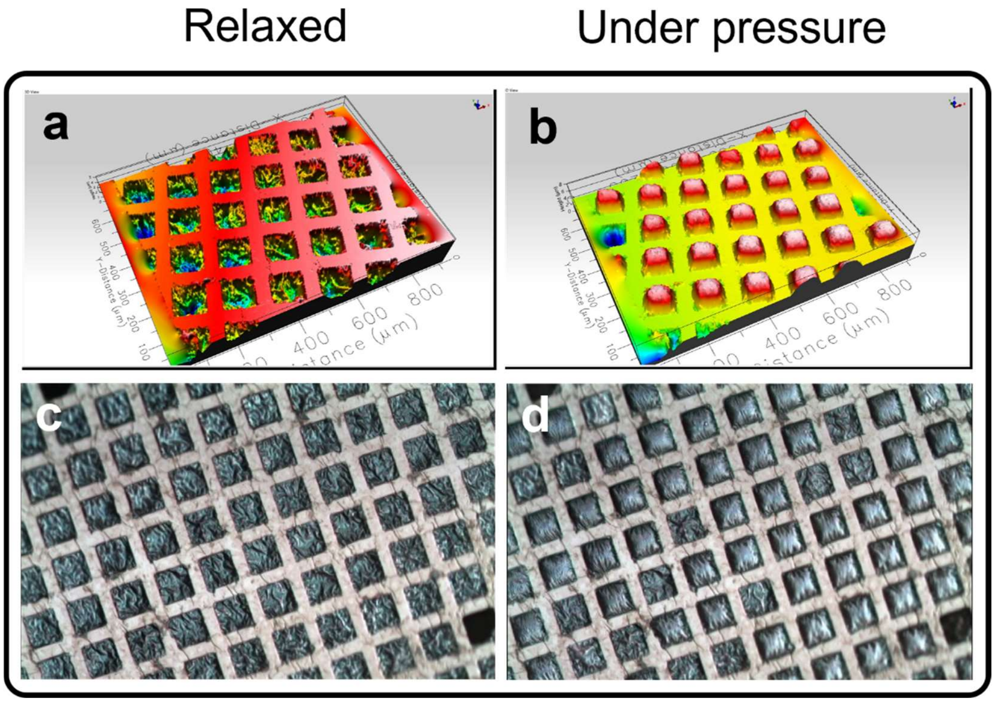

Figure 7 A grid sealed with 5 nm of titanium and responding to the pressure. Most of the holes responded to the pressure and presented the same deflection (3.5 µm).

was adjacent to good ones, these were responding to the pressure difference independently as shown in Figure 8, confirming that an air-tight sealing was obtained both by the cork against the back of the silicon grid and by the Gr/Ti membrane against the top of the silicon grid.

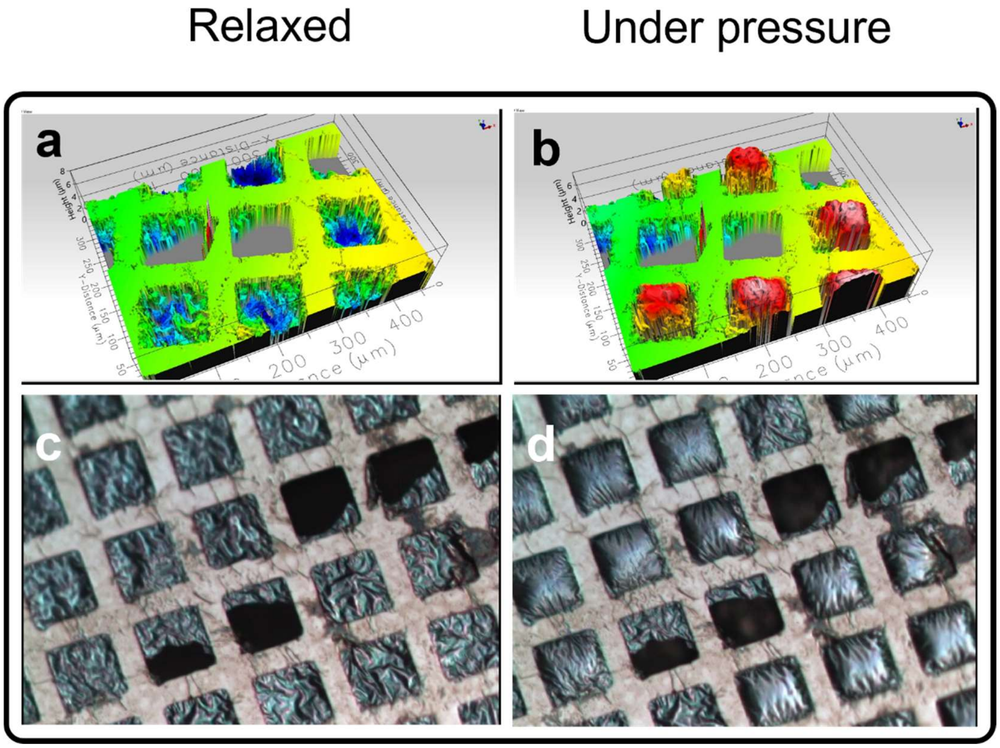

Figure 8 Even in the presence of extensive damage to the membrane (a group of them collapsed during a wrong handling of the sample), the neighboring sealed cells still responded indipendently.

The bonding between the silicon grid bottom and the silicone rubber is provided by weak interactions which allow for the easy detachment of the cork when not in use. For this reason after testing, the silicone cork was detached from the sample, washed with pure ethanol, and dried with dry nitrogen. Afterward, plasma treatment was applied to the cork, and it was attached again to the same sample and tested again under pressure. During and after the repeated detachment of the silicone, the membranes were left intact, and no collapsed membrane was observed. After 5 cycles of testing the surface of the silicone was measured with an optical profilometer to check the presence of deformations induced by the pressure repeatedly applied and measure the surface roughness (Figure 9). The surface of the cork did not present any residual deformation, contaminants, or defects that may have impeded the silicone-silicon sealing, and the repeated test did not show the presence of any inter-cell leakage induced by the cycles of testing, thus demonstrating the effective reusability of the cork-sealed grid system.

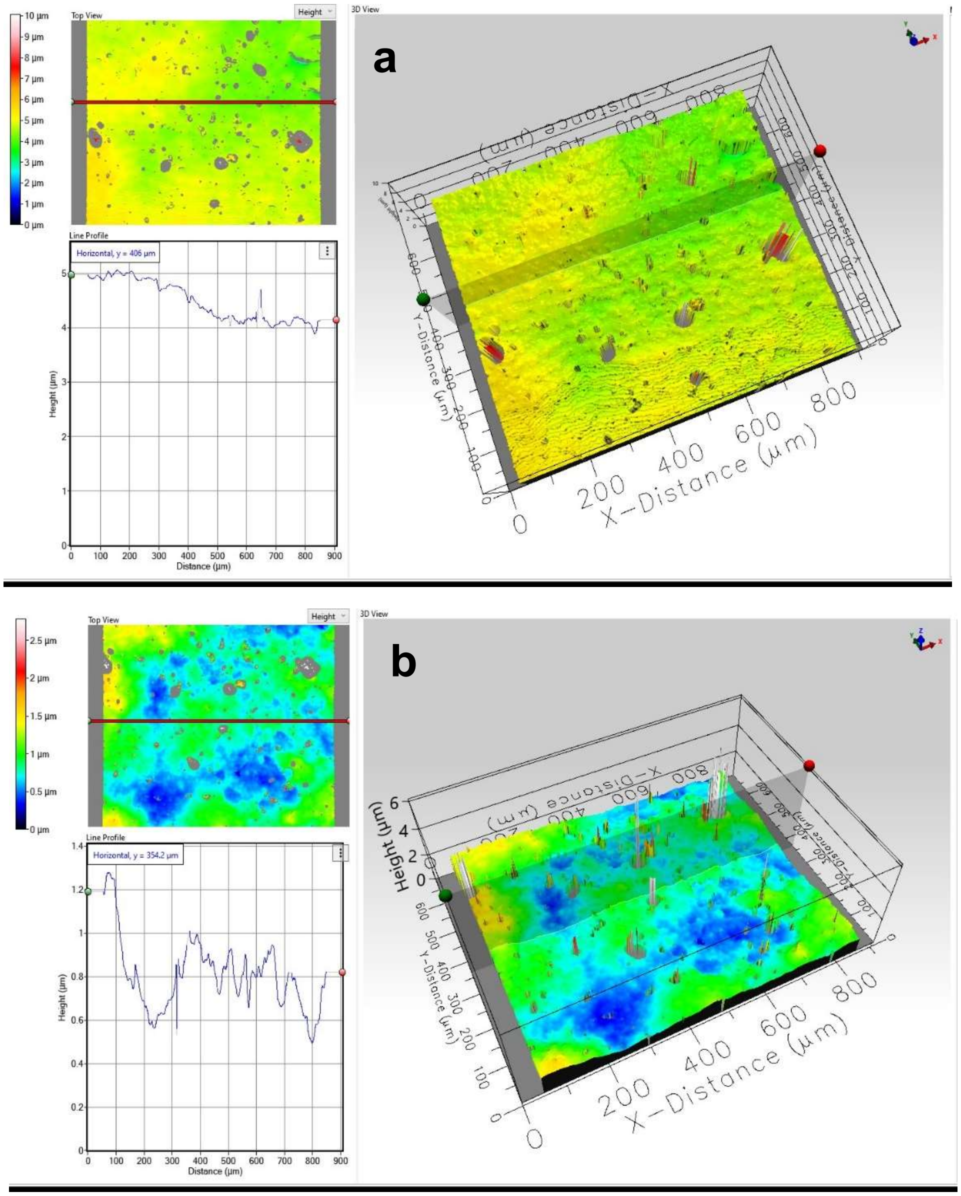

Figure 9 surface of the silicone rubber cork before (a) and after (b) the repeated testing presenting roughness parameter Ra ~30±5 nm in both cases, without the presence of permanent damage.

Limits of the systems and direct pressure on the membranes

These tests demonstrated the adhesion properties of the membranes deposited on the array, and the efficiency of silicone rubber as a secondary sealing, however, few details are known about the maximum pressure applicable directly to the membrane for two reasons: the first is that 0.2-0.25 bar was the maximum pressure that the grid was capable of withstanding before the breakdown of the silicon window. Beyond that pressure the silicone rubber applied enough force to generate a fracture in the silicon chip, that either destroyed the entire sample, propagating to the entire chip as in Figure 10a, or damaged part of the grid. The second reason was due to the approximation of the linear behavior of the silicon rubber. At higher stress, the elastic response of the membrane could not be considered uniform as the pressure was concentrated in the center of the silicone membrane that was beginning to vertically deflect. To apply the maximum pressure directly on the membranes and avoid the limitation of the transfer yield, a single cell device was fabricated instead of an array. The process used to create it is reported in Figure 10b and was similar to the microfabrication of the grid in the first patterning. The silicon/silicon nitride wafer was patterned on the backside with a square pattern (1200x1200 µm), the silicon nitride was then dry-etched and the silicon was fully wet etched up to the silicon nitride membrane on the front side was exposed. A circular hole of 100 µm was then milled with focused ion beam milling (FIB) with an LEO 1540 XB Carl Zeiss SEM-FIB CrossBeam. The resulting hole was then covered with the membrane with the same wet transfer process.

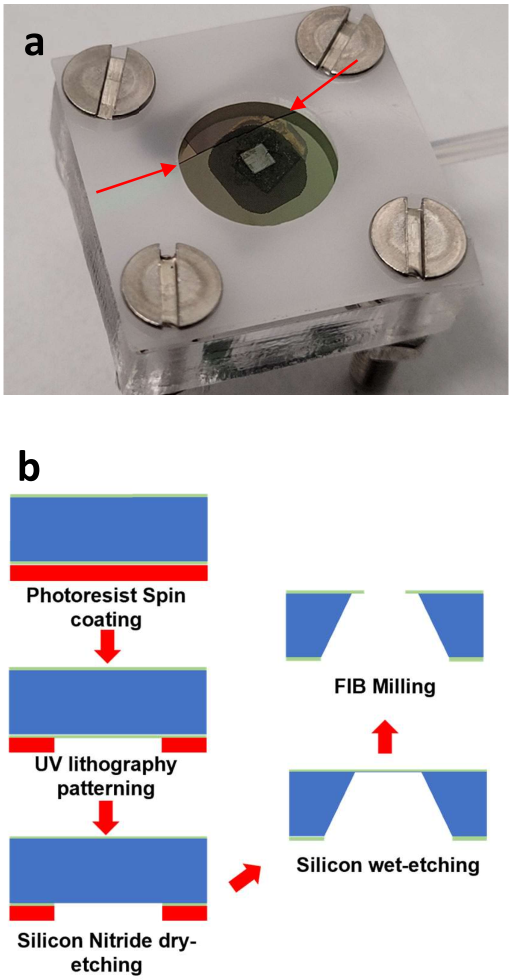

Figure 10 a) image of a cracked sample on the sample holder damaged by excessive pressure. b) schematic illustration for the fabrication of the single cells for direct pressure testing.

This hole was then repeatedly transferred with the membrane until the coverage was ensured and no collapse or damage were observed. The membrane thickness used was 5 and 10 nm and their yield for the transfer approached 90% for the 10 nm and 70-80% for 5 nm (Figure 11a). Patterned membranes were also attempted but the resulting fragility of the areas covered by only graphene as shown in Figure 11b reduced the sealing capability of the system.

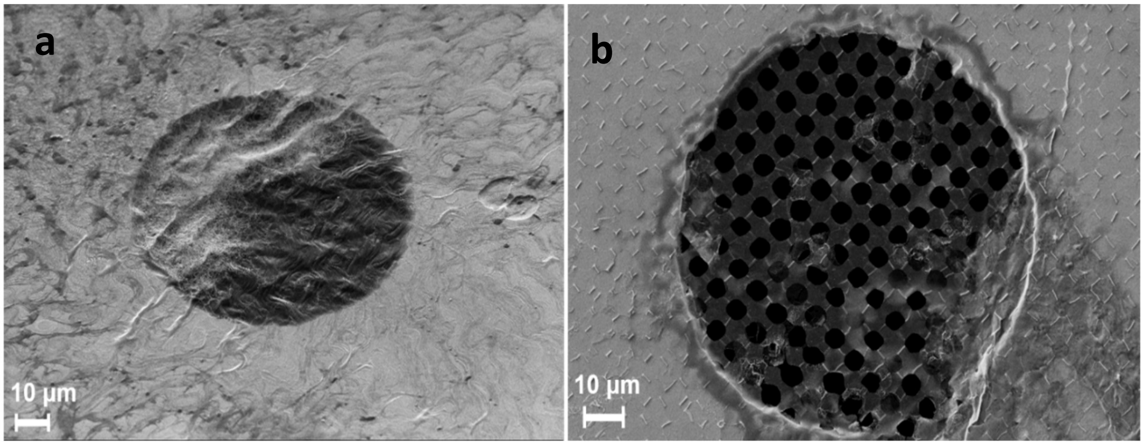

Figure 11 Single cells covered by a 10 nm (a) and patterned membrane (b). The grid of the patterned membrane was intact but almost all of the graphene windows were collapsed, thus voiding the sealing offered by the membrane.

The single-cell was then inserted in the same sample older previously described and mechanically clamped to obtain a sealed airtight system. In this case, however, the silicone rubber was absent and the pressure was directly applied to the membrane with the syringe. The membranes tested reached higher pressures compared to the array, with the 10 nm withstanding up to 35-40 kPa (0.3 bar). The pressure could also be maintained for more than 10 minutes without showing any relaxation at the optical microscope as demonstrated in Figure 12a and b. The ultimate pressure reached before breaking was 45 kPa.

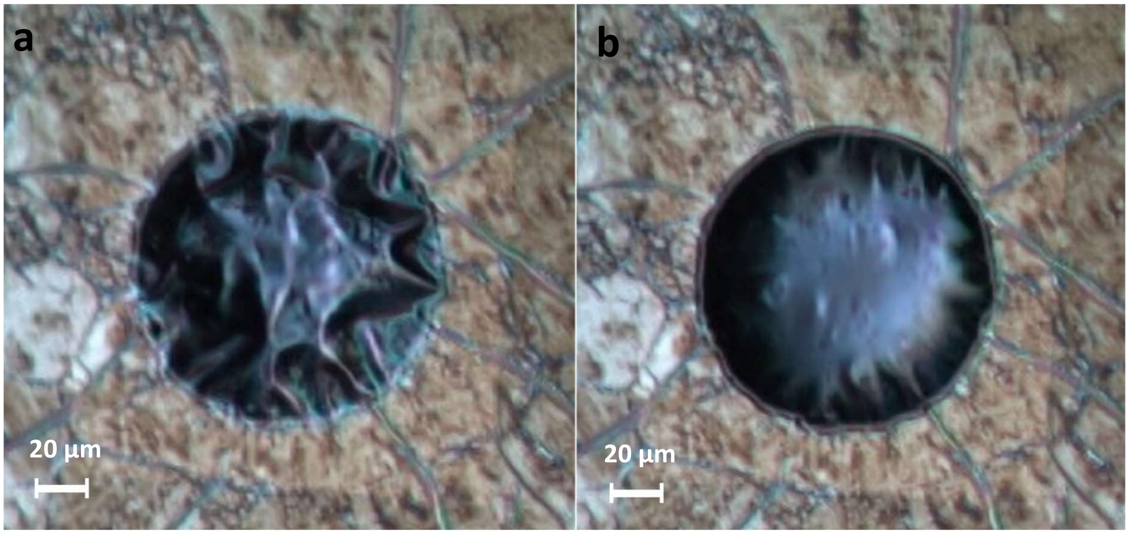

Figure 12 Microscope image of a 10 nm membrane relaxed (a) and under the maximum stress applicable (b)(40 kPa). Under pressure the membrane reached a vertical deflection of 5 µm for up to 10 minutes without any observable leakage.

In this chapter, a system to evaluate the membrane resistance to the pressure difference and the sealing efficiency was described. A simple method for the sealing of the bottom side of the cell array based on the fabrication of a silicone rubber cork was, developed and demonstrated. The sealing was proven to be effective even in the presence of damage, as the cells were responding independently to the pressure, and was even re-usable without damage or membrane collapses. We also highlighted the correlation between the thickness and the adhesion to the substrate with the 10 nm showing detachment under pressure. Among the thicknesses studied the 5 nm membrane resulted in the best balance between the yield of transfer and the adhesion strength and vacuum sealing, proving as a promising candidate for the efficient sealing of cells. Furthermore, the limits of the membranes were tested with a direct application of the pressure, on suspended areas even larger than previously shown. These ultra-large area membranes were strong enough to withstand pressure differences up to 40 kPa demonstrating their worth in sealing applications.

Chapter 6

THz Sensing with Golay cell array devices

The work described in the previous chapters concerned the creation, characterization, and testing of large area suspended membranes and arrays of sealed cells based on those membranes. In this chapter, a practical application of those micromachined cells will be discussed. The sealed cells containing humid air respond to all the properties required for the thermal detection of THz radiation. Thanks to its high absorption in the THz region, the air itself can work as an absorber and the ultrathin bilayer membrane present strong mechanical properties to cover and seal large cavities while still demonstrating a high vertical deflection. This vertical deflection in particular is essential, as it is directly correlated to the sensitivity of the resulting Golay cell. The higher the increase of the deflection at small pressure differences, the more sensitive the device. All of these qualities are fundamental to sense radiation through thermal detection with a Golay cell-like device. To apply the sealed arrays to the THz detection, we first characterized their response to temperature variation, and later we characterized their response using a properly filtered Globar source, a black body radiation emitter, with significant intensity in the THz region.

Thermal testing of the sealed cell

To characterize the response of a sealed cell to an increase in the gas temperature, we applied a thermal gradient using a Peltier cell. For this experiment, we used a single cell that was mounted on a 500 µm thick silicon wafer, sealed with a bi-component adhesive (Thin Pour, Reprorubber) as shown in Figure 1a, and let cure for two hours at room temperature. The sealed sample was then placed on the Peltier heater and the membrane vertical deflection was measured with an optical profilometer as in the setup represented Figure 1b. To increase the reflectivity and the profilometer signal-to-noise ratio, the bilayered membrane used was composed of graphene and 10 nm of evaporated gold.

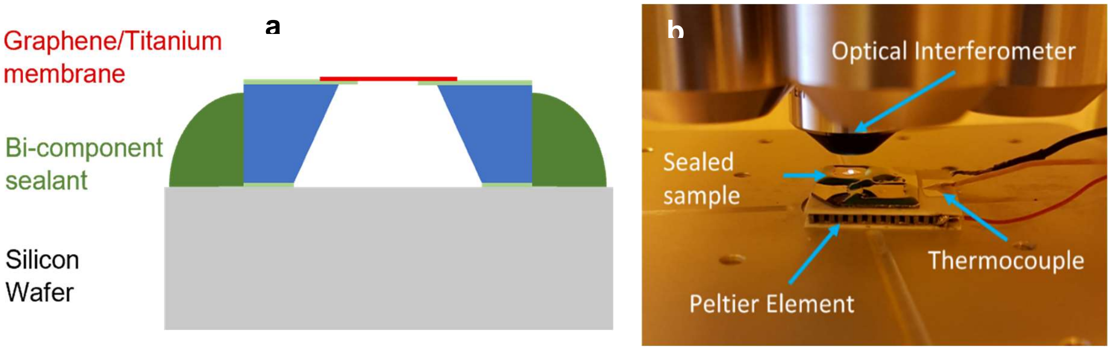

Figure 1 a) Illustration of the single cell sealed with the bicomponent on a silicon wafer. b) Setup for the analysis of the thermal response of sealed single cells. A peltier element was used to increase the temperature of the sealed sample which was constantly measured through a thermocouple. An optical interferometer was used to measure the deflection of the membrane during the experiment.

The experiment was performed switching from room temperature and 33°C, as measured by a thermocouple mounted directly on the Peltier, assuming that eventually, the systems thermalized at the Peltier temperature. The temperature was maintained constant for three minutes and optical measurements were taken every 3 seconds. The response time of the membrane shown in Figure 2, is limited by the thermal response of the whole system and is anyway faster than the scan time of the profilometer, which was limited to ~3 seconds. Interestingly, 27 seconds after the heater was switched on, while the system was still increasing its temperature, we observe a decrease in the membrane deflection. This relaxation may have been caused by the poor sealing with the bicomponent, as opposed to the sealing offered with the silicone rubber that did not demonstrate this effect under pressure variation, as reported in chapter 5.

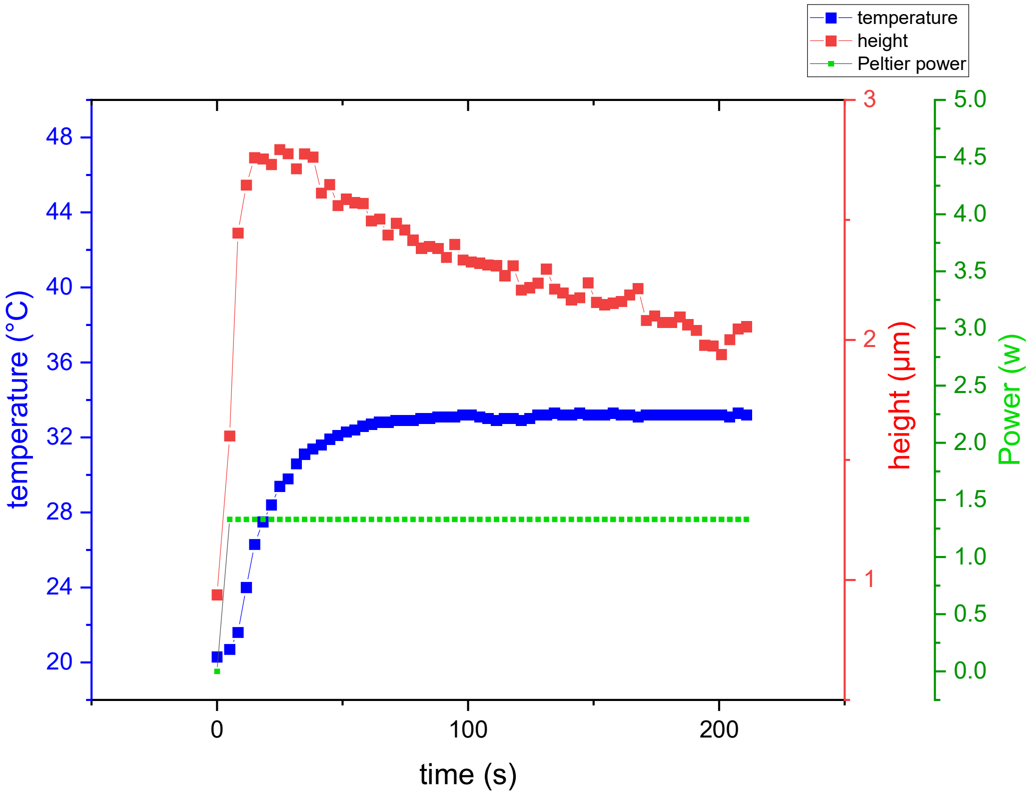

Figure 2 Graph representing the deflection of the membrane during the increase of the temperature with the Peltier heater. After reaching a peak, it slowly relax even while keeping the temperature constant.

To characterize the thermal response of the sealed cells with the titanium membrane described previously, single cells were prepared with titanium thickness 5 nm and 10 nm. The two single cells were mounted as illustrated in Figure 3b on a glass slide covered with a 250 µm thick silicone rubber film for the sealing already described in chapter 5. To keep the sample in position and impose a slight pressure in order to ensure airtightness, a Kapton tape was applied on the sides of the sample as in Figure 3a. The resulting system (the single cell, silicone rubber, and glass slide) was placed on the hot side of a Peltier element and a thermocouple was positioned near the sample on the glass slide.

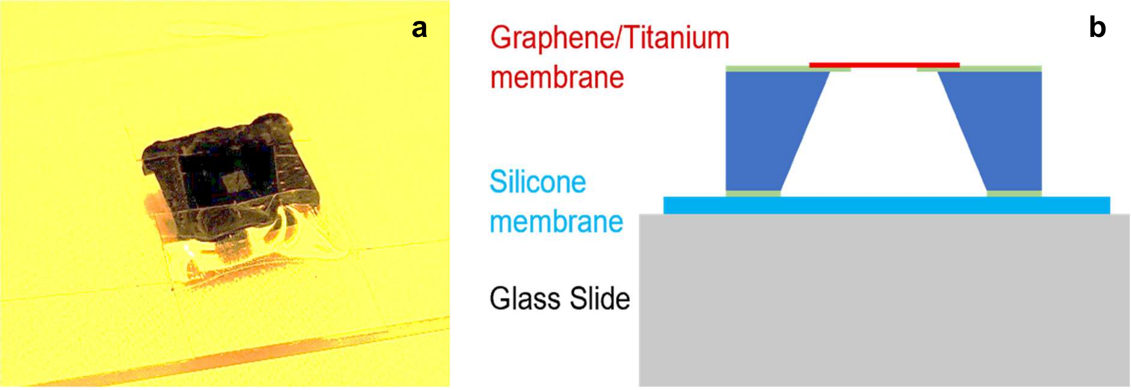

Figure 3 a) The sample was kept in position and pressed on the silicone rubber membrane with the aid of kapton tape, the color of photo of the sample was post-processed to highlight the silicon grid in the middle and the tape limited to the side of the sample. The yellow color is due to the illumination in the cleanroom. b) Illustration of the sample used for the characterization of the single cell thermal response.

The Peltier and the sample were then placed under the optical profilometer to measure the surface profile of the single cell. By using a DC power supply, the temperature difference generated by the Peltier element was controlled until reaching a temperature of 40° C as measured by the thermocouple, then the system was switched off and was left cooling at room temperature. Before and during the experiment the optical profilometer was used to manually scan the surface every 3 seconds resulting in the image sequence shown in Figure 4. The target temperature was reached in ~10 seconds and the 5 nm membrane reached a vertical deflection at the peak swelling of 3.5 μm before slowly relaxing while the system was cooling to room temperature. The 10 nm membrane showed a stiffer response as already shown in the mechanical characterization of chapter 4, where the full membranes demonstrated a linear response with a high slope since the contact point of the cantilever. This response was the opposite of the other full membranes tested that started with a low slope and reached a high stiffness only after the membrane unfolding while also presenting a higher deflection. The vertical deflection consequently was limited to 2.1 μm under heating before returning to the relaxed condition. Overall, this simple experiment allowed for the testing of the response of the single cells to temperature changes in the sealed volume. The cell response was relatively fast but limited by the thermal response of the system. Due to the presence of the corrugation, the response of the 10 nm Ti was not regular, and when unfolding and returning to the relaxed condition the membrane often showed step-like movements. To reduce the sudden and irregular response of the membrane, the following experiments took into consideration only 5 nm Ti membranes. Indeed, these membranes showed the best balance between a strong sealing, a high transfer yield, and a fast response to temperature variation with high deflection, and avoided most of the sudden changes compared to the 10 nm Ti. These properties made them promising candidates for the fabrication and testing of the Golay cells array.

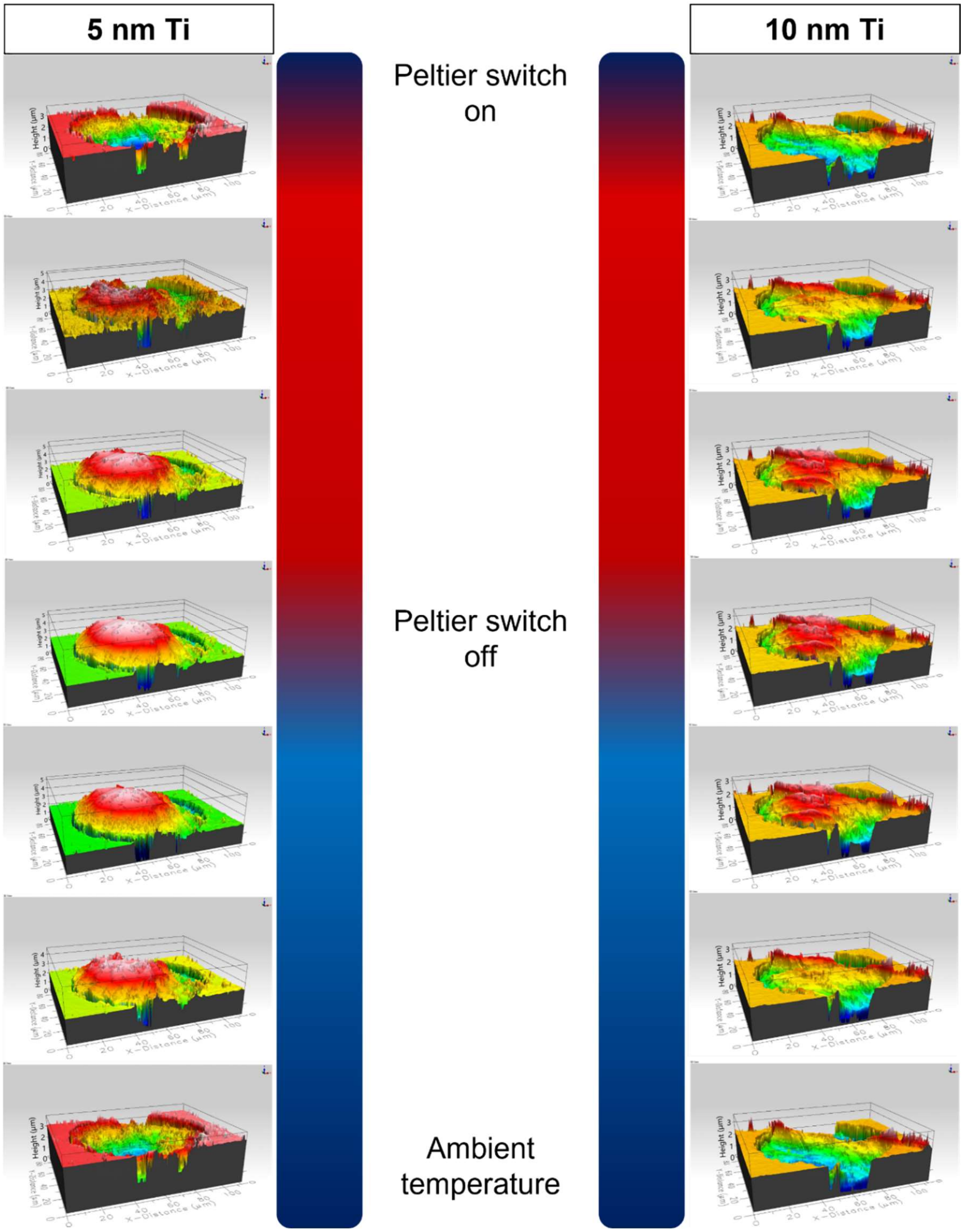

Figure 4 Thermal response of the single membranes. The 5 nm membrane reached a deflection of 3.5 microns while the stiffer 10 nm membrane reached 2.1 microns. During the heating, the membranes presented sudden changes in their morphology. This phenomenon was caused by the presence of the corrugation tensing during the membrane swelling.

Raman Spectroscopy of graphene in the composite bilayer

The high deflection observed in the previous thermal test demonstrates the responsivity of these cells to small pressure variation. To confirm the source of the deflection (either the strain of the material or the displacement of the corrugations, or both) we carried out a characterization of the stress state of the membrane with Raman spectroscopy. This technique has been used since the discovery of graphene to characterize its structure, strain, and the presence of defects in its structure[358]. Thanks to the lattice properties of graphene, the Raman spectrum provides quantitative information on the number of graphene layers (as the interaction between adjacent layers changes the phonon properties of the material), the presence of defects (the D peak is indicative of the presence of defects as they act as centers for phonon scattering), and its mechanical strain. For example, under tensile or compressive stress, such as those induced by the transfer on solid surfaces, or those present in a graphene-covered oscillating cantilever, or even those applied on elliptical graphene membranes, the peaks of the graphene are subjected to a Raman shift or the G band splitting[359]–[361].

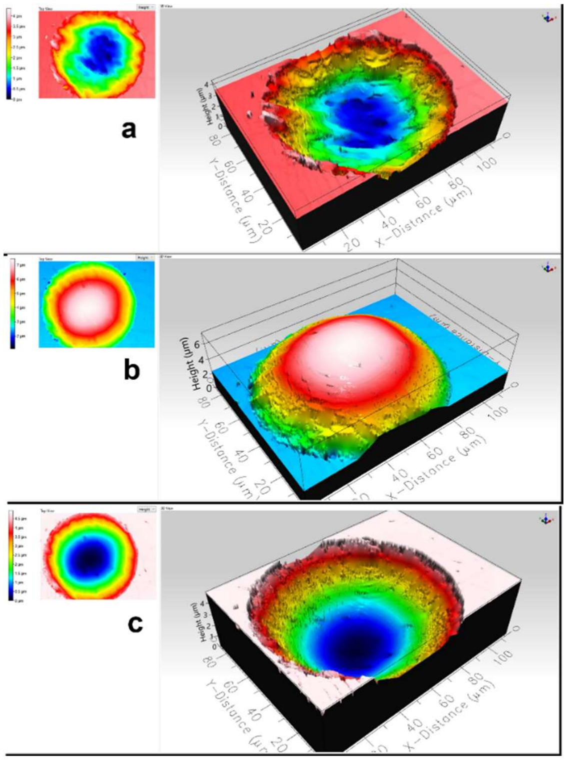

Figure 5 A 5 nm of Ti membrane relaxed (top) under positive pressure (middle) and negative pressure (bottom). The maximum vertical deflection measured in both cases was 5±0.3 µm.

To characterize the graphene, a pressure difference was applied with the sample holder to the membranes which were analyzed in an optical setup with a 532 nm laser (Cobolt Samba, 50 mW) and a spectrometer (Shamrock SR-750, Andor Technology plc). The power of the laser incident on the sample was controlled through a variable neutral density filter and kept at 1 mW. The spectrum was taken before applying the pressure (as the membrane in Figure 5a), and under positive and negative pressure (resulting in the large deflection shown in Figure 5b and c). The pressure applied was 30 kPa for 10 nm, 15 kPa for 5 nm, and 5 kPa for 2.5 nm. All of the membranes presented the characteristic peaks of graphene (2D, G, and D), and the intensity of the signal did not show significant variation with the thickness of the metal layer. To fit the samples, I applied a Voigt function and a Shirley background. After fitting, the spectra were compared but no Raman shift was observed in the peaks in all three thicknesses tested as reported in Figure 6. This suggests that under the applied pressure differences up to 45 kPa, the observed deflection is mainly due to the relaxation of the built-in corrugations, while the strain of the membrane plays a negligible role.

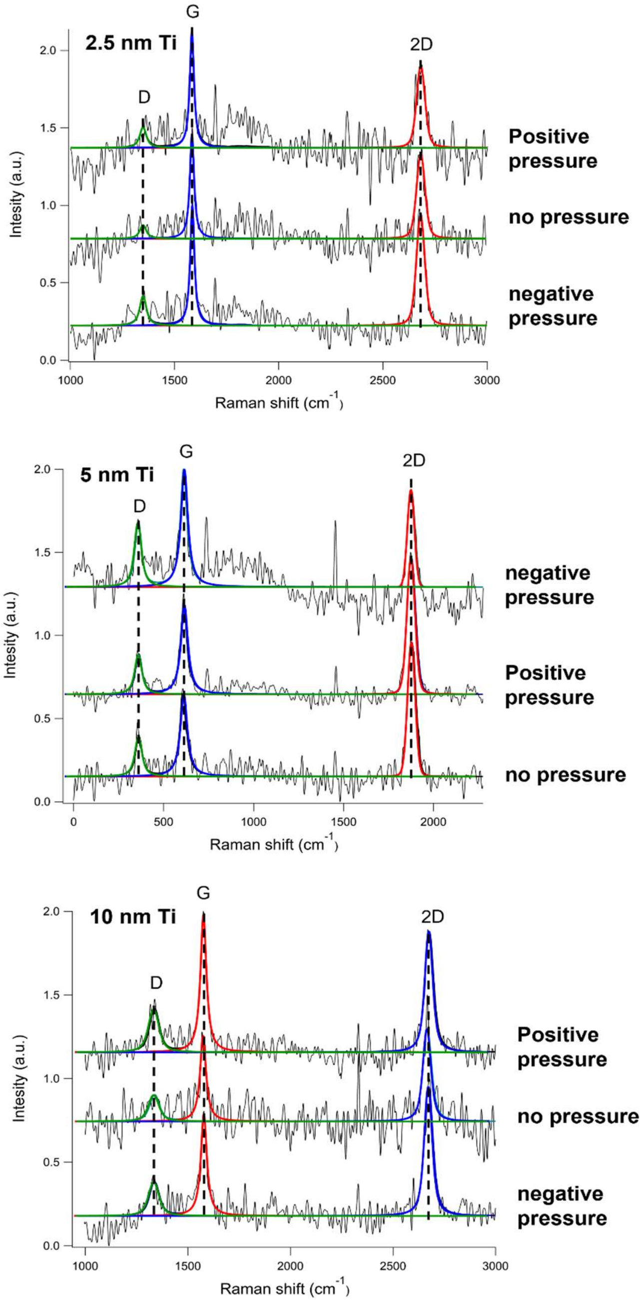

Figure 6 Raman characterization of the membrane under stressed conditions. The Raman peaks of graphene did not show any relevant shift indicating the low of mechanical stress directly applied on the graphene and indicating that the origin of the large deflection lies mainly in the unfolding of the corrugations.

Globar testing of the arrays

To demonstrate the potential of the arrays as Golay cell detectors, a Globar was chosen as the radiation source. The Globar (also called Glowbar) is based on a U-shaped silicon carbide (SiC) rod of 5 to 10 mm in diameter that is heated up to 1400 K. This source behaves as a black-body, emitting broadband radiation which is peaked in the infrared. This source is commonly used in infrared studies as it is practical, cheap and its emission can be easily filtered with bandpass filters to obtain the required wavelength range. The optical setup used for the measurements of the arrays under Globar radiation is shown in Figure 7. The radiation emitted by the Globar source is gathered by an off-axis gold-coated parabolic mirror and directed towards the radiation filter. After being filtered by either silicon, PE, PTFE, the bandpass filter, or a combination of them, the remaining radiation is focused by a second parabolic mirror on the sample, passing from the bottom. Finally, an optical microscope with attached a ThorLab CMOS camera captures the movement of the membrane during the irradiation. Compared to other detection electric readout-based systems, the lock-in amplifier was absent due to the nature of the detection system. The digital signal from the camera indeed, needed conversion to analog before any possible application of the amplifier, which would have increased the complexity of the system.

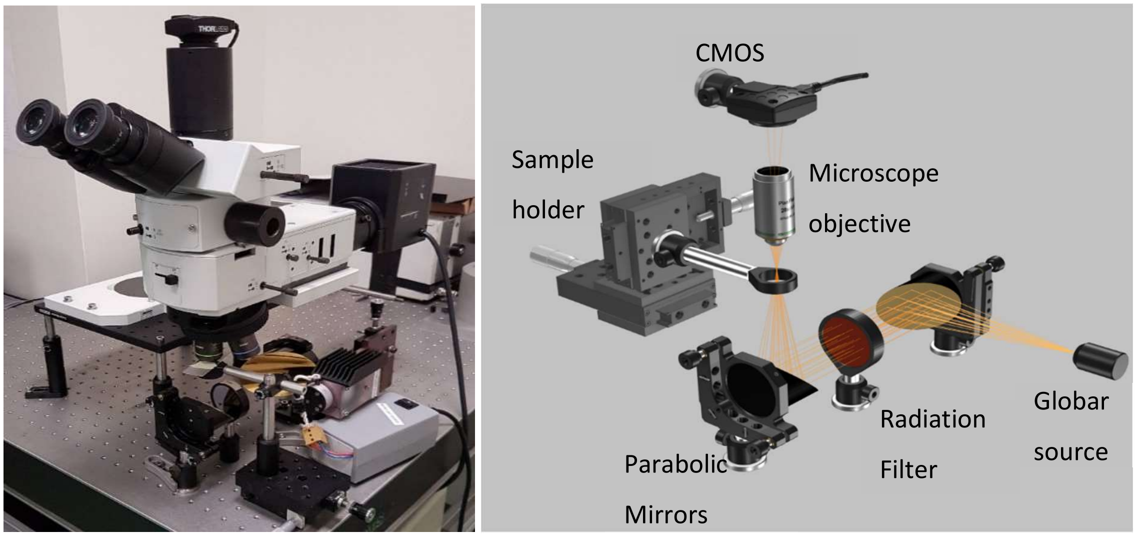

Figure 7 Optical setup used for the experiment. The radiation emitted by the Globar source was directed with two parabolic mirrors to the sample coming from the bottom. Over the sample, a microscope with a CMOS camera attached was used to capture the membrane swelling.

The filters used were undoped silicon, polytetrafluoroethylene (PTFE), polyethylene (PE), and a bandpass filter for 5 THz (BPF5.0 Tydex). The silicon filter was used to block out all the visible radiation but was transparent to the infrared radiation as shown in Figure 8. PE and PTFE, instead, are transparent to the THz radiation but not to the infrared and visible radiation emitted by the Globar. Thanks to their transparency in the THz region, they are commonly used as windows for the incident radiation in commercial Golay cells. Finally, the 5 THz band-pass filter was used to attenuate all the radiation in the visible and infrared while peaking in transmission in the 5 THz (Figure 8)[362].

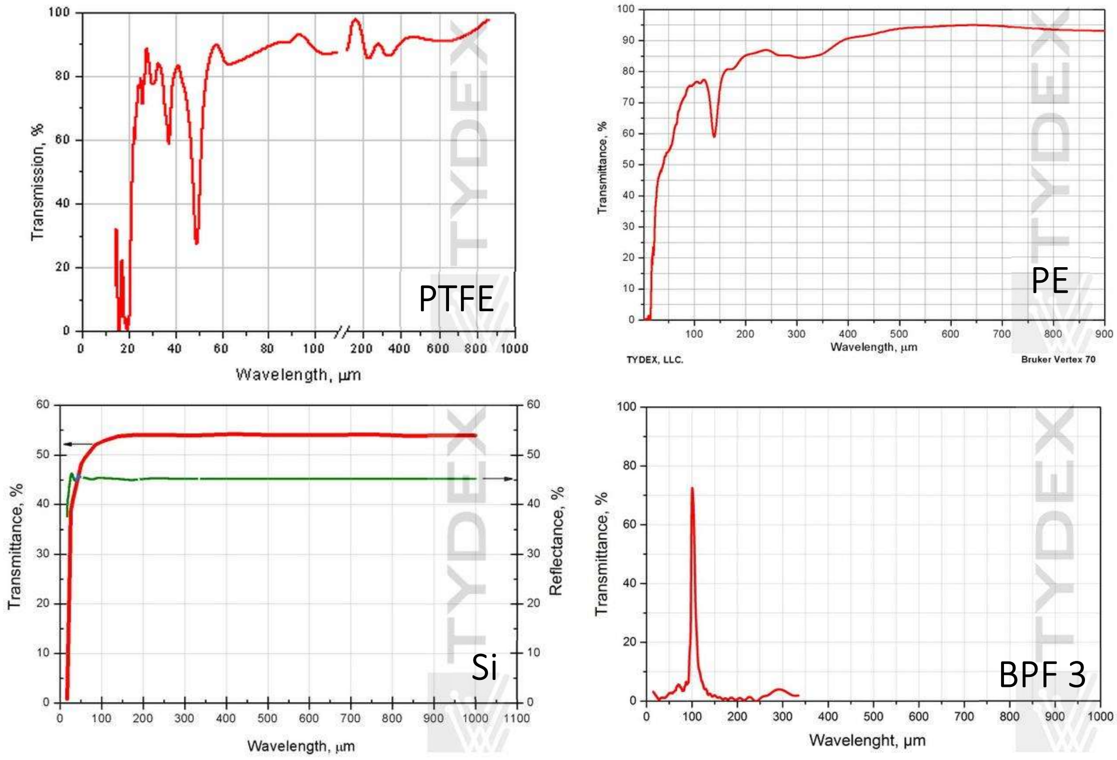

Figure 8 Transparency of PE, PTFE, band pass filter and silicon in the THz region. BPF 3 is for the band pass filter for 3 THz, the closest available from the manufacturer to the 5 THz we used. [362]

As shown in Figure 9, the emission of the globar source peak in the infrared region. The THz region, usually considered ranging from 0.3 to 30 THz, represent only a fraction of the intensity emitted. The application of the three filters together leaves an even smaller fraction of the emitted radiation and is highlighted in light blue in the figure below.

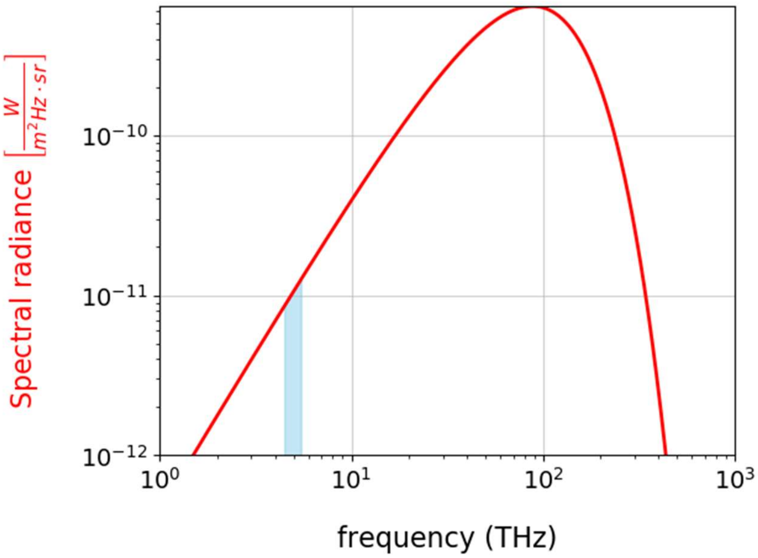

Figure 9 Globar black-body emission. The small section in light blue is the part of the spectrum that remained after the use of the silicon, PTFE or PE and bandpass filter combined.

The sample was positioned under the microscope with the radiation coming from the bottom and passing through the glass slide and the silicone cork, before heating the sealed cell and causing the swelling of the membranes. The Globar source was switched on 30 minutes prior to the experiments to allow the SiC rod to reach a stable working temperature while using a shutter to control the illumination of the sample. To test if the sample was responding to the radiation, a test was carried out without imposing any filter on the radiation. With the microscope in bright-field mode, the membrane demonstrated a fast response to the radiation (in the first second of irradiation the membrane is already showing visible deflection) presenting its peak height after ten seconds, shown in Figure 10.

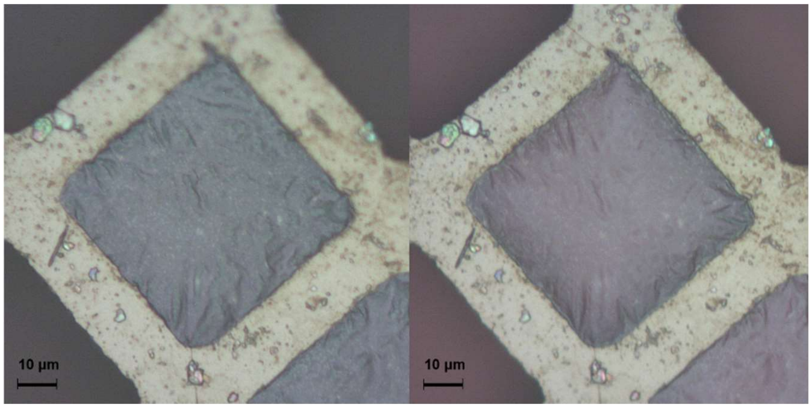

Figure 10 Membrane relaxed (left) and under Globar irradiation (right) showing visible swelling under the optical microscope.

After proving the response of the cell to the radiation, the silicon filter and the 5THz bandpass filter were applied to block the visible and IR part of the radiation. With the THz, the incident radiation presented noticeably less power than before and the time required before observing a visible response of the membrane increased to 3 seconds. During each following test, the membrane was subjected repeatedly to the Globar radiation in cycles composed of 20 seconds of illumination followed by 20 seconds of relaxation for the membranes. These cycles were repeated 3 times for each experiment. The measurements were carried out in dark-field mode as it highlighted the corrugations of the membrane, which were the most visible features that were modified due to the membrane swelling. To observe the membrane deflection the images were captured with a CMOS camera (Zelux ThorLabs) and the video was analyzed with the software ImageJ the plugin Time Series Analyzer. A region of interest (ROI) was manually selected for each cell on those parts that presented a higher contrast in the signal during the expansion of the membrane and were kept the same for the following experiments. The selected ROI was then analyzed by integrating each pixel intensity over the whole duration of the video. The resulting microscope video contained the 9 independent cells shown in Figure 11. The non-linear response obtained with silicon and the bandpass filter was matching the response expected for a thermal detector and confirmed the performance revealed by the single cell thermal test. The intensity of the signal varied between each membrane and was mirrored in the case of membranes 3, 4, and 9 of Figure 11. This can be explained by the ROI used to select the part of the membrane with the highest change in intensity. During the tensing of the membrane, not every corrugation behaves in the same way. If, for instance, the ROI was selected in a valley in the profile of the membrane, its signal will be specular to the response of the peak of a corrugation. The difference in the intensity of the signal instead may be deemed as either the different mechanical characteristics of each membrane of the array or the relative movement of the corrugation chosen for its signal. However, the different optical signal does not seem to depend directly on the total deflection of the membrane, as a ROI selected closer to the middle of the membrane (where the deflection is higher) did not show a higher response to the ROI closer to the side of the cell (where the total deflection is lower).

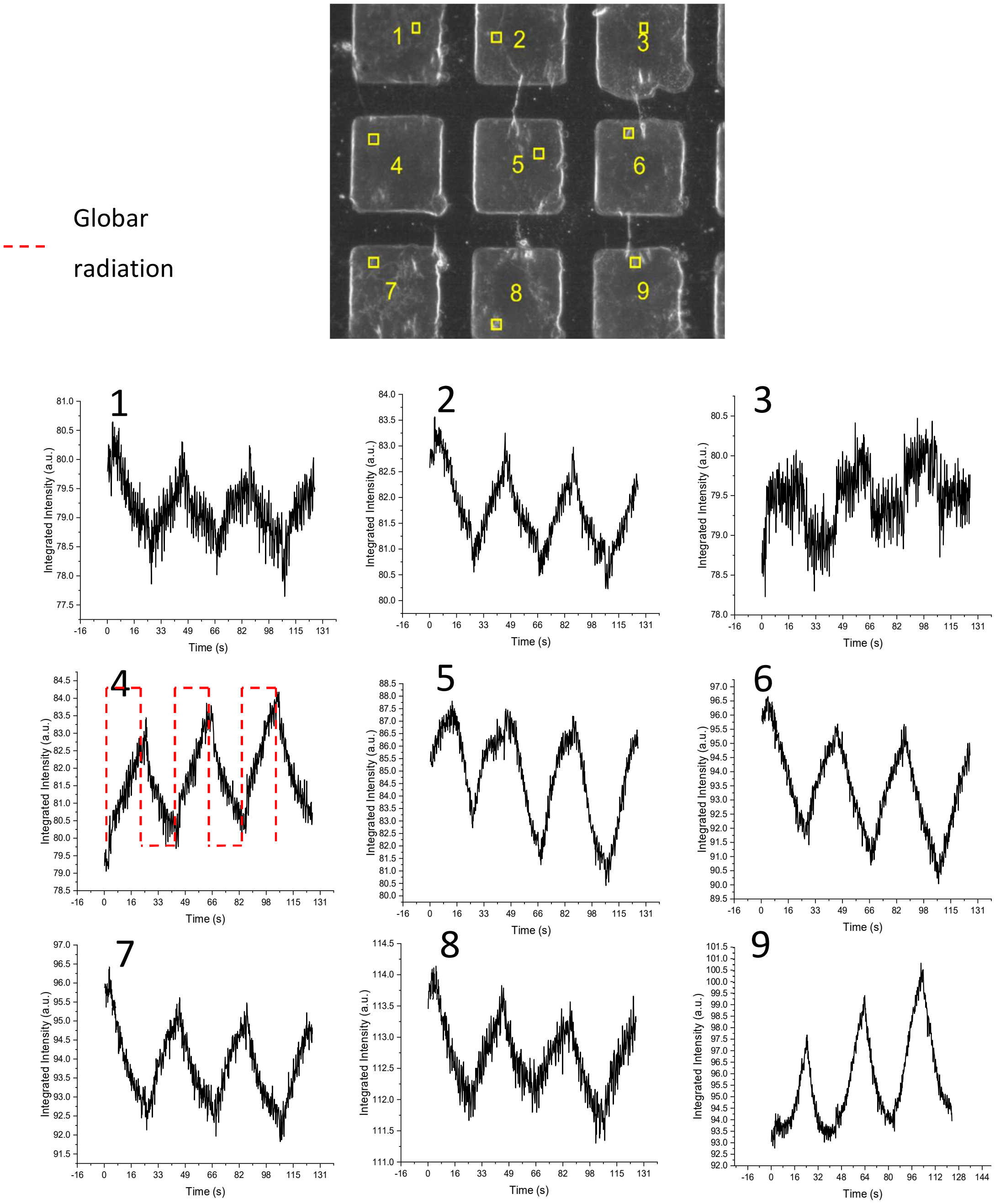

Figure 11 Response of the cells on the ROI arbitrarly selected. Adding a band pass filter for the 5 THz reduced and eliminated the sharp response that may have been caused by the detection from the camera sensor of some infrared bands. With the red line is illustrated the globar irradiation.

Due to the non-linear response of the cells, the peak of deflection was not reached in the 20-second cycles. Hence the following experiments, in which I used a combination of PTFE or PE and BP filter blocking most of the Globar radiation, were taken with 40-second cycles. This longer time of irradiation and relaxation allowed the membranes to get closer to the thermal equilibrium between the energy irradiated on the cells and the energy dissipated.

Substituting the silicon filter with PE or Teflon, both of which blocked the infrared and the visible region, further reduced the radiation arriving at the cells and by consequence also the membrane swelling. The optical measure was affected by the reduced radiation and some membrane (1 and 3) did not show noticeable swelling under irradiation (Figure 12).

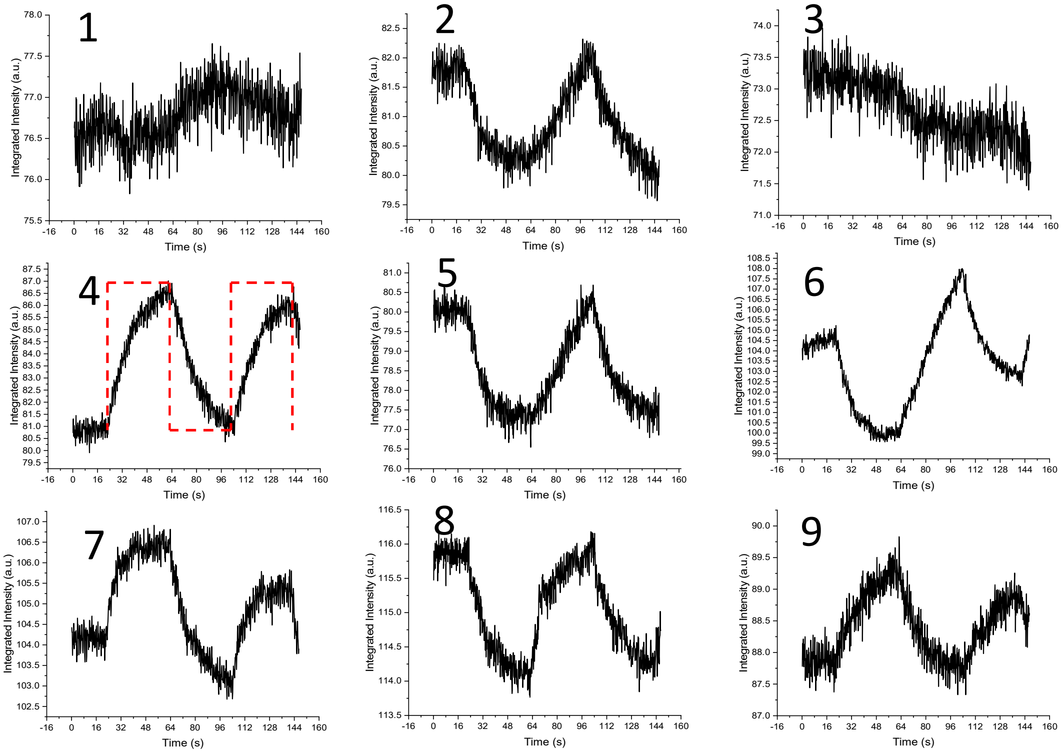

Figure 12 Response with cycles of 40s of the cells with the use of a PTFE filter in conjunction with the band pass filter for 5 THz. With the red line is illustrated the globar irradiation.

To characterize the responsivity of each membrane to the radiation, the non-linear thermal response of the membrane under a radiation pulse can be fitted by two exponential functions:

$$U(t) = \begin{cases} U_0\left(1 - \exp\left(-\frac{t}{\tau 1}\right)\right) & heating \\ U_0 \exp\left(-\frac{t}{\tau 2}\right) & cooling \end{cases}$$

where $U(t)$ is the time-dependent signal response for the heating and cooling phase, τ1 and τ2 are the respective time constants for heating and cooling, and U_0 is a constant proportional to the incident power [363]. The two exponentials describe the heating and cooling of the membrane as shown in Figure 13 and both are characteristics of the response of the single membrane to the radiation. In the case of cell #4 in the figure below, the time constant presents similar values 15.0 s and 17.1 s resulting in a similar response time during the cooling and heating phases.

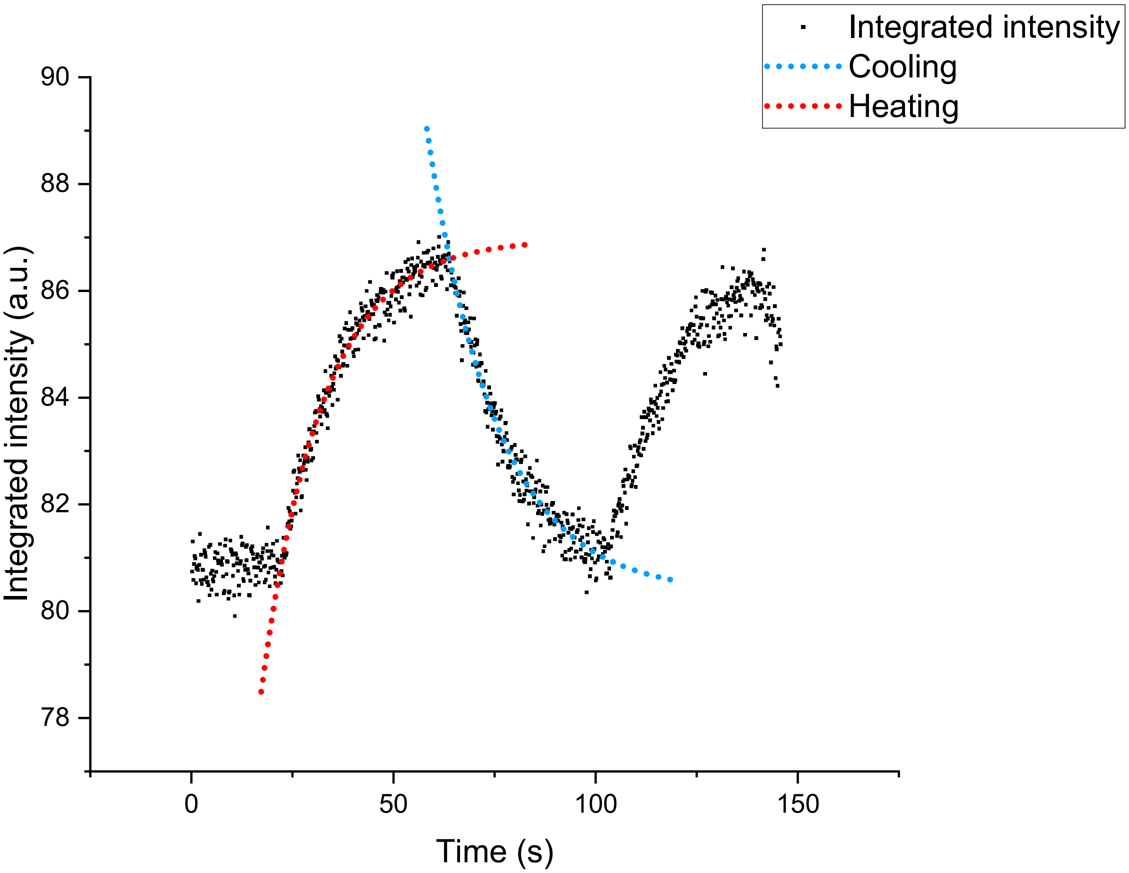

Figure 13 Fitting of the thermal response of the cell #4 with two exponential, for the swelling and cooling of the membrane.

Lastly, Figure 14 reports the signal measured with the silicon filter added again to the measurement, and the resulting combination (silicon, PE or PTFE, and bandpass filter) could block off or reduce almost all of the Globar radiation apart from the 5 THz bands. The optical measurement revealed how the cells were still responding to the radiation with a discernible signal, but the intensity of the response was lower than before and the response less reproducible.

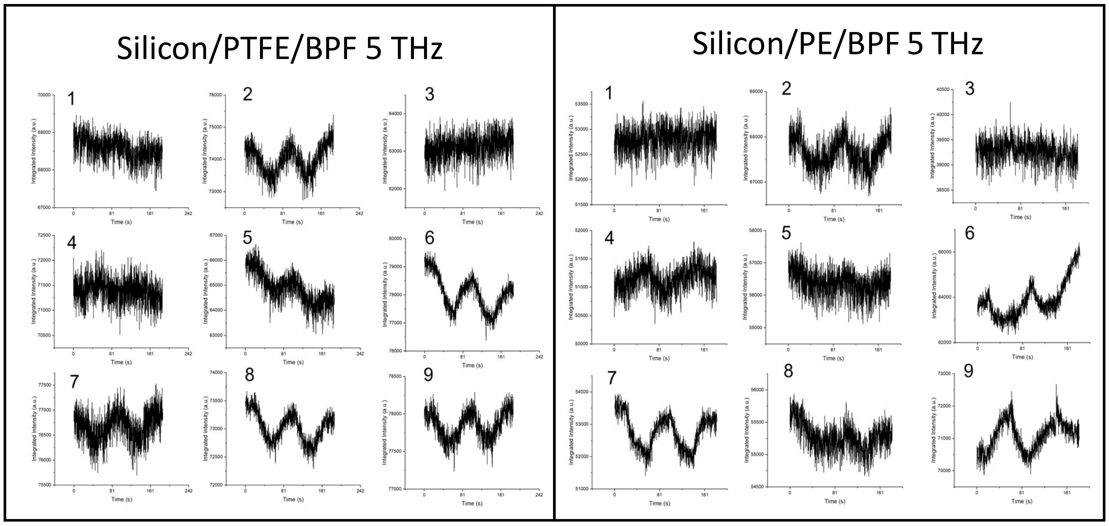

Silicon/PTFE/BPF 5 THz

Silicon/PE/BPF 5 THz

Figure 14 Response of the membranes under the presence of silicon, polymeric, and bandpass filters. The filtering reduced almost all the frequencies outside the 5 THz but most of the membranes were still able to detect a signal (albeit weak).

Time-Response of the array

To measure how fast our system was able to respond to the radiation, a chopper was added to the optical setup in place of the shutter. With the use of the chopper, the Globar source was intermittently emitted at frequencies of 0.5 and 1 Hz to understand the response of our system to the relatively fast variation (compared to the cycles used before of 20 and 40 seconds) of the Globar intensity. A first test was used to identify the time required by the system to reach thermal equilibrium at 1 Hz to avoid variables such as the signal increase over time, which would have added a nonlinear background due to the membrane heating, and could have interfered with the measured signal during the transient. The filter applied were the silicon and PE filter, which resulted in a broadband THz spectrum incident on the sample. This test demonstrated that after 60±5 s the system reached a stable deflection of the membrane, having reached its peak as shown in the signal measured from the sealed cell of Figure 15.

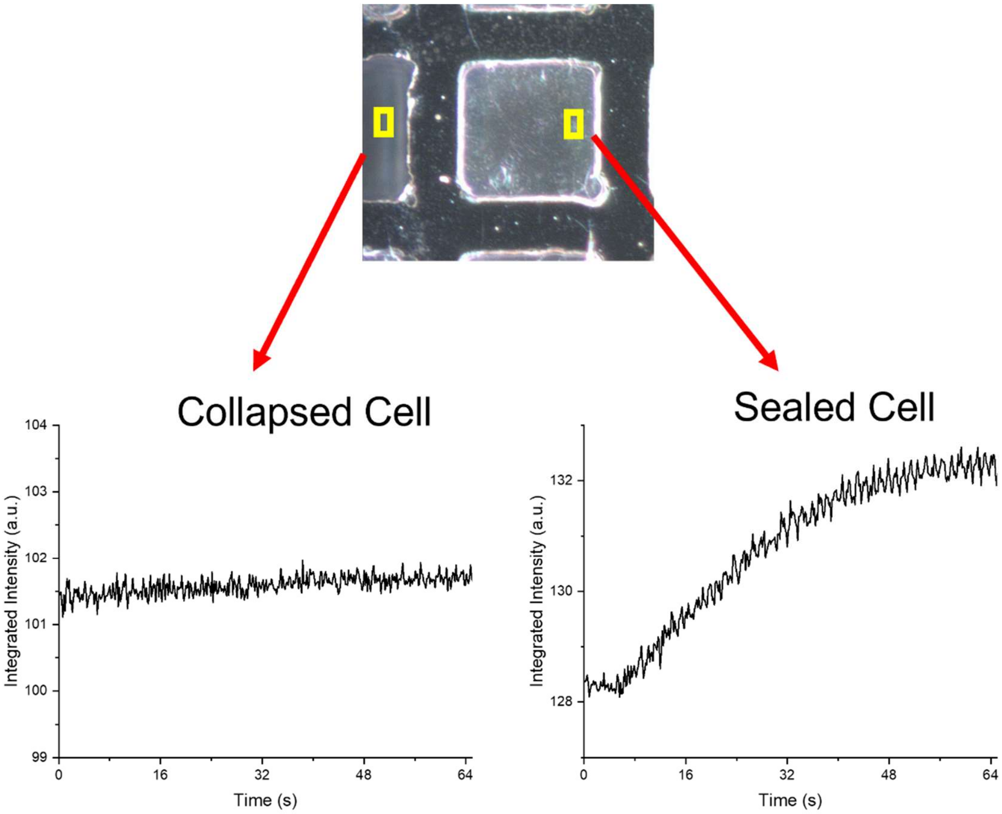

Figure 15 Calibration test to ensure the thermal equilibrium of the cells under intermittent irradiation of the sample.

After the equilibrium test, the array was kept for 65 seconds under irradiation at 1 Hz and 0.5 Hz to reach the equilibrium temperature and was measured for 16 seconds using a collapsed cell as a reference for the background noise. The results illustrated in Figure 16 show that the thermal response measured for both 1 Hz and 0.5 Hz was easily distinguishable compared to the noise reference, albeit close to the limits of the optical setup used for the measure. The limits were imposed by the need to keep the illumination low enough to not create itself a temperature drift, which in turn required relatively long exposure to capture frames of sufficient signal-to-noise, and consequently limited the frames-per-second captured to 6.25 FPS. The measured signal was then analyzed with a Fast Fourier Transform (FFT) as shown in Figure 17, confirming the equivalence of the frequencies of the measured signal and the chopper.

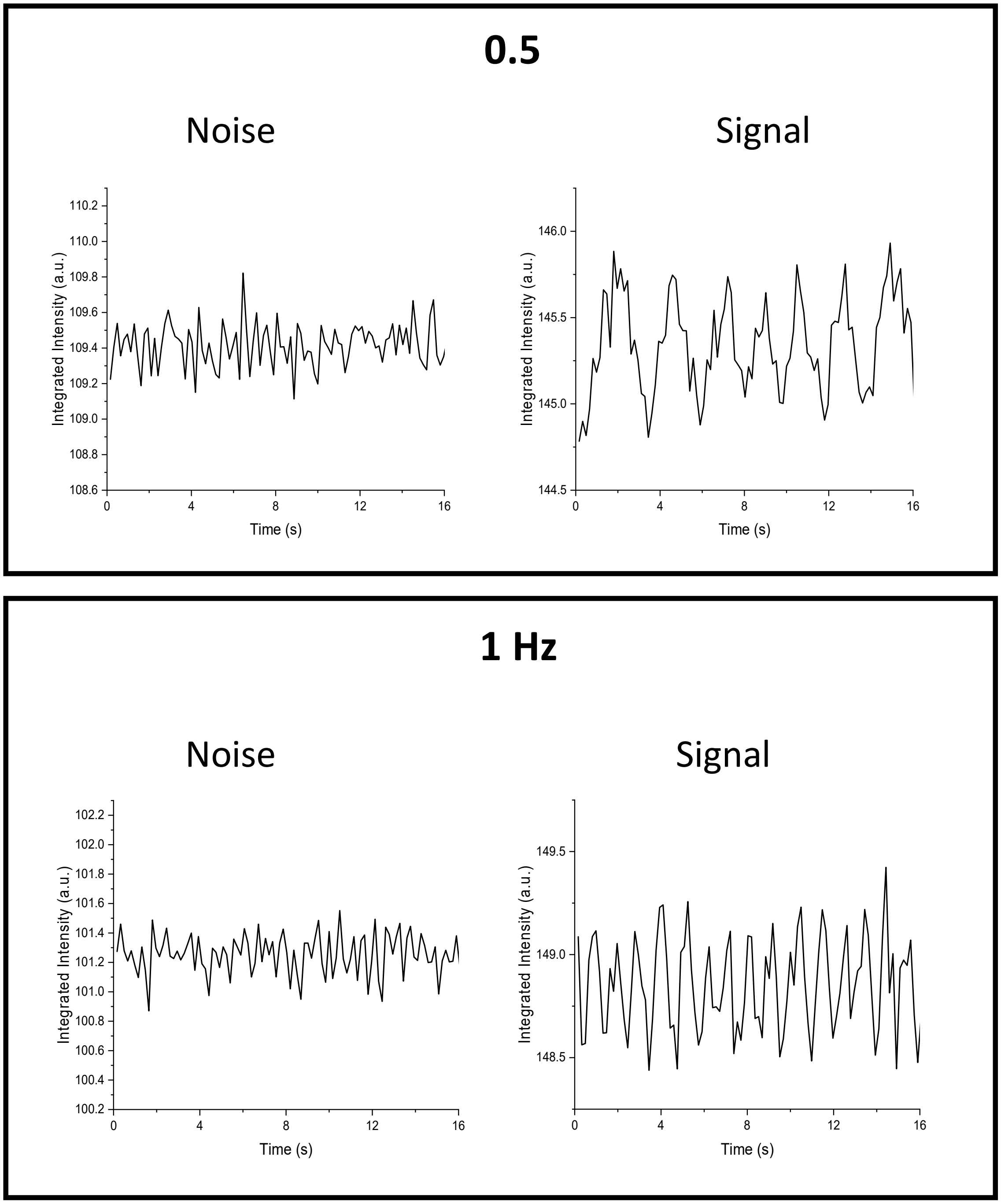

Figure 16 Response of the Golay cell to an intermittent globar irradiation. Compared to the reference noise, the clear signal indicates the movement of the membrane to a fast changing THz emission.

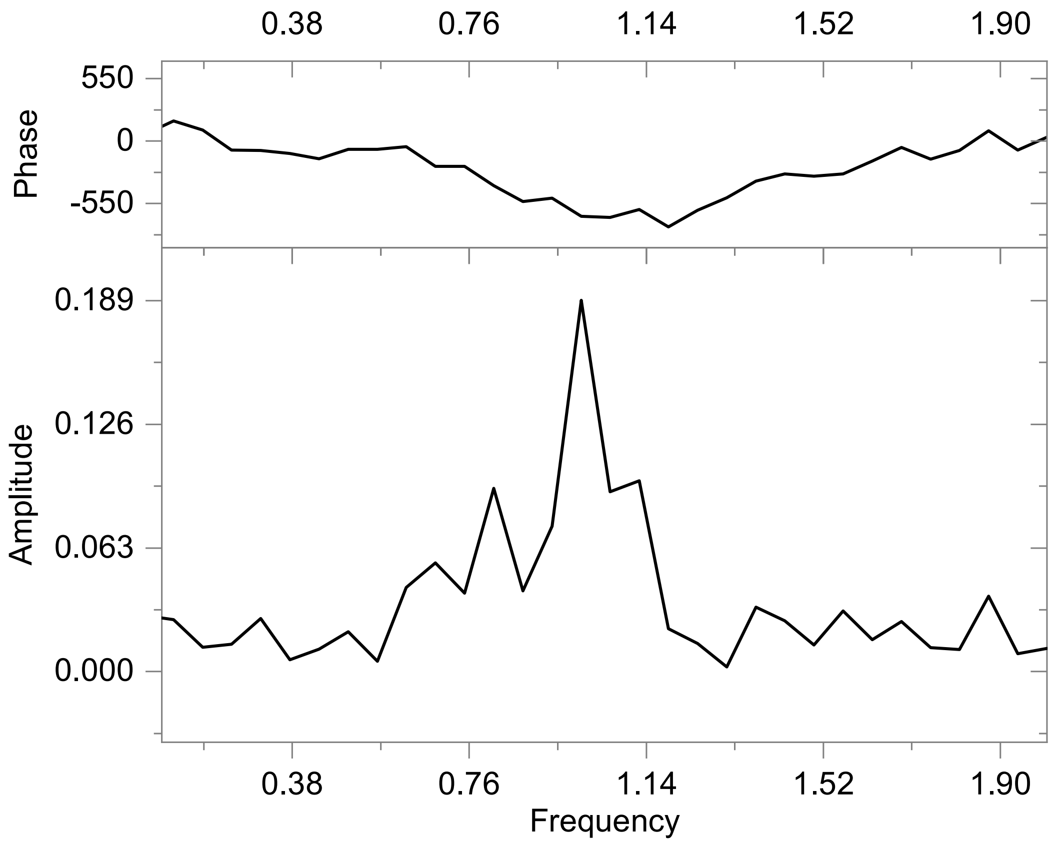

Figure 17 Applying a Fast Fourier Transform (FFT) to the 1Hz chopper signal highlighted and confirmed the frequency of the signal measured by the membrane.

The Golay cell array tested in this chapter demonstrated the ability to detect the THz radiation coming from the Globar source filter with 3 different filters. The system proposed is still afflicted by many uncertainties, like the manual selection of the ROI used for the experiment, or the variability of the response between each cell. This variability in particular was affected by both the membrane differences (and corrugations) between each cell, as well as other structural properties (i.e. wall thickness, distance from the border of the silicon bulk wafer etc.). Another element not considered in this chapter was the true absorbance of the single cell, as we supposed that only the umid air inside was absorbing and heating, without considering the absortion of the graphene layer, the titanium (especially is transparency or reflectivity towards THz radiation) and the silicon grid. Nonetheless, the signal was present in all the combinations of filters tested, even when only a fraction of the emitted radiation was allowed through the filters as shown in Figure 14. The detection of such weak intensity demonstrates the potential of this system for the THz detection using micromachined Golay cells with the ultrathin bilayered membranes.

Conclusions

A Golay cell and its main components can be described as a *cavity* that contains an *absorber* that converts the radiation to heat, *sealed* with a flexible *membrane*. When the radiation increases the temperature of the *gas* inside the cavity, the *membrane* deflects under the raising pressure and a *detection system* quantifies the deflection. In this thesis, I've designed, fabricated, developed, and characterized in particular the membrane and the sealed cavity required to produce an effective array of micromachined Golay cells capable of detecting the terahertz radiation.

Starting from a brief presentation of the potential of both the THz radiation and the graphene, I have discussed and tackled the problems correlated to these two new emerging topics. In chapter 3 I investigated the production and development of membranes thinner than 10 nm, but capable of freestanding over suspended areas of 2500 μm^2. These composite membranes showed the ability to go beyond the limitations imposed on the monoatomic graphene, being suspended over areas larger than the mean grain size of graphene. Their mechanical properties were characterized with atomic force microscopy, revealing a large variability in their response which presented irregular behaviors ascribed to the large corrugation induced by the high-temperature Ti deposition. Furthermore, this peculiar stressed structure presented high flexibility due to the higher real surface area, allowing large deflection in response to small pressure variations, which can be successfully applied to the design of high sensitivity Golay cells.

The membranes were also characterized with XPS revealing full oxidation of the Ti layer and in chapter 4 I explored the possibility to improve the membrane towards better electron transparency, with the graphene taking on the part of transparent windows. To improve such membranes, a simple UV lithography process was added, patterning the titanium layer. The grid pattern proposed was again characterized with the AFM and XPS, however, compared to the previous membrane, its properties were remarkably different. The XPS analysis revealed the electron transparency of the graphene when compared to the control membranes of full titanium, however, the photoemission was attenuated by an order of magnitude compared to the control plasma-treated patterned membrane. Furthermore, this attenuation of the photoemission was also observed in the signal coming from the titanium surface, indicating that most of the influence on the photoemission can be attributed to surface contamination. This surface contamination was also witnessed in high magnification SEM images of the membrane, aiding in finding the semi-transparent graphene windows by focusing on the contaminations suspended on the intact graphene membranes. From the AFM characterizations instead, the mechanical properties were demonstrated to be uniform and reproducible, as the thermal stress of the titanium deposition was released along the geometrical axis defined by the micropattern geometry, and, as a consequence, the mechanical response was much smoother than before.

Parallel to the development of the membranes, the substrate for the membrane was also improved, resulting in the fabrication of a strong grid with passing-through holes. This design was chosen for its high efficiency of transfer of the membrane, however, required a secondary sealing step for the sealing of the wells covered by the membrane which was implemented with a silicone rubber cork. This secondary sealing involved a simple fabrication process and an easy application and brings large benefits to the overall process of fabricating air- and water-tight micromachined cavities. Indeed, thanks to this additional step, the yield of coverage of the arrays was very high compared to closed-wells designs, which on the contrary presented an almost complete collapse of the membranes, and the weak interactions between the silicon and silicone allowed for a re-usable system thanks to the easily detachable silicone cork. Moreover, the soft silicone proved very efficient in the sealing of the membranes even in the presence of the non-negligible surface roughness introduced during the fabrication of the arrays. The sealed arrays were then tested with a custom sample holder that indirectly applied pressure to each cell of the array, revealing their independent and uniform response to pressure variations. Indeed, in the presence of membrane collapses or damage, the adjacent membranes were not affected and were independently responding demonstrating the advantage of higher tolerances when both fabricating and handling such devices. The mechanical robustness and the sealing efficiency of single membranes were characterized with the same sample holder, instead, the pressure was directly applied to the membranes without the silicone rubber. The membranes were capable of withstanding up to 0.4 bar of constant pressure without any leakage for up to ten minutes, confirming the airtightness of the system and its strong mechanical properties. The same membranes were tested for their response to pressure variation induced by temperature changes by sealing them with a polymeric adhesive and using a Peltier element to create a temperature variation. The resulting system showed a rapid response of the membranes later followed by relaxation at a constant temperature which may have been caused by the inefficient sealing compared to the silicon rubber. The membranes showed a high deflection under both direct pressure (up to 5 μm) and thermal-induced pressure (up to 3 μm) and a Raman characterization of the graphene layer confirmed that this large deflection was caused by the tensing of the corrugation instead of deformation of the membrane.

In the last part, the arrays sealed with the membranes on top and the silicone cork from the bottom were finally tested as Golay cells using the air inside the cells as absorber which expanded under the radiation of a Globar source. This source, composed of a heated silicon carbide rod, is a blackbody emitter with peak emission in the infrared. Thanks to its low cost and compact design it is one of the most used sources of infrared and THz radiation. A series of the filter were alternated before the sample, filtering the visible and infrared allowing only the passage of THz radiation, and an optical microscope in darkfield configuration was used to measure the variation in the membrane under irradiation. The cells showed a non-linear response to the THz, slowly heating and distending the corrugation under the increasing pressure. Albeit slow in their response due to the thermal process of the air absorbing the radiation, increasing in temperature, and expanding, the sealed cells showed a clear response even with all the filters applied, thus detecting only the 5 THz band emitted by the Globar. These results were obtained with only the use of ambient air as an absorber, however, the contribution of the graphene membrane (a material capable of broad absorption even in the THz region) was not investigated. Indeed using solid absorbers in the cells, such as carbon black, carbon nanotubes or even increasing the number of layers of graphene, (all materials that showed a high absorption coefficient from THz to the visible in literature) may drastically improve the responsivity of the sensor to the radiation. Other absorbers for future improvement of the Golay cells may be in either gaseous or liquid form like liquid water of gas molecule that present vibration modes in the THz region (such as CH_3, CH_2F_2, or CH_3OH). Furthermore, all of these absorbers may be changed at will by refilling the cellsthrough the detachment of the cork at the bottom and the unsealing of the arrays, thus allowing for a tunable and more sensitive response at certain wavelengths. Nonetheless, even in this simple design, the thermal response proved sensitive enough to detect fast variations in the source radiation, detecting a 1 Hz signal generated by the filtered Globar with an optical chopper and demonstrating the fundamental potential of the system.

This work proposes an alternative approach to the fast and sensitive detection of THz radiation. Among the most relevant results obtained, the potential of the composite ultrathin membranes was demonstrated and applied towards better and enhanced radiation detectors as well as cells for XPS *in-operando* experiments. These membranes proved to be strong and flexible enough to efficiently seal micro-scale volumes, presenting high deflection with an elastic behavior, and their patterning opened their use towards electron spectroscopies thanks to the enhanced electron transparency. The development of the substrate in conjunction with the membrane allowed for the creation of a re-sealable system, easy to fabricate and simple to use, increasing the potential of the micromachined cells and completing the creation of the arrays of Golay cells. Finally, these cells were tested under irradiation, showing the ability to detect the weak THz radiation coming from a filtered globar source. Yet several further improvements to the membrane and substrate can be identified: the use of multilayer graphene instead of a single layer, or the use of an alternating structure of graphene and metals; the development of a more stable, strong, adaptable microfabricated grid, or even a change in the pattern of the metal grid are only a few of the option available to continue the development of this technology. Indeed, increasing the number of graphene layers as well as fabricating alternated layers of thinner membranes could allow an even greater synergy between the titanium and the graphene, increasing the mechanical properties of the membranes and their absorption in the THz band. Another solution towards a stronger membrane could be the testing different metals, searching for the optimal interaction between the carbon membrane and the reinforcing layer. The microfabricated grid also constitutes a fundamental part of the system, and further work could aim at optimizing the structure for faster response time or increased sensibility, by varying the volume and shape of the cells. Finally, introducing different patterns such as honeycomb or hexagonal grids would allow the optimization of the strength and stress distribution, for an increased control on the membrane shape and corrugation, and thus better deflections while preserving the transparency of graphene towards electrons. All of these future paths for the further improvement of the arrays discussed in this thesis, reaffirm again the potential development of the Golay cells and this work could be a promising starting point towards a new generation of thermal radiation detectors based on 2D materials and micromachining techniques.

References

[1] C. Sirtori, “Applied physics: Bridge for the terahertz gap,” *Nature*, vol. 417, no. 6885. Nature Publishing Group, pp. 132–133, May 09, 2002, doi: 10.1038/417132b.

[2] A. Y. Pawar, D. D. Sonawane, K. B. Erande, and D. V. Derle, “Terahertz technology and its applications,” *Drug Invention Today*, vol. 5, no. 2. pp. 157–163, 2013, doi: 10.1016/j.dit.2013.03.009.

[3] R. Köhler *et al.*, “Terahertz semiconductor-heterostructure laser,” *Nature*, vol. 417, pp. 156–159, 2002, doi: 10.1038/417156a.

[4] L. Mahler, A. Tredicucci, and M. S. Vitiello, “Quantum cascade laser: A compact, low cost, solid-state source for plasma diagnostics,” *J. Instrum.*, 2012, doi: 10.1088/1748-0221/7/02/C02018.

[5] S. Rout and S. Sonkusale, “Introduction,” *Act. Metamaterials*, pp. 1–25, 2017, doi: 10.1007/978-3-319-52219-7_1.

[6] A. W. M. Lee, Q. Qin, S. Kumar, B. S. Williams, Q. Hu, and J. L. Reno, “Real-time terahertz imaging over a standoff distance (>25 meters),” *Appl. Phys. Lett.*, vol. 89, no. 14, p. 141125, Oct. 2006, doi: 10.1063/1.2360210.

[7] D. M. Mittleman, R. H. Jacobsen, R. Neelamani, R. G. Baraniuk, and M. C. Nuss, “Gas sensing using terahertz time-domain spectroscopy,” *Appl. Phys. B Lasers Opt.*, vol. 67, no. 3, pp. 379–390, 1998, doi: 10.1007/s003400050520.

[8] N. J. J. van Hoof, S. E. T. ter Huurne, J. G. Rivas, and A. Halpin, “Time-resolved terahertz time-domain near-field microscopy,” *Opt. Express*, vol. 26, no. 24, p. 32118, Nov. 2018, doi: 10.1364/oe.26.032118.

[9] C. Janke, M. Först, M. Nagel, H. Kurz, and A. Bartels, “Asynchronous optical sampling for high-speed characterization of integrated resonant terahertz sensors,” *Opt. Lett.*, vol. 30, no. 11, p. 1405, Jun. 2005, doi: 10.1364/ol.30.001405.

[10] N. Karpowicz, H. Zhong, J. Xu, K. I. Lin, J. S. Hwang, and X. C. Zhang, “Comparison between pulsed terahertz time-domain imaging and continuous wave terahertz imaging,” *Semicond. Sci. Technol.*, vol. 20, no. 7, Jul. 2005, doi: 10.1088/0268-1242/20/7/021.

[11] N. Karpowicz *et al.*, “Compact continuous-wave subterahertz system for inspection applications,” *Appl. Phys. Lett.*, vol. 86, no. 5, pp. 1–3, Jan. 2005, doi: 10.1063/1.1856701.

[12] A. Pashkin, P. Kuel, J. Petzelt, B. Gorshunov, and M. Dressel, “Time-resolved and backward-wave oscillator submillimetre spectroscopy of some ferroelectric ceramics and thin films,” in *Ferroelectrics*, Jan. 2002, vol. 272, pp. 219–224, doi: 10.1080/00150190211560.

[13] R. M. Woodward *et al.*, “Terahertz pulse imaging of ex vivo basal cell carcinoma,” *J. Invest. Dermatol.*, vol. 120, no. 1, pp. 72–78, 2003, doi: 10.1046/j.1523-1747.2003.12013.x.

[14] C. Hoberg, P. Balzerowski, and M. Havenith, “Integration of a rapid scanning technique into THz time-domain spectrometers for nonlinear THz spectroscopy measurements,” *AIP Adv.*, vol. 9, no. 3, p. 035348, Mar. 2019, doi: 10.1063/1.5080653.

[15] J. Shan *et al.*, “Single-shot measurement of terahertz electromagnetic pulses by use of electro-optic sampling,” *Opt. Lett.*, vol. 25, no. 6, p. 426, Mar. 2000, doi: 10.1364/ol.25.000426.

[16] T. Buzug, “Computed tomography: From photon statistics to modern cone-beam CT,” *Comput. Tomogr. From Phot. Stat. to Mod. Cone-Beam CT*, pp. 1–521, 2008, doi: 10.1007/978-3-540-39408-2.

[17] A. C. Kak and M. Slaney, “Principles of Computerized Tomographic Imaging,” *Princ. Comput. Tomogr. Imaging*, Jan. 2001, doi: 10.1137/1.9780898719277.

[18] M. Naftaly and R. E. Miles, “Terahertz time-domain spectroscopy for material characterization,” *Proc. IEEE*, vol. 95, no. 8, pp. 1658–1665, 2007, doi: 10.1109/JPROC.2007.898835.

[19] J. W. Handley, A. J. Fitzgerald, E. Berry, and R. D. Boyle, “Wavelet compression in medical terahertz pulsed imaging,” *Phys. Med. Biol.*, vol. 47, no. 21, pp. 3885–3892, Nov. 2002, doi: 10.1088/0031-9155/47/21/328.

[20] R. M. Woodward *et al.*, “Terahertz pulse imaging in reflection geometry of human skin cancer and skin tissue,” *Phys. Med. Biol.*, vol. 47, no. 21, pp. 3853–3863, Nov. 2002, doi: 10.1088/0031-9155/47/21/325.

[21] M. Koch, S. Hunsche, P. Schuacher, M. C. Nuss, J. Feldmann, and J. Fromm, “THz-imaging: A new method for density mapping of wood,” *Wood Science and Technology*, 1998. https://www.biologie.uni-hamburg.de/en/forschung/oekologie-biologische-ressourcen/holzbio/personen/mitarbeiter/fromm/publikationen/koch-1998.html (accessed Nov. 20, 2021).

[22] X. Yin, B. W. H. Ng, B. Ferguson, and D. Abbott, “Wavelet based local tomographic image using terahertz techniques,” *Digit. Signal Process. A Rev. J.*, vol. 19, no. 4, pp. 750–763, Jul. 2009, doi: 10.1016/j.dsp.2008.06.009.

[23] L. Young, V. V. Prabhu, E. W. Prohofsky, and G. S. Edwards, “Prediction of modes with dominant base roll and propeller twist in B-DNA poly(dA)-poly(dT),” *Phys. Rev. A*, vol. 41, no. 12, pp. 7020–7023, 1990, doi: 10.1103/PhysRevA.41.7020.

[24] P. H. Siegel, “Terahertz technology in biology and medicine,” *IEEE MTT-S Int. Microw. Symp. Dig.*, vol. 3, pp. 1575–1578, 2004, doi: 10.1109/mwsym.2004.1338880.

[25] Y. Ulgen and M. Sezdi, “Electrical parameters of human blood,” pp. 2983–2986, Nov. 2002, doi: 10.1109/iembs.1998.746117.

[26] D. Mittleman, “Sensing with Terahertz Radiation,” vol. 85, p. 337, 2010, doi: 10.1007/978-3-540-45601-8.

[27] E. Pickwell-MacPherson, Q. Sun, and J. Wang, “Terahertz in vivo skin imaging,” *Opt. InfoBase Conf. Pap.*, p. TuF1, Apr. 2018, doi: 10.1364/isuptw.2018.tuf1.

[28] T. Bowman *et al.*, “Pulsed terahertz imaging of breast cancer in freshly excised murine tumors,” *J. Biomed. Opt.*, vol. 23, no. 02, p. 1, Feb. 2018, doi: 10.1117/1.jbo.23.2.026004.

[29] D. A. Crawley *et al.*, “Terahertz pulse imaging: A pilot study of potential applications in dentistry,” *Caries Res.*, vol. 37, no. 5, pp. 352–359, Sep. 2003, doi: 10.1159/000072167.

[30] B. Ferguson, S. Wang, D. Gray, D. Abbott, and X. C. Zhang, “Towards functional 3D T-ray imaging,” *Phys. Med. Biol.*, vol. 47, no. 21, pp. 3735–3742, Oct. 2002, doi: 10.1088/0031-9155/47/21/309.

[31] T. Bowman, A. Walter, O. Shenderova, N. Nunn, G. M. Guire, and M. El-Shenawee, “A phantom study of terahertz spectroscopy and imaging of micro- and nano-diamonds and nano-onions as contrast agents for breast cancer,” *Biomed. Phys. Eng. Express*, vol. 3, no. 5, p. 055001, Sep. 2017, doi: 10.1088/2057-1976/aa87c2.

[32] J. O. Seung *et al.*, “Nanoparticle contrast agents for terahertz medical imaging,” 2008, doi: 10.1109/ICIMW.2008.4665813.

[33] B. Chakraborty, R. Sen, and A. K. Mandal, “A Survey on Machine Learning Techniques for THz Image Analysis,” *Terahertz Biomed. Healthc. Technol.*, pp. 167–176, Jan. 2020, doi: 10.1016/b978-0-12-818556-8.00009-4.

[34] H. Park and J. H. Son, “Machine learning techniques for thz imaging and time-domain spectroscopy,” *Sensors (Switzerland)*, vol. 21, no. 4, pp. 1–25, Feb. 2021, doi: 10.3390/s21041186.

[35] S. Zhong, “Progress in terahertz nondestructive testing: A review,” *Front. Mech. Eng.*, vol. 14, no. 3, pp. 273–281, Sep. 2019, doi: 10.1007/s11465-018-0495-9.

[36] V. P. Wallace, E. MacPherson, J. A. Zeitler, and C. Reid, “Three-dimensional imaging of optically opaque materials using nonionizing terahertz radiation,” *J. Opt. Soc. Am. A*, vol. 25, no. 12, p. 3120, Dec. 2008, doi: 10.1364/josaa.25.003120.

[37] J. Yang, S. C. Ruan, M. Zhang, and W. Zhang, “Real-time continuous-wave imaging with a 1.63THz OPTL and a pyroelectric camera,” *Optoelectron. Lett.*, vol. 4, no. 4, pp. 295–298, Sep. 2008, doi: 10.1007/s11801-008-8036-0.

[38] M. Tani, M. Herrmann, and K. Sakai, “Generation and detection of terahertz pulsed radiation with photoconductive antennas and its application to imaging,” *Meas. Sci. Technol.*, vol. 13, no. 11, pp. 1739–1745, 2002, doi: 10.1088/0957-0233/13/11/310.

[39] A. Dobroiu, C. Otani, and K. Kawase, “Terahertz-wave sources and imaging applications,” *Meas. Sci. Technol.*, vol. 17, no. 11, Nov. 2006, doi: 10.1088/0957-0233/17/11/R01.

[40] I. Duling and D. Zimdars, “Terahertz imaging: Revealing hidden defects,” *Nat. Photonics*, vol. 3, no. 11, pp. 630–632, Nov. 2009, doi: 10.1038/nphoton.2009.206.

[41] Y. Hirakawa *et al.*, “Nondestructive evaluation of rubber compounds by terahertz time-domain spectroscopy,” *J. Infrared, Millimeter, Terahertz Waves*, vol. 32, no. 12, pp. 1457–1463, Sep. 2011, doi: 10.1007/s10762-011-9832-3.

[42] T. Chady and P. Lopato, “Testing of glass-fiber reinforced composite materials using terahertz technique,” *Int. J. Appl. Electromagn. Mech.*, vol. 33, no. 3–4, pp. 1599–1605, Jan. 2010, doi: 10.3233/JAE-2010-1290.

[43] A. Anbarasu, “Characterization of Defects in Fiber Composites Using Terahertz Imaging,” *Analysis*, no. August, Jun. 2008, Accessed: Nov. 20, 2021. [Online]. Available: https://smartech.gatech.edu/handle/1853/24632.

[44] A. J. Fitzgerald, B. E. Cole, and P. F. Taday, “Nondestructive analysis of tablet coating thicknesses using Terahertz pulsed imaging,” *J. Pharm. Sci.*, vol. 94, no. 1, pp. 177–183, Jan. 2005, doi: 10.1002/jps.20225.

[45] J. A. Zeitler, Y. Shen, C. Baker, P. F. Taday, M. Pepper, and T. Rades, "Analysis of coating structures and interfaces in solid oral dosage forms by three dimensional terahertz pulsed imaging," *J. Pharm. Sci.*, vol. 96, no. 2, pp. 330–340, 2007, doi: 10.1002/jps.20789.

[46] R. K. May *et al.*, "Terahertz in-line sensor for direct coating thickness measurement of individual tablets during film coating in real-time," *J. Pharm. Sci.*, vol. 100, no. 4, pp. 1535–1544, 2011, doi: 10.1002/jps.22359.

[47] T. Yasui, T. Yasuda, K. I. Sawanaka, and T. Araki, "Terahertz paintmeter for noncontact monitoring of thickness and drying progress in paint film," *Appl. Opt.*, vol. 44, no. 32, pp. 6849–6856, Nov. 2005, doi: 10.1364/AO.44.006849.

[48] K. Su, Y. C. Shen, and J. A. Zeitler, "Terahertz sensor for non-contact thickness and quality measurement of automobile paints of varying complexity," *IEEE Trans. Terahertz Sci. Technol.*, vol. 4, no. 4, pp. 432–439, 2014, doi: 10.1109/TTHZ.2014.2325393.

[49] D. J. Cook, S. J. Sharpe, S. Lee, and M. G. Allen, "Terahertz time domain measurements of marine paint thickness," in *Optics InfoBase Conference Papers*, Mar. 2007, p. TuB5, doi: 10.1364/otst.2007.tub5.

[50] T. Fukuchi *et al.*, "Topcoat thickness measurement of thermal barrier coating of gas turbine blade using terahertz wave," *Electr. Eng. Japan (English Transl. Denki Gakkai Ronbunshi)*, vol. 189, no. 1, pp. 1–8, Oct. 2014, doi: 10.1002/eej.22624.

[51] C.-C. Chen, D.-J. Lee, T. Pollock, and J. F. Whitaker, "Pulsed-terahertz reflectometry for health monitoring of ceramic thermal barrier coatings," *Opt. Express*, vol. 18, no. 4, p. 3477, Feb. 2010, doi: 10.1364/oe.18.003477.

[52] R. Burger *et al.*, "Thz-tds reflection measurement of coating thicknesses at non-perpendicular incidence: experiment and simulation," *Sensors*, vol. 21, no. 10, May 2021, doi: 10.3390/s21103473.

[53] H. S. Kim, D. W. Park, G. H. Oh, and H. S. Kim, "Non-destructive evaluation of cement hydration with pulsed and continuous Terahertz electro-magnetic waves," *Opt. Lasers Eng.*, vol. 138, p. 106414, Mar. 2021, doi: 10.1016/j.optlaseng.2020.106414.

[54] I. Kemp, M. Peterson, C. Benton, and D. T. Petkie, "Sub-mm wave imaging techniques for non-destructive aerospace materials evaluation," *Natl. Aerosp. Electron. Conf. Proc. IEEE*, pp. 166–168, 2009, doi: 10.1109/NAECON.2009.5426634.

[55] N. Karpowicz, D. Dawes, M. J. Perry, and X.-C. Zhang, "Fire damage on carbon fiber materials characterized by THz waves," *Terahertz Mil. Secur. Appl. IV*, vol. 6212, p. 62120G, May 2006, doi: 10.1117/12.665852.

[56] C. D. Stoik, M. J. Bohn, and J. L. Blackshire, "Nondestructive evaluation of aircraft composites using transmissive terahertz time domain spectroscopy," *Opt. Express*, vol. 16, no. 21, p. 17039, Oct. 2008, doi: 10.1364/oe.16.017039.

[57] J. F. Federici *et al.*, "THz imaging and sensing for security applications - Explosives, weapons and drugs," *Semicond. Sci. Technol.*, vol. 20, no. 7, Jul. 2005, doi: 10.1088/0268-1242/20/7/018.

[58] C. A. Martin, S. E. Clark, J. A. Lovberg, and V. G. Kolinko, "Passive millimeter-wave imaging technology for phased-array systems," in *Passive Millimeter-Wave Imaging Technology VI and Radar Sensor Technology VII*, Aug. 2003, vol. 5077, p. 33, doi: 10.1117/12.488732.

[59] D. Zimdars and J. S. White, "Terahertz reflection imaging for package and personnel inspection," in *Terahertz for Military and Security Applications II*, Sep. 2004, vol. 5411, p. 78, doi: 10.1117/12.562216.

[60] W. R. Tribe, D. A. Newnham, P. F. Taday, and M. C. Kemp, "Hidden object detection: security applications of terahertz technology," in *Terahertz and Gigahertz Electronics and Photonics III*, Apr. 2004, vol. 5354, p. 168, doi: 10.1117/12.543049.

[61] M. B. Campbell and E. J. Heilweil, "Noninvasive detection of weapons of mass destruction using terahertz radiation," in *Terahertz for Military and Security Applications*, Jul. 2003, vol. 5070, p. 38, doi: 10.1117/12.504297.

[62] K. Kawase, Y. Ogawa, Y. Watanabe, and H. Inoue, "Non-destructive terahertz imaging of illicit drugs using spectral fingerprints," *Opt. Express*, vol. 11, no. 20, p. 2549, Oct. 2003, doi: 10.1364/oe.11.002549.

[63] G. Tzydynzhapov, P. Gusikhin, V. Muravev, A. Dremin, Y. Nefyodov, and I. Kukushkin, "New Real-Time Sub-Terahertz Security Body Scanner," *J. Infrared, Millimeter, Terahertz Waves*, vol. 41, no. 6, pp. 632–641, Mar. 2020, doi: 10.1007/s10762-020-00683-5.

[64] F. Huang *et al.*, "Terahertz study of 1,3,5-trinitro-s-triazine by time-domain and Fourier transform infrared spectroscopy," *Appl. Phys. Lett.*, vol. 85, no. 23, pp. 5535–5537, Dec. 2004, doi: 10.1063/1.1829793.

[65] D. J. Cook, B. K. Decker, G. Maislin, and M. G. Allen, "Through container THz sensing: applications for explosives screening," in *Terahertz and Gigahertz Electronics and Photonics III*, Apr. 2004, vol. 5354, p. 55, doi: 10.1117/12.525466.

[66] A. Bandyopadhyay, A. Sengupta, R. B. Barat, D. E. Gary, and J. F. Federici, "Grain size dependent scattering studies of common materials using THz time domain techniques," *Terahertz Gigahertz Electron. Photonics V*, vol. 6120, p. 61200H, Mar. 2006, doi: 10.1117/12.647868.

[67] S. K. Mathanker, P. R. Weckler, and N. Wang, "Terahertz (THZ) applications in food and agriculture: A review," *Trans. ASABE*, vol. 56, no. 3, pp. 1213–1226, 2013, doi: 10.13031/trans.56.9390.

[68] T. Suzuki, Y. Ogawa, and N. Kondo, "Application of THz spectroscopy to pesticide detection," *IRMMW-THz 2010 - 35th Int. Conf. Infrared, Millimeter, Terahertz Waves, Conf. Guid.*, 2010, doi: 10.1109/ICIMW.2010.5612606.

[69] Y. Hua and H. Zhang, "Qualitative and quantitative detection of pesticides with terahertz time-domain spectroscopy," *IEEE Trans. Microw. Theory Tech.*, vol. 58, no. 7 PART 2, pp. 2064–2070, Jul. 2010, doi: 10.1109/TMTT.2010.2050184.

[70] Y. Cui, K. Mu, X. Wang, Y. Zhang, and C. Zhang, "Measurement of mixtures of melamine using THz ray," in *International Symposium on Photoelectronic Detection and Imaging 2009: Terahertz and High Energy Radiation Detection Technologies and Applications*, Aug. 2009, vol. 7385, p. 73851E, doi: 10.1117/12.835293.

[71] A. Redo-Sanchez *et al.*, "Assessment of terahertz spectroscopy to detect antibiotic residues in food and feed matrices," *Analyst*, vol. 136, no. 8, pp. 1733–1738, Mar. 2011, doi: 10.1039/c0an01016b.

[72] H. Yoneyama, M. Yamashita, S. Kasai, H. Ito, and T. Ouchi, "Application of terahertz spectrum in the detection of harmful food additives," *IRMMW-THz2007 - Conf. Dig. Jt. 32nd Int. Conf. Infrared Millimetre Waves, 15th Int. Conf. Terahertz Electron.*, pp. 281–282, 2007, doi: 10.1109/icimw.2007.4516498.

[73] U. Møller, H. Merbold, J. R. Folkenberg, and P. U. Jepsen, "Determination of alcohol- and sugar concentration in aqueous solutions using reflection terahertz time-domain spectroscopy," *IRMMW-THz2007 - Conf. Dig. Jt. 32nd Int. Conf. Infrared Millimetre Waves, 15th Int. Conf. Terahertz Electron.*, pp. 289–290, 2007, doi: 10.1109/icimw.2007.4516502.

[74] U. Møller, J. R. Folkenberg, and P. U. Jepsen, "Dielectric properties of water in butter and water-AOT-heptane systems measured using terahertz time-domain spectroscopy," *Appl. Spectrosc.*, vol. 64, no. 9, pp. 1028–1036, Sep. 2010, doi: 10.1366/000370210792434422.

[75] B. S. Y. Ung, B. W. H. Ng, and D. Abbott, "A preliminary study of hydrogenation of oils using terahertz time domain spectroscopy," *IRMMW-THz 2010 - 35th Int. Conf. Infrared, Millimeter, Terahertz Waves, Conf. Guid.*, 2010, doi: 10.1109/ICIMW.2010.5612480.

[76] P. Parasoglou *et al.*, "Quantitative moisture content detection in food wafers," *34th Int. Conf. Infrared, Millimeter, Terahertz Waves, IRMMW-THz 2009*, 2009, doi: 10.1109/ICIMW.2009.5324623.

[77] Y. K. Lee, S. W. Choi, S. T. Han, D. H. Woo, and H. S. Chun, "Detection of foreign bodies in foods using continuous wave terahertz imaging," *J. Food Prot.*, vol. 75, no. 1, pp. 179–183, Jan. 2012, doi: 10.4315/0362-028X.JFP-11-181.

[78] C. Jördens, "Detection of foreign bodies in chocolate with pulsed terahertz spectroscopy," *Opt. Eng.*, vol. 47, no. 3, p. 037003, Mar. 2008, doi: 10.1117/1.2896597.

[79] J. F. Federici, R. L. Wample, D. Rodriguez, and S. Mukherjee, "Application of terahertz Gouy phase shift from curved surfaces for estimation of crop yield," *Appl. Opt.*, vol. 48, no. 7, pp. 1382–1388, Mar. 2009, doi: 10.1364/AO.48.001382.

[80] T. May *et al.*, "Passive stand-off terahertz imaging with 1 hertz frame rate," in *Terahertz for Military and Security Applications VI*, Apr. 2008, vol. 6949, p. 69490C, doi: 10.1117/12.777952.

[81] S. Fathololoumi *et al.*, "Terahertz quantum cascade lasers operating up to ∼ 200 K with optimized oscillator strength and improved injection tunneling," *Opt. Express*, vol. 20, no. 4, p. 3866, Feb. 2012, doi: 10.1364/oe.20.003866.

[82] J. Hesler, R. Prasankumar, and J. Tignon, "Advances in terahertz solid-state physics and devices," *J. Appl. Phys.*, vol. 126, no. 11, p. 110401, Sep. 2019, doi: 10.1063/1.5122975.

[83] J. A. Fülöp, S. Tzortzakis, and T. Kampfrath, "Laser-Driven Strong-Field Terahertz Sources," *Adv. Opt. Mater.*, vol. 8, no. 3, p. 1900681, Feb. 2020, doi: 10.1002/adom.201900681.

[84] M. Y. Glyavin, A. N. Kuftin, V. N. Manuilov, A. S. Sedov, V. E. Zapevalov, and A. I. Tsvetkov, "Development of THz Gyrotron with improved parameters in IAP RAS," *Prog. Electromagn. Res. Symp.*, vol. 2017-Novem, pp. 1454–1456, Nov. 2017, doi: 10.1109/PIERS-FALL.2017.8293359.

[85] P. Tan, J. Huang, K. F. Liu, Y. Q. Xiong, and M. W. Fan, "Terahertz radiation sources based on free electron lasers and their applications," *Science China Information Sciences*, vol. 55, no. 1. Springer, pp. 1–15, Dec. 30, 2012, doi: 10.1007/s11432-011-4515-1.

[86] J. H. Seok *et al.*, “High-Density Organic Electro-Optic Crystals for Ultra-Broadband THz Spectroscopy,” *Adv. Opt. Mater.*, vol. 9, no. 17, p. 2100618, Sep. 2021, doi: 10.1002/adom.202100618.

[87] N. M. Burford and M. O. El-Shenawee, “Review of terahertz photoconductive antenna technology,” *Opt. Eng.*, vol. 56, no. 1, p. 010901, Jan. 2017, doi: 10.1117/1.oe.56.1.010901.

[88] “Gunn diodes | TeraSense.” https://terasense.com/terahertz-technology/gunn-diodes/ (accessed Jan. 16, 2022).

[89] “What is Slot Antenna? Working and Applications of Slot Antenna - Electronics Desk.” https://electronicsdesk.com/impatt-diode.html (accessed Jan. 16, 2022).

[90] M. Feiginov, C. Sydlo, O. Cojocari, and P. Meissner, “Resonant-tunnelling diodes for THz applications,” in *Terahertz Emitters, Receivers, and Applications III*, Oct. 2012, vol. 8496, p. 84960A, doi: 10.1117/12.930490.

[91] “Far-infrared laser - Wikipedia.” https://en.wikipedia.org/wiki/Far-infrared_laser (accessed Jan. 17, 2022).

[92] C. O. Sullivan and J. A. Murphy, *Terahertz Sources , Detectors , and Optics*. .

[93] J. N. Hovenier *et al.*, “The p-Ge terahertz laser-properties under pulsed-and mode-locked operation,” *IEEE Trans. Microw. Theory Tech.*, vol. 48, pp. 670–676, 2000, doi: 10.1109/22.841958.

[94] “Guide to QCL Microscopy | Bruker.” https://www.bruker.com/en/products-and-solutions/infrared-and-raman/ft-ir-microscopes/what-is-QCL-microscopy.html (accessed Jan. 17, 2022).

[95] “The Quantum Cascade Laser – Quantum Optoelectronics Group | ETH Zurich.” https://qoe.ethz.ch/Tutorials/quantum_cascade_laser.html (accessed Jan. 17, 2022).

[96] F. Capasso, “Quantum cascade lasers,” in *Conference on Lasers and Electro-Optics Europe - Technical Digest*, 2000, p. 277, doi: 10.1201/b18634-13.

[97] Lightsources.org, “Light sources of the world - Lightsources.org,” 2021. https://lightsources.org/lightsources-of-the-world/ (accessed Jan. 17, 2022).

[98] “How does a synchrotron radiation source work?” https://photon-science.desy.de/research/students__teaching/primers/synchrotron_radiation/index_eng.html (accessed Jan. 14, 2022).

[99] F. Simoens, “Thz bolometer detectors,” *Springer Ser. Opt. Sci.*, vol. 173, pp. 35–75, 2014, doi: 10.1007/978-94-007-3837-9_2.

[100] V. Desmaris, H. Rashid, A. Pavolotsky, and V. Belitsky, “Design, simulations and optimization of micromachined Golay-cell based THz sensors operating at room temperature,” *Procedia Chem.*, vol. 1, no. 1, pp. 1175–1178, Sep. 2009, doi: 10.1016/j.proche.2009.07.293.

[101] J. Yang, X. Gong, and Y. Zhang, “Research of an infrared pyroelectric sensor based THz detector and its application in CW THz imaging,” in *International Symposium on Photoelectronic Detection and Imaging 2009: Terahertz and High Energy Radiation Detection Technologies and Applications*, Aug. 2009, vol. 7385, p. 738521, doi: 10.1117/12.832753.

[102] A. Maestrini *et al.*, “Multiplicateurs de fréquences et mélangeurs THz utilisant des diodes Schottky,” *Comptes Rendus Phys.*, vol. 11, no. 7–8, pp. 480–495, Aug. 2010, doi: 10.1016/j.crhy.2010.05.002.

[103] A. G. U. Perera, G. Ariyawansa, P. V. V. Jayaweera, S. G. Matsik, M. Buchanan, and H. C. Liu, “Semiconductor terahertz detectors and absorption enhancement using plasmons,” *Microelectronics J.*, vol. 39, no. 3–4, pp. 601–606, Mar. 2008, doi: 10.1016/j.mejo.2007.07.086.

[104] S. Pirro and P. Mauskopf, “Advances in Bolometer Technology for Fundamental Physics,” *Annual Review of Nuclear and Particle Science*, vol. 67. Annual Reviews, pp. 161–181, Oct. 19, 2017, doi: 10.1146/annurev-nucl-101916-123130.

[105] L. Vicarelli, A. Tredicucci, and A. Pitanti, “Micromechanical bolometers for sub-Terahertz detection at room temperature,” *http://arxiv.org/abs/2107.12170*, Jul. 2021, Accessed: Jan. 18, 2022. [Online]. Available: https://arxiv.org/abs/2107.12170v1.

[106] X. Du, D. E. Prober, H. Vora, and C. B. Mckitterick, “Graphene-based Bolometers,” *Graphene 2D Mater.*, vol. 1, no. 1, May 2014, doi: 10.2478/gpe-2014-0001.

[107] T. E. Sensor, “Transition Edge Sensor Bolometers,” pp. 38–57.

[108] A. Stockhausen, “Band 008 Optimization of Hot-Electron Bolometers for THz Radiation.”

[109] “Nová stránka 2.” http://www.studentportal.wz.cz/seminare/ped.htm (accessed Jan. 19, 2022).

[110] O. V. Minin, J. Calvo-Gallego, Y. M. Meziani, and I. V. Minin, “Improvement of an infrared pyroelectric detector performances in thz range using the terajet effect,” *Appl. Sci.*, vol. 11, no. 15, p. 7011, Jul. 2021, doi: 10.3390/app11157011.

[111] M. J. E. Golay, “Radiation detecting device,” *M. J. E. GOLAY*, vol. 2, pp. 1–11, Sep. 1951, Accessed: Nov. 28, 2021. [Online]. Available: https://patents.google.com/patent/US2557096.

[112] “Cella di carico - Wikipedia.” https://it.wikipedia.org/wiki/Cella_di_carico (accessed Nov. 29, 2021).

[113] “TYDEX Golay Detectors.” http://www.tydexoptics.com/products/thz_devices/golay_cell/#GC-1P (accessed Nov. 29, 2021).

[114] P. S. Stefanova, J. M. Hammler, A. K. Klein, A. J. Gallant, and C. Balocco, “Polymer-based micro-golay cells for THz detection,” *Int. Conf. Infrared, Millimeter, Terahertz Waves, IRMMW-THz*, vol. 2016-Novem, Nov. 2016, doi: 10.1109/IRMMW-THz.2016.7758964.

[115] E. Ledwosinska, T. Szkopek, A. Guermoune, and M. Siaj, “Application of graphene membrane in micro-Golay cell array,” in *Terahertz Technology and Applications V*, Feb. 2012, vol. 8261, p. 82610A, doi: 10.1117/12.914054.

[116] “Schottky barrier - Wikipedia.” https://en.wikipedia.org/wiki/Schottky_barrier (accessed Jan. 14, 2022).

[117] Electronic, “Schottky Diode or Schottky Barrier Semiconductor Diode,” *Https://Www.Electronics-Tutorials.Ws/Diode/Schottky-Diode.Html*, 2020. https://www.electronics-tutorials.ws/diode/schottky-diode.html (accessed Jan. 19, 2022).

[118] I. Mehdi, J. V. Siles, C. Lee, and E. Schlecht, “THz diode technology: Status, prospects, and applications,” *Proc. IEEE*, vol. 105, no. 6, pp. 990–1007, Jun. 2017, doi: 10.1109/JPROC.2017.2650235.

[119] T. Fukuchi, N. Fuse, T. Fujii, M. Okada, K. Fukunaga, and M. Mizuno, “Measurement of topcoat thickness of thermal barrier coating for gas turbines using terahertz waves,” *Electr. Eng. Japan (English Transl. Denki Gakkai Ronbunshi)*, vol. 183, no. 4, pp. 1–9, Jun. 2013, doi: 10.1002/eej.22385.

[120] D. R. Bacon, J. Madéo, and K. M. Dani, “Photoconductive emitters for pulsed terahertz generation,” *J. Opt. (United Kingdom)*, vol. 23, no. 6, p. 064001, Apr. 2021, doi: 10.1088/2040-8986/abf6ba.

[121] “Terahertz photoconductive antennas: Principles and applications | IEEE Conference Publication | IEEE Xplore.” https://ieeexplore.ieee.org/document/5782295 (accessed Jan. 19, 2022).

[122] V. K. Khanna, “Photoconductive antennas and photomixers,” *Pract. Terahertz Electron. Devices Appl. Vol. 2*, Dec. 2021, doi: 10.1088/978-0-7503-4886-7ch3.

[123] H. P. Boehm, R. Setton, and E. Stumpp, “Nomenclature and terminology of graphite intercalation compounds,” *Carbon*, vol. 24, no. 2. pp. 241–245, 1986, doi: 10.1016/0008-6223(86)90126-0.

[124] H. P. Boehm, R. Setton, and E. Stumpp, “International union of pure and applied chemistry inorganic chemistry division commission on high temperature and solid state chemistry* nomenclature and terminology of graphite intercalation compounds,” *Pure Appl. Chem.*, vol. 66, no. 9, pp. 1893–1901, 1994, doi: 10.1351/pac199466091893.

[125] K. S. Novoselov *et al.*, “Electric field in atomically thin carbon films,” *Science (80-.).*, vol. 306, no. 5696, pp. 666–669, Oct. 2004, doi: 10.1126/science.1102896.

[126] K. Ariga, M. Li, G. J. Richards, and J. P. Hill, “Nanoarchitectonics: A conceptual paradigm for design and synthesis of dimension-controlled functional nanomaterials,” in *Journal of Nanoscience and Nanotechnology*, 2011, vol. 11, no. 1, pp. 1–13, doi: 10.1166/jnn.2011.3839.

[127] X. Sun *et al.*, “Tuning the self-assembly of oligothiophenes on chemical vapor deposition graphene: Effect of functional group, solvent, and substrate,” *Chem. - An Asian J.*, vol. 9, no. 7, pp. 1888–1894, 2014, doi: 10.1002/asia.201402075.

[128] H. Zhang, H. F. Yin, K. B. Zhang, and J. H. Lin, “Progress of surface plasmon research based on time-dependent density functional theory,” *Wuli Xuebao/Acta Phys. Sin.*, vol. 64, no. 7, 2015, doi: 10.7498/aps.64.077303.

[129] D. H. Shin, S. W. Seo, J. M. Kim, H. S. Lee, and S. H. Choi, “Graphene transparent conductive electrodes doped with graphene quantum dots-mixed silver nanowires for highly-flexible organic solar cells,” *J. Alloys Compd.*, vol. 744, pp. 1–6, 2018, doi: 10.1016/j.jallcom.2018.02.069.

[130] S. Goenka, V. Sant, and S. Sant, “Graphene-based nanomaterials for drug delivery and tissue engineering,” *Journal of Controlled Release*, vol. 173, no. 1. pp. 75–88, 2014, doi: 10.1016/j.jconrel.2013.10.017.

[131] C. S. Casari and A. Milani, “Carbyne: From the elusive allotrope to stable carbon atom wires,” *MRS Commun.*, vol. 8, no. 2, pp. 207–219, 2018, doi: 10.1557/mrc.2018.48.

[132] K. Takai, S. Tsujimura, and M. Inagaki, *Graphene: Preparations, properties, applications, and prospects*. 2019.

[133] Z. Chen, C. Molina-Jirón, S. Klyatskaya, F. Klappenberger, and M. Ruben, “1D and 2D Graphdiynes: Recent Advances on the Synthesis at Interfaces and Potential Nanotechnological Applications,” *Ann. Phys.*, vol. 529, no. 11, p. 1700056, Nov. 2017, doi: 10.1002/andp.201700056.

[134] Z. Zhang, L. H. Klausen, M. Chen, and M. Dong, “Electroactive Scaffolds for Neurogenesis and Myogenesis: Graphene-Based Nanomaterials,” *Small*, vol. 14, no. 48, Nov. 2018, doi: 10.1002/smll.201801983.

[135] J. Kim, L. J. Cote, F. Kim, W. Yuan, K. R. Shull, and J. Huang, “Graphene oxide sheets at interfaces,” *J. Am. Chem. Soc.*, vol. 132, no. 23, pp. 8180–8186, 2010, doi: 10.1021/ja102777p.

[136] F. Kim, L. J. Cote, and J. Huang, “Graphene oxide: Surface activity and two-dimensional assembly,” *Adv. Mater.*, vol. 22, no. 17, pp. 1954–1958, 2010, doi: 10.1002/adma.200903932.

[137] S. Raval, “Ultrafast Pump-Probe spectroscopy of Graphene Oxide (GO) and Reduced Graphene Oxide (RGO),” 2018. https://www.researchgate.net/publication/328571850_Ultrafast_Pump-Probe_spectroscopy_of_Graphene_Oxide_GO_and_Reduced_Graphene_Oxide_RGO (accessed Nov. 30, 2021).

[138] S. S. Shams, R. Zhang, and J. Zhu, “Graphene synthesis: A Review,” *Mater. Sci. Pol.*, vol. 33, no. 3, pp. 566–578, Sep. 2015, doi: 10.1515/msp-2015-0079.

[139] A. Martinez, K. Fuse, and S. Yamashita, “Mechanical exfoliation of graphene for the passive mode-locking of fiber lasers,” *Appl. Phys. Lett.*, vol. 99, no. 12, p. 121107, Sep. 2011, doi: 10.1063/1.3641419.

[140] W. Dai *et al.*, “Superior field emission performance of graphene/carbon nanofilament hybrids synthesized by electrochemical self-exfoliation,” *Mater. Lett.*, vol. 205, pp. 223–225, Oct. 2017, doi: 10.1016/j.matlet.2017.06.022.

[141] I. Y. Jeon *et al.*, “Edge-carboxylated graphene nanosheets via ball milling,” *Proc. Natl. Acad. Sci. U. S. A.*, vol. 109, no. 15, pp. 5588–5593, Apr. 2012, doi: 10.1073/pnas.1116897109.

[142] Z. Lin, P. S. Karthik, M. Hada, T. Nishikawa, and Y. Hayashi, “Simple technique of exfoliation and dispersion of multilayer graphene from natural graphite by ozone-assisted sonication,” *Nanomaterials*, vol. 7, no. 6, Jun. 2017, doi: 10.3390/nano7060125.

[143] M. R. Habib, T. Liang, X. Yu, X. Pi, Y. Liu, and M. Xu, “A review of theoretical study of graphene chemical vapor deposition synthesis on metals: Nucleation, growth, and the role of hydrogen and oxygen,” *Reports Prog. Phys.*, vol. 81, no. 3, p. 036501, Jan. 2018, doi: 10.1088/1361-6633/aa9bbf.

[144] S. Forti *et al.*, “Electronic properties of single-layer tungsten disulfide on epitaxial graphene on silicon carbide,” *Nanoscale*, vol. 9, no. 42, pp. 16412–16419, Nov. 2017, doi: 10.1039/c7nr05495e.

[145] S. Amini, J. Garay, G. Liu, A. A. Balandin, and R. Abbaschian, “Growth of large-area graphene films from metal-carbon melts,” *J. Appl. Phys.*, vol. 108, no. 9, Nov. 2010, doi: 10.1063/1.3498815.

[146] C. Trudeau, L. I. Dion-Bertrand, S. Mukherjee, R. Martel, and S. G. Cloutier, “Electrostatic deposition of large-surface graphene,” *Materials (Basel).*, vol. 11, no. 1, p. 116, Jan. 2018, doi: 10.3390/ma11010116.

[147] “First Graphene Transistor and Alfred Nobel’s Will at Nobel Museum Can Impress Anyone.” https://interestingengineering.com/first-graphene-transistor-and-alfred-nobels-will-at-nobel-museum-can-impress-anyone (accessed Nov. 30, 2021).

[148] O. A. Shenderova, V. V. Zhirnov, and D. W. Brenner, “Carbon nanostructures,” *Crit. Rev. Solid State Mater. Sci.*, vol. 27, no. 3–4, pp. 227–356, 2002, doi: 10.1080/10408430208500497.

[149] J. Sakamoto, J. Van Heijst, O. Lukin, and A. D. Schlüter, “Two-dimensional polymers: Just a dream of synthetic chemists?,” *Angew. Chemie - Int. Ed.*, vol. 48, no. 6, pp. 1030–1069, Jan. 2009, doi: 10.1002/anie.200801863.

[150] A. K. Geim and A. H. MacDonald, “Graphene: Exploring carbon flatland,” *Phys. Today*, vol. 60, no. 8, pp. 35–41, Aug. 2007, doi: 10.1063/1.2774096.

[151] B. Jayasena and S. Subbiah, “A novel mechanical cleavage method for synthesizing few-layer graphenes,” *Nanoscale Res. Lett.*, vol. 6, no. 1, pp. 1–7, Jan. 2011, doi: 10.1186/1556-276X-6-95.

[152] S. Wang, C. Wang, and X. Ji, “Towards understanding the salt-intercalation exfoliation of graphite into graphene,” *RSC Adv.*, vol. 7, no. 82, pp. 52252–52260, Nov. 2017, doi: 10.1039/c7ra07489a.

[153] S. Maruyama, T. Fukutsuka, K. Miyazaki, and T. Abe, “Observation of the intercalation of dimethyl sulfoxide-solvated lithium ion into graphite and decomposition of the ternary graphite intercalation compound using in situ Raman spectroscopy,” *Electrochim. Acta*, vol. 265, pp. 41–46, 2018, doi: 10.1016/j.electacta.2018.01.035.

[154] I. Ovsiienko *et al.*, “Magnetoresistance of graphite intercalated with cobalt,” *J. Mater. Sci.*, vol. 53, no. 1, pp. 716–

726, Aug. 2018, doi: 10.1007/s10853-017-1511-x.

[155] L. Poláková *et al.*, “Poly(meth)acrylate nanocomposite membranes containing in situ exfoliated graphene platelets: Synthesis, characterization and gas barrier properties,” *Eur. Polym. J.*, vol. 94, pp. 431–445, Sep. 2017, doi: 10.1016/j.eurpolymj.2017.07.033.

[156] I. Jeon, B. Yoon, M. He, and T. M. Swager, “Hyperstage Graphite: Electrochemical Synthesis and Spontaneous Reactive Exfoliation,” *Adv. Mater.*, vol. 30, no. 3, Jan. 2018, doi: 10.1002/adma.201704538.

[157] T. Rozmanowski and P. Krawczyk, “Influence of chemical exfoliation process on the activity of NiCl2-FeCl3-PdCl2-graphite intercalation compound towards methanol electrooxidation,” *Appl. Catal. B Environ.*, vol. 224, pp. 53–59, May 2018, doi: 10.1016/j.apcatb.2017.10.024.

[158] M. Horie, K. Takahashi, H. Nanao, and M. Shirai, “Selective hydrogenation of cinnamaldehyde over platinum nanosheets intercalated between graphite layers,” *J. Nanosci. Nanotechnol.*, vol. 18, no. 1, pp. 80–85, 2018, doi: 10.1166/jnn.2018.14612.

[159] G. Mittal, V. Dhand, K. Y. Rhee, S. J. Park, and W. R. Lee, “A review on carbon nanotubes and graphene as fillers in reinforced polymer nanocomposites,” *J. Ind. Eng. Chem.*, vol. 21, pp. 11–25, Jan. 2015, doi: 10.1016/j.jiec.2014.03.022.

[160] G. Brumfiel, “Graphene gets ready for the big time,” *Nature*, vol. 458, no. 7237, pp. 390–391, Mar. 2009, doi: 10.1038/458390a.

[161] L. Jiao, L. Zhang, X. Wang, G. Diankov, and H. Dai, “Narrow graphene nanoribbons from carbon nanotubes,” *Nature*, vol. 458, no. 7240, pp. 877–880, Apr. 2009, doi: 10.1038/nature07919.

[162] D. V. Kosynkin *et al.*, “Longitudinal unzipping of carbon nanotubes to form graphene nanoribbons,” *Nature*, vol. 458, no. 7240, pp. 872–876, Apr. 2009, doi: 10.1038/nature07872.

[163] J. Chen, L. Chen, Z. Zhang, J. Li, L. Wang, and W. Jiang, “Graphene layers produced from carbon nanotubes by friction,” *Carbon N. Y.*, vol. 50, no. 5, pp. 1934–1941, Apr. 2012, doi: 10.1016/j.carbon.2011.12.044.

[164] R. Verdejo, M. M. Bernal, L. J. Romasanta, and M. A. Lopez-Manchado, “Graphene filled polymer nanocomposites,” *J. Mater. Chem.*, vol. 21, no. 10, pp. 3301–3310, Feb. 2011, doi: 10.1039/c0jm02708a.

[165] N. I. Zaaba, K. L. Foo, U. Hashim, S. J. Tan, W. W. Liu, and C. H. Voon, “Synthesis of Graphene Oxide using Modified Hummers Method: Solvent Influence,” *Procedia Eng.*, vol. 184, pp. 469–477, Jan. 2017, doi: 10.1016/j.proeng.2017.04.118.

[166] S. Gurunathan, J. W. Han, V. Eppakayala, and J. H. Kim, “Green synthesis of graphene and its cytotoxic effects in human breast cancer cells,” *Int. J. Nanomedicine*, vol. 8, pp. 1015–1027, Mar. 2013, doi: 10.2147/IJN.S42047.

[167] S. Pei and H. M. Cheng, “The reduction of graphene oxide,” *Carbon N. Y.*, vol. 50, no. 9, pp. 3210–3228, Aug. 2012, doi: 10.1016/j.carbon.2011.11.010.

[168] S. Bhattacharjee, R. Joshi, A. A. Chughtai, and C. R. Macintyre, “Graphene Modified Multifunctional Personal Protective Clothing,” *Adv. Mater. Interfaces*, vol. 6, no. 21, Nov. 2019, doi: 10.1002/admi.201900622.

[169] V. Eswaraiah, S. S. Jyothirmayee Aravind, and S. Ramaprabhu, “Top down method for synthesis of highly conducting graphene by exfoliation of graphite oxide using focused solar radiation,” *J. Mater. Chem.*, vol. 21, no. 19, pp. 6800–6803, Apr. 2011, doi: 10.1039/c1jm10808e.

[170] B. Shen, D. Lu, W. Zhai, and W. Zheng, “Synthesis of graphene by low-temperature exfoliation and reduction of graphite oxide under ambient atmosphere,” *J. Mater. Chem. C*, vol. 1, no. 1, pp. 50–53, Nov. 2013, doi: 10.1039/c2tc00044j.

[171] K. Parvez *et al.*, “Electrochemically exfoliated graphene as solution-processable, highly conductive electrodes for organic electronics,” *ACS Nano*, vol. 7, no. 4, pp. 3598–3606, Apr. 2013, doi: 10.1021/nn400576v.

[172] J. Lu, J. X. Yang, J. Wang, A. Lim, S. Wang, and K. P. Loh, “One-pot synthesis of fluorescent carbon nanoribbons, nanoparticles, and graphene by the exfoliation of graphite in ionic liquids,” *ACS Nano*, vol. 3, no. 8, pp. 2367–2375, Aug. 2009, doi: 10.1021/nn900546b.

[173] Y. Hernandez *et al.*, “High-yield production of graphene by liquid-phase exfoliation of graphite,” *Nat. Nanotechnol.*, vol. 3, no. 9, pp. 563–568, Sep. 2008, doi: 10.1038/nnano.2008.215.

[174] V. Alzari *et al.*, “Graphene-containing thermoresponsive nanocomposite hydrogels of poly(N-isopropylacrylamide) prepared by frontal polymerization,” *J. Mater. Chem.*, vol. 21, no. 24, pp. 8727–8733, Jun. 2011, doi: 10.1039/c1jm11076d.

[175] D. Nuvoli *et al.*, “High concentration few-layer graphene sheets obtained by liquid phase exfoliation of graphite in

ionic liquid," *J. Mater. Chem.*, vol. 21, no. 10, pp. 3428–3431, Feb. 2011, doi: 10.1039/c0jm02461a.

[176] A. Ciesielski and P. Samorì, "Graphene via sonication assisted liquid-phase exfoliation," *Chem. Soc. Rev.*, vol. 43, no. 1, pp. 381–398, Dec. 2014, doi: 10.1039/c3cs60217f.

[177] Y. Xu, H. Bai, G. Lu, C. Li, and G. Shi, "Flexible graphene films via the filtration of water-soluble noncovalent functionalized graphene sheets," *J. Am. Chem. Soc.*, vol. 130, no. 18, pp. 5856–5857, May 2008, doi: 10.1021/ja800745y.

[178] R. Hao, W. Qian, L. Zhang, and Y. Hou, "Aqueous dispersions of TCNQ-anion-stabilized graphene sheets," *Chem. Commun.*, no. 48, pp. 6576–6578, Dec. 2008, doi: 10.1039/b816971c.

[179] A. J. Patil, J. L. Vickery, T. B. Scott, and S. Mann, "Aqueous stabilization and self-assembly of craphene sheets into layered bio-nanocomposites using DNA," *Adv. Mater.*, vol. 21, no. 31, pp. 3159–3164, Aug. 2009, doi: 10.1002/adma.200803633.

[180] Q. Su, S. Pang, V. Alijani, C. Li, X. Feng, and K. Müllen, "Composites of craphene with large aromatic molecules," *Adv. Mater.*, vol. 21, no. 31, pp. 3191–3195, Aug. 2009, doi: 10.1002/adma.200803808.

[181] S. J. Woltornist, A. J. Oyer, J. M. Y. Carrillo, A. V. Dobrynin, and D. H. Adamson, "Conductive thin films of pristine graphene by solvent interface trapping," *ACS Nano*, vol. 7, no. 8, pp. 7062–7066, Aug. 2013, doi: 10.1021/nn402371c.

[182] V. León *et al.*, "Few-layer graphenes from ball-milling of graphite with melamine," *Chem. Commun.*, vol. 47, no. 39, pp. 10936–10938, Sep. 2011, doi: 10.1039/c1cc14595a.

[183] M. Borah, M. Dahiya, S. Sharma, R. B. Mathur, and S. R. Dhakate, "Few Layer Graphene Derived from Wet Ball Milling of Expanded Graphite and Few Layer Graphene Based Polymer Composite," *Mater. Focus*, vol. 3, no. 4, pp. 300–309, Aug. 2014, doi: 10.1166/mat.2014.1185.

[184] D. Pan *et al.*, "Li storage properties of disordered graphene nanosheets," *Chem. Mater.*, vol. 21, no. 14, pp. 3136–3142, Jul. 2009, doi: 10.1021/cm900395k.

[185] M. F. El-Kady, V. Strong, S. Dubin, and R. B. Kaner, "Laser scribing of high-performance and flexible graphene-based electrochemical capacitors," *Science (80-.).*, vol. 335, no. 6074, pp. 1326–1330, Mar. 2012, doi: 10.1126/science.1216744.

[186] L. J. Cote, R. Cruz-Silva, and J. Huang, "Flash reduction and patterning of graphite oxide and its polymer composite," *J. Am. Chem. Soc.*, vol. 131, no. 31, pp. 11027–11032, Aug. 2009, doi: 10.1021/ja902348k.

[187] E. Gao, W. Wang, M. Shang, and J. Xu, "Synthesis and enhanced photocatalytic performance of graphene-Bi 2WO6 composite," *Phys. Chem. Chem. Phys.*, vol. 13, no. 7, pp. 2887–2893, Feb. 2011, doi: 10.1039/c0cp01749c.

[188] V. Abdelsayed, S. Moussa, H. M. Hassan, H. S. Aluri, M. M. Collinson, and M. S. El-Shall, "Photothermal deoxygenation of graphite oxide with laser excitation in solution and graphene-aided increase in water temperature," *J. Phys. Chem. Lett.*, vol. 1, no. 19, pp. 2804–2809, Oct. 2010, doi: 10.1021/jz1011143.

[189] C. Zhang, J. Zhang, K. Lin, and Y. Huang, "Laser-assisted chemical vapor deposition setup for fast synthesis of graphene patterns," *Rev. Sci. Instrum.*, vol. 88, no. 5, p. 053907, May 2017, doi: 10.1063/1.4984004.

[190] B. N. Chichkov, C. Momma, S. Nolte, F. Von Alvensleben, and A. Tünnermann, "Femtosecond, picosecond and nanosecond laser ablation of solids," *Appl. Phys. A Mater. Sci. Process.*, vol. 63, no. 2, pp. 109–115, 1996, doi: 10.1007/BF01567637.

[191] P. W. Sutter, J. I. Flege, and E. A. Sutter, "Epitaxial graphene on ruthenium," *Nat. Mater.*, vol. 7, no. 5, pp. 406–411, 2008, doi: 10.1038/nmat2166.

[192] I. Pletikosić *et al.*, "Dirac cones and minigaps for graphene on Ir(111)," *Phys. Rev. Lett.*, vol. 102, no. 5, p. 056808, Feb. 2009, doi: 10.1103/PhysRevLett.102.056808.

[193] K. S. Kim *et al.*, "Large-scale pattern growth of graphene films for stretchable transparent electrodes," *Nature*, vol. 457, no. 7230, pp. 706–710, Feb. 2009, doi: 10.1038/nature07719.

[194] J. K. Wassei *et al.*, "Chemical vapor deposition of graphene on copper from methane, ethane and propane: Evidence for bilayer selectivity," *Small*, vol. 8, no. 9, pp. 1415–1422, May 2012, doi: 10.1002/smll.201102276.

[195] P. Sutter, "Epitaxial graphene: How silicon leaves the scene," *Nat. Mater.*, vol. 8, no. 3, pp. 171–172, 2009, doi: 10.1038/nmat2392.

[196] W. Norimatsu and M. Kusunoki, "Epitaxial graphene on SiC{0001}: Advances and perspectives," *Phys. Chem. Chem. Phys.*, vol. 16, no. 8, pp. 3501–3511, Jan. 2014, doi: 10.1039/c3cp54523g.

[197] T. Ohta, A. Bostwick, J. L. McChesney, T. Seyller, K. Horn, and E. Rotenberg, "Interlayer interaction and electronic

screening in multilayer graphene investigated with angle-resolved photoemission spectroscopy," *Phys. Rev. Lett.*, vol. 98, no. 20, p. 206802, May 2007, doi: 10.1103/PhysRevLett.98.206802.

[198] H. Cao *et al.*, "Electronic transport in chemical vapor deposited graphene synthesized on Cu: Quantum Hall effect and weak localization," *Appl. Phys. Lett.*, vol. 96, no. 12, p. 122106, Mar. 2010, doi: 10.1063/1.3371684.

[199] J. Hass *et al.*, "Why multilayer graphene on 4H-SiC(000$\bar{1}$) behaves like a single sheet of graphene," *Phys. Rev. Lett.*, vol. 100, no. 12, p. 125504, Mar. 2008, doi: 10.1103/PhysRevLett.100.125504.

[200] A. Tzalenchuk *et al.*, "Towards a quantum resistance standard based on epitaxial graphene," *Nat. Nanotechnol.*, vol. 5, no. 3, pp. 186–189, Sep. 2010, doi: 10.1038/nnano.2009.474.

[201] S. V. Morozov *et al.*, "Strong suppression of weak localization in graphene," *Phys. Rev. Lett.*, vol. 97, no. 1, p. 016801, Jul. 2006, doi: 10.1103/PhysRevLett.97.016801.

[202] G. He, N. Srivastava, and R. M. Feenstra, "Formation of graphene on SiC(0001¯) surfaces in disilane and neon environments," *J. Vac. Sci. Technol. B, Nanotechnol. Microelectron. Mater. Process. Meas. Phenom.*, vol. 30, no. 4, p. 04E102, May 2012, doi: 10.1116/1.4718365.

[203] M. Saeed, Y. Alshammari, S. A. Majeed, and E. Al-Nasrallah, "Chemical Vapour Deposition of Graphene—Synthesis, Characterisation, and Applications: A Review," *Molecules*, vol. 25, no. 17. 2020, doi: 10.3390/molecules25173856.

[204] J. W. May, "Platinum surface LEED rings," *Surf. Sci.*, vol. 17, no. 1, pp. 267–270, Sep. 1969, doi: 10.1016/0039-6028(69)90227-1.

[205] A. Cabrero-Vilatela, R. S. Weatherup, P. Braeuninger-Weimer, S. Caneva, and S. Hofmann, "Towards a general growth model for graphene CVD on transition metal catalysts," *Nanoscale*, vol. 8, no. 4, pp. 2149–2158, Jan. 2016, doi: 10.1039/c5nr06873h.

[206] H. Ago, "CVD growth of high-quality single-layer graphene," *Front. Graphene Carbon Nanotub. Devices Appl.*, pp. 3–20, Jan. 2015, doi: 10.1007/978-4-431-55372-4_1.

[207] H. Liu and Y. Liu, "Controlled Chemical Synthesis in CVD Graphene," *Phys. Sci. Rev.*, vol. 2, no. 4, Apr. 2019, doi: 10.1515/psr-2016-0107.

[208] K. H, "Variation of Band Gap in Graphene Grown by Plasma Enhanced Chemical Vapor Deposition," *Ann. Chem. Sci. Res.*, vol. 2, no. 1, 2020, doi: 10.31031/acsr.2020.02.000529.

[209] J. Wang *et al.*, "Tailoring the grain size of bi-layer graphene by pulsed laser deposition," *Nanomaterials*, vol. 8, no. 11, Nov. 2018, doi: 10.3390/nano8110885.

[210] R. Zan and A. Altuntepe, "Nitrogen doping of graphene by CVD," *J. Mol. Struct.*, vol. 1199, p. 127026, Jan. 2020, doi: 10.1016/j.molstruc.2019.127026.

[211] A. K. Singh *et al.*, "Molecular n-doping of chemical vapor deposition grown graphene," *J. Mater. Chem.*, vol. 22, no. 30, pp. 15168–15174, Jul. 2012, doi: 10.1039/c2jm32716c.

[212] X. Li *et al.*, "Large-area synthesis of high-quality and uniform graphene films on copper foils," *Science (80-.).*, vol. 324, no. 5932, pp. 1312–1314, 2009, doi: 10.1126/science.1171245.

[213] S. V. Morozov *et al.*, "Giant intrinsic carrier mobilities in graphene and its bilayer," *Phys. Rev. Lett.*, vol. 100, no. 1, 2008, doi: 10.1103/PhysRevLett.100.016602.

[214] M. D. Stoller, S. Park, Z. Yanwu, J. An, and R. S. Ruoff, "Graphene-Based ultracapacitors," *Nano Lett.*, vol. 8, no. 10, pp. 3498–3502, 2008, doi: 10.1021/nl802558y.

[215] V. B. Mohan, R. Brown, K. Jayaraman, and D. Bhattacharyya, "Characterisation of reduced graphene oxide: Effects of reduction variables on electrical conductivity," *Mater. Sci. Eng. B Solid-State Mater. Adv. Technol.*, vol. 193, no. C, pp. 49–60, Mar. 2015, doi: 10.1016/j.mseb.2014.11.002.

[216] K. I. Bolotin *et al.*, "Ultrahigh electron mobility in suspended graphene," *Solid State Commun.*, vol. 146, no. 9–10, pp. 351–355, 2008, doi: 10.1016/j.ssc.2008.02.024.

[217] C. Lee, X. Wei, J. W. Kysar, and J. Hone, "Measurement of the elastic properties and intrinsic strength of monolayer graphene," *Science (80-.).*, vol. 321, no. 5887, pp. 385–388, 2008, doi: 10.1126/science.1157996.

[218] G. Van Lier, C. Van Alsenoy, V. Van Doren, and P. Geerlings, "Ab initio study of the elastic properties of single-walled carbon nanotubes and graphene," *Chem. Phys. Lett.*, vol. 326, no. 1–2, pp. 181–185, 2000, doi: 10.1016/S0009-2614(00)00764-8.

[219] R. Ramírez and C. P. Herrero, "Elastic properties and mechanical tension of graphene," *Phys. Rev. B*, vol. 95, no. 4,

2017, doi: 10.1103/PhysRevB.95.045423.

[220] K. V. Zakharchenko, M. I. Katsnelson, and A. Fasolino, “Finite temperature lattice properties of graphene beyond the quasiharmonic approximation,” *Phys. Rev. Lett.*, vol. 102, no. 4, 2009, doi: 10.1103/PhysRevLett.102.046808.

[221] I. S. Burmistrov, I. V. Gornyi, V. Y. Kachorovskii, M. I. Katsnelson, J. H. Los, and A. D. Mirlin, “Stress-controlled Poisson ratio of a crystalline membrane: Application to graphene,” *Phys. Rev. B*, vol. 97, no. 12, 2018, doi: 10.1103/PhysRevB.97.125402.

[222] P. Zhang *et al.*, “Fracture toughness of graphene,” *Nat. Commun.*, vol. 5, 2014, doi: 10.1038/ncomms4782.

[223] Z. Zhang *et al.*, “Crack Propagation and Fracture Toughness of Graphene Probed by Raman Spectroscopy,” *ACS Nano*, vol. 13, no. 9, pp. 10327–10332, 2019, doi: 10.1021/acsnano.9b03999.

[224] C. M. Almeida *et al.*, “Giant and tunable anisotropy of nanoscale friction in graphene,” *Sci. Rep.*, vol. 6, 2016, doi: 10.1038/srep31569.

[225] X. Zeng, Y. Peng, and H. Lang, “A novel approach to decrease friction of graphene,” *Carbon N. Y.*, vol. 118, pp. 233–240, 2017, doi: 10.1016/j.carbon.2017.03.042.

[226] Z. Chen and S. H. Kim, “Measuring nanoscale friction at graphene step edges,” *Friction*, vol. 8, no. 4, pp. 802–811, 2020, doi: 10.1007/s40544-019-0334-y.

[227] Y. Huang, J. Wu, and K. C. Hwang, “Thickness of graphene and single-wall carbon nanotubes,” *Phys. Rev. B - Condens. Matter Mater. Phys.*, vol. 74, no. 24, 2006, doi: 10.1103/PhysRevB.74.245413.

[228] X. Liu, *Nanomechanics of Graphene and Design of Graphene Composites*. 2019.

[229] O. L. Blakslee, D. G. Proctor, E. J. Seldin, G. B. Spence, and T. Weng, “Elastic constants of compression-annealed pyrolytic graphite,” *J. Appl. Phys.*, vol. 41, no. 8, pp. 3373–3382, Nov. 1970, doi: 10.1063/1.1659428.

[230] I. W. Frank, D. M. Tanenbaum, A. M. van der Zande, and P. L. McEuen, “Mechanical properties of suspended graphene sheets,” *J. Vac. Sci. Technol. B Microelectron. Nanom. Struct.*, vol. 25, no. 6, p. 2558, 2007, doi: 10.1116/1.2789446.

[231] M. M. Shokrieh and R. Rafiee, “Prediction of Young’s modulus of graphene sheets and carbon nanotubes using nanoscale continuum mechanics approach,” *Mater. Des.*, vol. 31, no. 2, pp. 790–795, 2010, doi: 10.1016/j.matdes.2009.07.058.

[232] M. Mir, M. Tahani, and B. Hassani, “Analytical prediction of Young’s modulus of carbon nanotubes using a variational method,” *Appl. Math. Model.*, vol. 45, pp. 1031–1043, 2017, doi: 10.1016/j.apm.2017.01.038.

[233] S. H. Sargsyan, “Discrete-Continuous and Continuous-Moment Models of Graphene under In-Plane Deformation,” *Phys. Mesomech.*, vol. 23, no. 4, pp. 309–315, Sep. 2020, doi: 10.1134/S1029959920040049.

[234] F. Liu, P. Ming, and J. Li, “Ab initio calculation of ideal strength and phonon instability of graphene under tension,” *Phys. Rev. B - Condens. Matter Mater. Phys.*, vol. 76, no. 6, 2007, doi: 10.1103/PhysRevB.76.064120.

[235] E. Konstantinova, S. O. Dantas, and P. M. V. B. Barone, “Electronic and elastic properties of two-dimensional carbon planes,” *Phys. Rev. B - Condens. Matter Mater. Phys.*, vol. 74, no. 3, 2006, doi: 10.1103/PhysRevB.74.035417.

[236] G. Cao, “Atomistic studies of mechanical properties of graphene,” *Polymers (Basel).*, vol. 6, no. 9, pp. 2404–2432, Sep. 2014, doi: 10.3390/polym6092404.

[237] J. H. Lee, P. E. Loya, J. Lou, and E. L. Thomas, “Dynamic mechanical behavior of multilayer graphene via supersonic projectile penetration,” *Science (80-.).*, vol. 346, no. 6213, pp. 1092–1096, 2014, doi: 10.1126/science.1258544.

[238] Y. Xue, Y. Liu, F. Lu, J. Qu, H. Chen, and L. Dai, “Functionalization of graphene oxide with polyhedral oligomeric silsesquioxane (POSS) for multifunctional applications,” *J. Phys. Chem. Lett.*, vol. 3, no. 12, pp. 1607–1612, 2012, doi: 10.1021/jz3005877.

[239] F. Taherian, V. Marcon, N. F. A. Van Der Vegt, and F. Leroy, “What is the contact angle of water on graphene?,” *Langmuir*, vol. 29, no. 5, pp. 1457–1465, 2013, doi: 10.1021/la304645w.

[240] C. Te Hsieh and W. Y. Chen, “Water/oil repellency and work of adhesion of liquid droplets on graphene oxide and graphene surfaces,” *Surf. Coatings Technol.*, vol. 205, no. 19, pp. 4554–4561, 2011, doi: 10.1016/j.surfcoat.2011.03.128.

[241] S. A. Hasan *et al.*, “Transferable graphene oxide films with tunable microstructures,” *ACS Nano*, vol. 4, no. 12, pp. 7367–7372, 2010, doi: 10.1021/nn102152x.

[242] K. Shinjo and M. Hirano, “Dynamics of friction: superlubric state,” *Surf. Sci.*, vol. 283, no. 1–3, pp. 473–478, 1993,

doi: 10.1016/0039-6028(93)91022-H.

[243] M. Hirano and K. Shinjo, “Superlubricity and frictional anisotropy,” *Wear*, vol. 168, no. 1–2, pp. 121–125, 1993, doi: 10.1016/0043-1648(93)90207-3.

[244] Q. Zheng *et al.*, “Self-retracting motion of graphite microflakes,” *Phys. Rev. Lett.*, vol. 100, no. 6, 2008, doi: 10.1103/PhysRevLett.100.067205.

[245] R. Zhang *et al.*, “Superlubricity in centimetres-long double-walled carbon nanotubes under ambient conditions,” *Nat. Nanotechnol.*, vol. 8, no. 12, pp. 912–916, 2013, doi: 10.1038/nnano.2013.217.

[246] J. Yang *et al.*, “Observation of high-speed microscale superlubricity in graphite,” *Phys. Rev. Lett.*, vol. 110, no. 25, 2013, doi: 10.1103/PhysRevLett.110.255504.

[247] Z. Liu *et al.*, “Observation of microscale superlubricity in graphite,” *Phys. Rev. Lett.*, vol. 108, no. 20, 2012, doi: 10.1103/PhysRevLett.108.205503.

[248] S. Berber, Y. K. Kwon, and D. Tománek, “Unusually high thermal conductivity of carbon nanotubes,” *Phys. Rev. Lett.*, vol. 84, no. 20, pp. 4613–4616, 2000, doi: 10.1103/PhysRevLett.84.4613.

[249] S. K. Jaćimovski, M. Bukurov, J. P. Šetrajčić, and D. I. Raković, “Phonon thermal conductivity of graphene,” *Superlattices Microstruct.*, vol. 88, pp. 330–337, 2015, doi: 10.1016/j.spmi.2015.09.027.

[250] K. M. F. Shahil and A. A. Balandin, “Thermal properties of graphene and multilayer graphene: Applications in thermal interface materials,” *Solid State Commun.*, vol. 152, no. 15, pp. 1331–1340, 2012, doi: 10.1016/j.ssc.2012.04.034.

[251] J. D. Renteria, D. L. Nika, and A. A. Balandin, “Graphene thermal properties: Applications in thermal management and energy storage,” *Applied Sciences (Switzerland)*, vol. 4, no. 4. pp. 525–547, 2014, doi: 10.3390/app4040525.

[252] D. L. Nika, E. P. Pokatilov, A. S. Askerov, and A. A. Balandin, “Phonon thermal conduction in graphene: Role of Umklapp and edge roughness scattering,” *Phys. Rev. B - Condens. Matter Mater. Phys.*, vol. 79, no. 15, 2009, doi: 10.1103/PhysRevB.79.155413.

[253] J. W. Jiang, J. Lan, J. S. Wang, and B. Li, “Isotopic effects on the thermal conductivity of graphene nanoribbons: Localization mechanism,” *J. Appl. Phys.*, vol. 107, no. 5, 2010, doi: 10.1063/1.3329541.

[254] D. J. Liu, S. M. Wang, and P. Yang, “Thermal property of graphene/silicon carbide heterostructure by molecular dynamics simulation,” *Wuli Xuebao/Acta Phys. Sin.*, vol. 70, no. 18, 2021, doi: 10.7498/aps.70.20210613.

[255] R. R. Nair *et al.*, “Fine structure constant defines visual transparency of graphene,” *Science (80-.).*, vol. 320, no. 5881, p. 1308, 2008, doi: 10.1126/science.1156965.

[256] A. Kumar, G. Sachdeva, R. Pandey, and S. P. Karna, “Optical absorbance in multilayer two-dimensional materials: Graphene and antimonene,” *Appl. Phys. Lett.*, vol. 116, no. 26, p. 263102, Jun. 2020, doi: 10.1063/5.0010794.

[257] G. Dunn *et al.*, “Graphene-Sealed Flow Cells for in Situ Transmission Electron Microscopy of Liquid Samples,” *ACS Nano*, vol. 14, no. 8, pp. 9637–9643, 2020, doi: 10.1021/acsnano.0c00431.

[258] N. Noh, J. Park, J. S. Park, K. Koo, J. Y. Park, and J. M. Yuk, “Lithographically patterned well-type graphene liquid cells with rational designs,” *Lab Chip*, vol. 20, no. 15, pp. 2796–2803, 2020, doi: 10.1039/d0lc00440e.

[259] H. Rasool, G. Dunn, A. Fathalizadeh, and A. Zettl, “Graphene-sealed Si/SiN cavities for high-resolution in situ electron microscopy of nano-confined solutions,” *Phys. Status Solidi Basic Res.*, vol. 253, no. 12, pp. 2351–2354, 2016, doi: 10.1002/pssb.201600232.

[260] S. Nappini *et al.*, “Graphene nanobubbles on TiO2 for in-operando electron spectroscopy of liquid-phase chemistry,” *Nanoscale*, vol. 9, no. 13, pp. 4456–4466, 2017, doi: 10.1039/c6nr09061c.

[261] L. Nguyen *et al.*, “X-ray Photoelectron Spectroscopy Studies of Nanoparticles Dispersed in Static Liquid,” *Langmuir*, vol. 34, no. 33, pp. 9606–9616, 2018, doi: 10.1021/acs.langmuir.8b00806.

[262] M. Al-Hada, M. Amati, H. Sezen, L. Cozzarini, and L. Gregoratti, “Photoelectron Spectromicroscopy Through Graphene of Oxidised Ag Nanoparticles,” *Catal. Letters*, vol. 148, no. 8, pp. 2247–2255, 2018, doi: 10.1007/s10562-018-2451-z.

[263] K. Cui and B. L. Wardle, “Breakdown of Native Oxide Enables Multifunctional, Free-Form Carbon Nanotube-Metal Hierarchical Architectures,” *ACS Appl. Mater. Interfaces*, vol. 11, no. 38, pp. 35212–35220, 2019, doi: 10.1021/acsami.9b08290.

[264] Z. Ullah, G. Witjaksono, I. Nawi, N. Tansu, M. I. Khattak, and M. Junaid, “A review on the development of tunable graphene nanoantennas for terahertz optoelectronic and plasmonic applications,” *Sensors (Switzerland)*, vol. 20, no.

5. 2020, doi: 10.3390/s20051401.

[265] F. Bonaccorso, Z. Sun, T. Hasan, and A. C. Ferrari, “Graphene photonics and optoelectronics,” *Nat. Photonics*, vol. 4, no. 9, pp. 611–622, 2010, doi: 10.1038/nphoton.2010.186.

[266] Y. Li, K. Tantiwanichapan, A. K. Swan, and R. Paiella, “Graphene plasmonic devices for terahertz optoelectronics,” *Nanophotonics*, vol. 9, no. 7. pp. 1901–1920, 2020, doi: 10.1515/nanoph-2020-0211.

[267] Y. Bin Chen, J. S. Liu, and P. Lin, “Recent trend in graphene for optoelectronics,” *J. Nanoparticle Res.*, vol. 15, no. 2, 2013, doi: 10.1007/s11051-013-1454-3.

[268] B. H. Nguyen and V. H. Nguyen, “Advances in graphene-based optoelectronics, plasmonics and photonics,” *Adv. Nat. Sci. Nanosci. Nanotechnol.*, vol. 7, no. 1, 2016, doi: 10.1088/2043-6262/7/1/013002.

[269] L. Cui, J. Wang, and M. Sun, “Graphene plasmon for optoelectronics,” *Reviews in Physics*, vol. 6. 2021, doi: 10.1016/j.revip.2021.100054.

[270] D. C. Elias *et al.*, “Control of graphene’s properties by reversible hydrogenation: Evidence for graphane,” *Science (80-.).*, vol. 323, no. 5914, pp. 610–613, 2009, doi: 10.1126/science.1167130.

[271] S. M. Ghafary, S. Hatamie, M. Nikkhah, and S. Hosseinkhani, “The effect of graphite sources on preparation of photoluminescent graphene nano-sheets for biomedical imaging,” *Nanomedicine J.*, vol. 4, no. 3, pp. 164–169, 2017.

[272] A. P. Johnson, H. V. Gangadharappa, and K. Pramod, “Graphene nanoribbons: A promising nanomaterial for biomedical applications,” *Journal of Controlled Release*, vol. 325. pp. 141–162, 2020, doi: 10.1016/j.jconrel.2020.06.034.

[273] M. R. Younis, G. He, J. Lin, and P. Huang, “Recent Advances on Graphene Quantum Dots for Bioimaging Applications,” *Frontiers in Chemistry*, vol. 8. 2020, doi: 10.3389/fchem.2020.00424.

[274] A. Bianco, “Graphene: Safe or toxic? the two faces of the medal,” *Angewandte Chemie - International Edition*, vol. 52, no. 19. pp. 4986–4997, 2013, doi: 10.1002/anie.201209099.

[275] V. C. Sanchez, A. Jachak, R. H. Hurt, and A. B. Kane, “Biological interactions of graphene-family nanomaterials: An interdisciplinary review,” *Chemical Research in Toxicology*, vol. 25, no. 1. pp. 15–34, 2012, doi: 10.1021/tx200339h.

[276] Y. Xu, Q. Wu, Y. Sun, H. Bai, and G. Shi, “Three-dimensional self-assembly of graphene oxide and DNA into multifunctional hydrogels,” *ACS Nano*, vol. 4, no. 12, pp. 7358–7362, 2010, doi: 10.1021/nn1027104.

[277] H. Ren *et al.*, “DNA cleavage system of nanosized graphene oxide sheets and copper ions,” *ACS Nano*, vol. 4, no. 12, pp. 7169–7174, 2010, doi: 10.1021/nn101696r.

[278] C. H. Lu, C. L. Zhu, J. Li, J. J. Liu, X. Chen, and H. H. Yang, “Using graphene to protect DNA from cleavage during cellular delivery,” *Chem. Commun.*, vol. 46, no. 18, pp. 3116–3118, 2010, doi: 10.1039/b926893f.

[279] A. V. Titov, P. Král, and R. Pearson, “Sandwiched graphene-membrane superstructures,” *ACS Nano*, vol. 4, no. 1, pp. 229–234, 2010, doi: 10.1021/nn9015778.

[280] J. Li *et al.*, “Lateral size of graphene oxide determines differential cellular uptake and cell death pathways in Kupffer cells, LSECs, and hepatocytes,” *Nano Today*, vol. 37, p. 101061, Apr. 2021, doi: 10.1016/j.nantod.2020.101061.

[281] S. Mullick Chowdhury, G. Lalwani, K. Zhang, J. Y. Yang, K. Neville, and B. Sitharaman, “Cell specific cytotoxicity and uptake of graphene nanoribbons,” *Biomaterials*, vol. 34, no. 1, pp. 283–293, Jan. 2013, doi: 10.1016/j.biomaterials.2012.09.057.

[282] N. P. Pampaloni *et al.*, “Single-layer graphene modulates neuronal communication and augments membrane ion currents,” *Nat. Nanotechnol.*, vol. 13, no. 8, pp. 755–764, Jun. 2018, doi: 10.1038/s41565-018-0163-6.

[283] G. Lalwani, S. C. Patel, and B. Sitharaman, “Two- and Three-Dimensional All-Carbon Nanomaterial Assemblies for Tissue Engineering and Regenerative Medicine,” *Ann. Biomed. Eng.*, vol. 44, no. 6, pp. 2020–2035, Apr. 2016, doi: 10.1007/s10439-016-1623-5.

[284] X. Shi, H. Chang, S. Chen, C. Lai, A. Khademhosseini, and H. Wu, “Regulating cellular behavior on few-layer reduced graphene oxide films with well-controlled reduction states,” *Adv. Funct. Mater.*, vol. 22, no. 4, pp. 751–759, 2012, doi: 10.1002/adfm.201102305.

[285] O. Akhavan and E. Ghaderi, “Toxicity of graphene and graphene oxide nanowalls against bacteria,” *ACS Nano*, vol. 4, no. 10, pp. 5731–5736, 2010, doi: 10.1021/nn101390x.

[286] G. Wang, F. Qian, C. W. Saltikov, Y. Jiao, and Y. Li, “Microbial reduction of graphene oxide by Shewanella,” *Nano Res.*, vol. 4, no. 6, pp. 563–570, 2011, doi: 10.1007/s12274-011-0112-2.

[287] S. Liu *et al.*, “Antibacterial activity of graphite, graphite oxide, graphene oxide, and reduced graphene oxide: Membrane and oxidative stress,” *ACS Nano*, vol. 5, no. 9, pp. 6971–6980, 2011, doi: 10.1021/nn202451x.

[288] M. F. El-Kady, Y. Shao, and R. B. Kaner, “Graphene for batteries, supercapacitors and beyond,” *Nat. Rev. Mater.*, vol. 1, no. 7, p. 16033, 2016, doi: 10.1038/natrevmats.2016.33.

[289] R. Mukherjee, A. V. Thomas, A. Krishnamurthy, and N. Koratkar, “Photothermally reduced graphene as high-power anodes for lithium-ion Batteries,” *ACS Nano*, vol. 6, no. 9, pp. 7867–7878, Sep. 2012, doi: 10.1021/nn303145j.

[290] H. Kim, K. Y. Park, J. Hong, and K. Kang, “All-graphene-battery: Bridging the gap between supercapacitors and lithium ion batteries,” *Sci. Rep.*, vol. 4, no. 1, pp. 1–8, Jun. 2014, doi: 10.1038/srep05278.

[291] N. Li, Z. Chen, W. Ren, F. Li, and H. M. Cheng, “Flexible graphene-based lithium ion batteries with ultrafast charge and discharge rates,” *Proc. Natl. Acad. Sci. U. S. A.*, vol. 109, no. 43, pp. 17360–17365, Oct. 2012, doi: 10.1073/pnas.1210072109.

[292] J. A. Rogers, T. Someya, and Y. Huang, “Materials and mechanics for stretchable electronics,” *Science (80-.).*, vol. 327, no. 5973, pp. 1603–1607, Mar. 2010, doi: 10.1126/science.1182383.

[293] Y. Meng *et al.*, “All-graphene core-sheath microfibers for all-solid-state, stretchable fibriform supercapacitors and wearable electronic textiles,” *Adv. Mater.*, vol. 25, no. 16, pp. 2326–2331, Apr. 2013, doi: 10.1002/adma.201300132.

[294] X. Yang, C. Cheng, Y. Wang, L. Qiu, and D. Li, “Liquid-mediated dense integration of graphene materials for compact capacitive energy storage,” *Science (80-.).*, vol. 341, no. 6145, pp. 534–537, Aug. 2013, doi: 10.1126/science.1239089.

[295] Y. Yang, S. Jeong, L. Hu, H. Wu, S. W. Lee, and Y. Cui, “Transparent lithium-ion batteries,” *Proc. Natl. Acad. Sci. U. S. A.*, vol. 108, no. 32, pp. 13013–13018, Aug. 2011, doi: 10.1073/pnas.1102873108.

[296] T. Chen, Y. Xue, A. K. Roy, and L. Dai, “Transparent and stretchable high-performance supercapacitors based on wrinkled graphene electrodes,” *ACS Nano*, vol. 8, no. 1, pp. 1039–1046, Jan. 2014, doi: 10.1021/nn405939w.

[297] W. Choi, I. Lahiri, R. Seelaboyina, and Y. S. Kang, “Synthesis of graphene and its applications: A review,” *Crit. Rev. Solid State Mater. Sci.*, vol. 35, no. 1, pp. 52–71, 2010, doi: 10.1080/10408430903505036.

[298] F. Schedin *et al.*, “Detection of individual gas molecules adsorbed on graphene,” *Nat. Mater.*, vol. 6, no. 9, pp. 652–655, Jul. 2007, doi: 10.1038/nmat1967.

[299] M. H. Chakrabarti *et al.*, “Progress in the electrochemical modification of graphene-based materials and their applications,” *Electrochim. Acta*, vol. 107, pp. 425–440, Sep. 2013, doi: 10.1016/j.electacta.2013.06.030.

[300] C. Shan, H. Yang, J. Song, D. Han, A. Ivaska, and L. Niu, “Direct electrochemistry of glucose oxidase and biosensing for glucose based on graphene,” *Anal. Chem.*, vol. 81, no. 6, pp. 2378–2382, Mar. 2009, doi: 10.1021/ac802193c.

[301] S. Alwarappan, A. Erdem, C. Liu, and C. Z. Li, “Probing the electrochemical properties of graphene nanosheets for biosensing applications,” *J. Phys. Chem. C*, vol. 113, no. 20, pp. 8853–8857, May 2009, doi: 10.1021/jp9010313.

[302] Y. Dan, Y. Lu, N. J. Kybert, Z. Luo, and A. T. C. Johnson, “Intrinsic response of graphene vapor sensors,” *Nano Lett.*, vol. 9, no. 4, pp. 1472–1475, Apr. 2009, doi: 10.1021/nl8033637.

[303] A. Matruglio *et al.*, “Contamination-free suspended graphene structures by a Ti-based transfer method,” *Carbon N. Y.*, vol. 103, pp. 305–310, Jul. 2016, doi: 10.1016/j.carbon.2016.03.023.

[304] G. Liu, W. Jin, and N. Xu, “Graphene-based membranes,” *Chem. Soc. Rev.*, vol. 44, no. 15, pp. 5016–5030, Jul. 2015, doi: 10.1039/c4cs00423j.

[305] P. Bhol, S. Yadav, A. Altaee, M. Saxena, P. K. Misra, and A. K. Samal, “Graphene-Based Membranes for Water and Wastewater Treatment: A Review,” *ACS Appl. Nano Mater.*, vol. 4, no. 4, pp. 3274–3293, Apr. 2021, doi: 10.1021/acsanm.0c03439.

[306] K. Celebi *et al.*, “Ultimate permeation across atomically thin porous graphene,” *Science (80-.).*, vol. 344, no. 6181, pp. 289–292, 2014, doi: 10.1126/science.1249097.

[307] M. Šiškins *et al.*, “Sensitive capacitive pressure sensors based on graphene membrane arrays,” *Microsystems Nanoeng.*, vol. 6, no. 1, pp. 1–9, Nov. 2020, doi: 10.1038/s41378-020-00212-3.

[308] R. S. Weatherup, “2D Material Membranes for Operando Atmospheric Pressure Photoelectron Spectroscopy,” *Top. Catal.*, vol. 61, no. 20, pp. 2085–2102, Nov. 2018, doi: 10.1007/s11244-018-1075-2.

[309] L. Marton, “Electron microscopy of biological objects,” *Phys. Rev.*, vol. 46, no. 6, pp. 527–528, Sep. 1934, doi: 10.1103/PhysRev.46.527.

[310] N. Kohyama, “Observation of the Hydrated Form of Tubular Halloysite by an Electron Microscope Equipped with an Environmental Cell,” *Clays Clay Miner.*, vol. 26, no. 1, pp. 25–40, Feb. 1978, doi: 10.1346/ccmn.1978.0260103.

[311] N. De Jonge, D. B. Peckys, G. J. Kremers, and D. W. Piston, “Electron microscopy of whole cells in liquid with nanometer resolution,” *Proceedings of the National Academy of Sciences of the United States of America*, 2009. https://www.researchgate.net/publication/313194755_Electron_microscopy_of_whole_cells_in_liquid_with_nanometer_resolution (accessed Nov. 14, 2021).

[312] T. L. Daulton, B. J. Little, K. Lowe, and J. Jones-Meehan, “In Situ Environmental Cell–Transmission Electron Microscopy Study of Microbial Reduction of Chromium(VI) Using Electron Energy Loss Spectroscopy,” *Microsc. Microanal.*, vol. 7, no. 6, pp. 470–485, Nov. 2001, doi: 10.1007/s10005-001-0021-3.

[313] P. L. Gai and J. J. Calvino, “Electron microscopy in the catalysis of alkane oxidation, Environmental control, and alternative energy sources,” *Annu. Rev. Mater. Res.*, vol. 35, pp. 465–504, Jun. 2005, doi: 10.1146/annurev.matsci.35.100303.122141.

[314] S. Thiberge, O. Zik, and E. Moses, “An apparatus for imaging liquids, cells, and other wet samples in the scanning electron microscopy,” *Rev. Sci. Instrum.*, vol. 75, no. 7, pp. 2280–2289, Jun. 2004, doi: 10.1063/1.1763262.

[315] A. P. Hitchcock, C. Morin, Y. M. Heng, R. M. Cornelius, and J. L. Brash, “Towards practical soft X-ray spectromicroscopy of biomaterials,” *J. Biomater. Sci. Polym. Ed.*, vol. 13, no. 8, pp. 919–937, 2002, doi: 10.1163/156856202320401960.

[316] T. H. Yoon, “Applications of soft x-ray spectromicroscopy in material and environmental sciences,” *Appl. Spectrosc. Rev.*, vol. 44, no. 2, pp. 91–122, 2009, doi: 10.1080/05704920802352531.

[317] P. Leidinger *et al.*, “Toward the perfect membrane material for environmental x-ray photoelectron spectroscopy,” *J. Phys. D. Appl. Phys.*, vol. 54, no. 23, p. 234001, 2021, doi: 10.1088/1361-6463/abe743.

[318] A. Kolmakov *et al.*, “Graphene oxide windows for in situ environmental cell photoelectron spectroscopy,” *Nat. Nanotechnol.*, vol. 6, no. 10, pp. 651–657, 2011, doi: 10.1038/nnano.2011.130.

[319] J. Kraus *et al.*, “Photoelectron spectroscopy of wet and gaseous samples through graphene membranes,” *Nanoscale*, vol. 6, no. 23, pp. 14394–14403, Nov. 2014, doi: 10.1039/c4nr03561e.

[320] D. J. Kelly *et al.*, “Nanometer Resolution Elemental Mapping in Graphene-Based TEM Liquid Cells,” *Nano Lett.*, vol. 18, no. 2, pp. 1168–1174, 2018, doi: 10.1021/acs.nanolett.7b04713.

[321] H. Guo, A. Yulaev, E. Strelcov, and A. Kolmakov, “SEM and Auger Electron Spectroscopy of Liquid Water through Graphene Membrane,” *Microsc. Microanal.*, vol. 23, no. S1, pp. 880–881, Jul. 2017, doi: 10.1017/s1431927617005062.

[322] Y. Han, K. X. Nguyen, Y. Ogawa, J. Park, and D. A. Muller, “Atomically Thin Graphene Windows That Enable High Contrast Electron Microscopy without a Specimen Vacuum Chamber,” *Nano Lett.*, vol. 16, no. 12, pp. 7427–7432, Dec. 2016, doi: 10.1021/acs.nanolett.6b03016.

[323] J. D. Stoll and A. Kolmakov, “Electron transparent graphene windows for environmental scanning electron microscopy in liquids and dense gases,” *Nanotechnology*, vol. 23, no. 50, Dec. 2012, doi: 10.1088/0957-4484/23/50/505704.

[324] R. S. Weatherup, B. Eren, Y. Hao, H. Bluhm, and M. B. Salmeron, “Graphene Membranes for Atmospheric Pressure Photoelectron Spectroscopy,” *J. Phys. Chem. Lett.*, vol. 7, no. 9, pp. 1622–1627, May 2016, doi: 10.1021/acs.jpclett.6b00640.

[325] C. Jiang *et al.*, “Thermo-optical arrays of flexible nanoscale nanomembranes freely suspended over microfabricated cavities as IR microimagers,” *Chem. Mater.*, vol. 18, no. 11, pp. 2632–2634, May 2006, doi: 10.1021/cm060416x.

[326] E. Ledwosinska, A. Guermoune, M. Siaj, and T. Szkopek, “Fabrication and characterization of suspended graphene membranes for miniature Golay cells,” in *Terahertz, RF, Millimeter, and Submillimeter-Wave Technology and Applications VI*, Mar. 2013, vol. 8624, p. 86240U, doi: 10.1117/12.2008974.

[327] A. A. Balandin *et al.*, “Superior thermal conductivity of single-layer graphene,” *Nano Lett.*, vol. 8, no. 3, pp. 902–907, 2008, doi: 10.1021/nl0731872.

[328] K. F. Mak, M. Y. Sfeir, Y. Wu, C. H. Lui, J. A. Misewich, and T. F. Heinz, “Measurement of the opptical conductivity of graphene,” *Phys. Rev. Lett.*, vol. 101, no. 19, 2008, doi: 10.1103/PhysRevLett.101.196405.

[329] J. S. Bunch *et al.*, “Impermeable atomic membranes from graphene sheets,” *Nano Lett.*, vol. 8, no. 8, pp. 2458–2462, 2008, doi: 10.1021/nl801457b.

[330] M. H. Griep *et al.*, “Enhanced Quality CVD-Grown Graphene via a Double-Plateau Copper Surface Planarization

Methodology," *Cryst. Growth Des.*, vol. 17, no. 11, pp. 5725–5731, 2017, doi: 10.1021/acs.cgd.7b00687.

[331] D. C. Marcano *et al.*, "Improved synthesis of graphene oxide," *ACS Nano*, vol. 4, no. 8, pp. 4806–4814, 2010, doi: 10.1021/nn1006368.

[332] D. Cohen-Tanugi and J. C. Grossman, "Water desalination across nanoporous graphene," *Nano Lett.*, vol. 12, no. 7, pp. 3602–3608, 2012, doi: 10.1021/nl3012853.

[333] G. H. Lee *et al.*, "High-strength chemical-vapor-deposited graphene and grain boundaries," *Science (80-.).*, vol. 340, no. 6136, pp. 1074–1076, 2013, doi: 10.1126/science.1235126.

[334] L. P. Ma, W. Ren, and H. M. Cheng, "Transfer Methods of Graphene from Metal Substrates: A Review," *Small Methods*, vol. 3, no. 7. 2019, doi: 10.1002/smtd.201900049.

[335] X. Li *et al.*, "Transfer of large-area graphene films for high-performance transparent conductive electrodes," *Nano Lett.*, vol. 9, no. 12, pp. 4359–4363, 2009, doi: 10.1021/nl902623y.

[336] Y. Chen, X. L. Gong, and J. G. Gai, "Progress and Challenges in Transfer of Large-Area Graphene Films," *Advanced Science*, vol. 3, no. 8. 2016, doi: 10.1002/advs.201500343.

[337] Z. Jakšić and J. Matovic, "Functionalization of artificial freestanding composite nanomembranes," *Materials (Basel).*, vol. 3, no. 1, pp. 165–200, 2010, doi: 10.3390/ma3010165.

[338] X. Peng, J. Jin, E. M. Ericsson, and I. Ichinose, "General method for ultrathin free-standing films of nanofibrous composite materials," *J. Am. Chem. Soc.*, vol. 129, no. 27, pp. 8625–8633, 2007, doi: 10.1021/ja0718974.

[339] J. Matovic and Z. Jaki, "Nanomembrane: A New MEMS/NEMS Building Block," in *Micro Electronic and Mechanical Systems*, 2009.

[340] Y. Kim *et al.*, "Strengthening effect of single-atomic-layer graphene in metal-graphene nanolayered composites," *Nat. Commun.*, vol. 4, 2013, doi: 10.1038/ncomms3114.

[341] I. A. Ovid'ko, "Metal-graphene nanocomposites with enhanced mechanical properties: A review," *Reviews on Advanced Materials Science*, vol. 38, no. 2. pp. 190–200, 2014.

[342] C. Zhang, C. Lu, L. Pei, J. Li, R. Wang, and K. Tieu, "The negative Poisson's ratio and strengthening mechanism of nanolayered graphene/Cu composites," *Carbon N. Y.*, vol. 143, pp. 125–137, 2019, doi: 10.1016/j.carbon.2018.10.097.

[343] B. Hwang *et al.*, "Role of graphene in reducing fatigue damage in Cu/Gr nanolayered composite," *Nano Lett.*, vol. 17, no. 8, pp. 4740–4745, 2017, doi: 10.1021/acs.nanolett.7b01431.

[344] Y. Zhao, X. Liu, J. Zhu, and S. N. Luo, "Unusually high flexibility of graphene-Cu nanolayered composites under bending," *Phys. Chem. Chem. Phys.*, vol. 21, no. 31, pp. 17393–17399, 2019, doi: 10.1039/c9cp02980j.

[345] R. Rezaei, "Tensile mechanical characteristics and deformation mechanism of metal-graphene nanolayered composites," *Comput. Mater. Sci.*, vol. 151, pp. 181–188, 2018, doi: 10.1016/j.commatsci.2018.05.004.

[346] M. J. Gilleland and M. L. Bender, "Kinetics of α chymotrypsin dimerization," *Journal of Biological Chemistry*, 1976. http://srdata.nist.gov/xps.

[347] M. C. Biesinger *et al.*, "Quantitative chemical state XPS analysis of first row transition metals, oxides and hydroxides," in *Journal of Physics: Conference Series*, 2008, vol. 100, no. Part 1, doi: 10.1088/1742-6596/100/1/012025.

[348] M. C. Biesinger, L. W. M. Lau, A. R. Gerson, and R. S. C. Smart, "Resolving surface chemical states in XPS analysis of first row transition metals, oxides and hydroxides: Sc, Ti, V, Cu and Zn," *Appl. Surf. Sci.*, vol. 257, no. 3, pp. 887–898, 2010, doi: 10.1016/j.apsusc.2010.07.086.

[349] M. P. Seah and W. A. Dench, "Quantitative electron spectroscopy of surfaces: A standard data base for electron inelastic mean free paths in solids," *Surf. Interface Anal.*, vol. 1, no. 1, pp. 2–11, Feb. 1979, doi: 10.1002/SIA.740010103.

[350] T. S. Monteiro, P. Kastytis, L. M. Gonçalves, G. Minas, and S. Cardoso, "Dynamic wet etching of silicon through isopropanol alcohol evaporation," *Micromachines*, vol. 6, no. 10, pp. 1534–1545, 2015, doi: 10.3390/mi6101437.

[351] C. Chang *et al.*, "Etching submicrometer trenches by using the Bosch process and its application to the fabrication of antireflection structures," *J. Micromechanics Microengineering*, vol. 15, no. 3, pp. 580–585, 2005, doi: 10.1088/0960-1317/15/3/020.

[352] S. BRODETSKY, *Theory of Plates and Shells*, vol. 148, no. 3760. 1941.

[353] C. Cao *et al.*, "Role of graphene in enhancing the mechanical properties of TiO2/graphene heterostructures," *Nanoscale*, vol. 9, no. 32, pp. 11678–11684, 2017, doi: 10.1039/c7nr03049e.

[354] A. Castellanos-Gomez, M. Poot, G. A. Steele, H. S. J. Van Der Zant, N. Agraït, and G. Rubio-Bollinger, "Elastic properties of freely suspended MoS2 nanosheets," *Adv. Mater.*, vol. 24, no. 6, pp. 772–775, 2012, doi: 10.1002/adma.201103965.

[355] A. Castellanos-Gomez, V. Singh, H. S. J. Van Der Zant, and G. A. Steele, "Mechanics of freely-suspended ultrathin layered materials," *Ann. Phys.*, vol. 527, no. 1–2, pp. 27–44, 2015, doi: 10.1002/andp.201400153.

[356] A. I. Stadnichenko, L. S. Kibis, D. A. Svintsitskiy, S. V. Koshcheev, and A. I. Boronin, "Application of RF discharge in oxygen to create highly oxidized metal layers," *Surf. Eng.*, vol. 34, no. 1, pp. 1–5, Jan. 2018, doi: 10.1179/1743294415Y.0000000010.

[357] D. C. Duffy, J. C. McDonald, O. J. A. Schueller, and G. M. Whitesides, "Rapid prototyping of microfluidic systems in poly(dimethylsiloxane)," *Anal. Chem.*, vol. 70, no. 23, pp. 4974–4984, 1998, doi: 10.1021/ac980656z.

[358] J. Bin Wu, M. L. Lin, X. Cong, H. N. Liu, and P. H. Tan, "Raman spectroscopy of graphene-based materials and its applications in related devices," *Chem. Soc. Rev.*, vol. 47, no. 5, pp. 1822–1873, Mar. 2018, doi: 10.1039/c6cs00915h.

[359] F. F. Settembrini *et al.*, "Anisotropic straining of graphene using micropatterned SiN membranes," *APL Mater.*, vol. 4, no. 11, p. 116107, Nov. 2016, doi: 10.1063/1.4967937.

[360] M. B. B. S. Larsen, D. M. A. Mackenzie, J. M. Caridad, P. Bøggild, and T. J. Booth, "Transfer induced compressive strain in graphene: Evidence from Raman spectroscopic mapping," *Microelectron. Eng.*, vol. 121, pp. 113–117, Jun. 2014, doi: 10.1016/j.mee.2014.04.038.

[361] O. Frank *et al.*, "Graphene under uniaxial deformation: A raman study," *NANOCON 2011 - Conf. Proceedings, 3rd Int. Conf.*, pp. 225–230, 2011.

[362] Tydex, "TYDEX THz Materials." http://www.tydexoptics.com/products/thz_optics/thz_materials/ (accessed Nov. 29, 2021).

[363] Y. Wang, Z. Zhao, Z. Chen, and L. Wang, "Characterization of Golay detector for the absolute power measurement of terahertz radiation," *Int. Conf. Infrared, Millimeter, Terahertz Waves, IRMMW-THz*, 2012, doi: 10.1109/IRMMW-THz.2012.6380076.